COMPUTATIONAL AND EXPERIMENTAL STUDIES OF SOLIDS IN THE AMMONIA – WATER SYSTEM

A thesis submitted to the University of London

for the degree of Doctor of Philosophy

by

Andrew Fortes

Department of Earth Sciences,

University College London,

Gower Street, London WC1E 6BT, United Kingdom

January 2004

ABSTRACT

This thesis reports the results of first-principles computational studies of thirteen crystalline structures in the H_2O-NH_3 system. This includes eight low- and high-pressure polymorphs of pure water ice, two polymorphs of solid ammonia, and three low-pressure stoichiometric ammonia hydrates. These simulations have been used to determine the athermal equation of state (EoS) of each phase.

Where empirical data was lacking, experiments have been undertaken. Hence, this thesis also reports the results of time-of-flight neutron scattering studies of deuterated ammonia dihydrate powders down to 4 K, and up to a maximum pressure of 8.6 GPa.

In addition, I have developed a flexible and accurate planetary model that can be used to calculate the triaxial shape and gravitational field of any object, regardless of size or composition, given an assumed mineralogical constitution and provided the EoS of said minerals are known. The EoS parameters found in this work have therefore been used to model the structure and thermal evolution of icy moons orbiting Saturn in anticipation of the Cassini spacecraft arriving at Saturn in mid-2004. Models of Rhea, Saturn's second largest moon, suggest that its volatile component is likely to contain > 3 weight percent ammonia, but that one is unlikely to be able to constrain the bulk chemistry of the ice mantle from Cassini flyby data.

ACKNOWLEDGEMENTS

I would like to acknowledge the UCL Graduate School for financial support awarded in the form of a Postgraduate Scholarship.

My Ph.D Supervisors, Dr Lidunka Vočadlo, Dr Ian Wood, and Dr John Brodholt, provided me with the perfect mix of expertise and support throughout my studentship. Dr Vočadlo has pushed me forwards, despite my futile resistance, since I began my full-time undergraduate studies here seven years ago, championing my first publication and exhorting me to go to meetings and give talks and lectures, etc. All of which has been very good for me.

The following individuals have also provided support, advice, or helpful criticism: Prof. David Price (UCL), Prof. John Guest (UCL), Dr Hilary Downs (Birkbeck), Dr Ian Crawford (UCL), Dr H. Donald Jenkins (Warwick), Dr Maria Alfredsson (UCL/RI), and Dr Francis Nimmo (UCL/UCLA). From ISIS, I thank Dr Kevin Knight and Bill Marshall for their great efforts and patience during my experimental time on the HRPD and PEARL instruments. I would also like to thank John Dreyer and his technical staff at ISIS.

Prof. Claudio Vita-Finzi has provided me with unswerving friendship and tutelage, for which I am most grateful. His efforts to curtail the flowery verbiage in my writing have met with mixed contrafibularity.

I'd like to thank my fellow postgraduate students, who have shared a blast furnace….I mean office….over the past three years and kept me from being a total stranger to human interaction; namely Louise Bishop, Peter Grindrod, Roberto Bugiolacchi, Terry Hackwill, Joyce Vetterlein, Dr Matt Balme, and the remarkable Dr Emma Bowden.

I cannot even begin to thank my parents for their love and support in spite of their own troubles.

This work is dedicated to my Mum, who passed away in
November 2002 after a long illness.

CONTENTS

Chapter 1: Icy moons and the ammonia-water system

Chapter 2: Computational methods: VASP and DFT

Chapter 3: Water ices at high-pressure: ices VIII, X and beyond

Chapter 4: Water ices at low-pressure: ices II and XI

Chapter 5: Simulation of solid ammonia: Phases I and IV

Chapter 6: Simulation of ammonia monohydrate and ammonia hemihydrate

Chapter 7: Simulation of ammonia dihydrate

Chapter 8: Neutron diffraction experiments

Chapter 9: Discussion and implications: Planetary modelling

LIST OF FIGURES

LIST OF TABLES

CHAPTER ONE

THE AMMONIA-WATER SYSTEM

1 Introduction

This thesis is concerned with the physical properties of crystalline molecular compounds of ammonia and water, in particular ammonia dihydrate; the extent to which we can accurately compute their properties from first principles, and how these properties can be applied to understanding the interiors of planetary bodies that are rich in volatiles (i.e., the icy moons of the Gas Giant planets).

I shall begin by outlining the rationale behind this particular work program (Sec. 1.1), following this with an overview of the methods used to complete the work (Sec. 1.2), and ending with a description of the work I have done towards this thesis (Sec. 1.3). These subsections pose the vital questions; what did I do, how, and why?

1.1 Justification for studying the Ammonia-Water system

There are two reasons for carrying out a study of solids in the NH_3-H_2O system. The first is microscopic, and relates to the force that binds these molecules together, the hydrogen bond (Sec. 1.1.1). The second is macroscopic, and relates to the role these solids play as the building blocks of planets and moons in the outer solar system (Sec. 1.1.2).

1.1.1 The Hydrogen Bond

The hydrogen bond, in the sense first suggested by Latimer and Rodebush (1920), and subsequently defined by Pauling (1939), constitutes an interaction between a hydrogen atom (^{1}H, ^{2}D, or ^{3}T) and another negatively polarized atom, such that the hydrogen forms a 'bridge' between a donor atom (denoted 'D') and an acceptor atom (the aforementioned negatively polarized atom, denoted 'A'), as shown in Figure 1.1 below. This arrangement is written as D-H…A, where D-H is a strong covalent bond and H…A is the hydrogen bond.

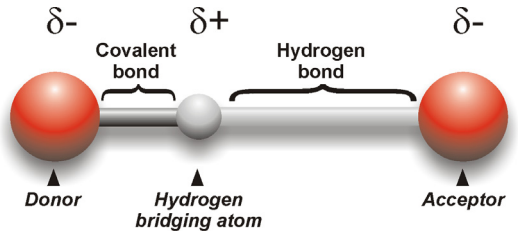

Figure 1.1. Cartoon illustration of a hydrogen bond. The δ- and δ+ denote small electrical charges that occur on formation of the bond. The covalent bond is typically 0.97 – 1.03 Å long, whereas the hydrogen bond is typically 1.75 – 2.50 Å long.

Hydrogen bonds are very weak interactions in comparison with covalent bonds; for example, to break the O-H covalent bond requires 498 kJ mol^{-1}, whereas the O-H…O hydrogen bond requires just 21 kJ mol^{-1}. Although there is a considerable range of hydrogen bond types (Gilli and Gilli 2000: Lutz 2003), this thesis is only concerned with two kinds of hydrogen bond, and two donor/acceptor species. These species are nitrogen and oxygen, and the bond types are homonuclear and heteronuclear. Homonuclear hydrogen bonds act between like species, i.e., when donor and acceptor are the same atom (O-H…O and N-H…N, for example). Heteronuclear hydrogen bonds act between unlike species, as in the case of O-H…N and N-H…O.

These four intermolecular bonds, O-H…O, O-H…N, N-H…O, and N-H…N, are arguably among the most important in chemistry. The properties of the most abundant liquid at the Earth's surface, the 'universal solvent,' water, are determined by the O-H…O hydrogen bond. Without it, life as we know it would be impossible; its melting and boiling points would be more than 200 K lower (see box overleaf). Indeed, hydrogen bonds alter the melting and boiling points, as well as the crystal structures, of many condensed phases, and allow for a wide range of polymorphic diversity (Scheiner 1997).

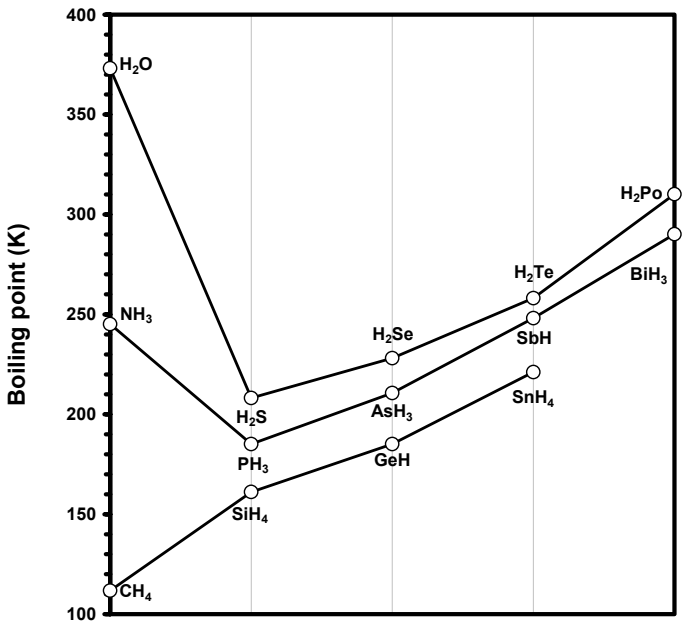

Figure 1.2. The boiling points of group 14 (bottom), group 15 (middle) and group 16 (top) hydrides: Plumbane, PbH_4 decomposes prior to boiling and is not shown. Moving down the periodic table, left to right.

As Figure 1.2 shows, there is a distinct trend in the boiling point of hydrides arising from the increasing atomic mass as one moves down the periodic table (to the right in Fig. 1.2). Methane, CH_4, which is not hydrogen bonded, follows the trend. However, ammonia, NH_3, which is weakly hydrogen bonded has a boiling point much higher than expected, and water, which is strongly hydrogen bonded, has a boiling point ~ 200 K above the expected value. The bonding strength is revealed in the enthalpy of vaporisation, ΔH_{vap}: CH_4, MP = 90.70 K, BP = 111.67 K , ΔH_{vap} = 8.2 kJ mol^{-1}: NH_3, MP = 195.41 K, BP = 239.82 K, ΔH_{vap} = 27.4 kJ mol^{-1}: H_2O, MP = 273.15 K, BP = 373.15 K, ΔH_{vap} = 40.7 kJ mol^{-1}. Moreover, the bonding influences the crystal structure; methane is a close-packed face centred cubic crystal, ammonia is pseudo-close-packed, and water ice has a low-density tetrahedral structure.

The remaining three hydrogen bonds (O-H…N, N-H…O, and N-H…N) play a central role in biology too. Hydrogen bonds between amine and hydroxyl groups form the scaffolding that holds proteins and enzymes in shape (Figs. 1.3a and b). Such hydrogen bonds also link together the nucleic acid base pairs in DNA and RNA. Without the N-H…O bond there could be no genetics.

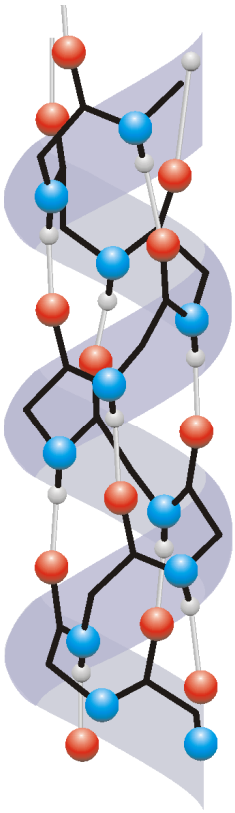

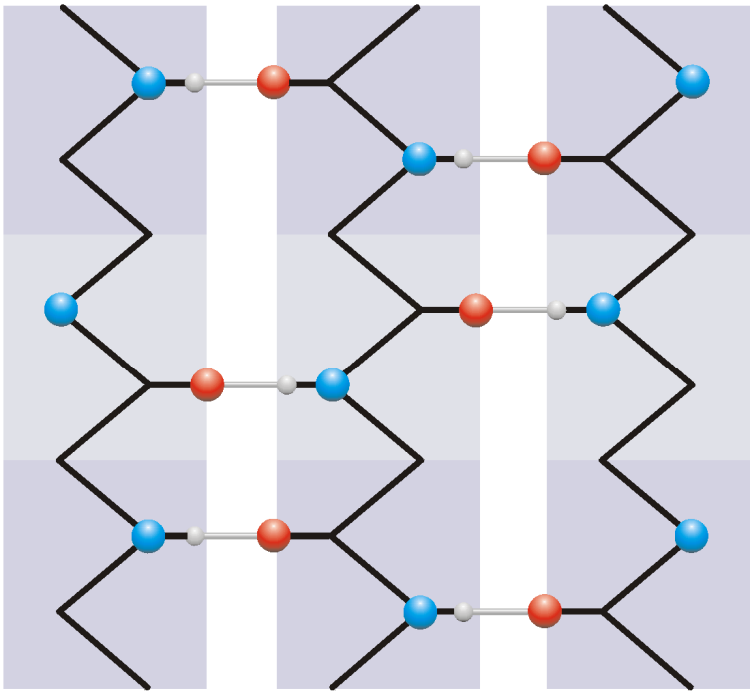

Above left, Fig. 1.3a, the secondary protein α-helix structure supported by N-H…O hydrogen bonds (light grey rods). N in blue, O in red, H in grey. The C-N polypeptide backbone, and C-O bonds, are shown by the thick black line. All other substituents and hydrogen atoms are omitted for clarity.

Above right, Fig. 1.3b, the secondary protein β-pleated sheet structure, showing hydrogen bonds between neighbouring polypeptide ribbons. These ribbons are corrugated in the plane of the paper; light squares are tilting down towards the top of the page, and the darker squares tilt down towards the bottom of the page.

Hydrogen bonded interactions also control the response of a structure to external changes in conditions; increases in pressure, raising or lowering of temperature. Because hydrogen bonds are rather weak, hydrogen bonded solids tend to be quite 'squashy;' that is, they have a low incompressibility. They also tend to have large thermal expansivities. Furthermore, since hydrogen bonding in some crystals has a directional bias, these properties (incompressibility and thermal expansivity) can be strongly anisotropic (Boldyreva 2003).

Under high pressures, hydrogen bonds change their character, usually becoming stronger, such that the bridging hydrogen moves further away from the donor until it is located midway between the donor and acceptor atoms. This process, due to the low mass of the hydrogen atom, is controlled by quantum phenomena such as tunnelling, and so observation of hydrogen bond centering is a sensitive test of quantum mechanical theory.

Clearly, there is a necessity to be able to study these types of hydrogen bonds at a microscopic level. The only practical means to study the potential energy phase-space associated with a given hydrogen bond is to carry out accurate computer simulations based on the fundamental equations of matter via quantum mechanics (the so-called *ab initio* method). Conventional computational quantum chemistry (correlated Hartree-Fock, see Ch.2: Sec. 2.2.2) is extraordinarily good at simulating hydrogen bonds (Scheiner 1997). However, this method scales as the fourth power (or higher) of the number of electrons (N) in the system, and is thus somewhat restricted in scope. Density functional theory (Ch 2: Sec. 2.2.3) achieves the same goal with a much lower power scaling in N (N^3, i.e., it is much more efficient) at the expense of introducing certain approximations, as I will discuss in Sec. 1.2. The ability of density functional theory to deal with hydrogen bonds is a problem of contemporary interest (Scheiner 1997: Koch and Holthausen 2001), and it is in part critically to test this ability that I have done this work.

Solids in the ammonia-water system are the simplest hydrogen bonded solids known. And yet there is a richness of bond types and polymorphism belied by that apparent simplicity. In the end member phases one finds homonuclear hydrogen bonds (i.e., O-H...O and N-H...N) of differing strengths; in water ice they are strong (~20 kJ mol^{-1}), in ammonia they are weak (<10 kJ mol^{-1}). In the ammonia hydrates one finds both homo- and heteronuclear hydrogen bonds (O-H...N and/or N-H...O). Furthermore, in the polymorphs of water and ammonia, one encounters a range of hydrogen bond geometries, from almost perfectly linear (ice VIII: O-$\hat{H}$-O ≈ 180°) to highly strained (ice II: O-$\hat{H}$-O = 166° - 178°).

There can be little doubt that the ammonia-water system is fertile ground for a density functional theory study of hydrogen-bonded solids, particularly when one considers that these hydrogen bonds control the structure and function of our own cellular building blocks, as well as the structure and dynamics of planets, as described next.

1.1.2 The Icy Bodies of our Solar System

The Gas Giant planets of the outer Solar System, Jupiter, Saturn, Uranus and Neptune, are each accompanied by a retinue of satellites that contain a significant component of condensed volatiles, dominantly water ice. We know this because the spectroscopic signature of water ice dominates their surfaces (Brown and Cruickshank 1997), and because of their low bulk density (~1000-1500 kg m^{-3}) as determined from observations of their orbital motions (e.g., Jacobson 2003). These icy moons range in diameter from a few kilometres across to over 5200 km (larger than the planet Mercury; Fig. 1.4).

Figure 1.4: A graphical comparison of the relative sizes (diameters in kilometres) of the largest moons of the solar system and the smallest planets. Reproduced courtesy of Calvin J. Hamilton.

In addition, icy bodies of varying sizes dominate the outer reaches of the solar system beyond Neptune. The largest of these is Pluto (and its moon Charon), but many icy bodies up to 1000km across populate the region beyond Neptune. These are often referred to as Kuiper-Edgeworth objects. In total, there may be several hundred Earth masses of icy materials in the outer solar system.

The satellites of the Gas Giants were surveyed in varying levels of detail during the 'Grand Tour' of the Voyager 1 and 2 spacecraft (1979-1989). The satellites of Jupiter have been studied in detail by the Galileo spacecraft (1995-2003), and the Saturnian system is due to be observed during the four-year orbital tour of the Cassini spacecraft (2004-2008).

Spectroscopic observations and disc-resolved photometry from Earth-based telescopes (including orbiting facilities such as the Hubble Space Telescope) remain our best source of data on the distribution and composition of volatiles on the surface of Pluto, Charon and Titan (e.g., Coustenis *et al*., 2001, 2003). Monostatic radar observations from Earth-based radio telescopes have also shed light on the composition and regolith structure of the icy Galilean moons and Titan (e.g., Campbell *et al*., 2002).

Such observations, from spacecraft or Earth-based telescopes, reveal that the majority of icy bodies with diameters greater than ~ 400 km show signs of extensive geological activity; in some cases there is evidence for the persistence of such activity to the present day. This is difficult, if not impossible, to reconcile with a pure H_2O composition for the volatile part of these objects, particularly at the lower end of the size range. At outer solar system temperatures (30-120K) water ice is amongst the most refractory of condensed volatile minerals (CVM's).

The energy budget (e.g., radiometric heating, accretional heating, and/or tidal dissipation) of most icy bodies is insufficient to melt a pure water ice mantle (Schubert *et al*., 1986). One would therefore expect icy bodies to exhibit only ancient, crater-saturated, surfaces dating to the end of the heavy bombardment era, circa 3.5 billion years ago. This is most certainly not the case (see Figs. 1.5 – 1.11); evidence is seen for widespread endogenic alteration, the eruption of fluids onto the surface, for example, causing flooding of cratered landscapes (Croft and Soderblom 1991: Schenk 1991: Kargel and Pozio 1996: Prieto and Kargel 1997). However, a cosmically abundant molecule such as ammonia can lower the melting temperature of the binary mixture by up to 100K (as can be seen on Fig. 1.13) bringing partial melting of icy bodies within the realm of their energy budgets, and hence plausibility. The resultant melts are buoyant with respect to their surroundings and the liquid may be extruded at the surface, or be intruded as high-level plutons. Such 'magmatic' processes where the liquid is water-based are usually called *cryovolcanism*. In sufficiently large icy bodies, the presence of ammonia may allow melt to persist as a global subsurface ocean, or 'aquasphere', throughout geological time (Carr *et al*., 1998: Pappalardo *et al*., 1999: Spohn and Schubert 2003), and perhaps this may occur even in smaller bodies (Ruiz and Torices 2000: England 2002). Certainly, very strong evidence for such aquaspheres is seen in the induced magnetic response of the Galilean moons to Jupiter's time-varying field (Zimmer *et al*., 2000: Kivelson *et al*., 2002).

But what is it that leads Planetary Scientists to believe that ammonia is present in these icy bodies, and is there any evidence to support that hypothesis? The first question is answered in Section 1.1.2.1, and the second is answered in Sections 1.1.2.2 - 5.

1.1.2.1 Models of icy moon formation

The solar system is believed to have formed circa 4.6 billion years ago from the collapse of an interstellar cloud of gas and dust, termed the presolar cloud. This cloud consisted of silicates, carbonaceous grains, metallic grains, ices and highly volatile gases (e.g., hydrogen and helium). The composition of the presolar cloud is reasonably well understood from studies of existing interstellar matter. Conservation of angular momentum caused the cloud to spin up as it shrank, with the result that the material in the cloud collected into a disk surrounding the proto-Sun. Gravitational and shock heating meant that most of the constituents of the disk were vaporised within ~ 30 A.U. (1 A.U. is the mean Earth-Sun distance, 149,597,870 km) of the proto-Sun (Chick and Casen 1997). Cooling of this primitive solar nebula (PSN) allowed gases to condense into solid grains, the composition of which, as a function of radial distance from the proto-Sun, depended on the temperature and pressure gradients in the PSN (Wood 2000). The abundances of the elements hydrogen, carbon, nitrogen and oxygen in the Sun (and thus the PSN) are well known (e.g., Anders and Grevesse 1989). The way in which these elements

combine to form molecules depends on the oxidation state of the PSN. Early models of PSN condensation in the outer solar system (Lewis 1971, 1972) indicated that nitrogen in the form of ammonia would be an important condensate in the outer PSN, becoming incorporated into icy planet mantles and leading to low temperature melting and cryovolcanism.

For carbon and nitrogen, the two gas phase reactions which govern the oxidation state of the most abundant species in a medium dominated by hydrogen gas are:

$$CO + 3\ H_2 \cdot CH_4 + H_2O \quad (1.1)$$

$$N_2 + 3\ H_2 \cdot 2\ NH_3 \quad (1.2)$$

Under conditions of equilibrium in the outer PSN, the stable compounds will be the products of reactions 1.1 and 1.2 (those species on the right); CH_4, H_2O and NH_3. In the warmer climes, within 5-10 A.U. of the proto-Sun, the reactants are favoured and the equilibrium is driven towards CO, H_2, and N_2. However, Lewis and Prinn (1980) recognised that, at the low temperatures in the outer PSN, the forward reaction to form CH_4 and NH_3, while favoured, is kinetically inhibited, since it occurs so slowly that the yield of reactants is too small (on the timescale of planetary formation) for them to be significant condensates. This kinetic inhibition model postulates that C and N were in the form of CO and N_2 throughout the PSN.

However, it was quickly perceived that the warmer, denser subnebulae surrounding each of the proto-gas-giant planets might allow the partial reduction of CO to CH_4 and N_2 to NH_3 (i.e., a small but significant yield from reactions 1.1 and 1.2 over the timescale of planet formation). Until very recently, this was the accepted model for the origin of methane and ammonia beyond 10 A.U. from the Sun (from the orbit of Saturn outwards). At Jupiter, nebula conditions were probably too warm to allow condensation of ammonia.

The model predicts a large inventory of ammonia in Titan's interior, 18 ± 6 wt% NH_3 (Hunten *et al*., 1984). A proportion of this NH_3 will have been outgassed during the latter stages of Titan's accretion and during differentiation of the interior. The outgassed NH_3 is thought to have been converted to N_2 by photolysis, radiolysis and thermolytic destruction in meteorite impacts (Atreya *et al*., 1978: Lunine and Stevenson 1987: McKay *et al*., 1988: Zahnle *et al*., 1992). This is the ultimate source of Titan's present N_2 atmosphere. Volatile-rich models of Titan, containing > 5 wt% NH_3, retain subsurface oceans of eutectic ammonia-water solution (32 wt% NH_3) which decouple the crust and mantle (Grasset and Sotin 1996: Grasset *et al*., 2000: Sohl *et al*., 2001). Such a subsurface ocean has been investigated as a possible biological habitat (Fortes 2000: Simakov 2001). However, volatile-rich models of Titan containing liquid subshells are inconsistent with the observed orbital eccentricity (Sohl *et al*., 2001), since frictional damping is greatly enhanced in a decoupled crust.

It has recently been shown (Mousis *et al*., 2002a) that the assumptions regarding the structure of the PSN and embedded subnebulae employed by Lewis and Prinn (1980), and Prinn and Fegley (1981), are incorrect. The new turbulent evolutionary model shows that the yield of CH_4 and NH_3 would actually have been insignificant even in the warm, dense Saturnian subnebula. Mousis *et al*. (2002a) conclude that the materials which went to form the saturnian satellites probably contained small quantities of primordial CH_4 and NH_3 from the PSN in roughly the same abundances as the presolar cloud; i.e., $CO / CH_4 \approx 5$ and $N_2 / NH_3 \approx 3$. This being the case, the mass fraction of NH_3 in Titan's mantle would have been just 1.6 wt% NH_3, all of which would have been outgassed from the interior, converted to N_2 and lost from the atmosphere over the last 4.6 Ga. In other words, assuming $N_2 / NH_3 = 3$ means that *Titan presently contains essentially no ammonia at all*. The authors admit that they have ignored the catalytic effect of iron grains in the PSN (a phenomenon which is exploited in the commercial production of ammonia), and the possibility that other grain surface reactions could yield $N_2 / NH_3 < 1$ (e.g., Ruffle and Herbst 2000). For example, taking $N_2 / NH_3 = 0.1$ yields a mass fraction of ammonia in Titan's mantle of 10.9 wt % NH_3. The majority of this would still be present in Titan's interior as an ammonia-water ocean and perhaps as polymorphs of crystalline ammonia dihydrate.

From these recent findings, it becomes apparent that forward modelling cannot determine unambiguously the oxidation state of nitrogen incorporated into the icy moons of Saturn. However, the oxidation state of nitrogen in the PSN will have mirrored the oxidation state of carbon; reduced carbon in the form of methane certainly does occur in Titan's atmosphere and provides an important clue to the ammonia abundance in the moons of Saturn.

1.1.2.2 Atmospheric spectroscopy

Titan's atmosphere is known to contain several wt % CH_4 (Courtin *et al*., 1995) which is constantly being destroyed by electromagnetic and particle radiation from the Sun, Saturn's magnetosphere, and from interstellar space (Johnson 1990). In this way CH_4 is converted to longer chain, and undersaturated, hydrocarbons that appear as a haze in the upper atmosphere (Sagan and Thompson 1984) and are likely to snow out onto the surface. The rate of CH_4 destruction in the atmosphere of Titan is known, and provides a lifetime for the remaining atmospheric inventory of ~ 30 million years (Yung *et al*., 1984). In order to sustain this loss rate for > 4 billion years requires a resupply mechanism from an initial reservoir several hundred times larger than the present atmospheric inventory, located either at the surface (liquid methane seas or crater lakes; Lorenz and Lunine 1997), or below the surface (a methane aquifer

or mantle outgassing). Since the spectroscopically observed ratio CH_4 / CO in Titan's atmosphere is currently ≈ 1000 (Hidayat *et al*., 1998), and must have been larger in the past, then one can deduce that Titan did indeed accrete a large volume of CH_4 from the Saturnian subnebula, and that this subnebula must have been sufficiently reducing for similarly large volumes of ammonia to be present. This being the case, we would expect the vast majority of the nitrogen incorporated into Titan to be in the form of NH_3 and not N_2. Spectroscopy also reveals that nitrogen isotopes in Titan's atmosphere have been strongly fractionated, ^{14}N / ^{15}N ≈ 60[1] (Lammer *et al*., 2000), which is taken to imply the loss of at least 100 times the present atmospheric inventory of N_2. That this has occurred whilst preserving the ^{12}C / ^{13}C ratio at (or near) its protosolar value demonstrates the existence of a distinct carbon reservoir which is separate from, but which can contribute to, the atmosphere (Lunine *et al*., 1999), further proving that Titan accreted a large volume of CH_4 (and hence NH_3).

Additional confirmation comes from the atmospheric argon abundance. If N_2 were accreted rather than NH_3, then this would need to be achieved by trapping in condensing water ice, and since Ar is trapped in the same proportions as N_2, this mechanism leads to an Ar/N ratio much larger than is actually observed (Owen 2000).

Hence, spectroscopic observations of the atmosphere of Titan lead to the conclusion that Titan is an ammonia-rich body (circa 5-15 wt% NH_3 in the condensed volatile component), and by extension so are the other Saturnian moons. Similar arguments apply to the moons of Uranus and Neptune.

1.1.2.3 Surface spectroscopy

If we are to argue for a significant admixture of ammonia in icy moons, resulting in cryovolcanism by ammonia-water solutions, it seems reasonable to assume that absorptions due to ammonia hydrates will be seen in reflection spectra of their surfaces.

However, the signatures of ammonia hydrates are virtually non-existent in spectra of most icy planet surfaces. For the majority there are upper limits on surface abundances (e.g., Clark *et al*., 1984), but Charon remains the only location where features attributable to ammonia hydrates have been seen (Brown and Calvin 2000: Dumas *et al*., 2001). Recent work on weak temperature-dependent features in the spectrum of ammonia-water ices has led to the suggestion that spectra of the icy Galilean moons need to be revisited (Dalton *et al*., 2001) to confirm previously reported observations of ammonia hydrates (e.g., Johnson and McCord 1971: Calvin

[1] The $^{14}N/^{15}N$ ratio in the Earth's atmosphere is 273; in the martian atmosphere, where considerable N_2 has been lost, the ratio is ~170 (A.O. Nier & M. B. McElroy, (1977) *J. Geophys. Res*. **82**, 4341).

et al., 1995). Work on the radiation weathering of planetary ices (Johnson 1990, 1996) has shown that ammonia is always preferentially depleted in surface layers (Lanzerotti *et al*., 1984: Strazulla and Palumbo 1998). This would explain why ammonia hydrates are apparently never seen (or exist in quantities below present detection limits) on most icy bodies. The detection of ammonia hydrates on Charon may indicate that they are very abundant in the regolith, or have been emplaced recently.

A combination of factors may lead to our inability conclusively to detect ammonia hydrates, apart from radiation weathering. Cooling cryolava flows will crystallise water ice first (*c*.*f*., Fig. 1.13), perhaps forming a crust which acts to conceal later-forming ammonia hydrates. Such hydrates might only be exposed by meteorite impacts. In other words, the areal abundance of ammonia hydrates, even where there are extensive flows, could make a near negligible contribution to the disk-integrated spectrum (the observations to date are not spatially resolved). It remains possible that high spatial resolution (>1km per pixel) multispectral imaging from the Cassini spacecraft will 'see' ammonia hydrates exposed on the surfaces of the Saturnian moons.

1.1.2.4 Geomorphology

Figures 1.5 – 1.11, on the following pages, show convincing geomorphological evidence for cryomagmatic activity. However, the observation of cryovolcanism on icy moons is itself not adequate evidence for the presence of ammonia. Firstly, partial melting may result by the dissipation of tidal energy in planetary interiors; orbital eccentricities can be maintained in the face of frictional dissipation if resonances between the orbital periods of satellites occur. The well-known Laplacian resonance acting upon Io, Europa and Ganymede continues to supply tidal heating to the interiors of these bodies, powering in particular the intense silicate volcanism on Io (Yoder 1979). The eccentricity history of other icy moons is poorly constrained. Some or all may have passed through resonances in their history, pumping in additional energy. Titan, for instance, has a large free orbital eccentricity (e = 0.0289), the origin of which has yet to be explained (Sohl *et al*., 1995).

Secondly, partial melting can be initiated by antifreeze components other than ammonia. It is widely acknowledged that hydration of chondritic minerals in protoplanetary materials leads to solutions rich in salts such as magnesium sulfate and sodium carbonate (Kargel 1990). Hydrated chondritic salts reduce melting temperatures by some tens of Kelvin and form low viscosity brines which, if extruded on to a planetary surface, would produce low-relief flood plains of the type observed on a number of solar system objects (Kargel 1991).

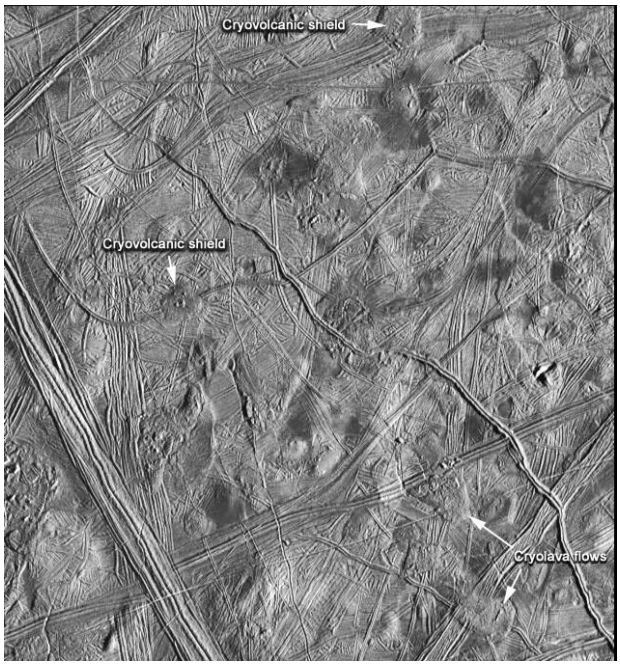

Figure 1.5. Galileo SSI image of part of the surface of Europa. The icy surface consists of a fabric of superposed ridged bands, the youngest cutting the bottom left-hand side of the image. The youngest features are a number of low hills, domes, and shield-like structures (many associated with dark patches) that are probably cryovolcanic in origin. Extensive flows are seen at lower right overlying an older ridge band. The image is 140km by 130km across and is centred at 12.3°N, 268°W. The resolution is 180m per pixel. Image acquired on February 20th 1997 from a distance of 17,700km. (NASA PIA00588)

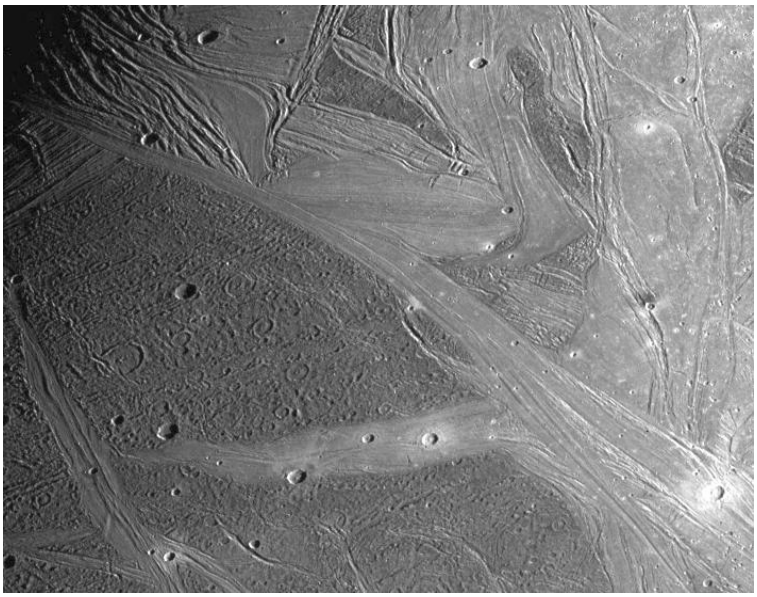

Figure 1.6. Galileo SSI image of part of the surface of Ganymede. The image shows the dark ancient terrain of Marius Regio. Notice the flattened profile of many of the craters – attributed to viscous relaxation of the crater floors. The area is cut by Nippus Sulcus, the brighter ridged unit. Compare the ridged area in the NW quadrant of the image with the folds on Enceladus (Fig. 1.7), and compare the chevron pattern of ridges in the upper centre part of the image with the coronae on Miranda (Fig. 1.9). The image is 664km by 518km across and is centred at 43°N, 194°W. The resolution is 940m per pixel. Image acquired on May 7th 1997 from a distance of 92,402km. (NASA PIA01618)

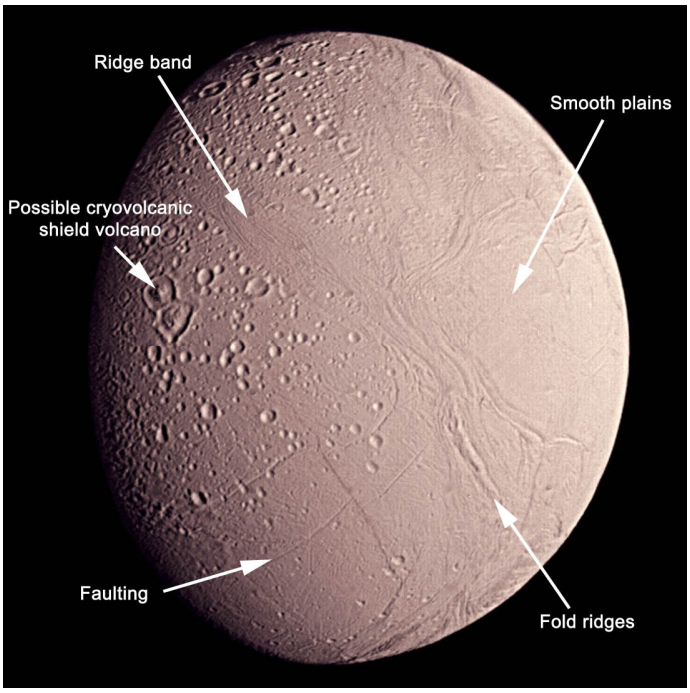

Figure 1.7. Colour mosaic of Enceladus constructed from images acquired by the Voyager 2 spacecraft on August 26th 1981. The surface exhibits a range of interesting (and unexpected) geological features mentioned in the text. Compare the ridge band and fold ridges with similar features on Ganymede (Fig. 1.6). This mosaic has a maximum resolution of 970 m per pixel from images recorded at a distance of 87,140km. (NASA PIA003477)

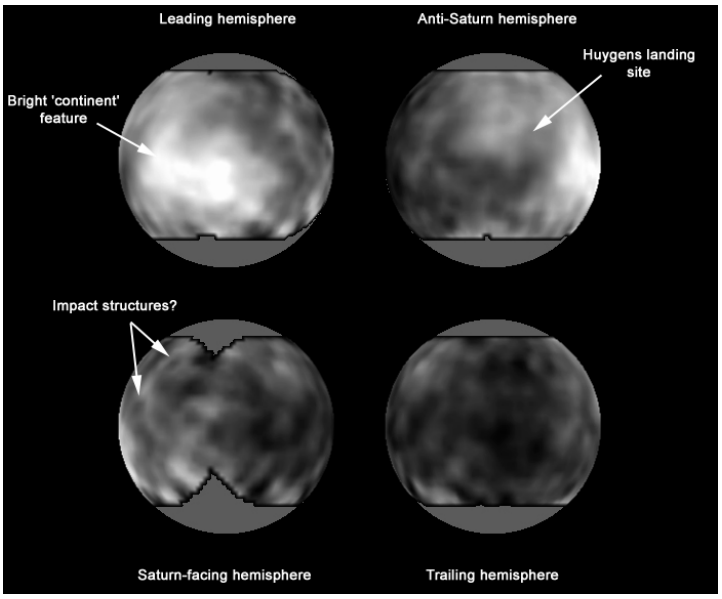

Figure 1.8. Four view of the surface of Titan as viewed by the Hubble Space Telescope. The images reveal infrared-bright patches on the surface, which may be 'clean' ice, and infrared-dark patches, which may be solid or liquid hydrocarbons. The images appear to show a number of bright circular features with dark interiors; these may be impact basins, or crater lakes. The images were recorded in the 0.94μm methane window over a number of days in October 1994. The resolution is ~250-300km (Smith *et al*., 1996).

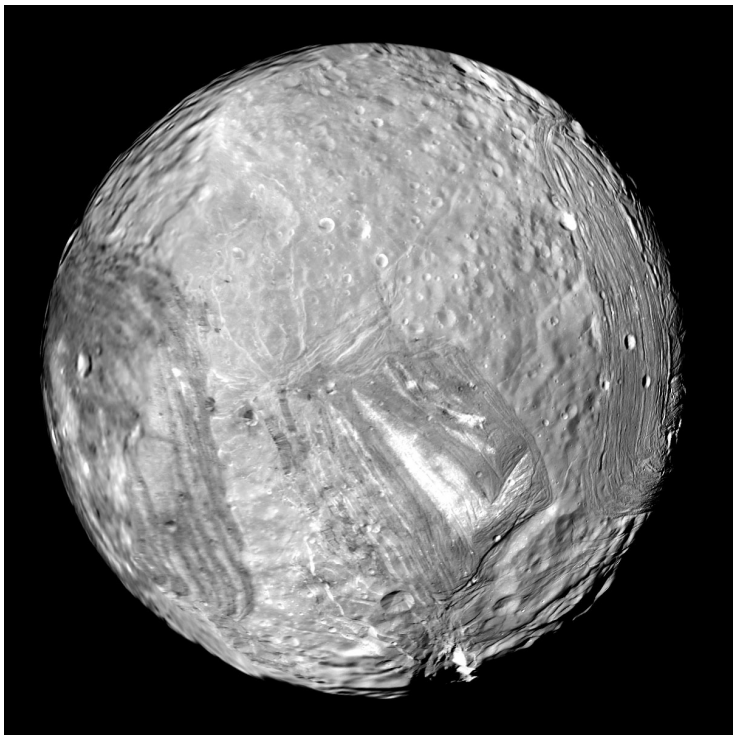

Figure 1.9. Mosaic of nine high-resolution images depicting the south polar regions of Miranda. Note the large rift at the bottom of the image (Verona Rupes) and the ridged chevron feature (Inverness Corona), which resembles features on the surface of Ganymede (Fig. 1.6). Two other arcuate ridged features are visible; Arden Corona on the left, and Elsinore Corona on the right. The ridged area surrounding Elsinore Corona (Naples Sulcus) is believed to be a cryovolcanic extrusion. The images were acquired by the Voyager 2 spacecraft on January 24th 1986. The highest resolution is 560m per pixel from images recorded at a distance of 30,160km. (NASA PIA01490)

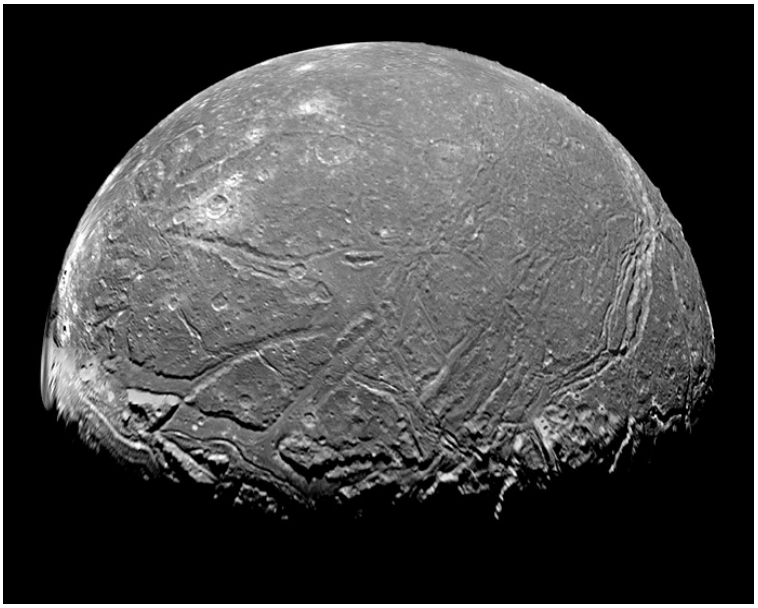

Figure 1.10. Voyager 2 mosaic of the south polar region of Ariel, acquired on January 24th 1986 from a minimum distance of 127,000km. The highest resolution is ~2.4km per pixel. The graben along the terminator are clearly filled with smooth material which has probably been extruded from beneath the surface. The sinuous feature visible in the centre of one of the graben may be a cryolava tube which fed the flow. (NASA PIA01534)

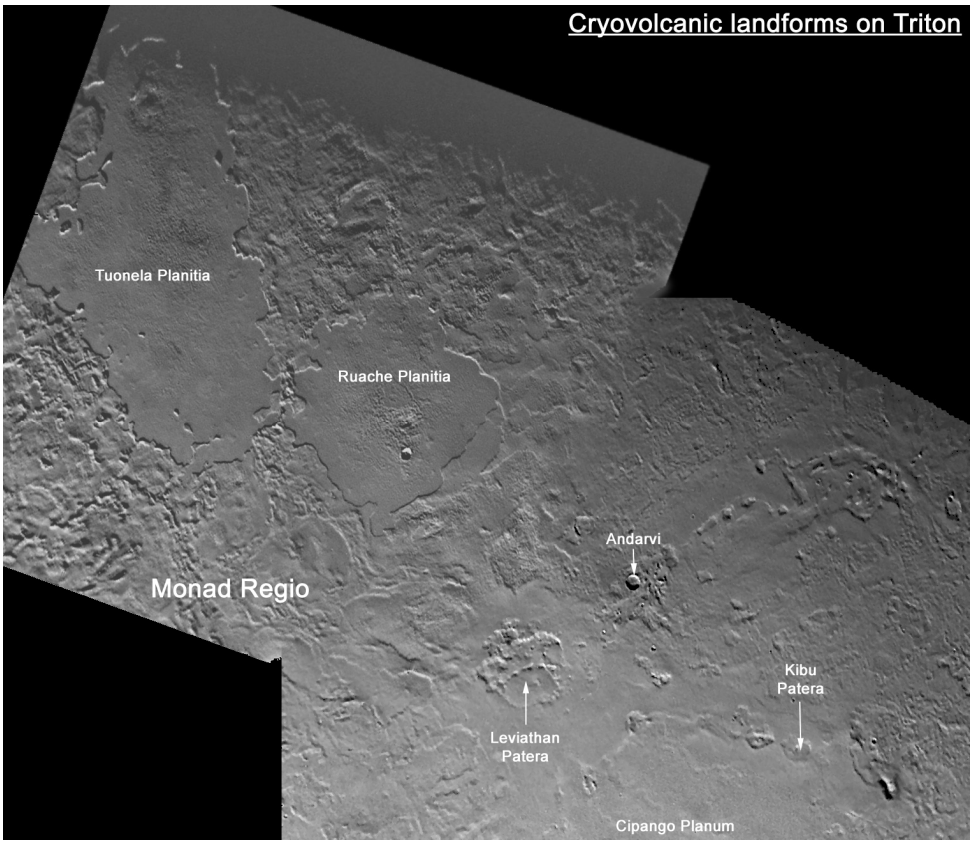

Figure 1.11. Mosaic of Voyager 2 images of part of the surface of Triton acquired in August 24th 1989. Important features include the two smooth plains, Tuonela and Ruache Planitiae, which are probably filled with cryovolcanic flood lavas, either erupted from buried vents within the basins or by flows emanating from the low shield volcano Leviathan Patera. Tuonela Planitia is ~400km long, and the caldera of Leviathan Patera is ~80km across. The image resolution is ~2.5km per pixel.

Nevertheless, there are lobate units on several icy bodies (for example, Miranda and Ariel) which are interpreted as cryovolcanic flows of high viscosity. Observed flow dimensions have been used to calculate emplacement viscosities and yield strengths. After accounting for the lower surface gravity, the corrected viscosity is found to compare very well with the viscosity of partially crystalline ammonia-water slurries (Kargel *et al*., 1991: Arakawa and Maeno 1994: Goldsby and Kohlstedt 1994). Although other components (e.g., methanol and methanal) yield viscous solutions, and may well be present as minor solutes, only ammonia is cosmically abundant enough to explain the observed flow morphologies (Schenk 1991).

In addition, many of the extensional tectonic features (rifts and graben) seen on nearly all icy moons have been attributed to global expansion upon freezing of subsurface oceans (Consolmagno 1985). The freezing process also supplies the pressure to extrude residual partially crystalline liquid up through crustal fractures into the aforementioned graben. This is a good explanation for the distribution of cryovolcanic deposits on Ariel (Prieto and Kargel 1997).

1.1.2.5 Summary of the evidence for ammonia in icy moons

There is no direct evidence for ammonia in icy moons, aside from a tentative spectroscopic identification of ammonia hydrates on Pluto's moon, Charon. There is quite strong circumstantial evidence from isotopic ratios and chemical abundances in Titan's atmosphere that Titan (and probably the other Saturnian moons) accreted most of their nitrogen as ammonia. Weak circumstantial evidence from geomorphological observations suggests that the Uranian satellites also contain significant amounts of ammonia. Modelling of planetary formation does not rule out ammonia as a major component of the condensed volatiles in icy moons.

On balance, I conclude that ammonia occurs with an abundance of ~5-15 wt % in most icy moons of Saturn, Uranus, and Neptune, and perhaps Pluto and Charon. From Fig. 1.13, one can see that the equilibrium mineral assemblage crystallising from such a weak ammoniacal solution will consist of ice Ih + ammonia dihydrate. Under non-equilibrium conditions, ammonia monohydrate may occur in preference to the dihydrate.

What is evident from this discussion is that the abundance of ammonia inside icy moons such as Titan is wholly unknown. The Cassini mission to Saturn is expected to make observations and measurements that will clarify this point. It is therefore important to prepare models of the internal structure of icy moons so as to better interpret the results of the Cassini orbital tour. My ultimate aim in this thesis is to model the internal structure of Titan (*c.f.* Sohl *et al*., 2002) so that I can predict the gravitational moments that would be measured by Cassini (Rappaport *et al*., 1997) for a given internal composition. Similar work relating internal structure to tidal love numbers has been reported recently by Castillo *et al*. (2002). In this fashion, we may be able to distinguish between NH_3-rich and NH_3-poor models of Titan's interior. Undertaking this modelling requires a detailed knowledge of the physical properties, particularly the equation of state, of solids in the ammonia-water system. In the next section I will describe the methods used for determining these physical properties.

1.2 Methods to satisfy the goals of this thesis

I use two methods to determine the physical properties of solids in the ammonia-water system. These are first-principles atomistic computer simulation and neutron diffraction experiments, each of which is described now.

1.2.1 Computer simulation

The calculation of material properties from nothing more than the mass and charge of the constituent atoms, and the rules of quantum mechanics, is known as first principles (or *ab initio*)

calculation. The advantages of *ab initio* calculations are that one can, in theory, exactly determine any physical property of an atomic system at any pressure – temperature point one chooses. Compare this with experimental investigations where there is always some uncertainty in pressure and temperature, issues with measurement resolution and sensitivity, and even an inability to make certain observations under conditions X, Y, or Z. *Ab initio* calculations obviously have an important role to play in any materials science study.

Unfortunately, in order to carry out *ab initio* calculations on systems more complicated than a single hydrogen atom, approximations are involved, as described in more detail in Chapter 2. The leading approximation is in the treatment of the electrons, not as a many-body interacting system, but as a system of individual electrons moving in an 'average' electrostatic field due to all the other electrons. These 'mean-field' approximations lose many of the nuances of non-local electron interactions (so-called correlation effects) and so care must be taken when interpreting the results of such calculations.

In *ab initio* methods which determine the energy of a system by iterative minimisation of trial wavefunctions (Hartree-Fock methods) there are ways of recapturing electron correlation to a certain extent by making increasingly complex corrections. However, this is computationally very demanding.

In *ab initio* methods which determine the energy of a system by minimising a functional of the electron density (Density functional theory, DFT, methods), incorporating electron correlation is less straightforward, since there is no systematic way of improving the treatment of electron correlation, as there is in Hartree-Fock theory. The commonest approach is to model correlation using an imaginary electron gas called 'jellium'. This local density approximation (LDA) works extremely well for many systems. Other methods include expressions for the gradient of the electron density (generalised gradient approximations, GGA's) and, more recently, the Laplacian of the electron density and the kinetic energy density (meta-GGA's).

One-electron mean-field calculations have enjoyed great success in recent decades, and this has grown with the development of increasingly powerful supercomputers. Chemists tend to prefer wavefunction-based methods for investigating molecular problems; DFT is experiencing broad acceptance in many branches of materials science, including Earth and Planetary mineral sciences as result of its low computational cost and impressive successes.

Methods for treating the full many-electron system have been around since the early 1980's. These work by using a statistical approach to solving the many-electron Schrödinger equation, hence their name; Quantum Monte Carlo (QMC) methods. QMC has no issue with electron correlation since it is 'built in' to the calculations. Nevertheless there are approximations which make the method tractable for real systems, specifically the use of finite time-steps and the use of small systems (order 10^3-10^5 electrons) with periodic boundary conditions. These approximations introduce errors, but they can be corrected for. Indeed QMC yields results

which are more than an order of magnitude better than any other method in terms of reproducing experimental binding energies. QMC is computationally expensive, and presently of limited (but quickly growing) applicability. QMC is even being used to aid the development of better mean-field approximations.

The *ab initio* calculations employed in this thesis are the least computationally demanding; static DFT in the athermal limit (i.e., at zero Kelvin less zero point vibrational energy). This affords the most comprehensive study of the greatest number of solids in the time available, and is the first step to doing calculations at finite temperatures (*ab initio* molecular dynamics). These calculations are extremely accurate. Nevertheless, it is true that they make small over-estimates or under-estimates of equilbrium properties when compared with experimental data. Hence, calculations and experiments are complimentary to one another, and I have made extensive comparisons between my *ab initio* work and experimental data (where it exists). Where data was lacking, I have carried out my own experiments, as described next.

1.2.2 Neutron diffraction experiments

Diffraction experiments allow a determination of the unit cell dimensions and atomic structure of crystals, amongst other things. By introducing a pressure cell and temperature controller (furnace or cryostat) into the path of the radiation beam being used to generate the diffraction pattern, it is possible to study the changes in the size of the unit cell, and the positions of the atoms at different temperatures and pressures. This yields important material properties such as the incompressibility and thermal expansivity.

In the case of ammonia dihydrate there was such a dearth of crystallographic and thermoelastic data, at all pressures and temperatures, that experiments inevitably became an essential part of this thesis. Not only do experiments provide a certain amount of 'ground truth' for the calculations, but they deliver results which are beyond the scope of the calculations done here (although not beyond the purview of calculations *per se*); for example, the identification of new phases, melting points, and thermal expansivity, to name a few.

The principal means of acquiring structural and thermoelastic data is by doing diffraction experiments, either with X-rays, or with neutrons. The wavelengths of X-rays and cold neutrons are in the region of 1 Å, and are therefore comparable to the distances between atoms in solids, rendering them suitable for the study of materials on an atomic scale.

Neutrons represent a particularly useful means of probing bulk solids with low atomic numbers. They are scattered by atomic nuclei, which are really very small indeed and consequently present a small target area (or cross-section) to the incoming neutron. Therefore, neutrons can penetrate the bulk of a sample. Conversely, X-rays are scattered by electron

clouds orbiting the nucleus, and bulk samples are therefore much more 'opaque' to X-rays than to neutrons. In addition, light elements, such as hydrogen, oxygen, and nitrogen scatter neutrons very strongly; hydrogen barely scatters X-rays at all.

Hence, neutron diffraction is ideally suited to the study of solids in the ammonia-water system.

A further advantage is that the neutron scattering properties of isotopes can be very different. Both hydrogen (^{1}H) and deuterium (^{2}H) have large bound coherent scattering lengths[2] (-3.7406 fermi and +6.671 fermi, respectively), so they scatter neutrons very well. However, ^{1}H also has a large incoherent scattering length (+25.274 fm) resulting in a very strong diffuse background which effectively swamps the rest of the diffraction pattern. Fortunately, deuterium does not suffer from this drawback (incoherent b = +4.04 fm), and it is normal to employ fully deuterated (*per*deuterated) samples in neutron diffraction work on hydrogen-bearing materials.

Strong differences in scattering can also be used to one's advantage in constructing sample environments. Titanium has a strong negative scattering length (-3.438 fm), and zirconium a strongly positive scattering length (+7.16 fm). An alloy of these two metals, $Ti_{66}Zr_{34}$ (called 'Tizer') therefore has a scattering length of zero, and is described as a null-scattering alloy. A sample environment constructed from TiZr will still contribute parasitic peaks to the sample diffraction pattern, but they will conveniently be of zero intensity.

Vanadium is a substance which scatters neutrons very weakly (coherent b = -0.382 fm); sample holders, or the windows of sample environments, are frequently fashioned from vanadium for this reason. Substances such as Gd_2O_3 and Cd have large scattering lengths and are often used to shield parts of the sample environment from incident neutrons.

The deep penetration of neutrons, combined with the use of null-scattering alloys, and/or shielding and collimation, means that very complex sample environments (e.g., bulky high-pressure cells) can be used on neutron beamlines (see Redfern 2002; Bailey 2003).

Neutrons are produced for research purposes in one of two ways; by nuclear fission, or by spallation. Fission in the core of a nuclear reactor produces a very high continuous flux (~10^{16} n cm^{-2} s^{-1}) of neutrons, which can be disseminated along beam-guides to a number of scientific instruments. Examples of continuous reactor sources include the Institut Laue-Langevin (ILL) in Grenoble, France, Laboratoire Léon Brillouin (LLB), Saclay, France, and the Joint Institute for Nuclear Research (JINR) at Dubna in Russia.

Spallation sources consist of a powerful synchrotron and one or more target stations. Protons are accelerated to high velocities in the synchrotron and periodically (10-50 times a

[2] All scattering lengths from Neutron News 3(3). 29-37 (1992).

second) 'fired' at a target. This target is typically a heavy metal; depleted uranium was commonly used, but tantalum, lead, bismuth, mercury, and tungsten have been employed of late. Illuminating the target with a high-energy proton beam produces a spray of neutrons, which are passed through a moderator (water, liquid methane or liquid hydrogen) to slow them down; this process actually takes advantage of the large scattering cross-section of hydrogen. These slowed neutron pulses are then available for scientific use. Examples of pulsed neutron sources include the Spallation Neutron Source (SNS) at Oak Ridge, Tennessee, USA, and the ISIS facility, Rutherford Appleton Laboratory, Oxfordshire, UK.

Compared to nuclear reactors, spallation sources are more environmentally friendly; many reactors are in the process of being decommissioned. Spallation sources also place a much lower thermal load on the target, compared with the high thermal output of nuclear reactors. At ISIS, the most intense pulsed source in the world, the total power delivered to the target station is ~ 160 kW, from a proton beam current of ~ 180 μA (2.3×10^{13} protons per pulse).

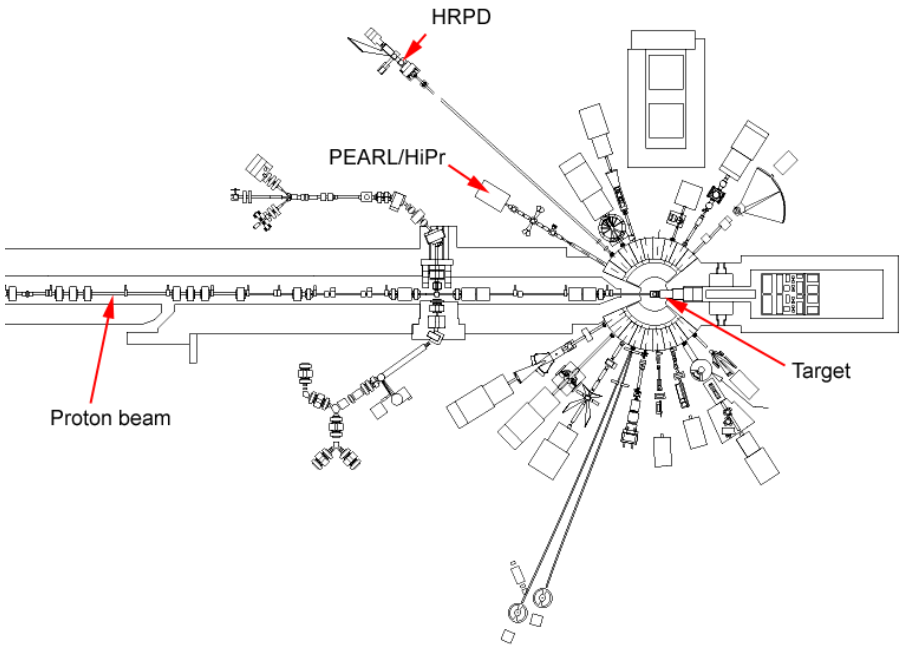

Fig. 1.12. Arrangement of the beamlines around the target station at ISIS. The two instruments used for experimental work in this thesis are highlighted.

Two neutron diffraction experiments were carried out for this thesis. Both were done at the ISIS spallation source (Fig. 1.12), the first on the HRPD beamline (February 2003), and the second on the PEARL/HiPr beamline (July 2003). The HRPD experiment was designed to take advantage of the diffractometer's high resolution (the highest in the world) to make a detailed study of ADH I at a range of temperatures (4 – 174 K) and up to a pressure of ~ 0.45 GPa. The

PEARL experiment was designed to take advantage of the Paris-Edinburgh large-volume press for studying ADH at pressures up to ~ 10 GPa. Both of these experiments are described in detail in Chapter 8.

1.3 Work done towards this thesis

This three-year study has involved the computational simulation, by means described in Chapter 2, of thirteen crystalline structures in the H_2O-NH_3 system (Fig. 1.13). This comprises eight low- and high-pressure polymorphs of pure water ice, two polymorphs of solid ammonia, and three low-pressure stoichiometric ammonia hydrates. This work has also included neutron powder diffraction of at least eight crystalline solids in the ammonia-water system. In addition, I have developed a flexible and accurate planetary model which can be used to calculate the triaxial shape and gravitational field of any object, regardless of size or composition, given an assumed mineralogical constitution and provided the equations of state of said minerals are known.

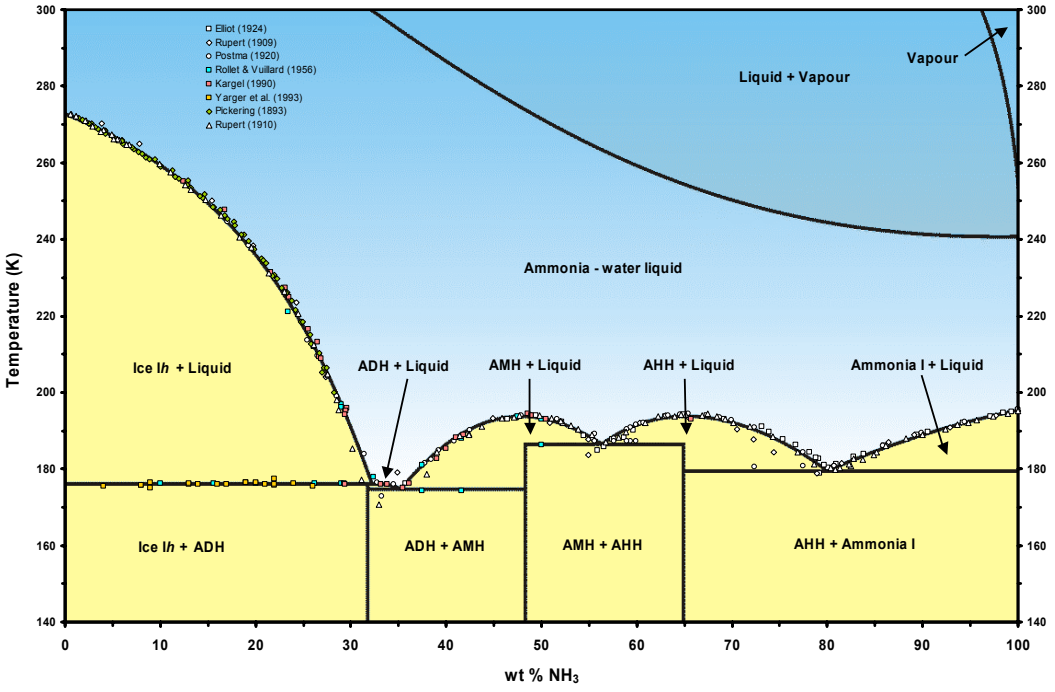

Figure 1.13. The equilibrium phase diagram for the binary ammonia-water system at atmospheric pressure (Pickering 1893; Rupert 1909, 1910; Smits and Postma 1910; Postma 1920; Elliott 1924; Clifford and Hunter 1933; Mironov 1955; Rollet and Vuillard 1956; Van Kasteren 1973; Kargel 1990; Yarger *et al.*, 1993). ADH = ammonia dihydrate; AMH = ammonia monohydrate; AHH = ammonia hemihydrate.

1.3.1 Pure H_2O Solids

I have carried out *ab initio* simulations of the proton-ordered low-pressure ice polymorphs ice II and ice XI. I have also simulated the higher-pressure proton-ordered polymorph ice VIII, and the proton-centred polymorph ice X, as well as four other hypothetical ultrahigh-pressure structures which have not yet been experimentally observed. This work has concentrated on determining the athermal equation of state of each phase, and on observing the pressure strengthening of the hydrogen bond in ice VIII up to the limit in which the proton sits midway between adjacent oxygen atoms (as in ice X).

The computational work on ices VIII, X, and the four post-ice X phases, is described in Chapter 3. Results of simulations on the ice XI and ice II structures appear in Chapter 4.

1.3.2 Pure NH_3 Solids

I have carried out *ab initio* simulation of the only two known proton-ordered polymorphs of solid ammonia, the low-pressure phase I, and the higher-pressure phase IV. Again, this work has focused upon determining the equation of state and the pressure dependence of the hydrogen bond length.

The work on solid ammonia comprises Chapter 5.

1.3.3 Mixed H_2O-NH_3 Solids

There are three stoichiometric hydrates in the H_2O-NH_3 system at ambient pressure (see Fig. 1.13); ammonia dihydrate ($NH_3.2H_2O$), ammonia monohydrate ($NH_3.H_2O$) and ammonia hemihydrate ($2NH_3.H_2O$). In this work, these are abbreviated to ADH, AMH, and AHH, respectively. I have carried out *ab initio* simulations of each of these solids to determine their equations of state. In AMH, I also made an extensive study of the proton transfer reaction, in particular the thermodynamics, which occurs when AMH transforms to solid ammonium hydroxide (NH_4OH).

ADH had been the subject of two neutron powder diffraction experiments, undertaken on the HRPD and PEARL beamlines at ISIS. The HRPD experiment involved the study of the low-pressure phase, ADH I, at a range of pressures and temperatures, as well as the collection of diffraction data for the higher pressure phase ADH II. The work on the higher pressure phases was continued up to ~ 8.6 GPa using the Paris-Edinburgh cell on the PEARL/HiPr beamline.

The simulation results for the AMH, ammonium hydroxide and AHH are presented in Chapter 6 and for ADH in Chapter 7. Results from the HRPD and PEARL experiments appear in Chapter 8.

1.3.4 Planetary modelling

A planetary modelling 'kit' (a collection of rules for building an icy moon) is developed in Chapter 9. This begins with the construction of a static model designed to calculate the mass and bulk density (as well as the triaxial distortion and second order gravitational coefficients) of a given mass distribution, for an assumed mineralogical and thermal profile. Applications of this model to Rhea and Titan are presented. The model is subsequently extended to allow for changes in radius in response to changes in the thermal profile. The method is applied to the thermal evolution of Rhea.

CHAPTER TWO

COMPUTATIONAL METHOD: DENSITY FUNCTIONAL THEORY AND VASP

2 Introduction

There have been, historically, two main approaches to the simulation of matter, best described as 'top-down' and 'bottom-up' methods. In the 'top-down' method, macroscopic material properties, such as the atomic structure or the elasticity, are used in the fitting of parameters to an *ad hoc* model of the forces acting between atoms. These empirical potentials are the basis of so-called atomistic or classical calculations. They have the attraction of being computationally inexpensive and therefore applicable to systems containing many thousands of atoms. Nevertheless, a given empirical parameterisation may work well in one physico-chemical environment, yet fail dismally in another. In other words, empirical potentials need to be tested for transferability. This is not to say that the method lacks merit, and empirically fitted potentials enjoy continued success (e.g., Gale, 1997, 1998) and wide applicability in, for example, mineral physics (Oganov *et al*., 2000) and biochemistry (Carloni, 2002).

The 'bottom-up' method employs the fundamental equations describing the behaviour of matter on a microscopic scale (i.e., quantum mechanics) to calculate, from first principles, any macroscopic material property of interest. These so-called '*ab initio*' methods use only the fundamental physical constants (e.g., the Planck Constant and the mass of the electron), the nuclear mass and the coordinates of the atoms present as inputs. There are no empirical parameters in the ideal solution and so the problem of transferability should not normally arise.

However, *ab initio* calculations can be very computationally expensive, and it has only recently become practical to simulate systems containing 100+ atoms.

There are several flavours of *ab initio* calculation, many of which will be mentioned or described briefly, but the bulk of this chapter is concerned with one particular flavour, or more correctly, combination of methodologies and approximations. That is the plane-wave pseudopotential method, within density functional theory, employing a gradient corrected functional to describe the exchange-correlation energy. The aim here is to give a clear account of that methodology and its execution within the computer program VASP (Vienna *Ab Initio* Simulation Package). The level of the following discussion is pitched between some of the more accessible reviews (e.g., Gillan, 1997: Pople, 1999: Hafner, 2000), and the many more mathematical descriptions of algorithms and implementations (e.g., Jones and Gunnarsson, 1989: Payne *et al*. 1992: Argaman and Makov, 2000).

2.1 The Theoretical Background

2.1.1 The Schrödinger Equation

Every aspect of a given non-relativistic physical system is described by the time independent Schrödinger equation:

$$\hat{H}\psi_i = E_i\psi_i \qquad \text{Eq. 2.1}$$

where $\hat{H}$ is the Hamiltonian operator, in the absence of magnetic or electric fields, for a system of nuclei and electrons. This operator is a quantum mechanical 'rulebook,' describing the way that particles interact with one another. ψ_i represents the wavefunction of the i^{th} state of the system, and contains the sum of all the information about the system. E_i is the energy of the state described by ψ_i. We are search for the energy corresponding to the ground-state of the system, E_0 (the ground-state being the configuration which minimises the energy of the system), which yields virtually all of the physical properties of interest. For example, the equilibrium cell volume is that volume at which the total energy as a function of cell volume, E(V), is a minimum. Many other properties may be determined by varying one or more of the degrees of freedom in a system to locate the energy minimum.

The wavefunction depends on the three spatial coordinates, and one spin coordinate of each electron (± ½, denoted here as 'up' or 'down' by ↑ and ↓ respectively), and the three spatial coordinates of each of the nuclei. By itself, the wavefunction is not an observable quantity, but

the square of the wavefunction can be interpreted as, $\int |\psi(\vec{r})|^2 d\vec{r}$ being the probability that an electron with wavefunction $\psi(\vec{r})$ will be found within a given volume element $d\vec{r}$.

The complete Hamiltonian of a system is a differential operator:

$$\hat{\mathrm{H}} = -\frac{1}{2}\sum_{i=1}^{\mathrm{N}} \nabla_i^2 - \frac{1}{2}\sum_{\mathrm{A}=1}^{\mathrm{M}} \frac{\nabla_{\mathrm{A}}^2}{\mathrm{M_A}} - \sum_{i=1}^{\mathrm{N}}\sum_{\mathrm{A}=1}^{\mathrm{M}} \frac{\mathrm{Z_A}}{r_{i\mathrm{A}}} + \sum_{i=1}^{\mathrm{N}}\sum_{i\neq j}^{\mathrm{N}} \frac{1}{r_{ij}} + \sum_{\mathrm{A}=1}^{\mathrm{M}}\sum_{\mathrm{A}\neq \mathrm{B}}^{\mathrm{M}} \frac{\mathrm{Z_A Z_B}}{R_{\mathrm{AB}}} \qquad \text{Eq. 2.2}$$

where the subscripts *i* and *j* denote the N electrons in the system, and the subscripts A and B denote the M nuclei in the system. $\mathrm{M_A}$ is the mass of nucleus A (in multiples of the electron mass, using this reduced notation) and $\mathrm{Z_A}$ is the nuclear charge (also in multiples of the electronic charge). The spatial coordinates of the electrons and nuclei are $\vec{r}_i$ and $\vec{R}_A$ respectively, and the distance between particles *i* and A, for example, is $r_{i\mathrm{A}} = |\vec{r}_i - \vec{R}_{\mathrm{A}}|$. The first two terms of Equation 2.2 represent the kinetic energy, $\hat{\mathrm{T}}$, of the electrons and nuclei respectively. The third term gives the attractive electrostatic interaction between electrons and nuclei, $\hat{\mathrm{V}}_{\mathrm{Ne}}$. The fourth and fifth terms are the repulsive potentials acting between one electron and another, $\hat{\mathrm{V}}_{\mathrm{ee}}$, and between two nuclei, $\hat{\mathrm{V}}_{\mathrm{NN}}$.

2.1.2 The Born-Oppenheimer Approximation

The most immediate simplification that can be introduced at this point is that the nuclei are stationary with respect to the electrons. Since even the hydrogen nucleus is ~1800 times heavier than an electron, it is reasonable to assume that the nuclei move only very slowly with respect to the electrons. In the limit of stationary nuclei (referred to variously as the Born-Oppenheimer, adiabatic, or clamped-nuclei approximation) the electrons are thought of as moving in the field of fixed nuclei. The result of this is that the kinetic energy terms can be separated and $\hat{\mathrm{V}}_{\mathrm{NN}}$ becomes a constant. Since the nuclear coordinates are no longer contributing to the full wavefunction, the Hamiltonian of the electron-only system reduces to the so-called electronic Hamiltonian, $\hat{\mathrm{H}}_{\mathrm{elec}}$:

$$\hat{\mathrm{H}}_{\mathrm{elec}} = -\frac{1}{2}\sum_{i=1}^{\mathrm{N}} \nabla_i^2 - \sum_{i=1}^{\mathrm{N}}\sum_{\mathrm{A}=1}^{\mathrm{M}} \frac{\mathrm{Z_A}}{r_{i\mathrm{A}}} + \sum_{i=1}^{\mathrm{N}}\sum_{i\neq j}^{\mathrm{N}} \frac{1}{r_{ij}} = \hat{\mathrm{T}} + \hat{\mathrm{V}}_{\mathrm{Ne}} + \hat{\mathrm{V}}_{\mathrm{ee}} \qquad \text{Eq. 2.3}$$

and

$$\hat{\mathrm{H}}_{\mathrm{elec}}\psi_{\mathrm{elec}} = \mathrm{E}_{\mathrm{elec}}\psi_{\mathrm{elec}} \qquad \text{Eq. 2.4}$$

The *total* energy of the system is then:

$$E_{tot} = E_{elec} + E_{nuc} \qquad \text{Eq. 2.5}$$

where $E_{nuc} = \sum_{A=1}^{M} \sum_{A \neq B}^{M} \frac{Z_A Z_B}{R_{AB}}$

The motion of the ions can usually be described satisfactorily by straightforward classical Newtonian mechanics. However, for light elements, such as hydrogen and helium, overlooking the quantum nature of the nuclei has consequences which cannot be ignored. This is discussed further in section 2.2.2.2.

The Born-Oppenheimer approximation does not cover certain phenomena associated with, for example, electronic conduction where coupling of electronic and nuclear dynamics is important.

The time independent non-relativistic Schrödinger equation (Eq. 2.1) can be solved precisely for systems containing only a single electron. The solution for the hydrogen atom is well known and is described elsewhere. However, as soon as another electron is introduced problems arise due to the complex electrostatic interactions between electrons, discussed next.

2.1.3 Electron interactions: exchange and correlation

When we encounter a system with more than one electron we are faced with an overwhelmingly difficult problem. Electrons repel one another by virtue of their charge; hence the motion of one electron is correlated with the motion of the other electrons in the system. Thus there exists an intractable relationship between the behaviour of the electrons in a many electron system. Secondly, the electrons follow the Pauli exclusion principle; the probability of finding two electrons within a volume element cannot change when their positions are interchanged so,

$$|\psi(\vec{r}_1, \vec{r}_2)|^2 = |\psi(\vec{r}_2, \vec{r}_1)|^2 \qquad \text{Eq. 2.6}$$

There are only two solutions to equation 2.6. Firstly, the two wavefunctions may be identical (so-called symmetric wavefunctions). This is true for bosons, particles which have zero or integer spin. On the other hand, for fermions (particles which have spin ± ½) the two wavefunctions may have opposite signs (so-called antisymmetric wavefunctions). Since

electrons are fermions, the electron wavefunction must be antisymmetric when either the spin or spatial coordinates are interchanged:

$$\psi(\vec{r}_1, \vec{r}_2) = -\psi(\vec{r}_2, \vec{r}_1) \qquad \text{Eq. 2.7}$$

Putting $\vec{r}_1 = \vec{r}_2$ in Equation 2.7, and substituting into Equation 2.6, reveals that there is zero probability of finding both electrons in the same place. This is the basis of the Pauli Exclusion Principle, which states that no two electrons can be in the same quantum state. In other words, two electrons with like spin cannot occupy the same space. This change of sign of the wavefunction when two electrons are interchanged is called exchange symmetry, and the reduction in the energy of the electron system due to this is called the exchange energy, E_X.

However, there is still no exact solution to this problem, and approximations have to be introduced. The difference between the true ground-state energy of a system and that calculated when this effect is ignored is called the correlation energy, E_C. Correlation energy is altogether more difficult to calculate and its inclusion within density functional theory is considered in detail later. In Density functional theory, exchange energy and correlation energy are frequently described together under the common heading of exchange-correlation energy, E_{XC}.

2.1.4 The Variational Principle

The solution of the Schrödinger equation is an eigenvalue problem. For a given system of electrons and nuclei, the only system dependent parameters are the number of electrons present, N, and the nuclear potential, $\hat{V}_{Ne}$ (often called simply the 'external' potential, V_{ext}). It is then necessary to determine the eigenfunctions (that is, the wavefunctions, ψ_i) and the corresponding eigenvalues, E_i, of the electronic Hamiltonian, $\hat{H}$.

To find the ground-state wavefunction, ψ_0, we employ the variational principle, which implies that the calculated energy for an arbitrary wavefunction is never less than the 'true energy'. Employing a trial wavefunction, ψ_{trial} (normalised such that that the integral over all spatial and spin coordinates is unity), thus yields an energy, E_{trial}, which will always be an upper bound to the ground-state energy:

$$E_0 \leq E_{trial}[\psi_{trial}] = \langle \psi_{trial} | \hat{H} | \psi_{trial} \rangle \qquad \text{Eq. 2.8}$$

where

$$\langle \psi_{trial} | \hat{H} | \psi_{trial} \rangle \equiv \int \cdots \int \psi^*_{trial} \hat{H} \psi_{trial} d\bar{x}_1 d\bar{x}_2 \ldots d\bar{x}_N \qquad \text{Eq. 2.9}$$

and ψ^*_{trial} is the complex conjugate of ψ_{trial}, $\hat{H}$ is the Hamiltonian, constructed from N and V_{ext}, and the electronic coordinates x_i incorporate spatial ($\vec{r}_i$) and spin (s_i) coordinates.

The ground-state energy itself is approached by searching through large numbers of trial wavefunctions so as to minimise E_{trial}. Hence, knowing N and V_{ext} allows us to find $\hat{H}$ which, via the variational principle, leads to the ground-state wavefunction ψ_0 and hence E_0, in principle. The issue is in coming up with a manageable number of eligible trial wavefunctions that can be used to approximate the true wavefunction (which is very complicated indeed).

2.2 Solutions to the many electron Schrodinger equation

2.2.1 Dealing with Exchange; the Hartree-Fock Approximation

One way of narrowing down the set of trial wavefunctions to search is to separate the complex N-electron wavefunction into N one-electron wavefunctions with the same properties as the wavefunctions of electrons in isolated atoms. In the *Hartree approximation* (Hartree, 1928), this amounts to a simple product:

$$\psi(\vec{x}_1, \vec{x}_2, \ldots \vec{x}_N) = \psi_1(\vec{x}_1)\psi_2(\vec{x}_2)\ldots\psi_N(\vec{x}_N) \qquad \text{Eq. 2.10}$$

The problem with this is that it ignores all the important effects of exchange symmetry and so, instead of a simple product, an antisymmetrised product is used. This is the *Hartree-Fock approximation*.

The antisymmetrised product of N one-electron wavefunctions, which is approximately the true N-electron wavefunction, ψ_0, is called a Slater determinant (Φ_{SD}), and the individual one-electron wavefunctions which comprise it, $\psi_i(\vec{x}_i)$, are called spin orbitals (Fock, 1930: Slater, 1930).

In the Hartree-Fock approximation, the variational principle is now employed to vary the spin orbitals and so yield the Slater determinant which gives the minimum energy (called the Hartree-Fock energy, E_{HF}, since it is lacking correlation energy and is not E_0). The description of the N-electron wavefunction as an antisymmetrised product of N one-electron wavefunctions means that the N-electron Hamiltonian must be replaced with N Fock operators, $\hat{f}_i$

$$\hat{f}_i = -\frac{1}{2}\nabla_i^2 - \sum_A^M \frac{Z_A}{r_{iA}} + V_{HF}(i) \qquad \text{Eq. 2.11}$$

and

$$\hat{f}_i \psi_i = \varepsilon_i \psi_i \qquad i = 1,2,\ldots\ldots,N \qquad \text{Eq. 2.12}$$

where ψ_i are the spin orbitals and ε_i are the eigenvalues of $\hat{f}_i$ corresponding to the energies of the appropriate orbitals.

What has happened here is that the complicated electron-electron repulsion term in $\hat{H}$ has been replaced by a simple one-electron potential, $V_{HF}(i)$. This Hartree-Fock potential describes the average repulsion felt by a given electron as a result of all the other electrons in the system. *In practical terms this means that, whilst the Hartree-Fock approximation incorporates exact exchange energy, the effect of electron correlation is ignored altogether*. Because the instantaneous electrostatic repulsion does not enter into $V_{HF}(i)$, electrons get too close to one another, and this causes the energy (E_{HF}) to be higher than the true ground state energy (E_0). The difference is referred to as the correlation energy, E_C (after Löwdin, 1959):

$$E_C = E_0 - E_{HF} \qquad \text{Eq. 2.13}$$

Since the Hartree-Fock potential itself depends on the spin orbitals we are seeking, the solution to the Hartree-Fock equations (2.11 and 2.12) needs to be found through an iterative process. Briefly, the Hartree-Fock equations are solved for a trial set of orbitals, and the output orbitals are used as the input for the next iteration. This continues until the input and output orbitals converge to within a level of accuracy predetermined by the user. This method of solution is referred to as the Self Consistent Field (SCF or HF-SCF) method.

2.2.2 Electron correlation in the Hartree-Fock Approximation.

It *is* possible to treat electron correlation in a wavefunction based approximation but it can be computationally very expensive. The problem with the Hartree-Fock approximation stems from the use of a single Slater determinant to represent the wavefunction. Improvements can be achieved by adding more determinants (i.e., by forming a linear combination of determinants) to describe excited electronic states. This method is referred to as configuration interaction (CI) and the labels CID, CISD, CISD(T), etc., define increasingly sophisticated combinations of determinants. However, the number of configurations increases enormously as the number of electrons in the system increases, making this method computationally intensive for all but the smallest molecular systems.

Other methods for dealing with electron correlation include the perturbation method of Møller and Plesset (1934), denoted MP2, MP3, MP4, etc., and the coupled-cluster (CC) method (Cizek, 1966).

The ability to systematically refine ones calculations towards the exact limit, albeit at huge computational expense, is one of the great advantages of wavefunction based methods in quantum chemistry. However, as is discussed in the following section, there is another way of determining the ground state energy which is both exact, in principle, and less computationally demanding. That is the method I have employed in my studies, Kohn-Sham Density functional theory.

2.2.3 Density Functional Theory

2.2.3.1 The Hohenberg and Kohn Theorems

One of the greatest computational expenses in wavefunction theories is their dependence on very complicated wavefunctions with three spatial and one spin coordinate for *each* of the N-electrons in the system. The attraction of density functional theory is that it depends on the electron density, $\rho(\vec{r})$, with only three spatial coordinates regardless of the size of the system. Although there were some early attempts to use the electron density instead of the wavefunction to solve the Schrödinger equation (Thomas, 1927: Fermi, 1928: Slater, 1951), it was the theorems of Hohenberg and Kohn (1964) which proved that a variational treatment of the electron density could yield the ground state energy of a system.

The first part of the Hohenberg-Kohn theorem was a proof that the electron density could uniquely determine the Hamiltonian, and hence (as we saw in 2.1.4.1) the ground state energy. Though Hohenberg and Kohn (1964) presented a mathematical proof, the basics can be appreciated as follows.

- The integral of the electron density over the whole system is N, the total number of electrons.
- The maxima in the electron density correspond to the positions of the nuclei, giving $\vec{R}_A$.
- The electron density at $\vec{R}_A$ depends on the nuclear charge Z_A.
- Together, $\vec{R}_A$ and Z_A define V_{ext}.
- V_{ext} and N are the components of $\hat{H}$, the electronic Hamiltonian.

Thus the electron density contains all the necessary information (uniquely, as the proof demonstrates) to determine $\hat{H}$. It is now possible to write the ground state energy, E_0, as a functional of the ground state electron density, ρ_0:

$$E_0[\rho_0] = T[\rho_0] + E_{ee}[\rho_0] + E_{Ne}[\rho_0] \qquad \text{Eq. 2.14}$$

where the components and their subscripts have the same meaning as in section 2.1.1 and are themselves functionals of the electron density. This expression is separable into components which depend on the system under consideration (i.e., on $\vec{R}_A$, Z_A and N), the electrostatic attraction between nuclei and electrons, $E_{Ne}[\rho_0] = \int \rho_0(\vec{r}) V_{Ne} d\vec{r}$, and the non-system-specific components, $T[\rho_0]$ and $E_{ee}[\rho_0]$. These system-independent components are grouped together into a single term, the Hohenberg-Kohn functional, $F_{HK}[\rho_0]$:

$$E_0[\rho_0] = \int \rho_0(\vec{r}) V_{Ne} d\vec{r} + T[\rho_0] + E_{ee}[\rho_0] = \int \rho_0(\vec{r}) V_{Ne} d\vec{r} + F_{HK}[\rho_0] \qquad \text{Eq. 2.15}$$

The second important aspect of Hohenberg and Kohn's work was to show that the variational principle (2.1.4.1) could be applied to find E_0. This consists of a proof that $F_{HK}[\rho]$ yields the lowest energy only if the input electron density is the true ground state electron density, ρ_0. This leads to an expression similar to equation 2.8:

$$E_0 \leq E[\rho_{trial}] = T[\rho_{trial}] + V_{ee}[\rho_{trial}] + \int \rho_{trial}(\vec{r}) V_{ext} d\vec{r} \qquad \text{Eq. 2.16}$$

Hohenberg and Kohn (1964) demonstrated that the functional $F_{HK}[\rho]$ was at a minimum with respect to all allowed densities only when $\rho \equiv \rho_0$. This seemingly simple statement hides the fact that this functional is a completely universal functional (that is, it applies to any system) which allows for the *exact* solution of the Schrödinger equation. As such, it has been described as the Holy Grail of density functional theory. Unfortunately, the functional form of $F_{HK}[\rho]$ is a total mystery. Much of what follows describes the search for suitable approximations, beginning with the next landmark paper in DFT history by Kohn and Sham (1965).

2.2.3.2 The Kohn-Sham equations

Kohn and Sham (1965) built on the theorems of Hohenberg and Kohn (1964) by showing how the mysterious $F_{HK}[\rho]$ could be dealt with. This was done by calculating as much as possible of $F_{HK}[\rho]$ exactly, and leaving the remainder in one smaller unknown term. In many respects, their work resembles aspects of the Hartree-Fock approximation and so some of what follows will not be unfamiliar. As in Hartree-Fock theory, the N-electron system is reduced to a set of N non-interacting one-electron systems. In Hartree-Fock theory this is the basic approximation upon which the solution is built, but in DFT it is simply a tool to calculate the exact component of an unknown term. For such a fictitious system, in which the electrons don't interact at all (i.e., they act like they are uncharged), the wavefunction *is* a Slater determinant,

and the kinetic energy for this (T_{HF}) is known exactly. The Slater determinant, Θ_S, consists of orbitals, $\varphi_i(\vec{x}_i)$, termed Kohn-Sham orbitals (to distinguish them from the spin orbitals of Hartree-Fock theory), and the result is similar to equation 2.12:

$$\hat{f}^{KS}\varphi_i = \varepsilon_i\varphi_i \qquad i = 1, 2, \ldots, N \qquad \text{Eq. 2.17}$$

where ε_i are the energies of the Kohn-Sham orbitals, φ_i, and the Kohn-Sham operator, $\hat{f}^{KS}$, is the one-electron Hamiltonian of the fictitious non-interacting system of electrons, which depends on the kinetic energy of the electrons and an effective one-electron potential, V_S (compare with eq. 2.3 and eq. 2.11):

$$\hat{f}^{KS} = -\frac{1}{2}\nabla^2 + V_S(\vec{r}) \qquad \text{Eq. 2.18}$$

The link between this model and reality is made by choosing V_S such that the resulting electron density, $\rho_S(\vec{r})$, is the same as the ground state density in the true system of interacting electrons, $\rho_0(\vec{r})$.

$F_{HK}[\rho]$ also contains the term $V_{ee}[\rho]$. This can be split into a Coulomb term, $J[\rho]$, which is known exactly, and another term, $E_{ncl}[\rho]$, which describes all of the non-classical interaction between electrons, such as exchange and correlation. So, the Coulomb terms, $J[\rho]$, and the non-interacting part of the kinetic energy, $T_C[\rho]$, have been found exactly. A small part of the kinetic energy, T_C, is influenced by correlation effects, and cannot be found by the method described above. The remainder, which cannot be treated exactly, is called the Exchange-correlation energy, E_{XC}, equal to $T_C[\rho] + E_{ncl}[\rho]$. $V_S(\vec{r})$ now becomes $V_{eff}(\vec{r})$:

$$V_{eff}(\vec{r}) = \int \frac{\rho(\vec{r}_2)}{r_{12}} d\vec{r}_2 + V_{XC}(\vec{r}_1) - \sum_A^M \frac{Z_A}{r_{1A}} \qquad \text{Eq. 2.19}$$

where

$$V_{XC} = \frac{\partial E_{XC}}{\partial \rho} \qquad \text{Eq. 2.20}$$

and the final Kohn-Sham equation is:

$$\left[-\frac{1}{2}\nabla^2 + V_{eff}(\vec{r})\right]\varphi_i = \varepsilon_i\varphi_i \qquad i = 1, 2, \ldots, N \qquad \text{Eq. 2.21}$$

where the electron density is given by,

$$\rho = \sum_{i}^{N} \langle \varphi_i \,|\, \varphi_i \rangle \qquad \text{Eq. 2.22}$$

$V_{eff}(\vec{r})$ depends on the electron density, and therefore on the orbitals, so the Kohn-Sham equations must be solved iteratively. Hence DFT is a SCF theory. Note that everything except the functional form of E_{XC} is known exactly, and this is the major difference between density functional theory and wavefunction theory. In wavefunction theory, the approximation appears at the outset, in the assumption that the real wavefunction is a Slater determinant. In density functional theory, the approximation appears in the final step – the search for a suitable expression for the exchange-correlation energy.

2.2.3.3 The local-density approximation

The simplest way of approximating the exchange-correlation energy, introduced by Kohn and Sham (1965), is called the local-density approximation (LDA). In this scheme the value of E_{XC} per electron is taken to be the same as that of an electron in a uniform 'gas' of electrons (often called 'jellium'). The exchange-correlation energy per electron in a homogeneous electron gas, $\varepsilon_{XC}^{hom}(\rho)$, is well known for a wide range of electron densities from quantum Monte Carlo simulations (Ceperley and Alder 1980). In the LDA, E_{XC}^{LDA} per electron in a real electron system at $\vec{r}$ is taken to be the appropriate jellium value, $\varepsilon_{XC}^{hom}(\rho)$, that corresponds to $\rho(\vec{r})$. Or,

$$E_{XC}^{LDA}[\rho(\vec{r})] = \int \varepsilon_{XC}^{hom}(\rho)\rho(\vec{r})d\vec{r} \qquad \text{Eq. 2.23}$$

and

$$V_{XC}^{LDA} = \frac{\partial E_{XC}^{LDA}[\rho(\vec{r})]}{\partial \rho(\vec{r})} = \frac{\partial\left[\rho(\vec{r})\varepsilon_{XC}^{hom}(\rho)\right]}{\partial \rho(\vec{r})} \qquad \text{Eq. 2.24}$$

The use of the term 'local' means that the exchange-correlation energy at $\vec{r}$ in this approximation depends only on the electron density at $\vec{r}$. In other words, contributions to E_{XC} from inhomogeneities in the *real* electron density at a distance from $\vec{r}$ (that is, 'non-local' contributions) are not considered.

Adapted from the LDA is a scheme in which the requirement that the population of spin-up and spin-down electron states be equal is relaxed. This local spin density approximation (LSDA) is written as,

$$E_{XC}^{LSDA}\left[\rho_{\uparrow}(\vec{r}),\rho_{\downarrow}(\vec{r})\right]=\int \varepsilon_{XC}^{hom}\left(\rho_{\uparrow}(\vec{r}),\rho_{\downarrow}(\vec{r})\right)\rho(\vec{r})d\vec{r} \qquad \text{Eq. 2.25}$$

where $\rho(\vec{r})=\rho_{\uparrow}(\vec{r})+\rho_{\downarrow}(\vec{r})$ and $\rho_{\uparrow}(\vec{r})\neq\rho_{\downarrow}(\vec{r})$.

The strength of this scheme is that it allows magnetic properties to be simulated. For many years the LDA and LSDA were cornerstones of DFT. Their performance in most areas of solid state studies was a significant improvement over the Hartree-Fock approximation. Nevertheless, the absolute accuracy of the LDA and LSDA calculations is quite poor in some cases. The principles failings are well known:

- Binding energies are almost always overestimated. In solid-state calculations, this leads to cell parameters being underestimated by several percent (3% is a widely quoted average). Consequently, the bulk modulus is frequently in error by > 10%. Generally, the more the volume is underestimated, the more the bulk modulus is overestimated.
- The wrong ground state is sometimes predicted to be stable. The most notorious example is that of iron, predicted to exist as a non-magnetic hcp structure under ambient conditions when it is, of course, a bcc ferromagnet (the α-phase).
- Insulating systems which exhibit strong correlation effects (e.g., NiO) are predicted to be metallic.
- Weak bonds, such as hydrogen bonds, are not well described, and van der Waals forces are not accounted for at all.

Indeed the LDA and LSDA work best of all for bulk metals, wherein the slowly varying electron density bears the greatest resemblance to the homogeneous electron gas. The reason the LDA and LSDA work at all is attributed to the fact that they obey a particularly important rule called the 'sum rule.' Surrounding each electron is an 'exclusion zone,' often described as an exchange-correlation hole. The total amount of charge excluded from this hole is simply equal to the charge on an electron, but the shape of the hole in a real electron system is rather complicated. When we replace the true hole with a jellium-type hole, the amount of charge excluded is correct (the sum of the charge due to all the infinitesimal volume elements in the hole equals the electronic charge) but the shape is wrong. Clearly, to move beyond the LDA and LSDA, the one property that has to retained is obedience of the sum rule.

2.2.3.4 The generalized gradient approximation

Moving beyond the LDSA means incorporating non-local correlation effects. This is partially achieved by introducing a dependence on the gradient in the electron density, and this is known as the generalised gradient approximation (GGA):

$$E_{XC}^{GGA} = \int f\left(\rho_{\uparrow}(\vec{r}), \rho_{\downarrow}(\vec{r}), \nabla\rho_{\uparrow}(\vec{r}), \nabla\rho_{\downarrow}(\vec{r})\right)d\vec{r} \qquad \text{Eq. 2.26}$$

Strictly, the gradient of the electron density is semi-local rather than non-local since it depends on the gradient at $\vec{r}$, but has a 'sense' of the electron density at a remove from $\vec{r}$.

A straightforward gradient expansion of the electron density violates the sum rules, and the result is that GGA functionals are constructed in piecemeal fashion to incorporate various elements of the LSDA, and even some empirical parameters fitted to, for example, the atomisation energies of certain molecules. There are many GGA functionals cited in the literature but, unlike the treatment of correlation in Hartree-Fock theory, there is no systematic trend in these functionals towards the equivalent of full configuration interaction. Certain functionals have been designed to reproduce specific properties of a system (e.g., elastic properties or vibrational frequencies), and there is no guarantee that a functional which works well in one branch of quantum chemistry, or on a given type of solid, will work well with another. It is often necessary, therefore, to 'shop around' and test possible functionals on the system of interest and for the property of interest.

Broadly speaking, GGA's correct many of the deficiencies of the LDA and LSDA. Specifically, they tend to undo the overbinding effect, though in some cases this leads to severe underbinding. Noble gas cryocrystals, and molecular cryocrystals like N_2, are not predicted to be bound at all by some GGA's. However, the correct magnetic and structural ground state is found for metals like iron, chromium and manganese (Hafner, 2000).

Functionals are frequently cited by the initials of the authors and the year of publication. All schemes break E_{XC} into components due to exchange, E_X, and correlation, E_C, presenting a separate parameterisation of each part. For example, the GGA functional called BLYP consists of the widely used parameterisation of E_X due to Becke (1988) combined with the parameterisation of E_C due to Lee, Yang and Parr (1988). The functional used in this thesis is named PW91 (Perdew, 1991: Perdew and Wang, 1992), though it would more consistently be named PW91PW91, or BPW91 since their expression for E_X is equivalent to that of Becke (1988).

Improvements have come about by pairing correlation functionals with exact exchange energy functionals. These hybrid functionals use the exact exchange corresponding to that for a Slater determinant (sometimes called Hartree-Fock exchange), and the preferred functional at

this time is B3LYP. More recently, meta-GGA's have introduced functional dependencies, not only on the gradient of the electron density, but on the curvature, or Laplacian, of the electron density, $\nabla^2\rho(\vec{r})$, and gradients in the kinetic energy density. For a detailed review consult Kurth *et al*. (1999).

The application of the GGA to the hydrogen bonded solids studied in this work are discussed in section 2.2.5.

2.2.3.5 Plane-waves as basis functions

For atoms and molecules, it is straightforward to implement DFT using a Gaussian-type basis set (e.g., Roothaan, 1951) to expand the Kohn-Sham orbitals. However, in the solid state we wish to investigate the properties of extended systems. This entails consideration of increasingly large numbers of electrons (for each of which a wavefunction must be calculated) and hence a huge increase in the numbers of basis functions required. The solution arises from exploiting the periodicity of crystalline lattices in solid-state calculations. What this means is that we actually only simulate the unit cell of a crystalline solid but treat it as though it were repeated infinitely in all directions.

The theorem of Bloch shows that the wavefunction in a periodic system can be written as the product of a periodic term and a wave-like term:

$$\varphi_i(\vec{r}) = \exp\left[i\vec{k}\cdot\vec{r}\right] f_i(\vec{r}) \qquad \text{Eq. 2.27}$$

Where the wave-like term, $\exp\left[i\vec{k}\cdot\vec{r}\right]$, is a solution of the Schrödinger equation for a free particle and $\vec{k}$ is related to the momentum, $\vec{p}$, of the wave by $\vec{p} = \hbar\vec{k}$. The periodic term, $f_i(\vec{r})$, is expanded as a linear sum of plane-waves with wave vectors that are reciprocal lattice vectors of the crystal, $\vec{G}$.

$$f_i(\vec{r}) = \sum_{\vec{G}} c_{i,\vec{G}} \exp\left[i\vec{G}\cdot\vec{r}\right] \qquad \text{Eq. 2.28}$$

where $c_{i,\vec{G}}$ is a coefficient to be varied.

Therefore, the wavefunctions may be expressed as a plane-wave sum:

$$\varphi_i(\vec{r}) = \sum_{\vec{G}} c_{i,\vec{k}+\vec{G}} \exp\left[i\left(\vec{k}+\vec{G}\right)\cdot\vec{r}\right] \qquad \text{Eq. 2.29}$$

This expansion of the Kohn-Sham orbitals constitutes the basis set in the plane-wave method. In principle, an infinite basis set is needed, but this is not possible. Instead the expansion is truncated at some finite cut off value, E_{cut}, of the plane-wave kinetic energy, E_{PW};

$$E_{PW} = \left(\frac{\hbar^2}{2m}\right)\left|\vec{k}+\vec{G}\right|^2 \qquad \text{Eq. 2.30}$$

Having a finite basis set with $E_{PW} < E_{cut}$ results in an incorrect value of the total energy. But since plane-waves with larger kinetic energies contribute much less to the overall energy, the error can be minimised by simply increasing E_{cut} until the total energy, E_{tot}, converges. In VASP, this entails increasing the ENCUT tag in the INCAR file over a set of total energy calculations, and then using the value for which the energy difference between calculations, ΔE_{tot}, is minimised to some acceptably small value. For most of the solids described in this work, E_{cut} is in the region of 1000eV.

There are several approaches to doing plane-wave calculations incorporating all of the electrons in the system. These methods are variously dubbed LAPW (linearized augmented plane-wave), FLAPW (full-potential LAPW), LMTO (linear muffin-tin orbital), and KKR (Kohn-Korringa-Rosotcker), etc,. These methods are not discussed further since an alternative approach is employed in VASP; the pseudopotential method.

2.2.3.6 Pseudopotentials

Electrons closest to the nucleus have higher kinetic energies than those further out (not unlike planets, which have a greater angular momentum the nearer they are to the Sun). Representing electrons with such large kinetic energies in a plane-wave basis set requires the inclusion of a prohibitive number of plane-waves. However, in most applications we are only interested in what the electrons involved in intermolecular bonding (so-called valence electrons) are doing. Since the more tightly bound core electrons don't play a signficant role in intermolecular bonding, it would be convenient to simplify the whole representation of the core region. This is the foundation of pseudopotential theory (Philips, 1958: Heine and Cohen, 1970).

In this approximation, the core electrons and strong ionic potential are replaced with a very much weaker pseudopotential that acts on a set of pseudowavefunctions. These psuedowavefunctions, ψ_{pseudo}, are a substitute for the wavefunction of the valence electrons, ψ_V, in the core region, which oscillate rapidly (see Figure 2.1). The pseudopotential is constructed so as to yield a much smoother wavefunction in the core region. Outside the core region (i.e., beyond a cutoff radius, r_c) the pseudopotentials and wavefunctions are identical to the all-

electron potentials and wavefunctions. Core electrons are assumed to occupy the same states as they would in an isolated atom. The interaction between core and valence electrons must also incorporate the effects of exchange and correlation. The pseudopotentials supplied, and which I have employed, are constructed using the PW91 scheme to describe the core-valence exchange-correlation energy.

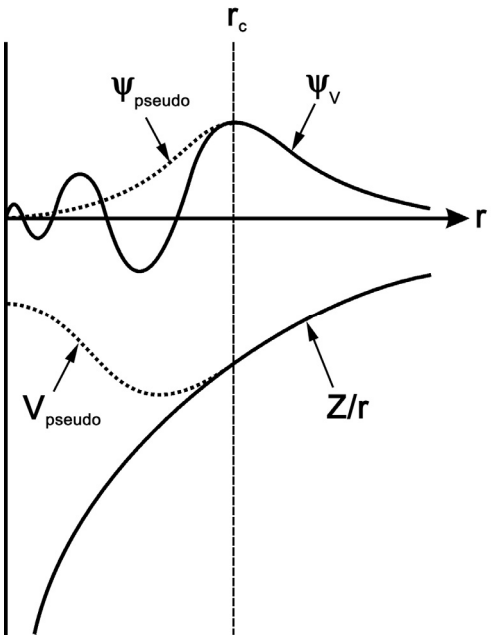

Figure 2.1.

Schematic illustration of the way in which the oscillating valence wavefunction, and strong ionic potential, in the core region (within r_c) are replaced with a smoother pseudo-wavefunction, ψ_{pseudo}, and a weaker pseudopotential.
After Payne *et al*. (1992).

Certain problems arise when generating pseudopotentials for in the first row of the periodic table, and also to hydrogen, which has no core electrons, at all. In this case, ψ_V tends to be strongly peaked in the core region and these atoms require rather large plane-wave cutoffs when conventional pseudopotentials are used. Vanderbilt (1990), by relaxing certain constraints on the way pseudopotentials are constructed, produced a set of so-called non-norm conserving ultrasoft pseudopotentials. These allow first-row atoms to be used with much lower plane-wave cutoffs. E_{cut} values of 25 Ry (340 eV) have been demonstrated to be sufficient for hydrogen bonded systems (Andrews *et al*. 1996), but strict convergence of geometric and elastic properties may require cutoffs of ~ 45 Ry (~ 600 eV) or more (Meier 1999).

2.2.3.7 $\vec{k}$ -point sampling

In the plane-wave approximation the total energy is evaluated from the contributions of each occupied electronic state at every wavevector (or $\vec{k}$ -point) in the solid. However, Bloch's theorem, and the inherent symmetry of the crystal being simulated, can be exploited so that the

electronic states at only a small number of $\vec{k}$-points need to be calculated. A given crystal space group consists of a set of symmetry operators that act upon an asymmetric unit to yield a complete unit cell. This is then repeated through space to form a crystal. In terms of reciprocal space, this asymmetric unit is called the irreducible Brillouin zone (IBZ). The problem is thus reduced to one of merely sampling the electronic states at $\vec{k}$-points in the IBZ.

In addition, the wavefunctions at $\vec{k}$-points which are close together will be virtually identical. We can therefore sample a less dense mesh of $\vec{k}$-points and interpolate between them. The particular method I have used to calculate the electronic states at to a set of special $\vec{k}$-points in the IBZ is that of Monkhorst and Pack (1976). The advantage of this approach is that the error due to inadequate sampling is easily reduced by increasing the sampling density. The error will diminish with increasing numbers of $\vec{k}$-points in the IBZ, converging towards the true total energy. As with the plane-wave cutoff, convergence tests are carried out to determine the size of the $\vec{k}$-point mesh which minimises the error in the total energy.

2.2.3.8 Ionic relaxation

From the point of view of quantum chemistry, we are interested in the equilibrium geometries (bond lengths, bond angles, etc,.) of molecules, dimers, clusters, and so forth. In condensed matter physics, we are interested in crystal structures at a range of pressures and temperatures, elastic properties and vibrational spectra. Each of these requires that the ions be able to feel forces acting upon them when they are sited away from their equilibrium positions, and can be moved by those forces.

The force on an ion, $\vec{f}_A$, is

$$\vec{f}_A = -\frac{dE}{d\vec{R}_A} \qquad \text{Eq. 2.31}$$

The motion of the ion is then described by classical Newtonian mechanics, specifically Newton's second law, $\vec{f} = M_A \vec{a}$, where $\vec{f}$ = force, $\vec{a}$ = acceleration (the second derivative of the position with respect to time, $d^2\vec{R}_A/dt^2$), and M_A = mass.

Therefore, the equation of motion of the ions is,

$$-\frac{dE}{d\vec{R}_A} = M_A \frac{d^2\vec{R}_A}{dt^2} = M_A \ddot{R}_A \qquad \text{Eq. 2.32}$$

Since the dimensions of the unit cell are free parameters which may also be relaxed to find equilibrium values, a similar equation is applied to the coordinates of the unit cell (with a fictitious mass assigned to those coordinates).

The forces are actually calculated using the Hellmann-Feynman theorem (Hellmann, 1937: Feynman , 1939), in which the physical force on the ion is the partial derivative of the Kohn-Sham energy with respect to $\vec{R}_A$ provided the electronic system is relaxed into its ground state. In practice, this means that the exact forces can only be calculated at the end of a self-consistent electronic relaxation.

It is worth noting that there is an additional force acting which is the derivative of the basis set with respect to $\vec{R}_A$ (Pulay, 1969). The Pulay forces on the *ions* are zero for a plane-wave basis set, but the Pulay stresses on the *unit cell* may be non-zero. This will be the case if the absolute total energy of a structure is not converged.

There are several computational schemes for getting the ions (and electrons) into their local (or global) energy minima. The scheme used most commonly is the conjugate-gradient technique. Rather than moving the ion in the direction in which the energy reduction is steepest at every step (the 'steepest descent method', which might seem to be the logical method), the ion is instead moved in a direction which contains some component of the previous movement. In other words, a given ionic move is conjugate to the one preceding it. This method requires fewer iterations than the steepest descent method to arrive at the energy minimum. In the conjugate-gradient method, the cycle of electronic relaxation + ionic movement is repeated until the energy difference between one ionic configuration and the next is minimised.

During the course of a typical ionic relaxation, the motion of all the nuclei is treated by classical Newtonian mechanics. However, ignoring the quantum nature of the hydrogen atom ignores important phenomena such as tunnelling and zero point motion. The effect of treating hydrogen nuclei as classical particles was investigated by Benoit *et al*. (1998a). Their Quantum Monte Carlo (QMC) study compared the classical and quantum approach to the hydrogen bond symmetrisation which occurs in the phase transition from ices VII and VIII to ice X (see Fig. 2.2, overleaf). The classical treatment of the hydrogen atom places the symmetrisation transition at a little over 100 GPa whereas the QMC simulation places it at ~70 GPa. The experimentally observed transition pressure is at ~ 60-70 GPa. This reduction in the transition pressure is due to the delocalisation of the hydrogen atoms position by quantum effects (tunnelling and zero point motion) at high pressure. Where this issue crops up, in respect of ice and ammonia in Chapters 3 and 5, it is discussed further.

Figure 2.2. Comparison between a classical and quantum treatments of the hydrogen atom in simulations of the hydrogen bond symmetrisation. After Benoit *et al*. (1998a).

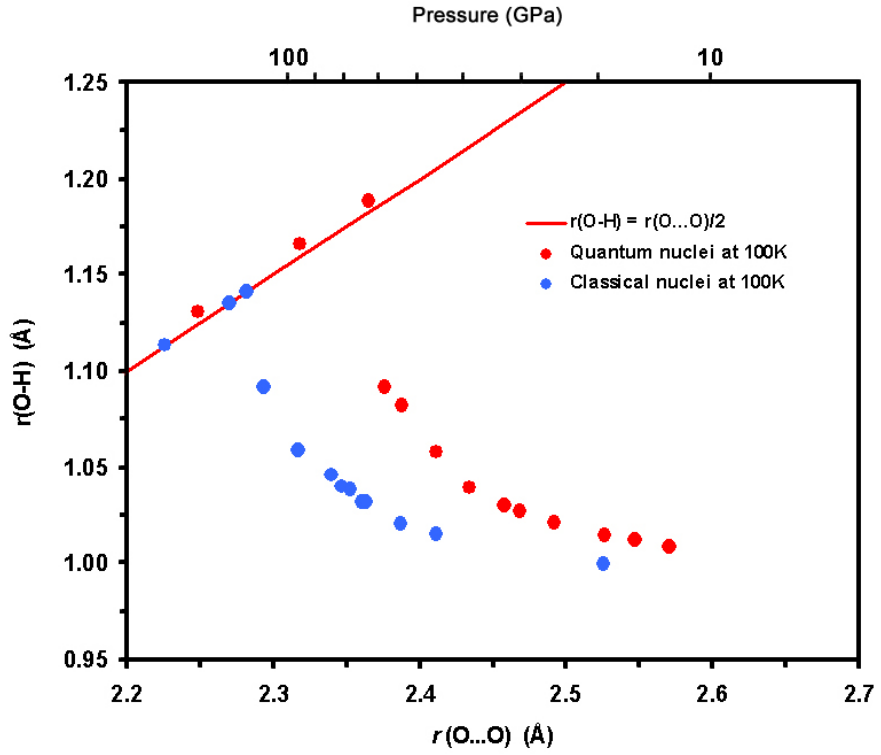

2.2.4 The practical application of density functional theory in this work

2.2.4.1 VASP: inputs and outputs

The solution of the Kohn-Sham equations is a job for very powerful computers. This requires software, in the form of an algorithm (that is, a specific set of steps), to run on such a computer. In this final part of Chapter Two, I intend to give an overview of the software code I have used to apply DFT calculations to the study of ammonia hydrates. This software, the Vienna *Ab-initio* Simulation Package (VASP), is described in more exhaustive detail in Kresse and Furthmüller (1996: VASP Guide).

The beauty of the *ab initio* method is that one can, in principle, determine any property of a given system simply by feeding in the types of atoms and their relative positions. To do a calculation in practice requires a little more. In VASP there are four essential input files from which information is read when the code is executed. These are the POSCAR, POTCAR, INCAR and KPOINTS files.

The POSCAR file is the most straightforward. It tells VASP which atoms are where in the unit cell.

The POTCAR file contains the pseudopotentials for each atomic species, and files for all elements exist in the VASP library. The individual files are concatenated into single files containing all the pseudopotentials pertinent to a calculation. The order in which they appear in the final POTCAR file (e.g., hydrogen, then nitrogen, then oxygen) must correspond to the order in which the coordinates of those species appear in the POSCAR file.

The KPOINTS file tells VASP how densely the irreducible Brillouin zone is to be sampled to calculate the total energy.

Finally, the INCAR file tells VASP what to do with these inputs and how. The file consists of a series of tags to which user defined values can be attached. The conjugate-gradient algorithm is activated by setting the tag IBRION = 2 in the INCAR file. One must also specify which degrees of freedom are to be relaxed. Normally, this means relaxing the ions and cell parameters but maintaining the unit cell at a fixed volume, for which the tag ISIF = 4 applies. In addition, the INCAR file must contain criteria for terminating both the electronic and ionic relaxation loops. The maximum number of self-consistent electronic steps is fixed by the NELM tag (and the minimum by NELMIN), or may be instructed to to cut off when the difference between steps falls below a value set by the EDIFF tag (usually 10^{-6} eV). The number of ionic movements to carry out is defined by the NSW tag, or is instructed to cut off when the difference in total energy between ionic relaxtions drops below EDIFFG.

There are many output files. Of particular interest are the OSZICAR and OUTCAR files, to which are written the total energies throughout each self-consistent iteration, and the stresses at each ionic relaxation step, amongst other things.

For the calculations I am doing, the CONTCAR file is written every time the ions are moved and at the very end of a calculation. The file gives the updated atomic positions and lattice vectors (in POSCAR format) and the velocities of the atoms. For the static calculations used in this work the velocities constitute a long list of zeroes.

Other files of interest include the CHGCAR file, from which the electron density can be visualised using the VASPview application; the EIGENVALUE file, which gives the eigenvalues of the Kohn-Sham orbitals at each $\vec{k}$ -point (for static calculations these are the solutions of the Kohn-Sham equation); and the DOSCAR file, from which the electronic density of states (DOS) can be extracted.

For the solids described in this thesis, there is the problem that hydrogen bonds are poorly dealt with, and dispersion forces are not covered at all, by GGA's. The non-local components of these increasingly weak binding forces (van der Waals forces are completely non-local) are simply not accounted for by local or semi-local approximations to E_{XC}. Whilst there are

schemes being developed to accommodate van der Waals forces, these are not available within VASP at present (Kohn *et al*. 1998: Engel *et al*. 2000).

The version of VASP used in this work (version 4.4) allows the use of one of four GGA functionals (set using the GGA tag in the INCAR file). These are LM (Langreth and Mehl, 1981, 1983), BP86 (Perdew, 1986: Becke, 1988), PW86 (Perdew and Wang, 1986), and PW91 (Perdew, 1991: Perdew and Wang, 1992). VASP 4.5 incorporates the PBE (Perdew *et al*. 1996) and RPBE (Hammer *et al*. 1999) GGA's which are semi-empirical extensions of PW91.

Of these available functionals in VASP, only the PW91 functional has been demonstrated to yield results which are comparable both with experimental data and with CCSD(T) calculations for hydrogen bonded and van der Waals bound systems (Tsuzuki and Lüthi, 2001). PW91 succeeds with 'difficult' systems such as the neon and argon dimers, which are predicted not to be bound by BLYP and B3LYP DFT calculations. The PW91 GGA functional achieves sufficiently good results on a number of weakly bound systems that it can be applied with care to other hydrogen bonded systems with some expectation of success.

2.2.4.2 From total energy to equation of state

The principal output from a static VASP calculation is the internal energy of the solid being simulated. All of the physical properties of a system are contained within the quantum mechanical description given by the Schrödinger equation, and these emerge as a change in the internal energy in response to some physical 'stimulus.' For example, the incompressibility is determined from the change in internal energy due to changes in the molar volume (at absolute zero temperature); elastic constants are found by calculating the change in internal energy when a crystal structure is strained; and vibrational frequencies are found from the change in internal energy as individual atoms are shifted fractionally from their equilibrium positions.

This work is concerned with determining the equation of state (EoS) of the solids being simulated, and so the total energy is calculated for a range of molar volumes. The total energy, E, may be used to determine the EoS state as follows. From the First and Second Laws of Thermodynamics, the pressure in the athermal limit is related to the internal energy by

$$dE = -P\,dV \quad \text{or} \quad -P = \left(\frac{\partial E}{\partial V}\right)_T \qquad \text{Eq. 2.33}$$

In other words, a plot of internal energy against molar volume has a slope equal to –P. The numerical value for the internal energy is then given by the integral of the pressure with respect to volume (at constant T);

$$E = -\int P \partial V \qquad \text{Eq. 2.34}$$

Pressure as function of volume is expressed through an isothermal equation of state. Although there are many different equations in use, I have used two well-known equations of state in this work. The 3rd order Birch-Murnaghan EoS (BMEOS3) (Birch 1952);

$$P_{V,T} = \frac{3}{2} K_{0,T} \left(x^{7/3} - x^{5/3} \right) \left[1 + \frac{3}{4} \left(K'_{0,T} - 4 \right) \left(x^{2/3} - 1 \right) \right] \qquad \text{Eq. 2.35}$$

where $x = V_{0,T} / V_{P,T}$, and $V_{0,T}$, $K_{0,T}$, and $K'_{0,T}$ are, respectively, the zero-pressure molar volume, the zero-pressure bulk modulus (or incompressibility), and the zero-pressure first derivative of the bulk modulus. The latter are defined as,

$$K = \frac{1}{V} \frac{dP}{dV} \quad \text{and} \quad K' = \frac{dK}{dP} \qquad \text{Eq. 2.36}$$

And the 4th order logarithmic EoS (LNEOS4) (Poirier and Tarantola 1998);

$$P_{V,T} = x \left[a \ln x + b \ln^2 x + c \ln^3 x \right] \qquad \text{Eq. 2.36}$$

where x has he same meaning as for Eq. 2.34 and

$$a = K_{0,T}$$

$$b = \frac{K_{0,T} \left(K'_{0,T} - 2 \right)}{2}$$

$$c = \frac{K_{0,T}^2 K''_{0,T} + K_{0,T} + K_{0,T} \left(K'_{0,T} - 2 \right) + K_{0,T} \left(K'_{0,T} - 2 \right)^2}{6}$$

In order to determine $V_{0,T}$, $K_{0,T}$, and $K'_{0,T}$ from the total energy, one must integrate these expressions for the pressure (Eqs. 2.34 and 2.36). The integrated forms which are then used in fitting to the total energy obtained from VASP calculations are, with the energy at $V_0 = E_0$;

For the BMEOS3,

$$E = \left(\frac{9}{4}\right)K_0V_0(x)\left[\frac{1}{2}(x)^{1/3} - (1/x)^{1/3}\right] + \left(\frac{9}{16}\right)K_0(K_0' - 4)V_0(x)\left[x - 3(x)^{1/3} + 3(1/x)^{1/3}\right] + E_0 - \left(\frac{9}{16}\right)K_0(K_0' - 6)V_0 \quad \text{Eq. 2.37}$$

And for the LNEOS4,

$$E = V_0\left[\frac{a\ln^2 x}{2} + \frac{b\ln^3 x}{3} + \frac{c\ln^4 x}{4}\right] + E_0 \quad \text{Eq. 2.38}$$

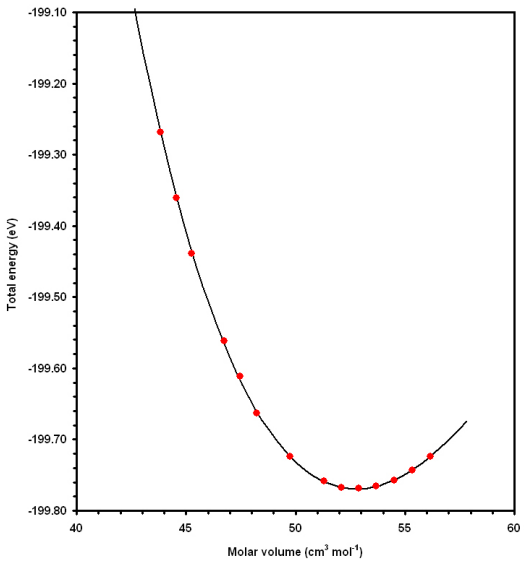

Figure 2.3.
Total energies output from VASP (red filled circles) for one unit cell of ammonia dihydrate, as a function of the molar volume. The black line is an integrated form of the 3rd order Birch-Murnaghan equation of state fitted to the total energies.

Non-linear regression was done using the DataFit package. (http://www.oakdaleengr.com)

Throughout this thesis, the EoS found by fitting to E(V) results are plotted in P(V) space along with the external stresses calculated by VASP at each volume. The extent to which the calculated stresses agree with the EoS pressures is an indication of how well converged is the calculation.

In hydrogen bonded crystals, the binding energy is very low and the change in energy with compression is small. Hence, the E(V) curves are quite flat, and this makes it challenging to accurately determine the values of the zero-pressure parameters. The problem becomes more acute in more weakly bound solids, so one observes an increase in the size of the standard errors in the fitting as one moves from ice to solid ammonia.

The lattice energies of ice and ammonia can be determined from the energies of the monomers. The lattice energy is defined as that needed to change a non-vibrating molecular solid to a non-vibrating gas of molecules. The difference between the total energy of the

molecule in the bulk solid and the energy in the isolated state is the lattice energy. In ice and ammonia, this is essentially the energy contained in the hydrogen bonds.

This energy of the monomer is found by setting up a large unit cell with a single molecule at the centre. Although this cell is repeated periodically, the molecules are sufficiently far apart (~15Å) to minimise long-range interactions. This is effectively a fictitious gas of non-vibrating molecules at zero Kelvin. The method described is actually rather inefficient with a plane-wave basis since a lot of empty space is needlessly filled with plane waves (and this places a high demand on memory allocation during the calculation). Gaussian-type functions, in contrast, are centred on the atoms and decay radially outward, making them ideal for molecular calculations. However, the simulation of the monomers requires only Γ-point sampling ($\vec{k}$ = 0, 0, 0) of the IBZ, and the default value of E_{cut} (set in the POTCAR file) to achieve total energy convergence. The energy of the isolated H_2O monomer is -14.206 eV, and of the NH_3 monomer is -19.560 eV.

2.3 Summary

I have described the use of quantum mechanics to determine the properties of matter using variational solutions implemented in both a wavefunction-based approach and an electron density-based approach. The latter method, Kohn-Sham density functional theory, is employed in this work and is implemented in the computer program VASP using approximations to describe the quantum interactions of electrons (GGA) and the highly energetic core electrons (pseudopotential approximations). In VASP, wavefunctions are expanded as a plane-wave basis set. The total energies output by VASP are used in the fitting of equations of state to determine the equilibrium structural and elastic properties of each crystalline solid.

Chapters 3 - 7 describe the results of my calculations on solids in the ammonia - water system, beginning with the end members, water and ammonia, and finishing with the stoichiometric hydrates.

CHAPTER THREE

WATER ICES AT HIGH PRESSURE: ICES VIII, X, AND BEYOND

3 High-pressure Water Ices

There exists a considerable volume of experimental and theoretical literature relating to water ice. This chapter presents the results of my *ab initio* calculations on the structure and elasticity of several high-pressure polymorphs of ice, the objective being to demonstrate the utility of the GGA pseudopotential method in accurately reproducing the properties of ice. The initial goal was to simply repeat the calculations of Tse and Klug (1998) on ice VIII. However, the scope of the study rapidly expanded to encompass other high-pressure phases. I begin with a brief description of phase relations in the H_2O system.

The water ice phase diagram (Figure 3.1) contains thirteen experimentally confirmed crystalline polymorphs, denoted by Roman numerals, from the hexagonal and cubic polytypes of low-pressure ice I (Ih and Ic, respectively) through to the recently identified ice XII (Lobban *et al*., 1998). A number of these phases, including ice XII, are in fact wholly metastable and thus do not appear in Figure 3.1. In addition, there is evidence for the existence of metastable proton-ordered forms of ices V and VI (denoted V′ and VI′), bringing the total to fifteen. Below ~ 2.1 GPa the phase relations are very complicated indeed, and the reader is referred to the text of Petrenko and Whitworth (1999).

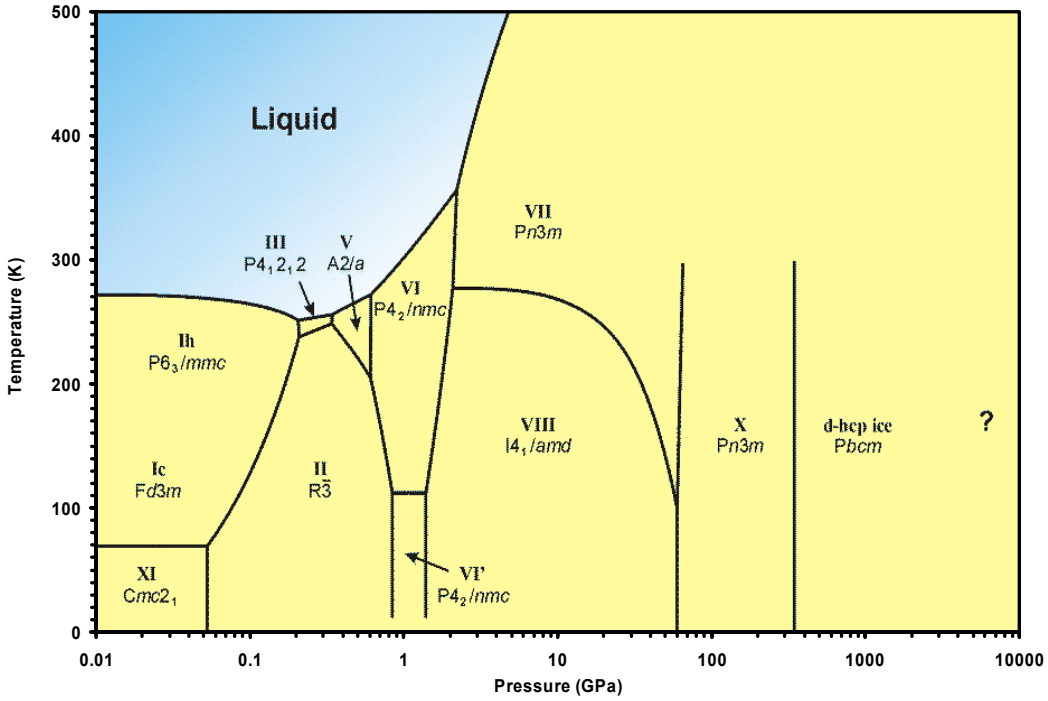

Figure 3.1. The equilibrium water ice phase diagram. Roman numerals denote the phases, space groups being indicated beneath. Melting curves are from Tchijov (1993), the VII ↔ VIII, VII ↔ X, and VIII ↔ X phase boundaries are from Goncharov *et al*. (1999). Low pressure phase boundaries and triple points are based on references reported in Petrenko and Whitworth (1999)

Immediately above ~ 2.1 GPa the phase diagram simplifies considerably, and there are only two high-density polymorphs, phases VII and VIII. The low temperature phase, ice VIII (Fig. 3.2a), is tetragonal (space group $I4_1/amd$, with the origin at inversion centre $2/m$). There are eight orientationally ordered water molecules in the unit cell, with site symmetry C_{2v}, comprising two distinct unbonded lattices. The structure is equivalent to two interpenetrating ice Ic lattices (space group $Fd\bar{3}m$) in which the dipole moments of the water molecules are oppositely directed along the *c*-axis (i.e., the structure is antiferroelectrically ordered). Interactions between the two lattices are purely via weak van der Waals forces. The *c*-axis offset between the two lattices defines the degree of tetragonal distortion, ε, and is given as $\varepsilon = 2c\,[\,\tfrac{1}{8} - z(\mathrm{O})\,]$. If the two lattices were in coincidence then the oxygen atoms would lie on the special positions $z(\mathrm{O}) = \tfrac{1}{8}$ and $\varepsilon = 0$. The result of this offset arrangement is that each oxygen atom has four hydrogen-bonded neighbours that are further away than the two non-bonded nearest neighbours (Kuhs *et al*., 1984).

Ice VIII can be quenched to ambient pressure at temperatures below 125 K, though this results in a modest lattice distortion that has been referred to as a phase transition.

Discrepancies between the vibrational spectra of ice VIII samples studied at high pressure and those quenched to ambient pressure led to suggestions of a phase transition in the metastable solid (e.g., Hirsch and Holzapfel 1986). Besson *et al.* (1997) identified a minor structural relaxation upon decompression, calling the relaxed structure ice VIII′. The relaxation involves a shift in the fractional z(O) coordinate from 0.110 to 0.107, equivalent to a ~20% increase in the tetragonal distortion (ε, see above). This separation of the two interpenetrating lattices occurs in D_2O at 85 K between 1 and 5 GPa (see Figure 3.6). Besson *et al*. (1997) considered that this was the result of crossing the extrapolated Ice Ih melting line. It is possible that the extrapolated first-order liquid-liquid transition seen in supercooled water is more important since it is this, and not the ice Ih melting line, which divides the amorphous ice phase diagram into high and low density forms.

Above 263 K (at 2.1 GPa), ice VIII undergoes a first-order phase transition to ice VII, a body centred cubic polymorph (space group P$n\bar{3}m$, Z = 4), which is orientationally disordered. Ice VII is structurally equivalent to a disordered form of Ice VIII with ε = 0. As can be seen in Figure 3.1, the slope of the phase boundary, $\partial T/\partial P$, is ~ 0 at pressures < 10 GPa, turning increasingly negative as pressure-induced translational proton tunnelling becomes important (Benoit *et al*., 1998). Above ~60 GPa, ices VII and VIII experience a transition to a hydrogen-bond symmetrised phase known as ice X (space group P$n\bar{3}m$, isostructural with cuprite, Cu_2O), shown in Figure 3.2b.

The existence of an ice phase isostructural with Cu_2O, in which hydrogen atoms are positioned half-way between nearest O…O neighbours, was predicted theoretically by Holzapfel (1972). Ice X has since been observed and studied by a variety of theoretical and experimental methods. The location of the ice VIII ↔ ice X transition has proven difficult to pin down experimentally, and the nature of the transition itself is the subject of continued debate. Many earlier experiments extrapolated X-ray diffraction data and vibrational frequencies to find the phase boundary. For example, Walrafen *et al*. (1982) predicted that the transition would occur when $r_{(O...O)} = 2.35 \pm 0.06$ Å, equivalent to 75 ± 20 GPa. At 300K the transition has reportedly been seen at 44 ± 2 GPa (Polian and Grimsditch, 1984), 80 GPa (Pruzan *et al*., 1993), 60 GPa (Goncharov *et al*., 1996), 62.1 GPa (Aoki *et al*., 1996), 67 ± 3 GPa (Struzhkin *et al*., 1997), 60 GPa (Goncharov *et al*., 1999), and ~100 GPa (Katoh *et al*., 2000). The most detailed X-ray diffraction study to date (Loubeyre *et al*., 1999), aimed at actually observing the position of the hydrogen atom as a function of pressure, found that bond centering takes place gradually over a wide pressure range. In polycrystalline ice, the transition is generally accepted to occur around 60-65 GPa, although Loubeyre *et al*. (1999) noted the onset of the transition in single crystals at ~ 40 GPa.

Ab Initio Molecular dynamics (MD) simulations have revealed superionicity and a metallic phase of liquid water at high temperatures and pressures (Cavazzoni, 1998: Cavazzoni *et al*. 1999), but questions remain over the series of phase transformations which occur in solid water ice at ultrahigh pressures. Classical MD simulations (Demontis *et al*., 1988, 1989) originally mooted the existence of a fcc proton-symmetric phase with the antifluorite structure (space group $Fm\bar{3}m$, Z = 4) at pressures of 100 - 300 GPa. Since then, *ab initio* MD calculations (Benoit *et al*., 1996) have shown this structure to be much less energetically favoured, and instead propose the existence of a transition from bcc ice X to a distorted hcp (d-hcp) proton-symmetric phase (space group P*bcm*, Z = 4) at 300 – 400 GPa. This agrees with the study of Hama *et al*. (1990) which indicates the evolution of the ice structure under compression to be bcc $\rightarrow$ hcp $\rightarrow$ fcc, with the fcc antifluorite structure becoming metallic at 1.76 TPa. Of these various hypothetical phases, one or another has at some time been referred to as ice XI, XII, or XIII. These designations are to be used only for experimentally confirmed structures (Petrenko and Whitworth 1999). In this work I will employ only the appropriate structure types in the following description of my computational methods and results.

3.1 Ice VIII

3.1.1 Computational Details

Static DFT calculations (as described in Chapter 2) of the relative energetics of the ice VIII, ice X, d-hcp, and antifluorite structures were carried out to determine the equation of state (EOS) of each of these ice polymorphs and constrain the transition pressures. In addition, I have calculated the energies of ice polymorphs with the $CaCl_2$, and α-PbO_2 structures. These two structures play a major role in the high-pressure polymorphism of many metal oxides, notably SiO_2 (e.g., Behnke *et al*., 1986: Demuth *et al*., 1999) and RuO_2 (Haines and Leger, 1993), both of which materials share some structural similarities with several ice polymorphs. Table 3.I (parts a – f, overleaf) provides the starting parameters from which the structural relaxations were begun.

Total energy convergence tests were carried out to optimise the sampling of the Brillouin zone, and the cut-off of the plane-wave basis set. The $\vec{k}$-point sampling of the irreducible Brillouin zone (IBZ), and electron kinetic energy cut-off (E_{cut}), for each phase was as follows: ice VIII and ice X*, 39 points, 800eV; d-hcp ice, 27 points, 900eV; antifluorite ice, 10 points, 700eV; $CaCl_2$ ice, 27 points, 900eV; α-PbO_2 ice, 64 points, 1400eV. These values were found to yield total energy convergence of better than 10^{-4} eV per unit cell.

*N.B. The ice X calculations were done using a supercell corresponding to the ice VIII unit cell with the oxygen atoms located on the special positions (0, ¼, ⅛) and the bond-centred hydrogens on the special positions (0, ½, ¼). The supercell lattice parameters are related to the lattice parameters of ice X as, $c_{\text{supercell}} = 2\ a_{\text{ice X}}$, and $a_{\text{supercell}} = \sqrt{2}\ a_{\text{ice X}}$

Table 3.I a – f. Starting structural parameters for the ice polymorph calculations. 3.Ia from Kuhs *et al*. (1984); 3.Ic from Benoit *et al*. (1996).

a. **Ice VIII**

Space group $I4_1/amd$ (no' 141) D_{4h}^{19}

a = 4.656Å c = 6.775Å

Atomic species	Wyckoff position	Fractional coordinates (*x,y,z*)
O	8e	(0, ¼, 0.1071)
H	16h	(0, 0.4157, 0.1935)

b. **Ice X**

Space group P$n\bar{3}m$ (no' 224) O_h^4

a = 2.54Å

Atomic species	Wyckoff position	Fractional coordinates (*x,y,z*)
O	2a	(0, 0, 0)
H	4b	(¼, ¼, ¼)

c. **d-hcp ice**

Space group P*bcm* (no' 57) D_{2h}^{11}

a = 2.220Å b = 3.574Å c = 3.441Å

Atomic species	Wyckoff position	Fractional coordinates (*x,y,z*)
O	4d	(0.252, 0.434, ¼)
H1	4d	(0, 0.184, ¼)
H2	4b	(½, ½, 0)

d. **Antifluorite ice**

Space group F$m\bar{3}m$ (no' 225) O_h^5

a = 3.11Å

Atomic species	Wyckoff position	Fractional coordinates (*x,y,z*)
O	4b	(0, 0, 0)
H	8e	(¼, ¼, ¼)

e. **$CaCl_2$ ice**

Space group P*nnm* (no' 58) D_{2h}^{12}

a = 3.120Å b = 3.215Å c = 2.10Å

Atomic species	Wyckoff position	Fractional coordinates (*x,y,z*)
O	2a	(0, 0, 0)
H	4g	(0.275, 0.325, 0)

f. **α-PbO_2 ice**

Space group P*bcn* (no' 60) D_{2h}^{14}

a = 2.474Å b = 2.976Å c = 2.749Å

Atomic species	Wyckoff position	Fractional coordinates (*x,y,z*)
O	4c	(0, 0.178, ¼)
H	8d	(0.276, 0.41, 0.425)

Overleaf: Figure 3.2a – f. The structures of the ice polymorphs under study. Oxygen atoms in red, hydrogen atoms in white. Covalent O-H bonds are shown as white rods, hydrogen bonds as grey rods. *a*) Ice VIII viewed along the a-axis with the *c*-axis vertical. *b*) Ice X. *c*) Antifluorite ice. *d*) d-hcp ice viewed along the *a*-axis with the *c*-axis vertical. *e*) $CaCl_2$ ice viewed along the *b*-axis with the *a*-axis vertical. *f*) α-PbO_2 ice viewed along the *a*-axis with the *c*-axis vertical.

Figure 3.2a – f. *(Caption on preceding page)*

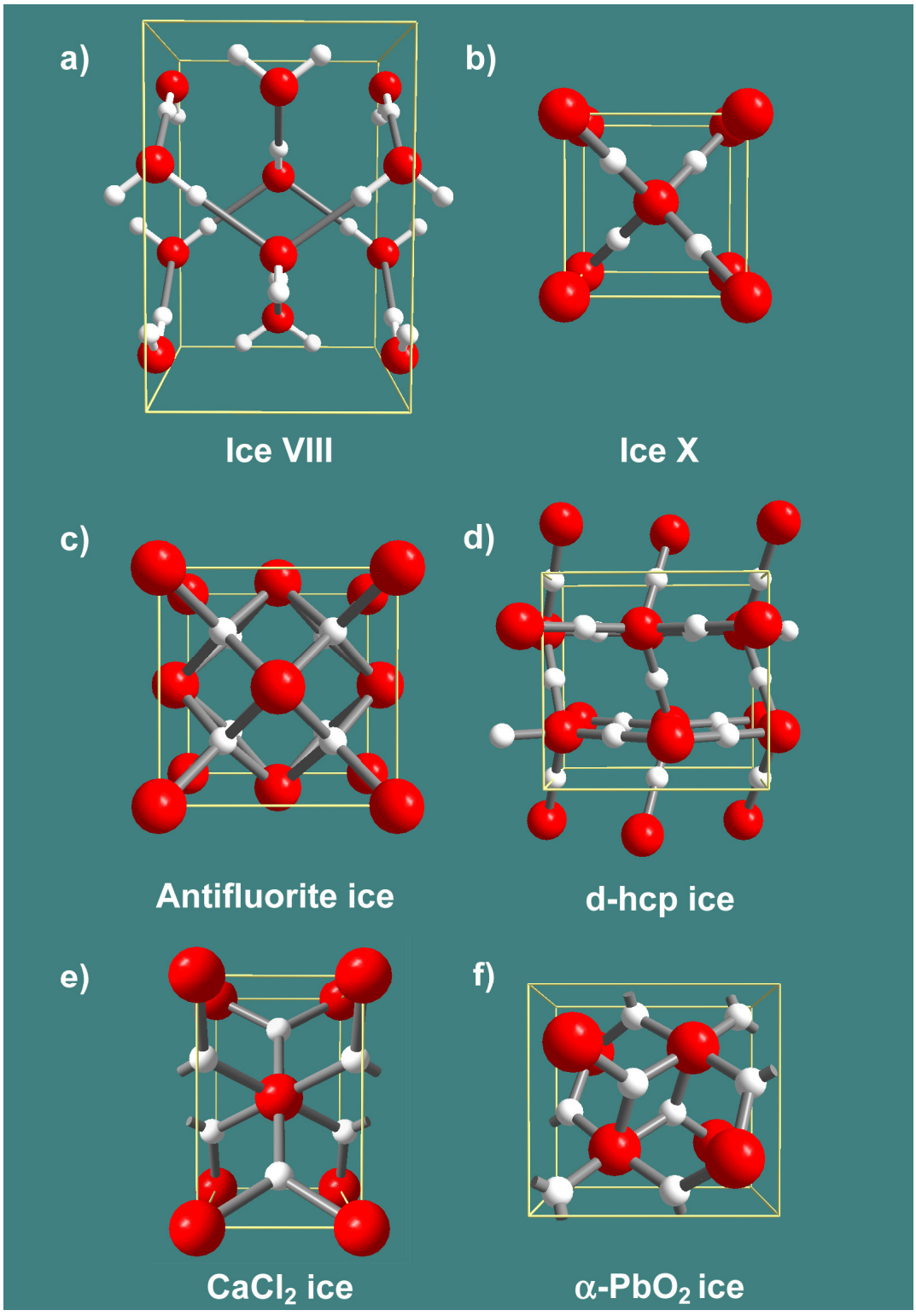

3.1.2 Equation of State of ice VIII

Structural relaxations were carried out over the range of cell volumes from 180Å^3 (13.55 cm^3 mol^{-1}) to 68Å^3 (5.12 cm^3 mol^{-1}). The plot of total energy against cell volume, E(V), shows no obvious discontinuities, indicating that there are no first-order phase transformations in this range. As Figure 3.3 shows, the correspondence between the results of my calculations and those of Tse and Klug (1998) is exceptionally good, which is unsurprising since their GGA functional was the same as that used here. Note that Tse and Klug employed a $\vec{k}$-point sampling mesh with 48 unique points in the IBZ, and E_{cut} = 600 eV (compared to 39 points and 800 eV in this work). Using the energy of the isolated H_2O molecule (see Chapter 2) and the minimum energy of the ice VIII structure, E_0, the lattice energy is found to be 54.96 ± 0.04 kJ mol^{-1}, and the average hydrogen bond enthalpy is 27.48 ± 0.02 kJ mol^{-1}.

Integrated forms of the third order Birch-Murnaghan EoS (BMEOS3) and a fourth order logarithmic EOS (LNEOS4) were fitted to the E(V) data, as described in Chapter 2. Parameters from these fits appear in Table 3.II, and the EoS are plotted in Figures 3.3 and 3.4 (overleaf).

Table 3.II. Calculated EOS parameters of ice VIII.

	V_0 (cm^3 mol^{-1})	K_0 (GPa)	K_0'	K_0'' (GPa^{-1})	E_0 (eV molecule^{-1})
BMEOS3: E(V) fit	12.03 ± 0.03	16.8 ± 0.7	6.0 ± 0.2	···	-14.7756±0.0004
LNEOS4: E(V) fit	12.06 ± 0.03	17.5 ± 0.8	4.3 ± 0.8	0.79 ± 0.45	-14.7760±0.0004

Overleaf:

Figure 3.3. Calculated E(V) curve for ice VIII. The solid line shows the best fit EOS (both BMEOS and LNEOS are indistinguishable on this scale).

Figure 3.4. Graphical representation of the EOS of Ice at low pressures. Data points are literature values for both ice VII and ice VIII. The solid red line shows my calculated BMEOS3.

Figure 3.3. *(Caption on preceding page)*

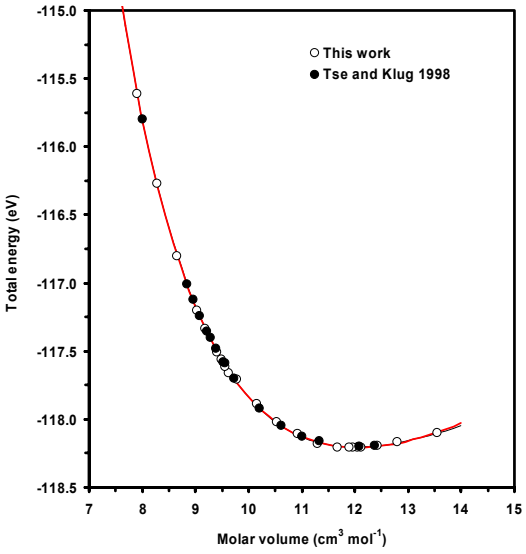

Figure 3.4. *(Caption on preceding page)*

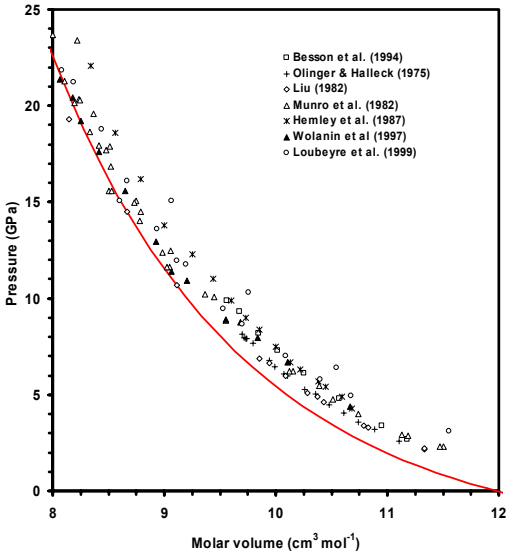

Table 3.III. Literature EoS parameters for ice VII and ice VIII, both of which phases are taken to have indistinguishable elastic properties.

	V_0 ($cm^3\ mol^{-1}$)	K_0 (GPa)	K'_0
Isothermal EOS, Olinger and Halleck, 1975.	12.843±0.315	12.54±0.27	5.56±0.14
Isothermal EOS, Munro *et al*. 1982	12.87	15.78	4.11
BMEOS3, 296K. Liu, 1982.	12.68±0.05	24.0±0.9	4.50
BMEOS3, 300K. Hemley *et al*. 1987.	12.3±0.3	23.7±0.9	4.15±0.07
BMEOS3, 300K. Besson *et al*. 1994.	12.450	20.4	4.70
As above extrapolated down to 0 K.	11.980	24.1	4.44
BMEOS3, 85K. Besson *et al*. 1997.	12.040	23.8±1.4	4.5±1.5

Figure 3.4 shows the calculated EoS of ice VIII at low pressures (0 – 25 GPa) along with literature P(V) data for ices VII and VIII, both of which have the same EoS. The offset of the calculated EoS appears to be due entirely to temperature: much of the experimental data in Table 3.III was acquired at ~ 300 K, whereas the calculated EoS corresponds to the athermal limit (absolute zero less zero point energy). The molar volume measured at 4 K at ambient pressure by Klotz and Loveday (1999) is 12.0136 ± 0.0004 $cm^3\ mol^{-1}$, which is within the errors on V_0 calculated from the BMEOS3 fit (Table 3.II). It is apparent, therefore, that for ice VIII the PW91 GGA functional does a superb job of correcting for the well-known overbinding seen in LDA calculations (Hafner, 2000).

The differences between the calculated and experimental values of K_0 and K_0' can be attributed to the correlation between the two when fitting an EoS. For example, at a relatively minor expense to the quality of fit (R^2 drops from 99.9897% to 99.9281%), K_0' can be fixed at 4.5 when fitting the EoS to E(V) data, yielding K_0 = 22.77 ± 0.49 GPa, very close to the 0 K value of Besson *et al*. (1994). The correct values can be independently constrained from elastic constant data. Shimizu *et al*. (1996) measured the elastic constants of ice VII at 300 K from 2 – 7 GPa. A linear fit to their bulk moduli, as determined from the measured stiffnesses, gives K_0 = 13.7 ± 0.4 GPa, and K_0' = 5.33 ± 0.09. This supports the results of the EoS fits to my calculated energies, wherein K_0 is smaller, and K_0' larger, than the experimental values quoted in Table 3.III.

3.1.3 Structure of ice VIII

The evolution of the cell parameters with compression (Figure 3.5) are (again, unsurprisingly) a superlative match to the results of Tse and Klug (1998). Table 3.IV also reveals that this work is a significantly better match to experimental cell parameters and internal coordinates than pre-existing *ab initio* simulations. It is noteworthy that none of the tabulated *ab initio* results reproduce the relaxation between the two interpenetrating lattices in ice VIII (see page 71), observed from 1 - 5 GPa (Besson *et al*., 1994), which is shown in Figure 3.6. Hartree-Fock calculations (Besson *et al.,* 1994: Ojamäe *et al.,* 1994) yield z(O) = 0.112 at all pressures. In contrast, the pseudopotential calculations of Tse and Klug (1998) do reproduce the observed structural relaxation., showing a sharp drop in z(O) from ~ 0.114 to 0.109 at a molar volume of 9.48 cm^3 mol^{-1} (~ 9 GPa). My calculations replicate the results of Tse and Klug very closely, showing a sharp drop in z(O) around 7 GPa (Figure 3.7).

Figure 3.5. Variation of the length of the *a*- and *c*-axes as a function of volume.

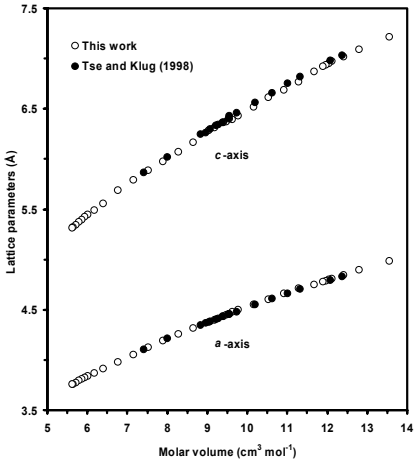

Figure 3.6. The *z* coordinate of the oxygen atom in ice VIII, from refinement of neutron diffraction patterns, as a function of pressure.

Figure 3.7. The z coordinate of the oxygen atom in ice VIII as calculated from first principles by Tse and Klug (1998) and myself.

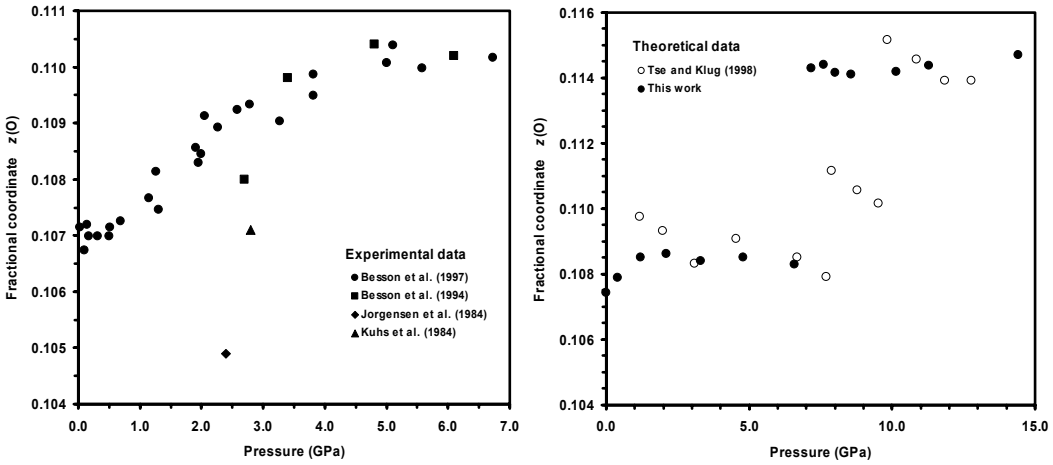

Table 3.IV. Ambient pressure lattice parameters and internal coordinates from experimental (Kuhs *et al*., 1984) and theoretical work (all others) compared with the results of my calculations. Cell edges and bond lengths are in Angstroms.

	a	*c*	*z*(O)	*y*(H)	*z*(H)	O-H	H···O	H-Ô-H
Kuhs *et al*. (1984), 0 GPa, 77 K	4.800	6.988	0.1071	0.4157	0.1935	0.999	1.970	105.60º
Ojamäe *et al*. (1994), HF/STO-3g	4.283	6.467	0.1158	0.4332	0.2097	0.992	1.691	104.53º
Ojamäe *et al*. (1994), HF/3-21G**	4.598	6.865	0.1171	0.4184	0.1979	0.952	1.917	108.77º
Ojamäe *et al*. (1994), HF/6-31G**	4.878	7.472	0.1140	0.4066	0.1898	0.951	2.121	106.89º
This work	4.788	6.935	0.1075	0.4149	0.1935	0.989	1.967	105.87º

3.1.4 Hydrogen Bonding in ice VIII

Hydrogen bonds are known to become stronger under compression. As a result, the hydrogen bond shrinks whereas the covalent O-H bond becomes longer. The limiting case is that in which the proton is symmetrically located midway between neighbouring oxygens. The hydrogen bond-symmetrised phase obtained from ice VIII is called ice X. The pressure

dependence of the O-H bond length, $r_{(O\text{-}H)}$, has been a matter of interest for some time. Theoretical calculations, and fits to the observed decrease of the O-H vibrational frequency with pressure, led to an expectation that the O-H bond should increase in length at a rate of 0.2 – 0.3 pm GPa^{-1} (Holzapfel 1972; Walrafen *et al*., 1982; Klug and Whalley 1984).

However, the directly measured rate of increase of $r_{(O\text{-}H)}$ up to 10 GPa was found to be just 0.04 ± 0.04 pm GPa^{-1} (Nelmes *et al*., 1993), although this shallow gradient is clearly due to an anomalously low value of $r_{(O\text{-}H)}$ at 9.9 GPa. The experimental results were supported by *ab initio* Hartree-Fock calculations, which yielded $\partial r_{(O\text{-}H)} / \partial P = 0.04 \pm 0.04$ pm GPa^{-1} (Besson *et al*., 1994) and 0.014 pm GPa^{-1} (Ojamäe *et al*., 1994).

Figure 3.8. Experimental and calculated variation of the O-H bond length in ice VIII as a function of pressure, up to 25 GPa.

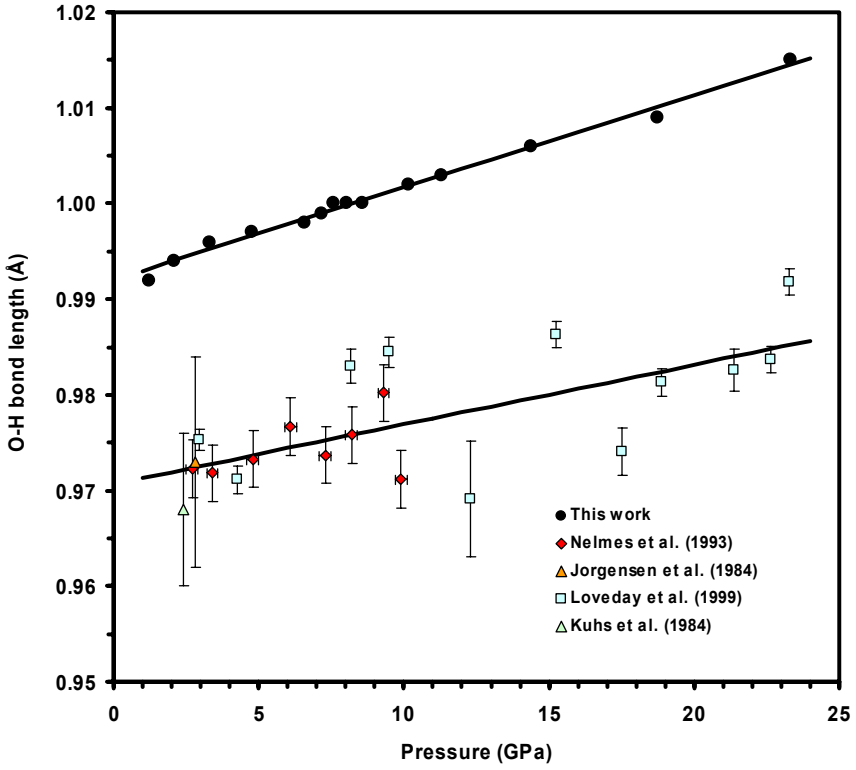

Developments in high pressure technology has since allowed the measurement of $r_{(O\text{-}H)}$ up to ~25 GPa (Loveday *et al*., 1999: Nelmes *et al*., 2000). These data are shown in Figure 3.8, above. Weighted linear regression yields $\partial r_{(O\text{-}H)} / \partial P = 0.062 \pm 0.012$ pm GPa^{-1}. A linear fit to my *ab initio* results gives $\partial r_{(O\text{-}H)} / \partial P = 0.094 \pm 0.003$ pm GPa^{-1} up to 25 GPa. Whilst this figure is not in precise agreement, it is at least of the correct order of magnitude, and given the scatter in the experimental data, the difference in the slopes is probably not significant.

3.2 Ice X

3.2.1 The transition from ice VIII to ice X

At pressures > 50 GPa, $\partial r_{(O\text{-}H)} / \partial P$ increases until $r_{(O\text{-}H)}$ reaches a value equal to one half the distance between neighbouring oxygen atoms, $r_{(O\ldots O)}$ (Figure 3.9). Thereafter, $r_{(O\text{-}H)}$ declines, but remains equal to $r_{(O\ldots O)} / 2$. Concurrently, the tetragonal distortion parameter, ε, goes to zero. Indeed $r_{(O\text{-}H)}$ becomes $r_{(O\ldots O)} / 2$ at the same cell volume as ε goes to zero (5.62 $cm^3\ mol^{-1}$, ≈ 105 GPa) indicating that the two are behaving as coupled order parameters. Above this transition pressure, the ice VIII unit cell is essentially a supercell of ice X.

Figure 3.9. Calculated variation of $r_{(O\text{-}H)}$ as a function of $r_{(O\ldots O)}$. The red line is indicative of the hydrogen bond-symmetrised phase, ice X.

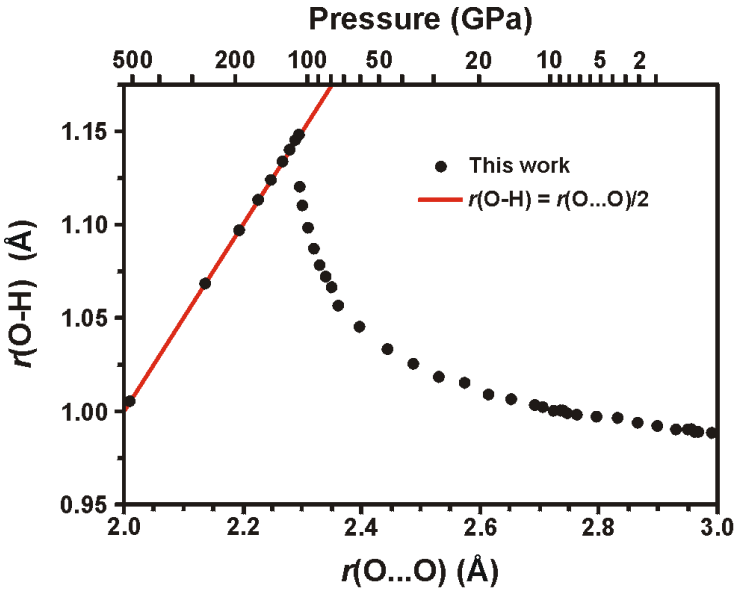

Total energy calculations on the ice X supercell, with the atoms fixed on special positions (as described in 3.1.2), were carried out at molar volumes from 2.26 – 10.54 $cm^3\ mol^{-1}$. Third order Birch-Murnaghan and 4th order logarithmic equations of state were fitted to the calculated E(V) values. Fitted EoS parameters are given in Table 3.V. Figure 3.10 shows E(V) data for ice VIII and ice X, and Figure 3.11 shows all available experimental P(V) data with my calculated equations of state. The EoS of ice X is in agreement with the observed density of ice at pressure up to 210 GPa.

Figure 3.10. Calculated E(V) curves for ice VIII and ice X. Solid lines are the fitted EoS; that for ice VIII in red, and that for ice X in blue.

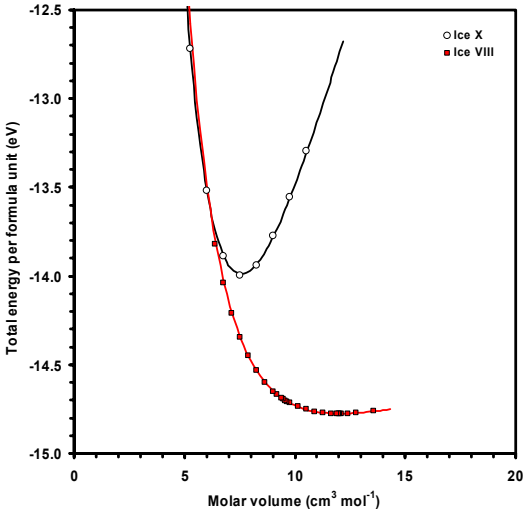

Figure 3.11 Experimental P(V) data for ices VII, VIII, and X, up to 210 GPa. My calculated EoS for ice VIII is shown in red, and that for ice X in blue.

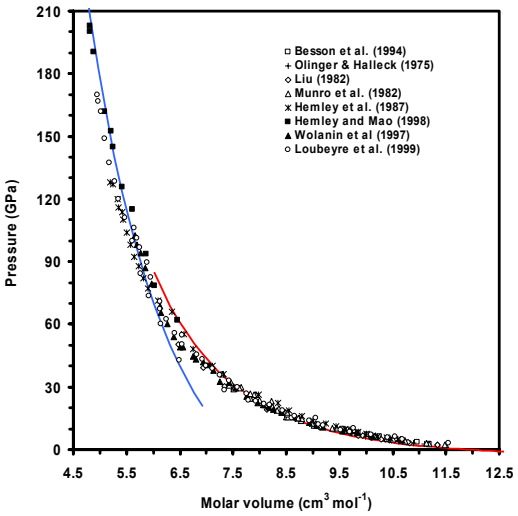

Table 3.V. Calculated EoS parameters of ice X.

	V_0 (cm^3 mol^{-1})	K_0 (GPa)	K'_0	K''_0 (GPa^{-1})	E_0 (eV molecule^{-1})
BMEOS3: E(V)	7.58 ± 0.01	196.0 ± 0.8	3.80 ± 0.01	···	-13.988 ± 0.003
LNEOS4: E(V)	7.60 ± 0.01	195.9 ± 1.1	3.59 ± 0.05	-0.0088±0.0015	-13.994 ± 0.003

The calculated enthalpy (Figure 3.12, overleaf) reveals that ice X becomes thermodynamically stable at 70.5 ± 1 GPa, which is close to the observed range of transition pressures (60 – 65 GPa) from ice VIII to ice X. An *ab initio* MD study previously placed the transition to ice X at 49 GPa (Lee *et al*., 1992, 1993).

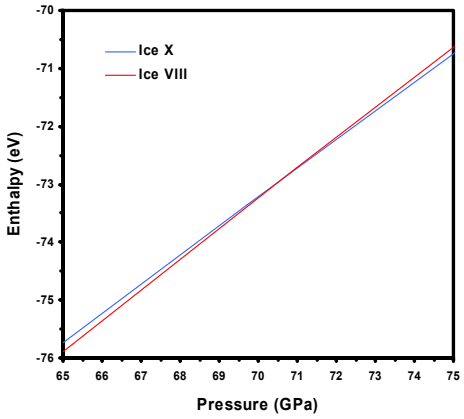

Figure 3.12.

Enthalpy, H, of ice VIII (red) and ice X (blue), calculated from the fitted equations of state, around the transition pressure. Enthalpy is calculated from H = U + PV, where U is the total energy found from *ab initio* calculations, P = pressure, and V = molar volume.

3.3 Post-ice X Polymorphs

The objective of this subsection is to compare my results with the existing *ab initio* results on the d-hcp and antifluorite ices, and to explore the stability of two novel phases of my own devising. I chose the $CaCl_2$, and α-PbO_2 structures because they play a major role in the high-pressure polymorphism of many metal oxides, notably SiO_2 (e.g., Behnke *et al*., 1986: Demuth *et al*., 1999) and RuO_2 (Haines and Leger, 1993), both of which materials share some structural similarities with several ice polymorphs. No other theoretical studies of ice polymorphs with these structures exist.

Each phase is discussed in turn, but the EoS parameters from the fits to the relevant E(V) curves (Figure 3.13) are detailed in Tables 3.VI and 3.VII.

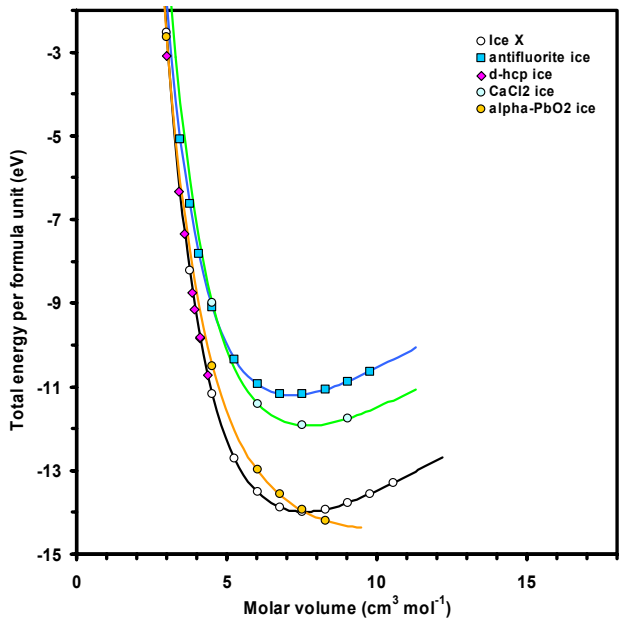

Figure 3.13.

Calculated E(V) data for all of the ultrahigh-pressure ice polymorphs studied. This plot does not show the E(V) curve for ice VIII, which has a lower energy than all of the depicted phases at molar volumes larger than ~ 6 cm^3mol^{-1}.

Table 3.VI. BMEOS3 parameters from fits to the energies calculated for the various high pressure ice polymorphs included in this study.

	3rd Order Birch-Murnaghan EoS			
	V_0 ($cm^3\ mol^{-1}$)	K_0 (GPa)	K'_0	E_0 (eV $molecule^{-1}$)
d-hcp ice	8.4 ± 0.2	124 ± 13	3.87 ± 0.03	-14.31 ± 0.14
Antifluorite ice	7.210 ± 0.002	196.1 ± 0.3	3.790 ± 0.002	-11.1979 ± 0.0008
$CaCl_2$ ice	7.712 ± 0.002	187.2 ± 0.2	3.776 ± 0.001	-11.9280 ± 0.0006
α-PbO_2 ice	10.9 ± 0.4	47 ± 8	4.1 ± 0.1	-14.43 ± 0.04

Table 3.VII. LNEOS4 parameters for those high pressure ice polymorphs for which it was possible to fit a fourth-order equation of state (see text).

	4th Order Logarithmic EoS				
	V_0 ($cm^3\ mol^{-1}$)	K_0 (GPa)	K'_0	K''_0 (GPa^{-1})	E_0 (eV $molecule^{-1}$)
Antifluorite ice	7.205 ± 0.002	194.2 ± 0.3	3.81 ± 0.02	-0.017±0.001	-11.196 ± 0.001
$CaCl_2$ ice	7.715 ± 0.005	188 ± 2	3.66 ± 0.05	-0.014±0.002	-11.929 ± 0.002

3.3.1 The d-hcp structure.

The d-hcp ice structure was relaxed at a series of unit cell volumes between 15 $Å^3$ (2.26 $cm^3\ mol^{-1}$) and 29 $Å^3$ (4.37 $cm^3\ mol^{-1}$). The smallest volume corresponds to an applied pressure of ~ 2 TPa. At volumes larger than ~ 30 $Å^3$ (4.52 $cm^3\ mol^{-1}$) the structure spontaneously assumed the atomic arrangement of ice X. With no calculations at volumes greater than 30 $Å^3$ to constrain the value of V_0, the EoS parameters in Table 3.VI are necessarily subject to larger standard errors than the other phases described below. Furthermore, it was not possible to fit a 4th order LNEOS with standard errors of smaller magnitude than the fitted parameters themselves. E(V) curves for the d-hcp phase are plotted alongside ice X results in Figure 3.14 (overleaf).

Figure 3.14. Calculated E(V) curves for ice X and the d-hcp phase. The solid lines are fitted equations of state.

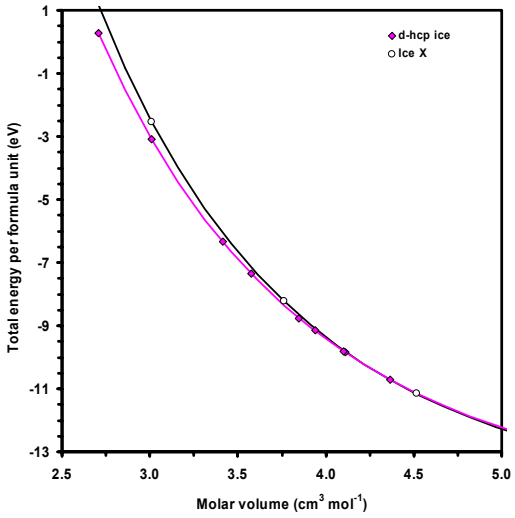

Figure 3.15. Calculated stresses for ice X (white circles) and the d-hcp phase (pink diamonds), E(V) equations of state (solid lines), and experimental data.*

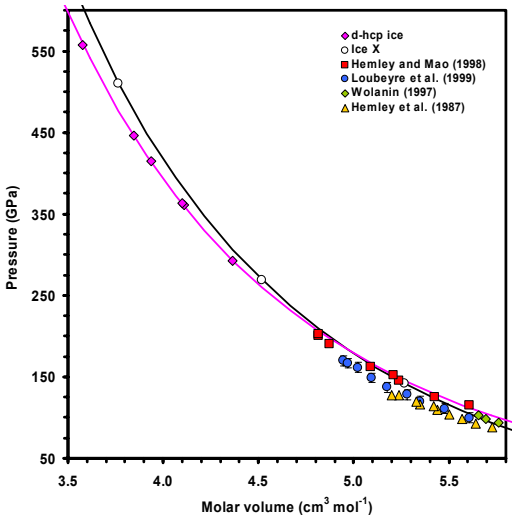

*Note that these high-pressure experimental data points are from X-ray experiments, which merely sense the bcc arrangement of the oxygen atoms, and hence cannot distinguish ice VII from ice X.

Several of the relaxations were run at the same volumes as were tabulated in the paper of Benoit *et al*. (1996) so as to draw a direct comparison. The two sets of results are compared in Table 3.VIII. The agreement between the data sets is generally very good. For a given volume, my calculated pressure is typically lower by 15-20 GPa, the *a*-axis is fractionally shorter, and the *b*/*a* and *c*/*a* ratios are fractionally larger. There are also minor differences in the atomic coordinates. However, Benoit *et al*. (1996) themselves noted a reduction in pressure of ~ 40 GPa in moving from one exchange-correlation functional to another, and there seems no reason not to ascribe the small differences between their work and mine to the use of the PW91 GGA functional herein as opposed to the BLYP functional used by Benoit *et al*. (1996).

The calculated EoS for the d-hcp ice structure and for ice X are shown in Figure 3.14. This plot also shows recent high-pressure experimental P(V) data (Hemley *et al*., 1987: Wolanin, 1997: Hemley and Mao, 1998: Loubeyre *et al*., 1999). The calculated enthalpies of d-hcp ice and ice X as a function of pressure overlap at 578 GPa, although it is worth observing that the error bars on the respective equations of state first overlap at a much lower pressure (~420 GPa).

Table 3.VIII. Structural parameters of d-hcp ice. Top: Calculations of Benoit *et al*. (1996). Bottom: my own results. Oxygen atoms occupy the positions (u, v, ¼), and the angle ϕ defines the distortion from the bcc Ice X structure (i.e., $\phi = 0°$ in bcc ice X, and $\phi = 30°$ for an ideal hcp structure).

Benoit et al. (1996)								
V ($Å^3$)	V ($Å^3$/atom)	P (GPa)	*a* (Å)	*b/a*	*c/a*	*u*	*v*	ϕ
22.68	1.89	660	2.01	1.71	1.63	0.255	0.415	29.5º
23.76	1.98	580	2.06	1.69	1.62	0.255	0.419	28.0º
25.56	2.13	470	2.14	1.64	1.59	0.254	0.429	24.7º
26.16	2.18	430	2.18	1.61	1.58	0.253	0.437	21.7º
27.24	2.27	380	2.22	1.59	1.57	0.252	0.443	19.8º
This work								
V ($Å^3$)	V ($Å^3$/atom)	P (GPa)	*a* (Å)	*b/a*	*c/a*	*u*	*v*	ϕ
15.00	1.2500	2050.24	1.6868	1.8454	1.6934	0.2623	0.3788	43.26º
18.00	1.5000	1253.6	1.8095	1.8074	1.6809	0.2616	0.3883	40.27º
20.00	1.6667	930.51	1.8890	1.7791	1.6678	0.2597	0.3955	37.73º
22.68	1.8900	642.37	1.9972	1.7304	1.6452	0.2580	0.4058	33.97º
25.56	2.1300	446.46	2.1187	1.6690	1.6104	0.2541	0.4243	27.20º
26.16	2.1800	414.57	2.1441	1.6555	1.6030	0.2538	0.4273	26.06º
27.24	2.2700	363.29	2.1942	1.6263	1.5856	0.2531	0.4325	23.96º
27.30	2.2753	360.47	2.1968	1.6251	1.5847	0.2531	0.4328	23.87º
29.00	2.4167	292.97	2.2641	1.5962	1.5654	0.2527	0.4397	21.28º

3.3.2 The antifluorite structure.

Since the atoms in the antifluorite ice structure occupy special positions, it is straightforward to perform total energy calculations at all relevant pressures (Figure 3.15), thus determining the EoS quite accurately (Tables 3.VI and 3.VII). Calculations were carried out at cell volumes between 17$Å^3$ (2.56 cm^3 mol^{-1}) and 65$Å^3$ (9.79 cm^3 mol^{-1}). The smallest volume corresponds to an applied pressure of ~ 1.4 TPa.

The transition pressure from the d-hcp to antifluorite phase, predicted from the calculated enthalpy is far beyond the reach of current high-pressure technology. The calculated enthalpies of the d-hcp and antifluorite phases become equal at a pressure of 6.05 TPa, but as with the ice X ↔ d-hcp transition, the error bars overlap at a much lower pressure (~2.5 TPa). This places the transition in a pressure regime where antifluorite ice is almost certainly metallic (Hama *et al*., 1990).

3.3.3 The $CaCl_2$ and α-PbO_2 structures.

The total energy calculations on both of these structure types (Figure 3.13) reveal that neither is energetically stable with respect to the other ice polymorphs investigated under any compression. EoS parameters are given in Tables 3.VI and 3.VII. The α-PbO_2 phase was found to revert to a molecular solid, albeit with odd bifurcated hydrogen bonds, at low pressures and so the EoS parameters are poorly constrained. Moreover, it was not possible to sensibly fit a 4^{th} order LNEOS to the calculation results.

3.4 Summary

The simulation of the structures of known and suspected ultrahigh-pressure polymorphs yields superb agreement with existing experimental and theoretical studies. The series of phase transitions at zero Kelvin is found to be; ice VIII $\rightarrow$ ice X (71 GPa); ice X $\rightarrow$ d-hcp ice (500 - 600 GPa); d-hcp $\rightarrow$ ice antifluorite ice (> 2.5 TPa). The close concurrence between the experimental data and the *ab initio* calculations presented here leads me to believe that the method will yield reliable results on the water-rich ammonia hydrates. In the following chapter I apply the same techniques used here to much more weakly bound, low-pressure, ice polymorphs; phases XI and II.

CHAPTER FOUR

WATER ICES AT LOW PRESSURE: ICES II AND XI

4 Low-pressure Water Ices

It is interesting to simulate the structure of low-pressure ice polymorphs as a test of the PW91 GGA's ability to deal with rather less dense solids than ice VIII. In an allied series of simulations, I carried out work upon the structure of two proton-ordered phases of ice stable at pressures < 0.5 GPa; ice II and ice XI. The ice II work is described in Sec. 4.2, the ice XI work is detailed in the following pages (Sec. 4.1), beginning with a description of the phase relations and structure of this polymorph.

4.1 Ice XI

4.1.1 Phase Relations

Ice XI, in the strict sense, is the fully proton ordered form of ice Ih: its location on the equilibrium phase diagram is shown in Chapter 3, Fig. 3.1 (page 65). However, the phase transition to ice XI occurs at such low temperatures (72 K in H_2O and 76 K in D_2O: Tajima *et al*., 1982; Matsuo *et al*., 1986) that the proton, or deuterons, are essentially immobile. Hence, on normal laboratory time-scales the transition does not occur, and disordered ice Ih persists to limiting low temperature. Indeed, in pure ice, the transition is expected to run to completion on timescales of order 10^6 years (Suga 1985). Therefore, ice XI is the likely stable form of low-

pressure solid H_2O on planetary bodies with surface temperatures below 72 K (Triton and Pluto for example). The transformation to ice XI can only be studied in the laboratory by introducing extra lattice defects, which enhance proton or deuteron mobility at the requisite temperatures. This is usually achieved by doping pure ice Ih with ~10^{-1} mole KOH or KOD. Under such circumstances, an ice Ih sample will, after several days of annealing, partially transform to ice XI. The yield of ice XI is variable, but may be as much as 60%. The most recent experimental work dealing with the kinetics of the ice Ih - ice XI transformation is that of Fukazawa *et al*., (2002).

4.1.2 Structure of ice XI

Prior to the structure of ice XI being positively established, a number of ordering schemes, with different symmetries, were proposed for ice Ih (e.g., Howe 1987). Neutron diffraction studies of partially transformed ice Ih / ice XI powders (Leadbetter *et al*., 1985: Howe and Whitworth 1989: Line and Whitworth 1996) showed that the most likely structure was face centred orthorhombic (space group $Cmc2_1$, Z = 8), although a small monoclinic distortion (in space group *Cc*), of around 0.2°, could not be ruled out. This orthorhombic space group has the distinction of rendering ice XI ferroelectric (by virtue of being non-centrosymmetric), a feature which is confirmed by dielectric permittivity measurements (Jackson and Whitworth 1995). Single crystal neutron diffraction has since confirmed the structure as belonging to space group $Cmc2_1$ (Fukazawa *et al*., 2002) The cell parameters and fractional atomic coordinates of the experimental structure are supplied in Table 4.I, and are the starting parameters for the simulations. The structure itself is shown in Figure 4.1.

Table 4.I. Starting structural parameters for the ice XI simulations, based on neutron diffraction data collected at 5 K by Leadbetter *et al*. (1985).

Ice XI

Space group $Cmc2_1$ (no' 36) C_{2v}^{12}

a = 4.502Å b = 7.798Å c = 7.328Å

Atomic species	Wyckoff position	Fractional coordinates (x,y,z)
O1	4a	(0, 0.665, 0.063)
O2	8b	(½, 0.826, -0.063)
H1	4a	(0, 0.664, 0.196)
H2	4a	(0, 0.536, 0.018)
H3	8b	(0.677, -0.225, -0.018)

4.1.3 Computational Details

Static DFT calculations (as described in Chapter 2) of the total energy of the ice XI structure were carried out to determine the equation of state (EoS) of this polymorph. Table 4.I provides the starting parameters from which the structural relaxations were begun.

Total energy convergence tests were carried out to optimise the sampling of the Brillouin zone, and the cut-off of the plane-wave basis set. The $\vec{k}$-point sampling of the irreducible Brillouin zone (IBZ), and electron kinetic energy cut-off (E_{cut}), for ice XI were 27 $\vec{k}$-points, and 1100 eV respectively. These values were found to yield total energy convergence of better than 10^{-4} eV per unit cell. As will be discussed in Sec. 4.1.4, the convergence parameters that were used for ice XI were rather more strict than was the case with other solids simulated.

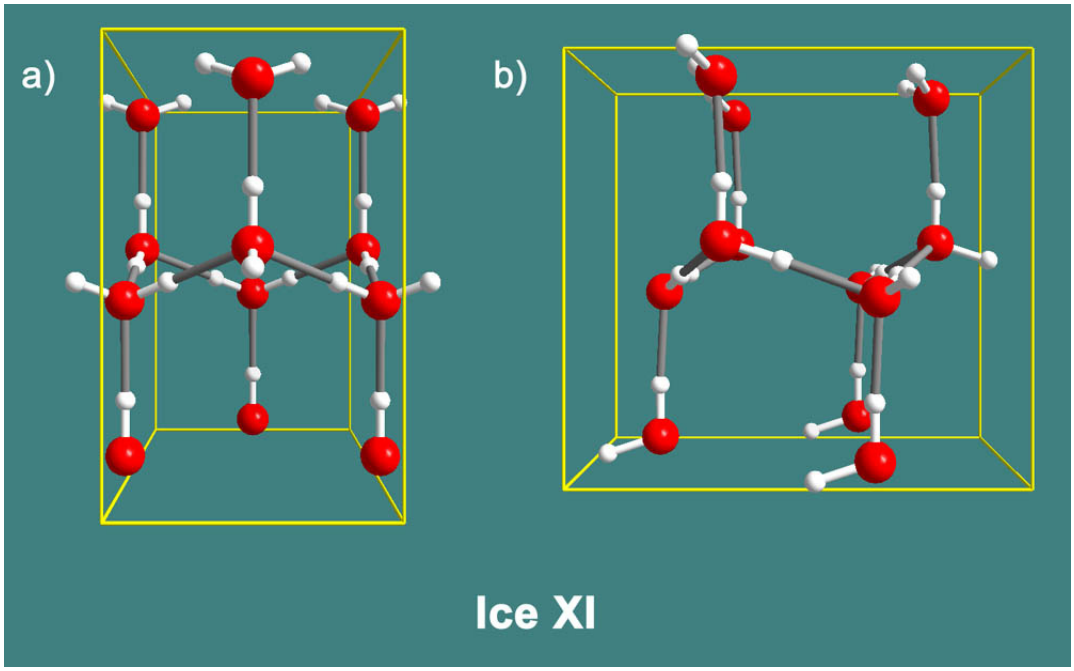

Figure 4.1: The crystal structure of ice XI; a) viewed along the *b*-axis with the *c*-axis vertical, and b) viewed along the *a*-axis with the *c*-axis vertical. The ferroelectric ordering of protons along the *c*-axis is very clear.

4.1.4 Equation of State of ice XI

Structural relaxations were carried out over the range of cell volumes from 16.1 - 19.4 cm3 mol^{-1}. The smallest volume simulated corresponds to an applied pressure of ~ 2.2 GPa, and the largest to a dilation of – 1.1 GPa. Integrated forms of the third order Birch-Murnaghan EoS

(BMEOS3) and a fourth order logarithmic EoS (LNEOS4) were fitted to the E(V) data (Fig. 4.2), as described in Chapter 2. Using the energy of the isolated H_2O molecule (see Chapter 2) and the minimum energy of the ice XI structure, E_0, the lattice energy is found to be 74.800 ± 0.005 kJ mol^{-1}, and the average hydrogen bond enthalpy is 37.400 ± 0.003 kJ mol^{-1}. As will be discussed shortly, this is a great overestimate; a more appropriate value would be ~ 25 kJ mol^{-1}.

Figure 4.2. Calculated E(V) curve for ice XI and fitted EoS. The BMEOS and LNEOS are indistinguishable at this scale.

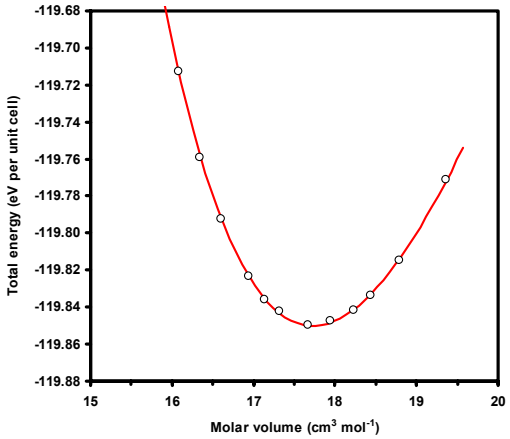

Figure 4.3. Calculated stresses (points) and best fit EoS fit to E(V) curve (red line).

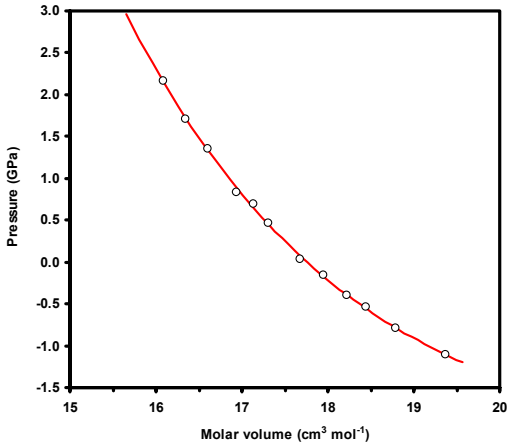

Table 4.II. Calculated EoS parameters of ice XI.

	V_0 (cm^3 mol^{-1})	K_0 (GPa)	K'_0	K''_0 (GPa^{-1})	E_0 (eV molecule^{-1})
BMEOS3: E(V) fit	17.73 ± 0.01	16.3 ± 0.1	7.9 ± 0.4	···	-14.98127 ± 0.00005
LNEOS4: E(V) fit	17.73 ± 0.01	15.1 ± 0.3	7.8 ± 0.3	-0.23 ± 1.44	-14.98117 ± 0.00003

The first point to note is that the standard errors are better than for almost any other solid simulated in this work. This is almost certainly due to the very strict convergence criteria imposed upon these calculations, for reasons to be outlined shortly.

However, the equations of state overall are a relatively poor match to experimental data. The molar volume of ice XI is known at 5 K (likely to be insignificantly different to the volume at 0 K) and is 19.364 ± 0.005 cm^3 mol^{-1}. Hence, the calculated value of V_0 differs from the experimental value by -8.4 % (resulting from the large overestimate in binding energy mentioned previously). This figure, which corresponds to a dilation of just over 11 kbar necessary to bring the volumes into coincidence, is larger even than that found in solid ammonia

I (Chapter 5), although in the opposite sense. The calculated bulk modulus is also greatly over-estimated, although this is largely due to the over-estimate in V_0. The incompressibility of ice XI at absolute zero can be found from measured stiffness coefficients for ice Ih. Proctor (1966) and Dantl (1968) determined the elastic stiffness coefficients (c_{11}, c_{33}, c_{44}, c_{12}, and c_{13}) in natural polycrystalline ice Ih at a range of temperatures from speed of sound measurements. I have used their data to calculate the adiabatic bulk modulus, K_S (at 0 Kelvin, $K_S = K_T$), as a function of temperature (Figure 4.4, below), and fitted an equation of the form $K(T) = K_0 \exp (- (A / (B+1)) T^{(B+1)})$, where K_0 is the bulk modulus at 0 K and A and B are constants. This fit (the red line on Fig 4.4) is given by, $K_0 = 10.85 \pm 0.01$ GPa, $A = 1.918 \times 10^{-5} \pm 1.43 \times 10^{-6}$, $B = 0.800 \pm 0.015$. The temperature dependence of K, $\partial K/\partial T = K(T)\, A\, B^T$.

Clearly the calculated bulk modulus at the calculated value of V_0 is seriously at odds with the athermal incompressiblity of ice Ih ($\Delta K/K$ = ~50%). The bulk modulus which corresponds to the experimental volume (at a negative pressure of 1.106 GPa) is easily found, and this corrected bulk modulus is 7.60 ± 0.61 GPa, giving $\Delta K/K = -30 \pm 6$ %, which does not appear to be a great improvement.

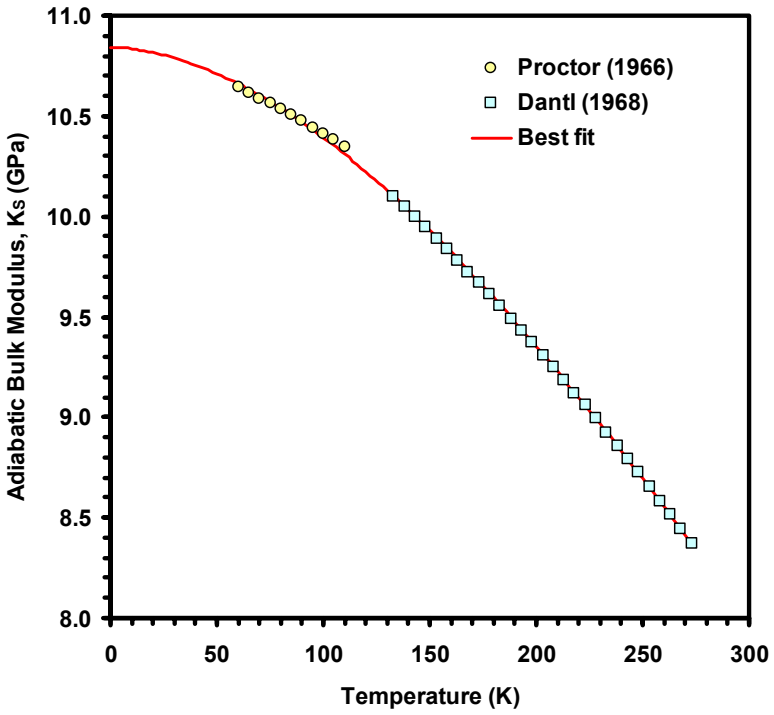

Figure 4.4. The measured adiabatic bulk modulus, K_S in pure ice Ih as a function of temperature as determined from elastic stiffness coefficients.

The problem of the large discrepancy in V_0 initially appeared when ice XI was simulated with a smaller $\vec{k}$-point mesh and lower E_{cut}. The only option was to increase the density of the $\vec{k}$-point mesh and the cut-off in an effort to resolve the problem. However, even with these stricter criteria the problem remained. All of the results presented here were found using 27 $\vec{k}$-points in the IBZ and a cut off of 1100 eV. The plots below (Figures 4.5 and 4.6) depict the convergence of total energy and stress as a function of $\vec{k}$-point mesh density and kinetic energy cut off. The criteria used for these calculations are greater than those necessary to achieve an acceptable level of convergence. Hence, the reason why V_0 differs so much from the experimental value is unknown, but is likely to be the result of weak long-range dispersion forces not being accomodated in the GGA approximation to E_{XC}.

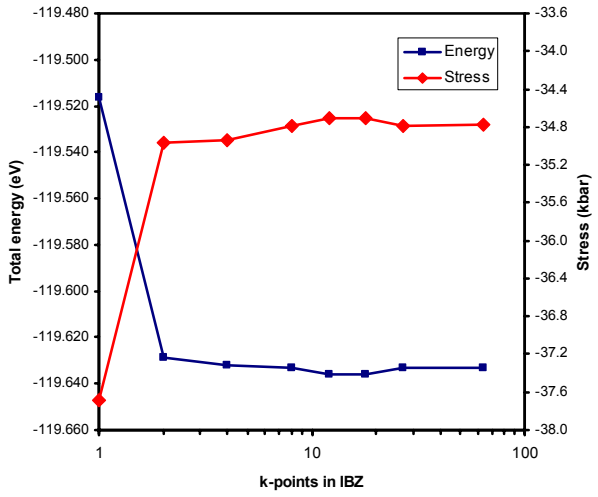

Figure 4.5.

Convergence of total energy and stress in ice XI with increasing $\vec{k}$-point mesh density.

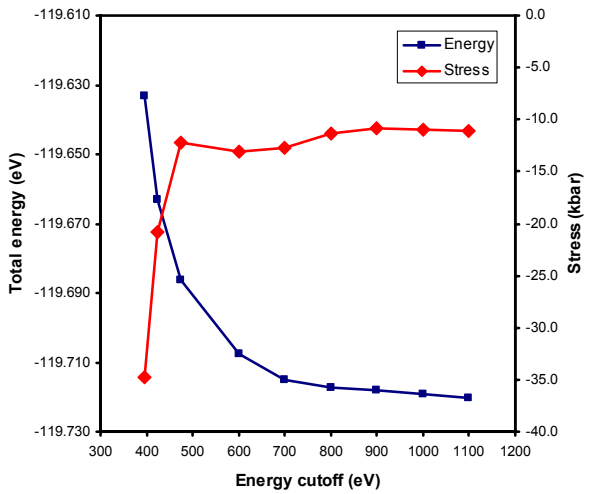

Figure 4.6.

Convergence of total energy and stress in ice XI as a function of E_{cut} (with 27 $\vec{k}$-points in the IBZ)

4.1.5 The simulated structure of ice XI

In spite of the serious under-estimate in the zero-pressure volume, the simulated structure of ice XI, on an equivalent-volume basis, is a very good match to the experimental structure. Table 4.III compares the experimental structure of ice XI at 5 K with the simulated structure *at the same volume* (though, of course, at a very different pressure). The shape of the unit cell (*b/a* and *c/a* ratios) agree well, as do the fractional atomic coordinates. Inspection of the bond lengths reveals the only significant difference to be that the simulated structure has all of its O-H bonds (and consequently the H...O bonds) approximately the same length. This is a feature in simulations of all of the solids described in this thesis.

Table 4.III. Cell parameters, atomic coordinates and bond lengths in ice XI.

	Experimental structure[a]			This work[b]		
a (Å)	4.5019(5)			4.4923		
b (Å)	7.7928(8)			7.7860		
c (Å)	7.3280(2)			7.3551		
b/a	1.7321(4)			1.7332		
c/a	1.6278(2)			1.6373		
V (Å^3)	257.249(62)			257.261		
Fractional atomic coordinates						
	x	*y*	*z*	*x*	*y*	*z*
O1	0	0.6648(18)	0.0631(2)	0	0.66588	0.06135
O2	½	0.8255(21)	-0.0631(2)[c]	½	0.83280	-0.06470
H1	0	0.6636(29)	0.1963(4)	0	0.66414	0.19765
H2	0	0.5363(14)	0.0183(3)	0	0.54321	0.01995
H3	0.6766(19)	-0.2252(13)	-0.0183(3)[c]	0.67906	-0.23022	-0.18126
Bond lengths (Å)						
O1-H1	1.054(17)			1.003		
O1-H2	0.976(3)			1.002		
O2-H3	0.947(11)			1.003		
H3...O1	1.792(11)			1.754		
H2...O2	1.749(19)			1.753		
H1...O2	1.765(3)			1.748		

[a]Leadbetter *et al*. (1985), at ambient pressure, 5 K
[b]This work, athermal limit, -1.106 GPa
[c]The authors did not provide ESD's for these coordinates, so they have been set equal to the errors on the *z*-coordinates of O1 and H2, respectively.

Figure 4.7. The volume dependence of the unit cell edges.

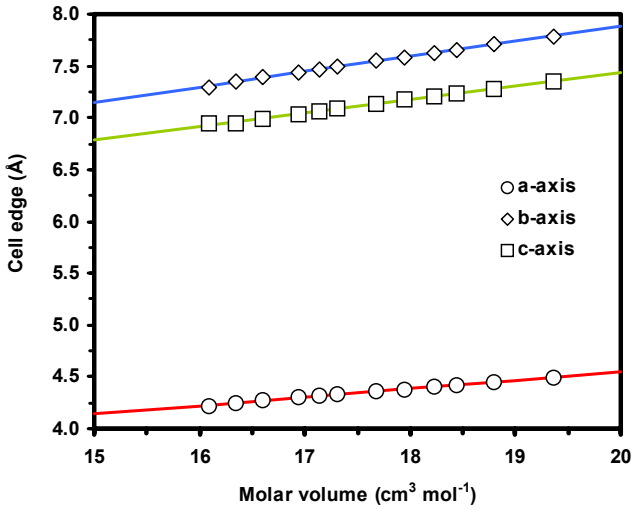

The volume dependence of the unit cell edges (Fig. 4.7) is linear. The variation in the length of each axis is given by, $a = 0.083V + 2.90$, $b = 0.147V + 4.95$, $c = 0.130V + 4.83$, where V is in $cm^3\ mol^{-1}$. The compressibilities of each direction in the crystal, defined as $(1/a)(\partial a/\partial V)$ for the *a*-axis for example, are virtually identical, being 0.018 ± 0.001 for each at the experimental volume quoted in Table 4.III.

4.1.6 Summary

The results for ice XI give the poorest estimates of V_0 ($V_{calc} - V_{expt} / V_{expt} = -8.4$ %) and K_0 ($K_{calc} - K_{expt} / K_{expt} \approx 50\%$) of any substance simulated in this study. However, for low-density, 'squashy', hydrogen-bonded solids, these values are actually quite respectable, and indeed the calculated equilibrium structure is in reasonable concurrence with empirical data.

In the following section I describe the simulation of an ice phase intermediate in density between ice VIII and ice XI, ice II.

4.2 Ice II

4.2.1 Phase Relations

Ice II is a crystalline polymorph of solid water which is formed under moderate pressure (See Chapter 3, Fig. 3.1). Under equilibrium conditions, compression of ordinary hexagonal ice I leads to the formation of ice II at ~0.2 GPa. Compression beyond ~0.5 GPa transforms ice II into denser polymorphs, ice V or ice VI. Ice II does not melt to liquid water; heating above ~240 K causes a phase change to either ice III, V, or VI depending on pressure. Ice III may persist metastably upon cooling into the stability field of ice II, but ice II cannot be superheated above the II-III transition line (Petrenko and Whitworth 1999). Ice II is unique among the low-pressure polymorphs (i.e., < 2 GPa) in that it has a fully ordered proton arrangement throughout its stability field. Ice II is also of interest because its structure (described in 4.2.2) permits the inclusion of small atoms, such as hydrogen, helium and neon, to form so-called 'stuffed' ices. These have very different phase boundaries and physical properties to pure ice II, and their occurrence is known to complicate experiments in which the pressure-transmitting medium can permeate the structure.

In addition to its intrinsic value to materials science, ice II is very likely to be an important planetary mineral (Johnson 1998). Pressure and temperature conditions within a large proportion of the Solar System's icy moons are suitable for the stability of ice II: inside a large icy moon, such as the Jovian satellite Ganymede, ice II may form a layer several hundred kilometres deep. The physical properties of ice II are therefore pertinent to an understanding of the geophysics of icy moons influencing, amongst other things, the convective regimes in their interiors (Johnson 1998).

It is thus surprising that we know so little about ice II. Structural analyses, via X-ray and neutron diffraction, have been carried out at ambient pressures, upon quenched samples (Kamb 1964: Finch *et al*., 1971: Kamb *et al.,* 1971), and within the stability field of ice II (Arnold *et al*., 1971: Londono *et al*., 1992: Lobban 1998: Lobban *et al*., 2002). Of the latter, only Lobban *et al*. (2002) can categorically assert that their structure was 'pure' ice II, and even their structure refinements were affected by the formation of cage-clathrates with the argon pressure medium. Indeed, this very recent work of Lobban *et al*. (2002) provides us with the only three reliable structural data points within the stability field of ice II.

The density of ice II was measured from 0.23 - 0.33 GPa at 237.65 K in a piston apparatus by Gagnon *et al*. (1990): in addition, Brillouin spectroscopy was used to determine the bulk modulus. Lobban *et al*. (2002) estimated the bulk modulus from just two data points at 200 K and found a similar value to Gagnon *et al*. (1990).

Piston compression experiments on both H_2O and D_2O ice have been carried out to explore phase boundaries between high-pressure polymorphs (Sirota and Bizhigitov 1987, 1988: Sirota and Zhapparov 1994). However, the phase boundaries observed by these workers disagree with the equilibrium phase boundaries observed in other experiments, and since there was no independent identification of phases (e.g., by X-ray diffraction), it is at least possible that their proposed ice Ih - II boundary actually represents the transformation of ice Ih to an amorphous solid (e.g., Mishima *et al*., 1984) or ice IX (e.g., Mishima 1996).

Previous computational studies of ice II have concentrated on calculating the vibrational densities of states for comparison with inelastic incoherent neutron scattering spectra (Dong *et al*., 1998: Zheligovskaya *et al*., 2001). Báez and Clancy (1995) used a point charge model to calculate the density of ice II at atmospheric pressure from 180-320 K.

Computational simulation of ice II has a number of benefits. One can calculate the properties of wholly uncontaminated ice II. This allows for the improved definition of structural changes which occur when other substances are occluded within the crystal. Furthermore, one can study ice II at pressures far outside its stability field: in this study I have made calculations over a pressure range approximately ten times larger than the natural stability field of ice II. Access to this wider phase space permits the characterisation of very small structural changes, such as the pressure strengthening of hydrogen bonds or changes in the shape of the unit cell, which may be too small to be observed experimentally.

I will commence with a description of the ice II structure (4.2.2), followed by the computational method (4.2.3); results are presented in Sec. 4.2.4.

4.2.2 Structure of ice II

The crystal structure of ice II is trigonal, space-group $R\bar{3}$, with primitive unit cell dimensions, a = 7.78 Å and α = 113.1º at atmospheric pressure and 123.15 K (Kamb 1964). The fractional coordinates of atoms in the asymmetric unit are quoted in Table 4.IV. The crystal is composed of two varieties of hexagonal rings (hereafter 6A- and 6B-rings) of hydrogen bonded water molecules. For the purposes of describing the arrangement of these rings it is convenient to adopt the non-primitive hexagonal setting of space-group $R\bar{3}$: the two types of 6-rings are stacked alternately parallel to the *c*-axis, forming six-sided columns (6-tubes), as shown in Figures 4.8 and 4.9. The dangling O-H bonds of the 6A-rings extends outwards, although not quite perpendicular to the *c*-axis, forming hydrogen bonds from 6A-rings in one column to 6B-rings in another (Figure 4.10). The dangling O-H bonds of the 6B-rings are directed alternately up and down the *c*-axis, although not precisely parallel to it, binding adjacent 6A- and 6B-rings into tubes. This arrangement leads to the 6A-rings being relatively

flat, and the 6B-rings being more corrugated, or puckered. Adjacent rings along the 6-tubes are rotated by ~16º relative to one another. The structure preserves the open tetrahedral bonding of low-pressure ice Ih yet yields a higher density crystal.

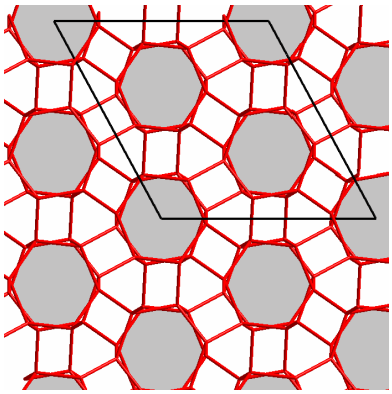

Figure 4.8: A representation of the ice II structure viewed down the *c*-axis of the non-primitive hexagonal cell. Observe that the structure consists of a 'sheaf' of 6-tubes (shaded grey) parallel to the *c*-axis.

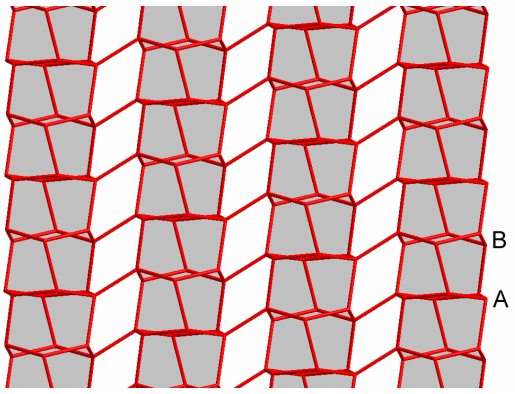

Figure 4.9: A representation of the ice II structure viewed perpendicular to the *c*-axis of the non-primitive hexagonal cell, showing the lateral bonding of 6A- and 6B-rings to join the 6-tubes (shaded grey) together.

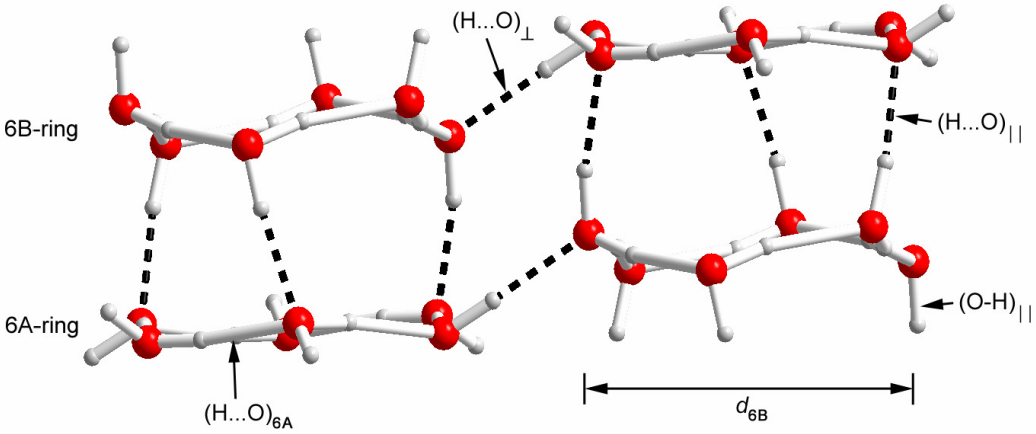

Figure 4.10: Detail showing the arrangement of the water molecules in the 6A- and 6B-rings, and the disposition of the hydrogen bonds (dashed lines) which join them together.

Figure 4.10 also serves to introduce my notation for describing the different interatomic distances, as will be used in Sec. 4.2.5. Interatomic distances within the flat and puckered 6-rings are denoted with the subscripts 6A and 6B; for example, r(O-H)$_{6A}$ or r(O...O)$_{6B}$. The diagonal diameters of the 6-rings, the distance between oxygen atoms on opposing corners, are d_{6A} and d_{6B} respectively. Interatomic distances between adjacent rings in the same 6-tube are

r(O-H)$_{||}$, r(H...O)$_{||}$, and r(O...O)$_{||}$, whereas those between rings in neighbouring 6-tubes are r(O-H)$_{\perp}$, r(H...O)$_{\perp}$, and r(O...O)$_{\perp}$.

4.2.3 Computational Method

Static DFT calculations (as described in Chapter 2) of the relative energetics of the ice II structure were carried out to determine the equation of state (EoS) of this ice polymorph.

Total energy convergence tests were carried out to optimise the sampling of the Brillouin zone, and the cut-off of the plane-wave basis set. The $\vec{k}$-point sampling of the irreducible Brillouin zone (IBZ), and electron kinetic energy cut-off (E_{cut}), for ice II were 32 $\vec{k}$-points and 900 eV respectively. A series of fixed volume calculations were then performed in which the ions were allowed to move according to the calculated Hellman-Feynman forces. For each volume specified the structure was relaxed via the conjugate-gradient technique in order to optimise the lattice parameters and internal coordinates.

In the following section I report the results of structural relaxations for ice II, which were started from the ambient pressure experimental structure of Kamb (1964) using the trigonal primitive unit cell setting of space group $R\bar{3}$ (Table 4.IV).

Table 4.IV. Starting structural parameters for the ice II simulations, based on X-ray diffraction data collected at ~123 K and ambient pressure by Kamb (1964).

Ice II

Space group $R\bar{3}$ (no' 148) C_{2v}^{12}

a = 7.78Å α = 113.1°

Atomic species	Wyckoff position	Fractional coordinates (x,y,z)
O1	6*f*	(0.273, 0.024, -0.146)
O2	6*f*	(0.478, 0.750, 0.332)
H1	6*f*	(0.165, 0.069, -0.190)
H2	6*f*	(0.413, 0.205, -0.003)
H3	6*f*	(0.719, 0.401, 0.395)
H4	6*f*	(0.741, 0.203, 0.360)

4.2.4 Equation of State

Structural relaxations were carried out at a series of fixed primitive unit cell volumes from ~250Å^3 to ~300Å^3 (covering the pressure range from -1 to 3.5 GPa) at which the total energy of the crystal was calculated. A third-order Birch-Murnaghan equation of state was fitted to the E(V) results (Figures 4.11 and 4.12), yielding V_0 = 14.525 ± 0.008 cm^3 mol^{-1} (289.43 ± 0.15 Å^3), K_0 = 16.1 ± 0.3 GPa and K'_0 of 6.2 ± 0.3.

At the end of November 2003, shortly before the submission of this thesis, I carried out a neutron diffraction study of D_2O ice II using the HRPD instrument at ISIS (Rutherford Appleton Laboratory, Oxfordshire, U.K.); Experiment number RB 14058. For comparison with these calculations, I report my initial findings from this experiment. The molar volume of D_2O ice II at 4.2 K at atmospheric pressure was found to be 15.036 ± 0.001 cm^3 mol^{-1}. This means that the calculations under-estimate the zero-pressure molar volume by – 3.4 ± 0.1 %, equivalent to roughly 5 kbar of dilation to give the simulated cell the correct volume.

Figure 4.11. Calculated E(V) curve for ice II and fitted EoS. The BMEOS and LNEOS are indistinguishable at this scale.

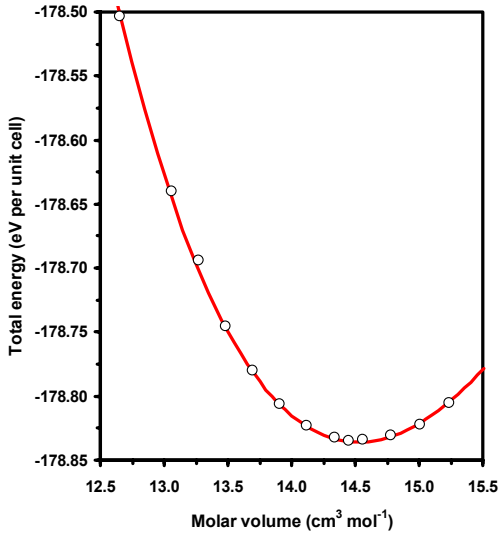

Figure 4.12. Calculated external pressures (points) and the BMEOS curve fitted to E(V) results (red line).

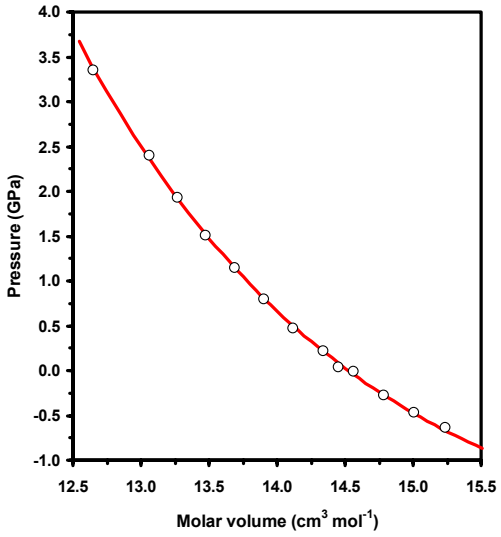

The bulk modulus of ice II has been determined from acoustic measurements to be 14.39 GPa at 0.283 GPa and 237.65 K (Gagnon *et al.*, 1990), and estimated to be 14.8 ± 0.1 GPa at 0.35 GPa, 200 K (Lobban *et al.*, 2002). In my own neutron diffraction experiment, nine data points, from 0.25 – 0.45 GPa along the 225 K isotherm, were collected from a sample of

polycrystalline D_2O ice II in a TiZr pressure cell compressed under argon gas. Although K'_0 was very poorly constrained from fitting a third order Birch-Murnaghan EoS to such a narrow range of pressure points, fixing $K'_0 = 6.0$ yielded $V_0 = 15.404 \pm 0.002$ cm^3 mol^{-1}, and $K_0 = 12.13 \pm 0.07$ GPa. This fit gives a bulk modulus of 14.23 GPa at 0.35 GPa, in agreement with the earlier determinations.

The value of the *calculated* bulk modulus at the *experimental* 4 K volume is 13 GPa, which is in excellent agreement with my recent high-pressure neutron diffraction experiment.

4.2.5 Structural changes under pressure

I derived a range of internal parameters, as well as the unit cell dimensions, from each volume relaxation. The experimental and calculated structures are compared at the same pressure (~0.48 GPa), though not the same volume, in Table 4.V (overleaf). These included each of the different types of covalent O-H bond, H...O hydrogen bond, and O...O separation. I also observed the change in the diameter of the two types of 6-rings, and the variation in the many H-Ô-H angles in the structure. Second order polynomials were fitted to these data (Figure 4.13 gives an example), and the parameters from all of these polynomial fits are quoted in Table 4.VI. I will briefly discuss my findings and relate them to the experimental data.

The unit cell of ice II undergoes only a very slight change in shape over the pressure range examined. The rhombohedral angle, α, increased by approximately 0.2° from –1 to 3.5 GPa, the pressure dependence being given by a second order polynomial: $\alpha = 112.85° + 0.1062P - 0.0127P^2$ (with P in GPa). Over the pressure range studied by Lobban *et al*. (2002) the calculations show that one should expect α to increase by 0.019°.[1] In terms of the non-primitive hexagonal *c/a* ratio, this translates to a change in *c/a* of -0.00074. Lobban *et al*. (2002) report that *c/a* changes by -0.00066(2) from 0.28 - 0.48 GPa at 200 K; this is in agreement with both the sign and the magnitude that the calculations indicate.

Table 4.VI (page 97) shows that all of the covalent O-H bonds in the simulated cell increased in length very slightly with pressure. This occurs because the H...O hydrogen bonds increase in strength (and thus shorten) at a greater rate than the O...O separation decreases. This pressure strengthening of the hydrogen bond in ice is a well-known phenomenon that ultimately leads to the hydrogen-bond symmetrised form of ice called ice X (see Chapter 3). Hence, the overall behaviour of the interatomic bonds in ice II is not surprising. There are some interesting findings to be had in the detail however.

[1] My neutron diffraction work, covering the range 0.25 – 0.45 GPa, observed a change in $\alpha = 0.027°$.

Table 4.V: Comparison of calculation results at 0.474 GPa and 0 K with neutron diffraction data acquired at 0.48 GPa and 200 K.[8]

	Ice II Experiment[a]			Ice II Simulation[b]		
a (Å)	7.7081(1)			7.551		
α	113.119(1)º			112.914º		
V (Å^3)	295.54(1)			281.385		
ρ (kg m^{-3})[c]	1214.69(4)			1275.79		
Fractional atomic coordinates						
	x	*y*	*z*	*x*	*y*	*z*
O1	0.0204(16)	0.8513(14)	0.2681(14)	0.0217	0.8567	0.2706
O2	0.5225(16)	0.2516(14)	0.6707(15)	0.5173	0.2492	0.6662
H1	0.0416(13)	0.7924(12)	0.1447(13)	0.0415	0.7923	0.1416
H2	0.1929(13)	0.9853(12)	0.4221(11)	0.1981	0.9923	0.4295
H3	0.5902(12)	0.2686(11)	0.5914(11)	0.5921	0.2710	0.5842
H4	0.6247(12)	0.2537(11)	0.7938(11)	0.6287	0.2560	0.7997

[a]Lobban *et al*., (2002): At 0.48 GPa and 200 K. The authors published their results in the hexagonal setting of space-group $R\bar{3}$, but I have converted the cell dimensions and fractional atomic coordinates to the trigonal setting for ease of comparison.

[b]This work: At 0.474GPa and 0 K

[c]For hydrogenous ice II; note that in Lobban *et al*. (2002) the density is quoted for deuterated ice II.

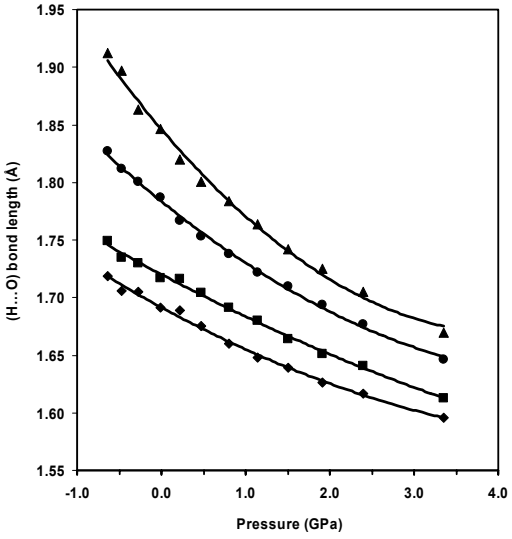

Figure 4.13: Example plot depicting the variation in the length of the four types of H...O hydrogen bond in the structure as a function of pressure. The fitted lines are second order polynomials, the parameters of which are quoted in Table 4.VI. Top to bottom these lines are $(H\ldots O)_{\perp}$, $(H\ldots O)_{||}$, $(H\ldots O)_{6B}$, and $(H\ldots O)_{6A}$.

Table 4.VI: Pressure dependence of the covalent O-H bonds lengths, H...O hydrogen bond lengths, and O...O separations in different parts of the ice II structure. The nomenclature is described in Sec. 4.2.2. Column three gives the change in a given bond length over the interval 0.28 - 0.48 GPa, for comparison with the experimentally observed values over the same pressure interval in column four.

Bond	Pressure dependence (P in GPa)	Change (Å) from 0.28 - 0.48 GPa[a]	Change (Å) from 0.28 - 0.48 GPa[b]
$r(\text{O-H})_{6A}$	$-0.000259P^2+0.002987P+1.003063$	0.000558	0.012 ± 0.015
$r(\text{O-H})_{6B}$	$-0.000218P^2+0.002922P+1.003938$	0.000551	0.000 ± 0.014
$r(\text{O-H})_{\perp}$	$-0.000319P^2+0.003985P+0.993840$	0.000749	-0.020 ± 0.013
$r(\text{O-H})_{\|\|}$	$-0.000254P^2+0.003339P+0.997569$	0.000629	0.023 ± 0.015
$r(\text{H...O})_{6A}$	$0.003328P^2-0.039716P+1.691501$	-0.00744	-0.009 ± 0.014
$r(\text{H...O})_{6B}$	$0.001961P^2-0.038545P+1.720096$	-0.00741	-0.033 ± 0.020
$r(\text{H...O})_{\perp}$	$0.010440P^2-0.086028P+1.846157$	-0.01562	-0.010 ± 0.016
$r(\text{H...O})_{\|\|}$	$0.005642P^2-0.059186P+1.783642$	-0.01098	-0.006 ± 0.019
$r(\text{O...O})_{6A}$	$0.003270P^2-0.037654P+2.69009$	-0.00703	0.000 ± 0.013
$r(\text{O...O})_{6B}$	$0.002222P^2-0.037935P+2.708256$	-0.00725	-0.031 ± 0.017
$r(\text{O...O})_{\perp}$	$0.009827P^2-0.080824P+2.831469$	-0.01467	-0.034 ± 0.017
$r(\text{O...O})_{\|\|}$	$0.005576P^2-0.056197P+2.763110$	-0.01039	0.017 ± 0.019
d_{6A}	$0.005137P^2-0.068330P+5.353402$	-0.01289	0.004 ± 0.015
d_{6B}	$0.004621P^2-0.075252P+5.212510$	-0.01435	-0.046 ± 0.017

[a]This work (athermal limit)

[b]Lobban *et al*., 2002 (200 K)

All of the bonds which form the 6A- *and* the 6B-rings exhibit near identical pressure dependencies. That the 6B-rings decrease in diameter more readily under pressure is due to changes in bond angles rather than bond lengths. It is noteworthy that the structure appears to compress dominantly as a result of the 6-tubes moving closer together: the rate at which the bonds joining the 6-tubes decrease in length is twice the rate at which the intra-ring bonds shrink, and it is ~50% greater than the rate at which bonds joining rings *within* the 6-tubes shrink. In effect, the 6-tubes are behaving like monocoques, wherein the bulk of the external

load is carried through their walls. This is in agreement with the experimental observation of Lobban *et al*. (2002) that increasing pressure drives the channels closer together in the helium-free structure.

Column four of Table 4.VI presents the experimental values for the tabulated bond length changes. In every single instance, the magnitude of the experimental standard error is larger than the calculated value of the change in bond length. The bond length changes are therefore so small that one cannot easily use the experimental data to arrive at useful conclusions as to how the structure behaves under compression; there must be a reduction in the standard errors of approximately an order of magnitude from those of Lobban *et al*. (2002) if we are reliably to observe structural changes in ice II under compression by experimental methods.

4.3 Summary

The under-estimate in V_0 for ice II (-3.4%) falls midway between that for ice XI (-8.4 %) and ice VIII (essentially zero), which is not surprising since the stronger hydrogen bonds in the higher density structures are better reproduced by calculations. The PW91 GGA tends to overbind low density H_2O solids, leading to large under-estimates in V_0, which become smaller in denser polymorphs. However, as the next chapter shows, this effect is turned around in solid ammonia; V_0 in the low density polymorph is greatly over-estimated (+6 %) but appears to be better reproduced in the high-pressure polymorph.

CHAPTER FIVE

SIMULATION OF SOLID AMMONIA: PHASES I AND IV

5 Introduction

Glacial ammonia (NH_3), first crystallized by Michael Faraday (Faraday 1845), is intermediate in character between the other two isoelectronic hydrides (DeKock and Gray 1989), water (H_2O), which forms strongly hydrogen bonded tetrahedral structures, and methane (CH_4), a quantum cryocrystal that forms close-packed structures. Weak hydrogen bonding between neighbouring ammonia molecules results in a pseudo-close-packed arrangement in the solid state (Reed and Harris 1961). It is therefore of relevance to chemical physics to understand the nature of hydrogen bonding in crystalline ammonia. Moreover, ammonia is a molecule of some cosmic abundance, believed to comprise a significant fraction of Uranus and Neptune (Hubbard and McFarlane 1980) and play a role in the chemistry of cloud layers on Jupiter and Saturn (Irwin 1999). In this chapter I characterize solid ammonia at 0 K, up to ~500 GPa, using DFT calculations.

My aim is to simulate the behavior of the weak hydrogen bonds in ammonia under compression. I can assess the veracity of my calculations by comparing other calculated quantities, such as the equation of state and lattice energy, with existing theoretical results and empirical data. I will therefore start by describing the phase relations of ammonia under pressure, and then my computational method, subsequently comparing the calculated structural, elastic, and thermodynamic properties with known values. This will allow me to discuss my results relating to the hydrogen bonding in solid ammonia in the subsequent section.

5.1 Ammonia I and IV

5.1.1 Structures and phase relations

The cubic unit cell (space group $P2_13$) of ammonia I (Fig. 5.1) contains four orientationally ordered ammonia molecules on symmetry sites C_{3v} (Hewat and Riekel 1979). The dipole moments of the ammonia molecules are directed towards the crystallographic [111] directions. Each molecule both accepts and donates three hydrogen bonds, each of which deviates significantly from the almost perfectly linear hydrogen bonds seen in water ice. Since a single lone-pair orbital is being shared between three nearest neighbors, the hydrogen bonding in ammoniacal solids is very weak, and the result is a pseudo-fcc molecular packing normal to [111].

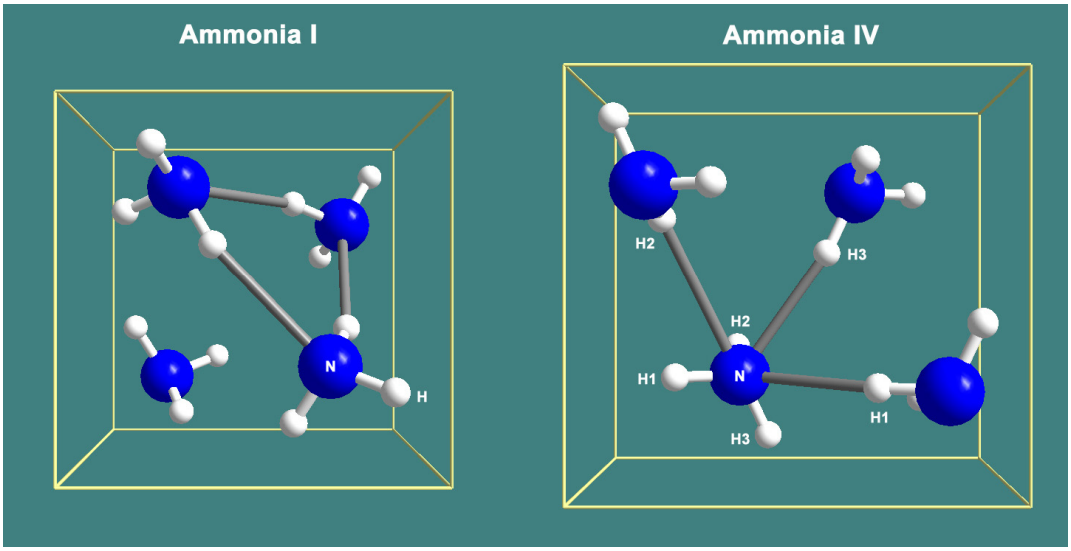

Figure 5.1. The unit cell of ammonia I

Figure 5.2. The unit cell of ammonia IV

With increasing pressure and temperature, ammonia experiences a series of phase transitions (Fig. 5.3, overleaf), first to hexagonal ammonia II ($P6_3/mmc$: Eckert *et al*., 1983) and then to 12-coordinated fcc ammonia III ($Fm3m$: Von Dreele 1984). Both ammonia II and III are rotationally disordered. Above 3.8 GPa at room temperature, ammonia III transforms to an ordered orthorhombic solid, ammonia IV, which crystallizes in space group $P2_12_12_1$ (Loveday *et al*., 1996). This phase is stable over a wide range of temperatures and pressures. Ammonia IV exhibits pseudo-hcp packing in layers normal to [001] and a more distorted hydrogen bond geometry than in phase I (Fig. 5.2). X-ray (Reed and Harris 1961: Olovsson and Templeton

1959b: Otto *et al*., 1989: Boese *et al*., 1997: Olinger and Mills, unpublished) and neutron diffraction studies (Hewat and Riekel 1979: Leclerq *et al*., 1995: Loveday *et al*., 1996, 2000b) have yielded cell-volume data for solid ammonia from 2–300 K in temperature, and up to 56 GPa in pressure. Structure refinements are available for the ambient pressure phase I up to 0.51 GPa (Eckert *et al*., 1983).

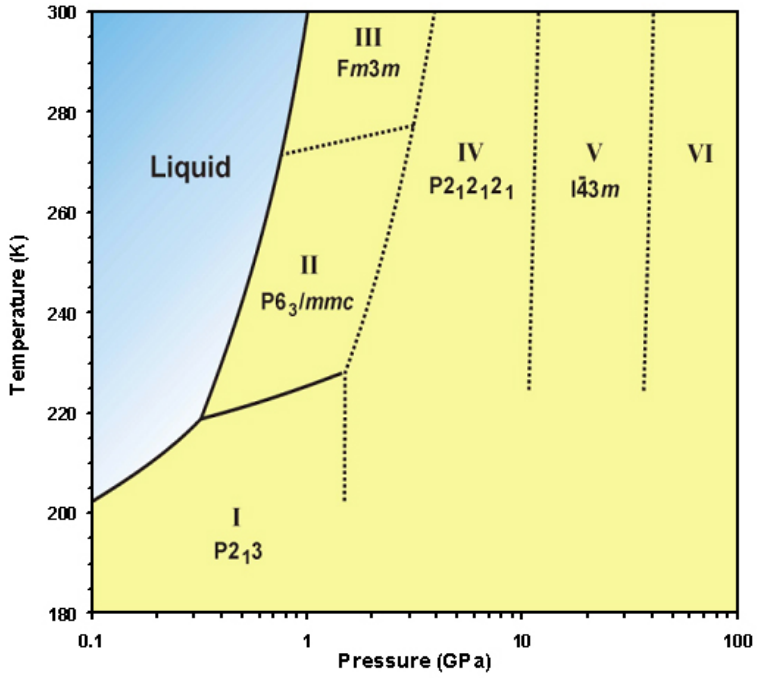

Figure 5.3. Phase diagram of solid ammonia, redrawn after Gauthier *et al*. (1988). Note that phases V and VI are speculative at present.

5.1.2 Previous computational studies

Ab initio methods have been applied to the simulation of ammonia clusters (see Koch and Holthausen 2001). This work, however, represents the first time that the plane-wave pseudopotential method has been applied to crystalline ammonia I. Ammonia IV was the subject of a detailed *ab initio* molecular dynamics study, using density functional theory, at pressures up to 300 GPa, and temperatures up to 7000 K, by Cavazzoni (1998, 1999). This study used the Becke exchange functional (Becke 1988) combined with the Lee, Yang, and Parr correlation functional (collectively BLYP, Lee *et al*., 1988), a particularly popular semi-empirical approach to gradient corrections in quantum chemistry, which has been used successfully on other hydrogen-bonded solids (Tsuzuki and Lüthi 2001). However, the LYP

functional violates the requirement that a correlation functional should preserve the correct features of the local spin-density approximation (LSDA) even when there are no regions of small density gradient (Burke *et al*., 1997). The locally based (i.e., nonempirical) Perdew–Wang gradient corrected functional which I use here (Chapter 2), does not violate this requirement. See Tsuzuki and Lüthi (2001) for a quantitative comparison of the performance of the two functionals. The details of my own computational efforts to study ammonia I and IV are presented in the following section.

5.1.3 Computational method

Convergence tests were carried out to optimize the sampling of the Brillouin zone, and the cutoff of the plane-wave basis set: The Monkhorst–Pack scheme was used for sampling of the Brillouin zone. It was found that for ammonia I (IV) a grid with 32 (27) symmetrically unique *k* - points in the irreducible wedge, combined with a kinetic energy cutoff of 900 (1200) eV, yielded total energy convergence to better than 10^{-4} eV per unit cell. A series of fixed volume calculations were then performed in which the ions were allowed to move according to the calculated Hellman–Feynman forces. For each volume specified the structure was relaxed via the conjugate–gradient technique in order to optimize the lattice parameters and internal coordinates. In the following section we report the results of structural relaxations for ammonia I, which were started from the 2 K experimental structure of Hewat and Riekel (1979), and for ammonia IV, which were started from the 5 GPa experimental structure of Loveday *et al.*(1996).

5.2 Results

5.2.1 Macroscopic elastic properties

5.2.1.1 Equation of state

Calculations were performed on the ammonia I structure at unit cell volumes from 4 - 25.6 $cm^3\ mol^{-1}$, and ammonia IV from 5.25 - 19.5 $cm^3\ mol^{-1}$. Integrated forms of the Birch–Murnaghan third order EoS (BMEOS3), and the fourth order logarithmic EoS (LNEOS4), were fitted to the E(V) data (see Chapter 2). The resulting parameters are given in Tables 5.I and 5.II.

Also shown for comparison in Table 5.II are the results of a fit to the combined data sets of Olinger and Mills (unpublished) and Otto *et al.* (1989) for ammonia IV. Figures 5.4 and 5.5 offer a graphical comparison between the calculated E(V) EoS and the experimental pressure–volume, P(V), data. Note that the EoS of Otto *et al.* (1989) is based on an incorrect indexing of

the diffraction pattern. However, the error resulting from this is likely to be smaller than the error bars depicted. The E(V) curves of ammonia I and IV are very flat around V_0 , which makes the accurate fitting of an EoS rather difficult.

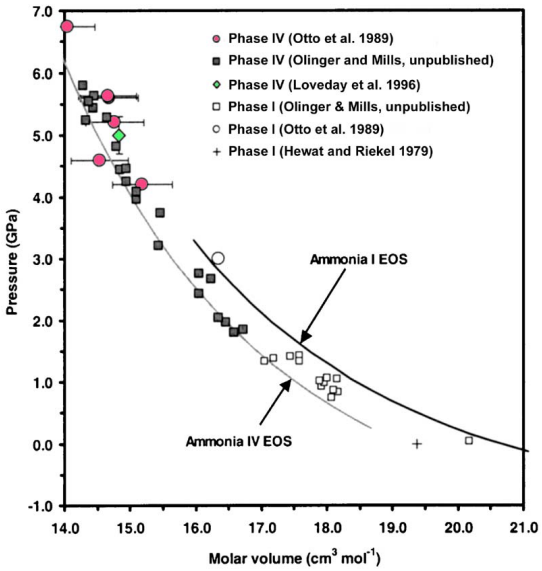

Figure 5.4. Low-pressure experimental P(V) data for ammonia I and IV (points), and my EoS fitted to the calculated E(V) curve (solid lines).

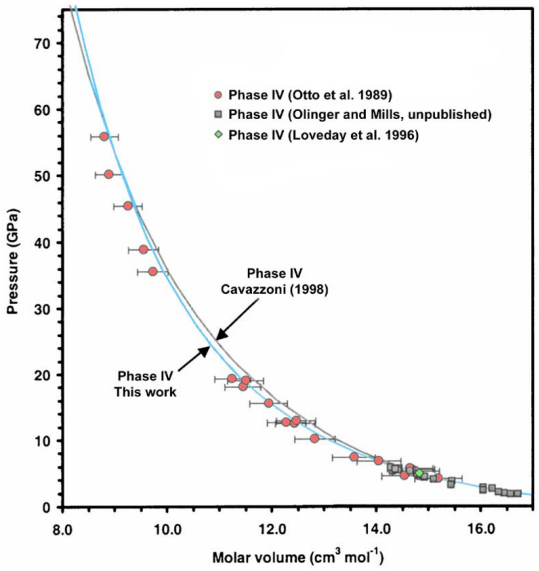

Figure 5.5. High-pressure experimental P(V) data for ammonia I and IV (points), and my EoS fitted to the calculated E(V) curve (solid lines).

In ammonia I, the GGA appears to overcompensate slightly for the excessive binding seen in typical LDA calculations (Hafner 2000), resulting in an inflated unit cell. The calculated zero pressure, zero temperature molar volume for ammonia I is ~20.5 cm^3 mol^{-1}, compared with an experimental value of 19.365 cm^3 mol^{-1} at 2 K (Hewat and Riekel 1979), a difference of +5.9%. Hence the ammonia I EoS makes a modest overestimate of the pressure for a given volume, although bearing in mind the relative softness of the bulk modulus, this value is not as problematic as it at first appears. Indeed a pressure of ~3.6 kbar brings the calculated and theoretical volumes into coincidence. The bulk modulus, K_0 = 6.6 GPa, bears comparison with that found from experimental elastic stiffness coefficients (Kiefte *et al.*, 1985, 1987) and ultrasonic velocity measurements (Voitovich *et al.*, 1971) at much higher temperatures (6 GPa at 90 K).

Figures 5.4 and 5.5 show that my EoS falls within all of the error bars of Otto *et al.* (1989). For clarity, error bars on Olinger and Mills' unpublished data are not shown but are of the order of 1% in volume.

Table 5.I. Calculated and experimental EoS parameters of ammonia I.

	V_0 ($cm^3\ mol^{-1}$)	K_0 (GPa)	K'_0	K''_0 (GPa^{-1})	E_0 ($eV\ molecule^{-1}$)
BMEOS3 E(V)	20.7 ± 0.3	6.7 ± 0.7	5.0 ± 0.2	-	-19.924 ± 0.002
LNEOS4 E(V)	20.5 ± 0.1	6.9 ± 0.4	5.5 ± 0.0	-1.65 ± 0.14	-19.924 ± 0.001
Experimental*	19.365	5.8(6)	-	-	-

*Molar volume at 2K (Hewat and Riekel 1979). Average bulk modulus at 195K, see text.

Table 5.II. Calculated and experimental EoS parameters of ammonia IV.

	V_0 ($cm^3\ mol^{-1}$)	K_0 (GPa)	K'_0	K''_0 (GPa^{-1})	E_0 ($eV\ molecule^{-1}$)
BMEOS3 E(V)	19.2 ± 0.01	8.7 ± 0.4	5.1 ± 0.1	-	-19.880 ± 0.001
LNEOS4 E(V)	19.3 ± 0.2	9.2 ± 1.3	3.5 ± 0.7	1.3 ± 0.2	-19.880 ± 0.001
Experimental[a]	19.94 ± 0.04	7.56 ± 0.06	5.29 ± 0.03	-	-
Experimental[b]	19.0 ± 0.5	10 ± 2	5.0 ± 0.2	-	-

[a]Parameters quoted by Otto *et al*. (1989)

[b]My own BMEOS3 fit to experimental data of Otto *et al*. (1989) at ~210K, and Olinger and Mills unpublished X-ray work (175-296K), kindly provided by Stefan Klotz, Paris J.M.C.

From the energy of the isolated ammonia monomer (-19.560 eV), the lattice energy of ammonia I is found to be 35.1 ± 0.2 kJ mol^{-1} and the average hydrogen bond enthalpy is 11.9 ± 0.1 kJ mol^{-1}. Empirical and theoretical values of the lattice energy are compared in Table 5.III (below)

Table 5.III. Experimental and calculated lattice energy of ammonia I

	Lattice energy (kJ mol^{-1})
Experiment (Shipman *et al*., 1976)	-36.32 ± 0.08
Potential model (Shipman *et al*., 1975)	-36.40
Potential model (Hellens 1951)	-33.97
Potential model (Snir *et al.,* 1978)	-37.91
Potential model (Brink and Glasser 1987)	-34.23
This work (DFT)	-35.1 ± 0.2

The lattice energy of ammonia IV is found to be 30.9 ± 0.1 kJ mol^{-1} at 0 GPa. The similarity in the lattice energies of ammonia I and IV reflect the similarity in their structures and bonding, which differ only in the second nearest neighbor. The pressure at which the calculated enthalpies of ammonia I and IV are equal (and hence the phase transition occurs) is 7.6 ± 0.1 GPa. The Raman study of Kume *et al.* (2001) indicates that the I–IV transition at 20 K is at ~3 GPa. However, the calculated energy difference between the two phases is so small that the transition pressure is very sensitive indeed to errors in the fitted EoS.

5.2.2 Microscopic bonding phenomena

5.2.2.1 Crystal Structure and bonding

The detailed structural parameters of ammonia I and IV at fixed pressure are presented in Tables 5.IV and 5.V, respectively. For direct comparison, experimental and theoretical results are given at the same molar volume. The structural parameters for ammonia I agree very well with the experimental values (Hewat and Riekel 1979). The most significant difference is the overestimate of the N–H bond length, which is carried over from the gas-phase calculation and may be due to inadequacies in the pseudopotentials (see Chapter 2).

Table 5.IV. The experimental and calculated structures of ammonia I compared at the same molar volumes.

	Experimental values[a]			Calculated values[b]		
a (Å)	5.048			5.048		
V (Å^3)	128.63			128.63		
Fractional atomic coordinates						
	x	*y*	*z*	*x*	*y*	*z*
N	0.2109(3)	0.2109(3)	0.2109(3)	0.2086	0.2086	0.2086
H	0.3750(3)	0.2712(4)	0.1129(3)	0.3724	0.2713	0.1060
Bond lengths (Å)						
N-H	1.012(2)			1.026		
H…N	2.357(2)			2.327		
Bond angles						
H-$\hat{\text{N}}$-H	107.53(19)°			108.31°		
N-$\hat{\text{H}}$…N	160.00(15)°			161.12°		

[a]Hewat and Riekel (1979), 0 GPa, 2 K. These authors do not quote errors on their unit cell edge refinements.

[b]This work – 0.359 GPa, 0 K.

Table 5.V. The experimental and calculated structures of ammonia IV compared at the same molar volumes.

	Experimental values[a]			Calculated values[b]		
a (Å)	3.2495(4)			3.2476		
b (Å)	5.6576(6)			5.5977		
c (Å)	5.3556(5)			5.4155		
b/a	1.7411(4)			1.7236		
c/a	1.6481(3)			1.6679		
V (Å^3)	98.45(3)			98.45		
Fractional atomic coordinates						
	x	*y*	*z*	*x*	*y*	*z*
N	0.2604(11)	0.3509(4)	0.2563(5)	0.2640	0.3574	0.2543
H1	0.3795(16)	0.1918(9)	0.2352(11)	0.3816	0.1885	0.2318
H2	0.9706(23)	0.3340(9)	0.3240(12)	0.9727	0.3382	0.3232
H3	0.2312(24)	0.4238(5)	0.0902(12)	0.2281	0.4290	0.0805
Bond lengths (Å)						
N-H1	0.980(6)			1.027		
N-H2	1.014(8)			1.023		
N-H3	0.985(7)			1.029		
H1…N	2.257(6)			2.183		
H2…N’	2.338(8)			2.334		
H2…N”	2.572(7)			2.629		
H3…N	2.196(6)			2.133		
Bond angles						
H1- N̂ -H2	106.3(5)°			106.87°		
H1- N̂ -H3	115.0(4)°			107.01°		
H2- N̂ -H3	105.8(6)°			105.67°		
N-Ĥ…N	171.86(45)°			166.82°		
N- Ĥ2…N’	149.06(63)°			148.08°		
N-Ĥ2…N”	126.71(51)°			126.94°		
N-Ĥ3…N	167.71(48)°			166.87°		

[a]Loveday *et al*. (1996), 5 GPa, unknown temperature.

[b]This work – 0.359 GPa, 0 K.

I can confirm that the structure is hydrogen bonded in the expected manner by investigating the electron density along the bond paths between atoms. Interatomic interactions are readily studied in terms of the topological properties of the electron density according to Bader's atoms in molecules theory (Bader 1990). Saddle points, or bond critical points, in the charge density (ρ_{bcp} where $\nabla\rho = 0$) between atoms have a number of useful properties, not least of which is an estimate of the bond strength. Following Kock and Popelier (1995), I will consider hydrogen bonds as those bonds with $\rho_{bcp} \approx 10^{-2}$ a.u. (1 a.u. = 6.7483 eÅ^{-3}) and van der Waals interactions as those with $\rho_{bcp} \approx 10^{-3}$ a.u.

I used the VASPViewer program to visualise the electron density in a selected plane which contains the bond under consideration. While this does not allow one to make detailed calculations of quantities such as the Laplacian of the electron density, it does allow the manual location of bond critical points, and the study of electron density along bond paths. For phase I of solid ammonia, I find that, at the H…N bond critical point, $\rho_{bcp} = 0.0137$ a.u., which meets the criterion for a regular hydrogen bond.

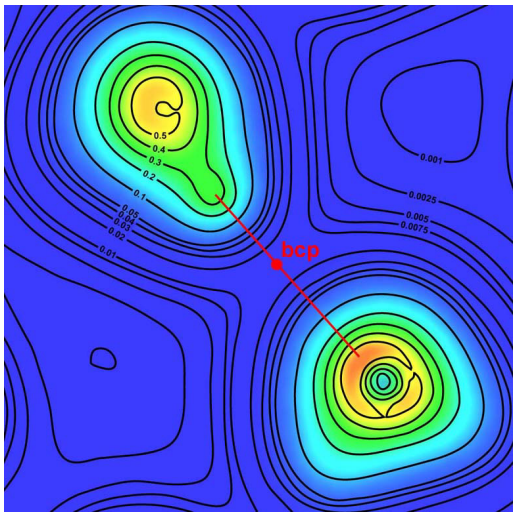

Figure 5.6. Electron density in ammonia I in the plane of the hydrogen bond. The bonding path is denoted by the red line, and the bond-critical-point by the filled circle. Contours are in atomic units (see text).

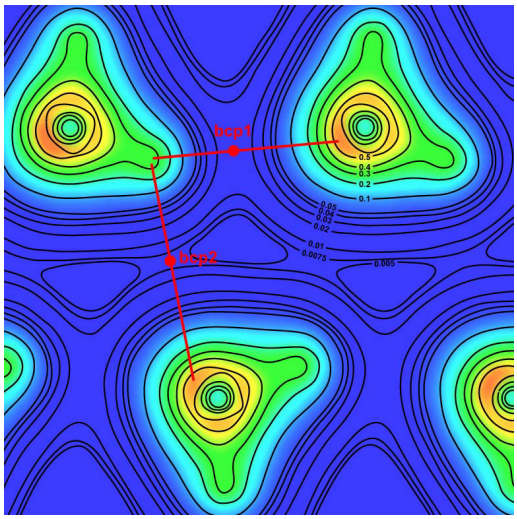

Figure 5.7. Electron density in ammonia IV in the plane of the proposed bifurcated hydrogen bond. The possible bonding paths are denoted by the red lines, and the bond-critical-points by the filled circles.

Electron densities in the plane of the hydrogen bonds are shown for ammonia I and ammonia IV in Figs. 5.6 and 5.7. I also compared the electron density at the N–H bond critical point with earlier DFT and Hartree–Fock studies (Wang *et al.*, 1996), and with experimental values (Table 5.VI). Wang *et al.* (1996) employ a variety of different exchange–correlation

functionals (although not PW91), including hybrid functionals. In common with our results, all of their DFT calculations yield N–H bond lengths that are 1–1.5 % too long.

Table 5.VI. Electron densities at the N-H bond critical point.

	Experiment[a]	MP2/6-31G(3d)[b]	DFT[c]	This work
ρ_{bcp} (a.u.)	0.317(6)	0.332	0.327-0.336	0.314
$r_{(N-H)}$ (Å)	1.010	1.020	1.019-1.028	1.026
$r_{(bcp-H)}$ (Å)	0.245	0.246	0.242-0.253	0.245

[a]Electron diffraction at 160K (Boese *et al*., 1997))

[b](Wang *et al*., 1996)

[c]Density functional theory calculations with various gradient approximations (Wang *et al*., 1996)

The structural parameters of ammonia IV also agree very well with the experimental values (Loveday *et al*., 1996). Once again, there is a systematic overestimate of the N–H bond length. However, an interesting feature of our calculated structure is the similarity in the lengths of N–H1, N–H2, and N–H3 (a spread of 0.006 Å) compared with the structure refinement of Loveday *et al.* (1996) wherein there is a spread of 0.034 Å in bond lengths. What is worthy of note is that Loveday *et al*. (1996) report no significant worsening in the Rietveld fit to their data when all bond lengths and angles are constrained to be equal. We have observed a similar discrepancy between our results and experimental structure refinements for N–H bond lengths in ammonia monohydrate phase I (Chapter 6) and ammonia dihydrate phase I (Chapter 7).

As mentioned previously, the structure of ammonia IV is of particular note because of the possibility that it might contain a bifurcated hydrogen bond (Loveday *et al*., 1996), or more strictly, a three-centred interaction: a three-centred hydrogen bond describes the situation where a hydrogen atom is surrounded by three electronegative atoms lying approximately in a plane containing the hydrogen atom, and where the hydrogen atom is covalently bound to one of the three surrounding atoms. Bifurcated hydrogen bonds play a very important role in, for example, the structure and stability of biological molecules such as DNA (Bhattacharya and Majumdar 2001), and the occurrence of such a bond in as simple a material as glacial ammonia would be of great potential interest. Loveday *et al.* (1996) proposed a bifurcated bond on the grounds of the strained character of the N-Ĥ2-N' bond angle ~149° (compared with ~170° for the other N-Ĥ-N angles) and the observation that the H2-N" distance is slightly less than the sum of the van der Waals radii for deuterium and nitrogen (2.75 Å).

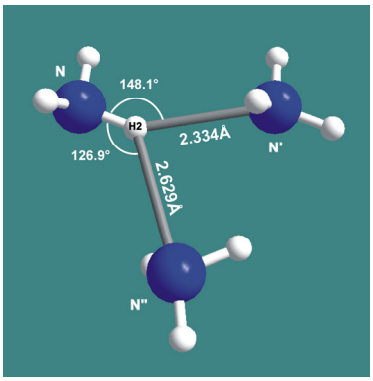

Figure 5.8.
The geometry of the proposed bifurcated hydrogen bond in ammonia IV. This view corresponds approximately to that depicted in Figure 5.7. Bond lengths and angles are as Table 5.V.

The geometry of the proposed bifurcated hydrogen bond is strikingly similar to structure-type **II4** examined by Rozas *et al.* (1998) in their computational study of three-centred interactions. Their example of a proposed asymmetric three-centre inter-action failed to reveal a second hydrogen bond (on the basis of ρ_{bcp}) which would be the equivalent of H2…N" in the ammonia IV structure. Instead it was concluded that this geometry corresponds to a single strong hydrogen bond perturbed by van der Waals forces from a nearby interacting atom. It is therefore intriguing to examine the electron density in my calculated ammonia IV structure so as to shed light on the existence, or otherwise, of a bifurcated hydrogen bond. The simulated structure confirms the presence of this strained bond, and also reveals that it is present at all pressures studied (up to ~500 GPa). Bond critical points are present in the charge density topology of ammonia for the three expected hydrogen bonds, H1…N (ρ_{bcp} = 0.0196 a.u.), H2…N' (ρ_{bcp} = 0.0150 a.u.), and H3…N (ρ_{bcp} = 0.0250 a.u.), and the bond strength indicated by these values (at 5 GPa) agrees with the order inferred from inspecting the bond lengths (Table 5.V). In other words, the hydrogen bond strength, E_{HB}, follows the pattern (H3…N) > (H1…N) > (H2…N'). As Fig. 5.7 shows, the electron density along the proposed H2…N" bond path (solid red line) is very small, ~0.0074 a.u. at the saddle point, which indicates no hydrogen bond. This value is no higher than the electron density between other *nonbonded* nitrogen and hydrogen atoms. I therefore conclude that this bond geometry in ammonia IV is entirely analogous to that in structure-type **II4** of Rozas *et al*. (1998) in which a single hydrogen bond is perturbed by a neighbouring atom: ammonia IV does not contain a bifurcated hydrogen bond. (See Fig. 5.8).

5.2.2.2 Hydrogen-bond symmetrisation

In ice the hydrogen bond is pressure strengthened, leading to an increase of the covalent O–H bond length, $r_{(O–H)}$, up to the limit in which the proton is symmetrically located midway between neighboring oxygen atoms, producing the Cu_2O structured ice X (as described in

Chapter 3). A similar phenomenon has been proposed for ammonia on the basis of Raman observations. Two possible high-pressure (>60 GPa) structures were mooted (Gauthier *et al*., 1988): The first is isostructural with Cu_3N (space group P*m3m,* O_h^1) with H–$\hat{N}$–H angles of 90°. The second proposed structure has space group P*n3m* (O_h^4), and H–$\hat{N}$–H bond angles of 141°. An X-ray study up to 56 GPa (Otto *et al*., 1989) failed to observe the proposed precursor (Gauthier *et al*. 1988) to these structures, ammonia V (space group $I\bar{4}3m$), and more recent infrared spectroscopy has ruled out bond symmetrisation up to 120 GPa (Sakashita *et al*., 1998). Moreover, Cavazzoni (1998) did not see bond symmetrisation at pressures up to 300 GPa, and found that the proposed cubic structure was energetically disfavored with respect to ammonia IV. I have studied the behavior of the hydrogen bonds under compression up to > 300 GPa in both ammonia I and ammonia IV. The results are shown in Fig. 5.9, alongside Cavazzoni's results and my previous calculations for the ice VIII/X transition, quoted as r (X–H) / [r (X–H) + r (H…X)], where X = O in ice and N in ammonia. Observe that the data for ammonia I is downshifted for ease of viewing, and values should be read from the axis on the right. The data for ammonia IV consists of an average of the three N–H bond lengths. Similarly, Cavazzoni (1998) plots the abscissa of the peak in the radial distribution function (effectively an average of the three N–H bond lengths).

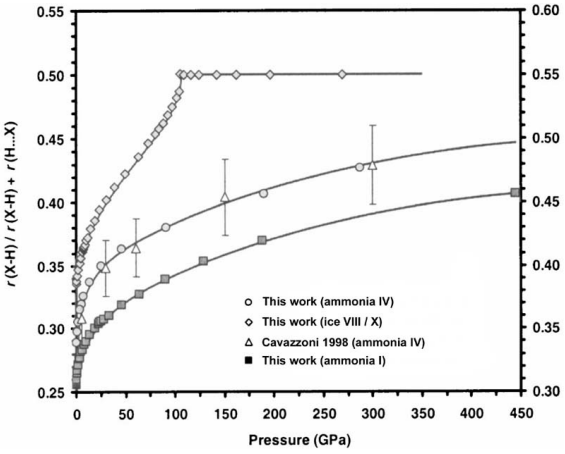

Figure 5.9. Variation of the fractional hydrogen bond length with pressure in ice and ammonia. The ice VIII results show a continuous trend towards symmetrical hydrogen bonds at ~105 GPa (see text), whereas the hydrogen bonds in ammonia do not approach this condition under any compression simulated here. Note that the results for ammonia I should be read from the right-hand axis, that for ammonia IV and ice from the left hand axis.

In ice VIII, I observed in my calculations that the fractional hydrogen bond length and the degree of tetragonal distortion from the cubic ice X structure behaved as coupled order parameters, tending continuously to a cubic symmetrised phase near 100 GPa. However, the ice X structure was found to be thermodynamically stable at much lower pressures, as determined from the separately calculated EoS of each phase, and I placed the transition at 70(1) GPa (see Chapter 3). This pressure is in agreement with experimental values. The apparent contradiction in the phase transition pressures (between the case where ice VIII and ice X are simulated

separately, and the case where ice VIII is compressed until it becomes ice X) occurs because the calculations treat the hydrogen atom as a classical entity (subject to Newtonian mechanics) rather than as a quantum entity. Since this overlooks the important delocalising effects of tunnelling and zero-point motion (Benoit *et al*., 1998a,b), the transition pressure (under continuous compression of the ice VIII structure) is pushed to 100 GPa, rather than 70 GPa.

Within the stability field of ammonia I, the N–H bonds behave in the same way as the O–H bonds in ice VIII, increasing in length at a rate of 0.038(1) pm GPa^{-1} up to 4 GPa. Beyond that pressure, in phases I and IV, the N–H bonds decrease in absolute length but continue to increase in fractional length, r (X–H) / [r (X–H) + r (H…X)], trending towards the symmetrical limit. Nonetheless, this limit is not reached up to the highest pressure investigated. My overall finding is that hydrogen bond symmetrisation should not occur in ammonia IV at any experimentally reasonable pressure (i.e., < 300 GPa). Indeed, extrapolating these results to r (X–H) / [r (X–H) + r (H…X)] suggests a symmetrisation pressure well in excess of 2 TPa. This is not to say that ammonia IV does not transform via a first order process to some other structure in which symmetrical hydrogen bonding is achievable at a much lower pressure. This conclusion also does not include the important quantum effects of tunnelling and zero-point motion, which would act to bring the symmetrisation transition to a lower pressure.

5.3 SUMMARY

I have undertaken plane-wave pseudopotential calculations on the ambient-pressure phase of glacial ammonia, and the high-pressure phase, ammonia IV. The structure, equation of state, and lattice energy for ammonia I are in reasonable agreement with experimental data. Similarly, where there is experimental data for ammonia IV, the calculations yield very good results. The results on the pressure dependence of the hydrogen bond strength in ammonia IV are in excellent accord with an earlier DFT study and confirm the latest Raman studies. Moreover, I have shown that ammonia IV does not contain a bifurcated hydrogen bond; rather it contains a hydrogen bond which is perturbed by van der Waals forces. The principle error in the method is the classical treatment of the hydrogen atoms.

CHAPTER SIX

SIMULATION OF AMMONIA MONOHYDRATE AND AMMONIA HEMIHYDRATE

6 Introduction

The first half of this chapter presents the results of my investigation of $NH_3 \cdot H_2O$, ammonia monohydrate (AMH), and NH_4OH, ammonium hydroxide. Unlike ice and ammonia, there is little experimental data against which the results of this work can be compared to, and there is only a single example of a classical simulation reported in the literature. AMH is the most straightforward and computationally inexpensive of the ammonia hydrates to simulate. The unit cell is smaller than that of either ADH or AHH (28 atoms vs 40 and 44 atoms per unit cell, respectively) and it is ordered throughout its stability field.

I begin by outlining the practical aspects of simulating AMH phase I, and in the second part of this chapter, describe the simulation of AHH.

6.1 Ammonia Monohydrate and ammonium hydroxide.

Early structural work on the more ammonia rich monohydrate phase, which melts congruently at 194.15 K, (Olovsson and Templeton 1959) showed that the ambient pressure monohydrate is orthorhombic (space group $P2_12_12_1$) with a = 4.51 ± 0.01 Å, b = 5.587 ± 0.003 Å, and c = 9.700 ± 0.005 Å at 113 K. An earlier study (Siemons and Templeton 1954) erroneously purported to show that the monohydrate was hexagonal (a = 11.21 ± 0.05 Å, c = 4.53 ± 0.02Å). Neutron diffraction studies of AMH confirmed the space group assignment ($P2_12_12_1$, a = 4.51108 Å, b = 5.58691 Å, c = 9.71452 Å at 110 K: Loveday and Nelmes, 2000).

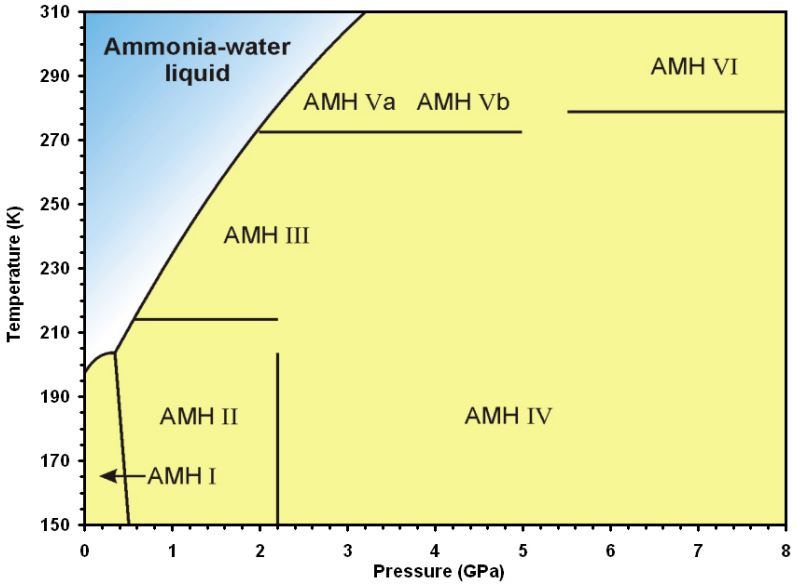

Figure 6.1. P-T phase diagram for AMH. Redrawn after (Loveday and Nelmes 1999a).

Koumvakalis (1988) reported Raman studies of AMH at pressures up to 12 GPa, including a determination of the melting curve. No phase transitions were apparently observed, although this is belied by the detection of a higher pressure phase (AMH II) by Hogenboom *et al*. (1995, 1997), recently confirmed by Loveday and Nelmes (1999b: 2000), along with five other high-pressure monohydrate phases (Figure 6.1). The simplicity of the AMH VI diffraction pattern has allowed a rapid structural determination, showing it to be cubic (space group $Im\bar{3}m$, a = 3.2727 Å: Loveday and Nelmes 1999a). AMH VI is the first known example of a hydrogen-bonded molecular solid solution which has the potential to be stable to very high pressures. This has implications for the interiors of Uranus and Neptune where a solid solution of AMH VI and Ice VII may be stable over a large P-T range (Loveday and Nelmes 1999a). Indeed, evidence to support this will be presented in Chapter 8 when I describe the results of my high-pressure neutron diffraction experiments.

6.1.1 Computational detail

The neutron diffraction derived structure of AMH I, from which the simulations were begun, is orthorhombic (space group $P2_12_12_1$), at ambient pressure, and contains four molecules per unit cell (Loveday and Nelmes, 2000). The structure (Figure. 6.2) is fully proton ordered, consisting of strongly hydrogen-bonded chains of water molecules, extending along the *a*-axis, cross-linked by weakly hydrogen-bonded ammonia molecules. Each ammonia molecule is tetrahedrally coordinated by four water molecules, donating three weak hydrogen bonds, and

accepting a single stronger hydrogen bond. Each water molecule is 6-coordinated, bonding to four ammonia molecules and two other water molecules. Cell parameters and internal coordinates are given in Table 6.III. The fractional coordinates in Table 6.III were the starting point for the structural relaxations.

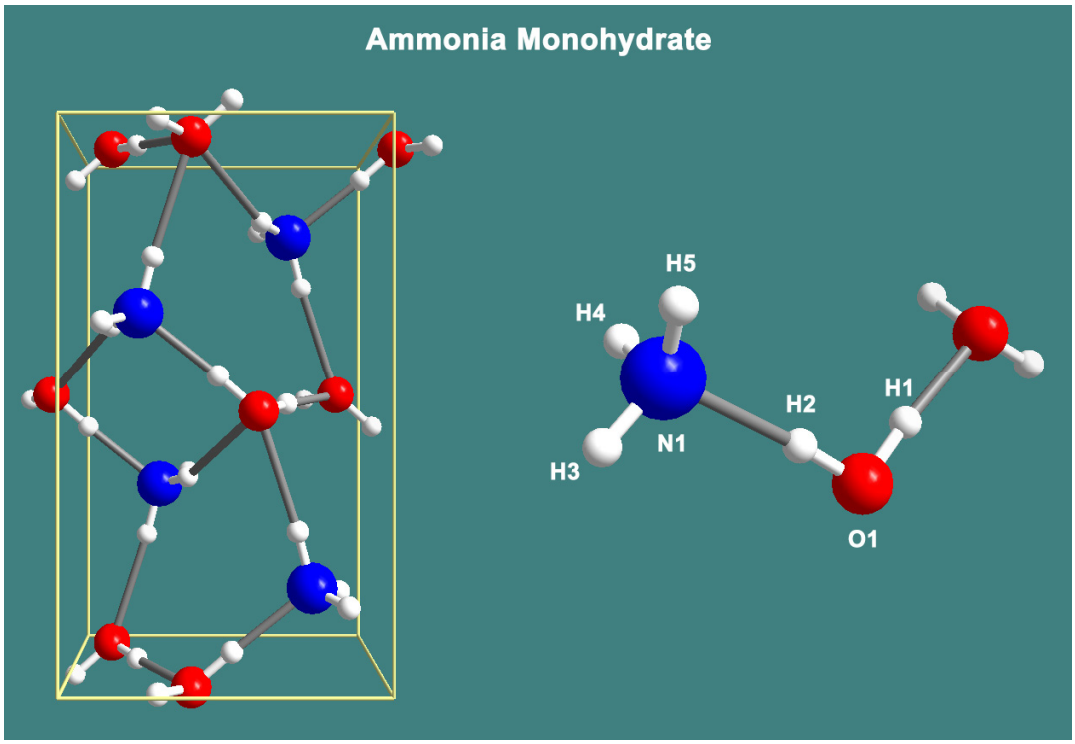

Figure 6.2. Left; the unit cell viewed along the *a*-axis, with the *c*-axis vertical. Right; the designation of the atoms in the asymmetric unit, as given in Table 6.III.

Total energy convergence tests were carried out to optimise the sampling of the Brillouin zone and the cut-off of the plane-wave basis set. It was found that a grid with 32 symmetrically unique $\vec{k}$ -points in the IBZ, combined with E_{cut} = 1100 eV, yielded total energy convergence to better than 10^{-4} eV per unit cell.

6.1.2 Equation of State

Structural relaxations were carried out at fixed cell volumes from 18 - 42 cm^3 mol^{-1} (-1 to +37 GPa). These revealed a discontinuity at ~ 27 cm^3 mol^{-1} in the slope of the total energy curve (Figure. 6.3) and the pressure (Figure. 6.4) indicative of a first order phase transition. Examination of the fractional atomic coordinates showed that the molecular AMH I structure had become an ionic solid, transforming via a solid-state protolytic reaction to ammonium

hydroxide (NH_4OH). This is the first time that this structure has been simulated. Subsequently, I was able to relax the ionic structure at volumes within the field of stability of AMH I. An integrated form of the third order Birch-Murnaghan equation of state (BMEOS3), and of the fourth order logarithmic equation of state (LNEOS4) were fitted (as per Chapter 2) to the E(V) data for the molecular and ionic phases (Figure. 6.3), and the EoS parameters appear in Tables 6.I and 6.II.

Figure 6.3. Calculated E(V) curves for AMH I and NH_4OH, and fitted equations of state.

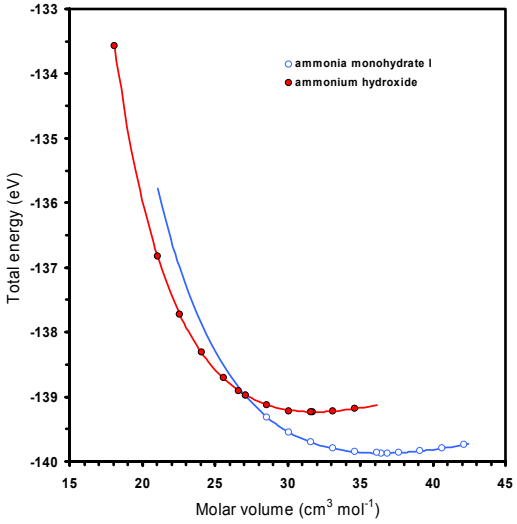

Figure 6.4. Experimental P(V) data for AMH I and AMH IV, and my calculated E(V) EoS fits for AMH I (blue line) and NH_4OH (red line).

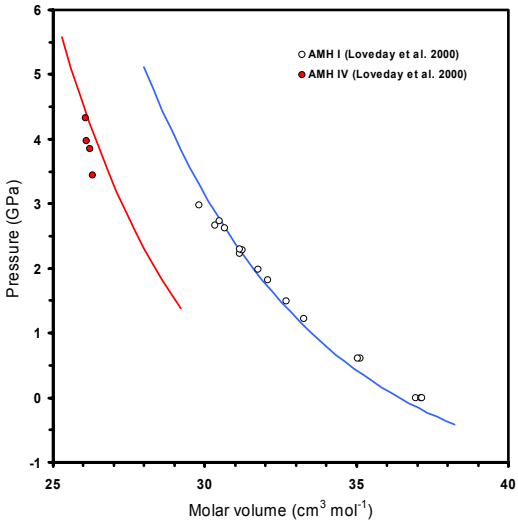

Table 6.I. Calculated EoS parameters for molecular AMH I.

	V_0 ($cm^3\ mol^{-1}$)	K_0 (GPa)	K'_0	K''_0 (GPa^{-1})	E_0 ($eV\ molecule^{-1}$)
BMEOS3: E(V) fit	36.40 ± 0.01	9.7 ± 0.1	5.3 ± 0.1	···	-34.9678 ± 0.0001
LNEOS4: E(V) fit	36.42 ± 0.04	9.7 ± 0.1	5.1 ± 0.3	-0.01 ± 0.005	-34.9679 ± 0.0001
Experimental*	37.24	8.60	4.56	···	···

*Loveday *et al*. (2000). Murnaghan fit to data at 115, 130, and 150 K.

The equations of state of AMH I and AMH IV were measured recently (Loveday *et al*., 2000): The calculated EoS of AMH I compares very well with the experimental data points in Figure. 6.4. The experimental Murnaghan EoS parameters of Loveday *et al*. (2000) are reported in Table 6.I. These parameters are fitted to neutron diffraction derived P(V) data acquired at temperatures of 115, 130, and 150 K. It is therefore unsurprising that V_0 is larger, and K_0 softer, than the athermal values I have calculated. The benchmarking work conducted on ice and solid ammonia (Chapters 3-5) shows that the PW91 GGA functional compensates well for the known deficiencies of the local density approximation (LDA) in strongly hydrogen bonded solids, such as ice. Indeed, applying the thermal expansion coefficient derived by Croft *et al*. (1988) to the data of Loveday *et al*. (2000) provides a value for V_0 at zero Kelvin of 36.552 ± 0.003 $cm^3\ mol^{-1}$, and this differs by just 0.25 ± 0.13% from the closest calculated value of V_0 in Table 6.I.

Table 6.II. Calculated EoS parameters for ammonium hydroxide.

	V_0 ($cm^3\ mol^{-1}$)	K_0 (GPa)	K'_0	K''_0 (GPa^{-1})	E_0 (eV $molecule^{-1}$)
BMEOS3: E(V) fit	32.00 ± 0.08	11.3 ± 0.4	6.4 ± 0.2	···	-34.809 ± 0.001
LNEOS4: E(V) fit	32.07 ± 0.10	11.6 ± 0.8	5.2 ± 1.0	0.69 ± 0.84	-34.810 ± 0.001

Although there are no experimental values for ammonium hydroxide, the accuracy of the calculations may be gauged by reference to published volumetric data (Jenkins *et al*., 1999) for the ions concerned. The thermochemical volume for the NH_4^+ ion is given as 0.021 ± 0.015 nm^3, and that of the OH^- ion as 0.032 ± 0.008 nm^3. These values yield a molar volume for NH_4OH of 31.92 ± 13.85cm^3mol^{-1}, which (errors aside) is in close agreement with the calculated value (Table 6.II). A further constraint may be applied using the volume of the hydration water in ammonium hydroxide. The proposed value of 13.0 ± 2.1 $cm^3\ mol^{-1}$ (Mercury *et al*., 2001), added to the molar volume of solid ammonia at zero Kelvin, 19.37 $cm^3\ mol^{-1}$ (Leclerq *et al*., 1995), gives V_0 for NH_4OH = 32.37 ± 2.1 $cm^3\ mol^{-1}$.

In the following section I compare the calculated and experimental structures and describe the behaviour of simulated AMH I and ammonium hydroxide under compression.

6.1.3 Structure of AMH I

A comparison of the experimental and simulated cell parameters, internal coordinates, bond lengths, and bond angles of AMH I at zero pressure (Table 6.III) shows close agreement. The volume dependence of the cell parameters is presented in Figure 6.5.

The greatest differences between the observed and calculated bond lengths (Table 6.III) are for the covalent O-H and N-H bonds. This discrepancy arises from the hydrogen pseudopotential, as described in Chapter 2. What is puzzling about the experimental structure is the large variation in the experimental N-H bond lengths that should appear as a difference of several hundred wavenumbers in the N-D stretching frequency, $\nu_{N\text{-}D}$. Published spectroscopic data does not support this, $\nu_{N\text{-}D}$ being quoted as 2464.1, 2467.0, and 2471.3 cm^{-1} (Bertie and Shehata, 1985). The calculated N-H bond lengths are tightly clustered around 1.025Å while the experimental values range from 0.973Å to 1.025Å. Large differences between O-H1 and O-H2 are endorsed by the published O-D stretching frequencies: $\nu_{O\text{-}D}$ = 2410 and 2197 cm^{-1} (Bertie and Shehata, 1985). The difference in length between the O-H bonds (0.032Å) is similar to the experimental value (0.058Å). A parallel discrepancy in N-H bond lengths, between calculated and experimental values, crops up in the structure of ammonia IV (see 5.2.2.1).

Figure 6.5. Volume dependence of the cell parameters of AMH I. Lines are a guide to the eye.

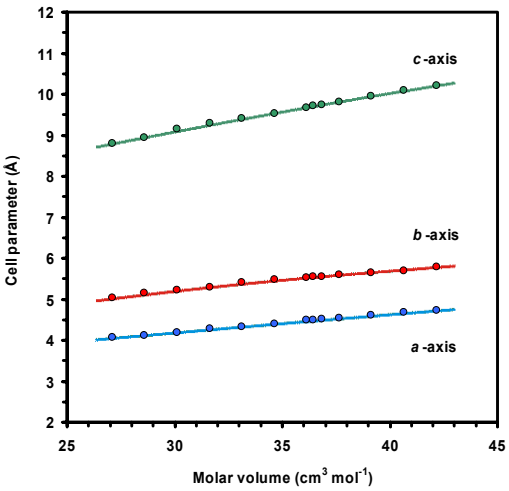

Figure 6.6. $\partial r_{(O\text{-}H)} / \partial P$ for the O-H1 and O-H2 bonds in AMH I. Lines are a guide to the eye.

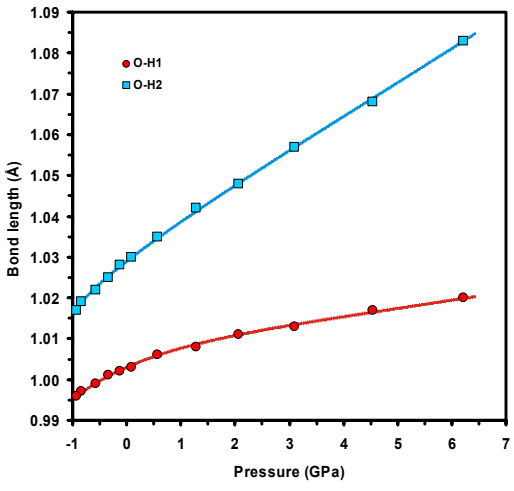

Table 6.III. Calculated and experimental cell parameters, internal coordinates, and selected bond lengths in AMH I at zero pressure.

	Experimental values[a]	Calculated values[b]
a (Å)	4.51108(14)	4.49505
b (Å)	5.58691(20)	5.54476
c (Å)	9.71452(34)	9.70787
b/a	1.2385(1)	1.2335
c/a	2.1535(1)	2.1597
V (Å^3)	244.835(25)	241.959

Fractional atomic coordinates

	x	*y*	*z*	*x*	*y*	*z*
O1	0.2475(12)	0.1065(5)	0.0136(3)	0.2654	0.1141	0.0246
H1	0.4348(7)	0.2047(5)	0.0021(5)	0.4472	0.2136	0.0059
H2	0.2422(14)	0.0219(4)	0.4490(3)	0.2346	0.0210	0.4520
N1	0.2437(9)	0.2740(3)	0.3336(2)	0.2418	0.2547	0.3413
H3	0.4172(15)	0.3758(9)	0.3542(6)	0.4253	0.3588	0.3616
H4	0.0713(15)	0.3731(9)	0.3530(6)	0.0603	0.3626	0.3578
H5	0.2378(11)	0.2287(5)	0.2313(2)	0.2455	0.2084	0.2390

Bond lengths (Å)

O1-H1	1.013(5)	1.003
O1-H2	0.955(3)	1.029
H1…O1	1.768(5)	1.745
O1…O1	2.780(3)	2.748
N1-H3	0.988(6)	1.026
N1-H4	0.973(6)	1.024
N1-H5	1.025(3)	1.026
H3…O1	2.367(7)	2.271
H4…O1	2.335(7)	2.322
H5…O1	2.223(4)	2.148
H2…N1	1.800(3)	1.683

[a]Loveday and Nelmes, 2000.

[b]This work.

The behaviour of the hydrogen bond strength under pressure in AMH is of some interest and has yet to be studied experimentally. In both ice and ammonia, the hydrogen bond is pressure strengthened, leading to an increase of $r_{(O-H)}$, or $r_{(N-H)}$. In ice this continues up to the limit in which the proton is symmetrically located halfway between the heavy atoms, producing the Cu_2O isomorph dubbed ice X (See Chapter 3).

My best estimate of $\partial r_{(O-H)} / \partial P$ in ice VIII, up to 25 GPa, is 0.094 ± 0.003 pm GPa^{-1}. In AMH however, up to 5 GPa, I find that $r_{(O-H1)}$ increases at 0.27 ± 0.02 pm GPa^{-1}, and $r_{(O-H2)}$ increases at 0.85 ± 0.01 pm GPa^{-1} (Figure 6.6). By contrast, the N-H bond length remains constant (i.e., $\partial r/\partial P = 0$) at all pressures up to 5GPa: $r_{(N-H3)}$ = 1.026 ± 0.01 Å, $r_{(N-H4)}$ = 1.023 ± 0.01 Å, and $r_{(N-H5)}$ = 1.025 ± 0.01 Å. Once again, this differs from the work on solid ammonia in which $r_{(N-H)}$ increased by 0.038 ± 0.01 pm GPa^{-1} up to 4 GPa.

A critical test of the simulation would be the direct measurement of the variation in inter-atomic distances as a function of pressure by neutron diffraction, or by inference from spectroscopic data. Koumvakalis (1988) measured the pressure dependence of features in the Raman spectrum of AMH from 3 – 10 GPa. Hence, the phases investigated were higher pressure polymorphs than AMH I. Nevertheless, Koumvakalis (1988) observed no detectable shift of the N-H stretching frequencies (ν_1 and ν_3) of the ammonia molecule, or the weak features assigned to the O-H…O vibrations between water molecules comprising the chains along the *a*-axis. The only stretching vibration affected by pressure was seen to be the O-H stretch assigned to the O-H…N bond. This vibration exhibits a negative pressure dependence, shifting at –31.5 cm^{-1} GPa^{-1}. These observations broadly support my calculations, showing that $r_{(O-H2)}$ increases at the greatest rate, and that $\partial r_{(N-H)} / \partial P \approx 0$.

6.1.4 Structure of NH_4OH

An interesting feature, revealed in Table 6.IV, is the similarity of all of the hydrogen bond lengths in ammonium hydroxide. This represents a significant departure from the structure of AMH wherein the O-H…O, O-H…N, and N-H…O hydrogen bonds are all of greatly differing lengths, and is the result of the OH^- anion being a particularly strong hydrogen bond acceptor (Giguerre 1983).

My determination of the equilibrium O-H bond length for the isolated hydroxide molecule is 0.984Å (done as for the H_2O and NH_3 monomers in Chapter 2), compared with the spectroscopically observed value of 0.96973Å (Amano *et al*., 1984), a difference of ~1.5%, which is in line with the overestimation of the X-H bond lengths of the water and ammonia molecules reported in Chapters 3-5.

Table 6.IV. Cell parameters, atomic coordinates, and bond lengths in ammonium hydroxide at ~ 5 GPa.

Cell parameters	
a (Å)	3.80112
b (Å)	5.70064
c (Å)	7.84538
b/a	1.4997
c/a	2.0640
V (Å^3)	170.000

Fractional atomic coordinates

	x	*y*	*z*
O1	0.11109	0.08134	0.98168
H1	0.28924	0.20608	0.98614
N1	0.37757	0.35231	0.33872
H2	0.35236	0.17760	0.37769
H3	0.58731	0.42664	0.40485
H4	0.16114	0.44800	0.37820
H5	0.43323	0.36829	0.20811

Bond lengths (Å)

O1-H1	0.999
H1…O1	1.736
O1…O1	2.725
N1-H2	1.057
N1-H3	1.063
N1-H4	1.046
N1-H5	1.057
H2…O1	1.690
H3…O1	1.667
H4…O1	1.746
H5…O1	1.699

I also performed calculations to determine the equilibrium geometry of the isolated ammonium monomer (as for OH^-, H_2O and NH_3) and found the N-H bond length, $r_{(N-H)}$ = 1.055Å, and the bond angle, H-$\hat{N}$-H = 109.38°. The bond angle is very close to what one would expect for a molecule with T^D symmetry, i.e., H-$\hat{N}$-H = arcos(-$^1/_3$) = 109.47°. The equilibrium N-H bond length for the gas phase NH_4^+ ion has been measured spectroscopically,

and has also been the subject of numerous *ab initio* simulations. These results yield a best estimate of $r_{(N-H)}$ = 1.0203Å (Demaison *et al*., 2001). My value of $r_{(N-H)}$ exceeds this by over 3% however. It is not clear why the X-H bond length should be overestimated by so much more than for the other molecules investigated.

It might be expected that hydrogen bonding would tend to increase the length of X-H bonds in the solid state. However, in ammonium crystals, with the exception of NH_4F, the evidence for hydrogen bonding is very weak (Brown, 1995). Even in the strongly hydrogen bonded crystals NH_4F(I) and NH_4HF_2 the N-H bond lengths are increased to just 1.025 ± 0.005 Å (Lawson *et al*., 1989) and 1.030 ± 0.002 Å (van Reeuwijk *et al*., 2000), respectively. In the higher density NH_4F(II), the N-H bonds are generally shorter than in NH_4F(I), although $r_{(N2-D5)}$ = 1.068 ± 0.005 Å (Lawson *et al*., 1989). Whilst I will offer evidence in the ensuing subsection for the presence of hydrogen bonding, it appears to have little effect on the X-H bond lengths in ammonium hydroxide.

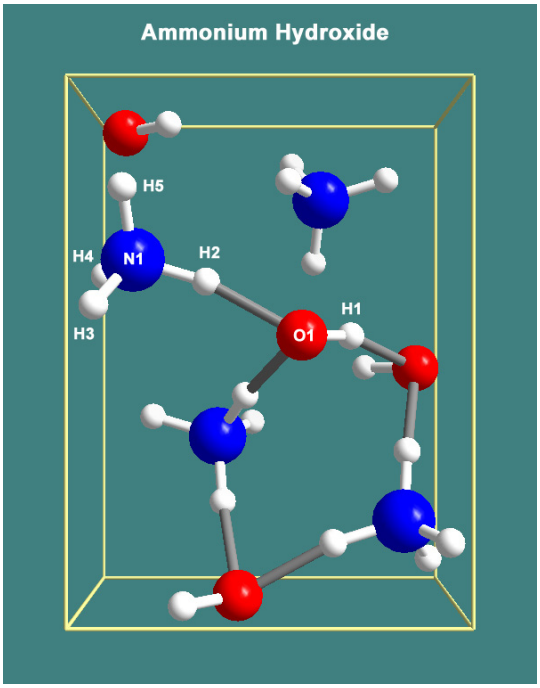

Figure 6.7. The structure of ammonium hydroxide. The designation of atoms in the asymmetric unit is as Table 6.IV.

In NH_4OH, the variation in bond lengths differs from AMH. Within its field of stability, above 5 GPa, $r_{(O-H1)}$ increases at 0.05 pm GPa^{-1}. The N-H bond created upon the formation of ammonium hydroxide increases at a very much reduced rate: $\partial\, r_{(N-H2)} / \partial P$ = 0.005 pm GPa^{-1}. The other N-H bonds all decrease in length at approximately the same rate as each other, -0.05 ± 0.01 pm GPa^{-1}.

Figure 6.4 shows that there is an encouraging agreement between the equations of state of AMH IV and the simulated ionic phase. However, the ammonium hydroxide structure retains all of the symmetry elements of space group $P2_12_12_1$ (Figure. 6.7). Given that the atomic structure of AMH IV is presently unknown, I can confirm that the hydroxide is not AMH IV by simulating the neutron diffraction pattern of ND_4OD. Figure 6.8 (overleaf) shows the measured diffraction pattern of AMH IV, and the calculated pattern of ND_4OD, respectively.

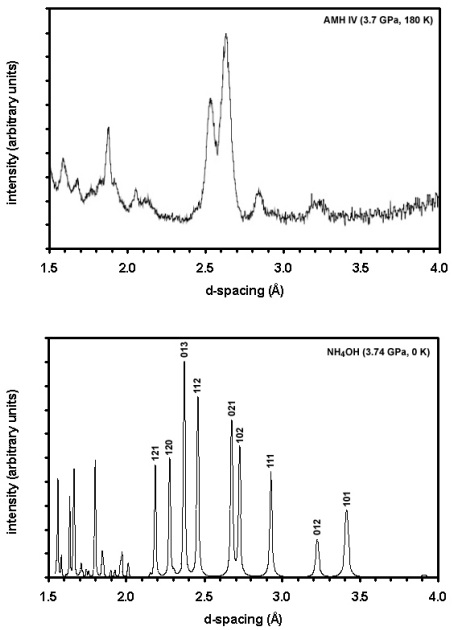

Figure 6.8.

Top, the neutron diffraction pattern of deuterated AMH phase IV (Loveday *et al*., (1998) at 3.7 GPa and 180 K.

Bottom, the calculated diffraction pattern of the ND_4OD structure at 3.74 GPa and 0 K. The {*hkl*} assignments for each peak are indicated.

Clearly, the two patterns are very different. I conclude from this, therefore, that the protolysis reaction in AMH, at least above 130 K, is interrupted by a phase transformation to a denser molecular solid (AMH II or AMH IV). The similarity in the EoS of AMH IV and NH_4OH is coincidental. This does not rule out the existence of an ionic solid at lower temperatures, or at higher pressures, than have been studied experimentally to date.

In addition to structural parameters, the total energy calculations permit me to arrive at some thermodynamic quantities for ammonium hydroxide via the known thermodynamic properties of AMH I, and this is the subject of the following section.

6.1.5 Thermodynamics

The enthalpy of the two phases (Figure. 6.9) is calculated from the respective equations of state (H = U+PV), yielding the transition pressure in the athermal limit as 5.5 ± 0.4 GPa. The calculation of the enthalpy difference between the two phases can also be used to constrain more closely certain thermodynamic quantities that, for ammonium hydroxide, have previously only been estimated. The earliest estimate of the enthalpy of formation, $\Delta_f H$ (NH_4OH,s), appears in Karapet'yanets and Karapet'yanets (1970). However, the value of –326 kJ mol^{-1} does not appear in their referenced source. Johnson (1988) surveyed the thermochemistry of known ammonium salts and used the results to determine the stability of ammonium hydroxide. The thermodynamic quantities quoted by Johnson (1988) are $\Delta_f H$ (NH_4OH,s) = -275 kJ mol^{-1},

and ΔG ($NH_3 \cdot H_2O$,s $\rightarrow$ NH_4OH,s) = 98 kJ mol^{-1}, at 110 K, neglecting the entropy term, $T\Delta S$. Interpolation of the molar volumes of KOH and RbOH yielded an estimated molar volume of 28.40 cm^3 mol^{-1} for NH_4OH. Combined with the estimated free energy change of the protolytic reaction, a transition pressure of ~12 GPa was forecast.

Figure 6.9. Calculated enthalpy of AMH I and NH_4OH.

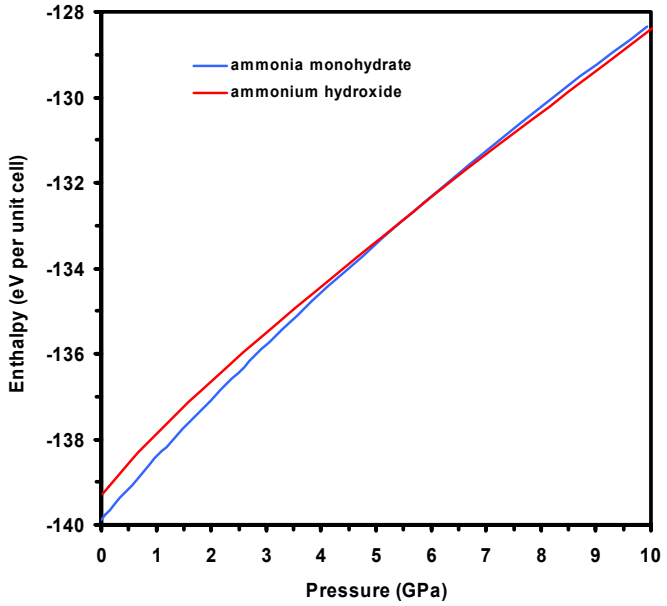

My total energy calculations allow the determination of the relative enthalpy differences between ammonia monohydrate and ammonium hydroxide. Figure 6.9 shows that the protolytic reaction occurs (i.e., the enthalpy change, $\Delta H = 0$) at a pressure of ~5 GPa, and that the enthalpy difference between the two phases at zero pressure is 14.8 ± 0.5 kJ mol^{-1}. The latter figure corresponds to ΔH for the reaction $NH_3 \cdot H_2O$,s $\rightarrow$ NH_4OH,s at zero Kelvin. It is then straightforward to calculate $\Delta_f H|$ (NH_4OH,s) using existing thermodynamic data for AMH. From Hildenbrand and Giauque (1953), $\Delta_f H|$ ($NH_3 \cdot H_2O$,l) = -361.8 kJ mol^{-1}. The change in enthalpy from 298 K to 0 K, $H|_{298} - H|_0$, is found from the measured heat capacity and added to the heat of fusion (6560.5 J mol^{-1}) to give $\Delta_f H|$ ($NH_3 \cdot H_2O$,s) = -391.8 kJ mol^{-1} at zero Kelvin. Combining this with the calculated reaction enthalpy gives $\Delta_f H|$ (NH_4OH,s) = -376 kJ mol^{-1}. The enthalpy of formation at 298K may now be estimated by assuming that the heat capacities of the solid monohydrate and hydroxide are the same, yielding $\Delta_f H|$ (NH_4OH,s) = -356 kJ mol^{-1}. There are two significant corollaries to this result.

The first arises from the difference between my results and those of Johnson (1988), and so it is necessary to evaluate the sources of error noted in the earlier work. Most important of all is the neglect of lattice stabilisation due to lowered cation symmetry (SLCS) (Johnson, 1988, 2000):

$$\text{SLCS} \approx E_a = 142 - \frac{1}{n}\{\Delta_f H^{\ominus}[(NH_4)_nX,c] - \Delta_f H^{\ominus}(Rb_nX,c)\} \text{ kJ mol}^{-1} \quad (6.1)$$

where E_a is the activation energy barrier to reorientation of the ammonium ion.

Johnson (1988) predicted that the departure from sphericity of the NH_4^+ ion, and resulting cation-anion hydrogen bonding, should stabilise the lattice energy by ~50 kJ mol^{-1}. However, in estimating $\Delta_f H^{\ominus}(NH_4OH,s)$, Johnson (1988) assumed a value of zero for SLCS. Applying the simple ionic model (Eq 6.1), my value of $\Delta_f H^{\ominus} = -356$ kJ mol^{-1} gives a stabilisation energy of ~84 kJ mol^{-1}, which is rather large but agrees with the expectation that ammonium hydroxide is very strongly hydrogen bonded. Moreover, the ionic model allows us to predict that 84 kJ mol^{-1} is a likely upper limit for the energy barrier to cation reorientation (E_a) in solid ammonium hydroxide: By comparison with other materials in which the ammonium ion is strongly hydrogen bonded (i.e., aqueous NH_4^+, and NH_4F), I can predict that the energy barrier is almost certainly much smaller, perhaps by as much as 50% (Johnson, 2000). This appears to be the result of a different rotation mechanism (carousel rotation of the NH_4^+ ion about the C_3 axis, as opposed rotation about an S_4 axis) to that seen in other ammonium salts (Alavi *et al*., 1999: Johnson, 2000). This mechanism, in which the axial N-H bond length in the transition state increases, has the implication that the ammonium ion might return its axial proton to the neighbouring OH^- ion, reversing the protolysis to yield AMH (Alavi *et al*., 1999). The height of the energy barrier could be experimentally determined by nuclear magnetic resonance (NMR) spectroscopy.

The second major corollary to our calculation of the reaction enthalpy is the determination of the lattice potential energy (U_{POT}), and the enthalpy of solution ($\Delta_{soln}H^{\ominus}$), of ammonium hydroxide. There are two ways to find U_{POT}. Firstly, one can construct a conventional Born-Fajans-Haber cycle (Figure 6.10) using the known enthalpy of formation of the salt in question. Or, secondly, one can use a volume-based empirical formula to calculate the lattice enthalpy.

Table 6.V Thermodynamic quantities pertinent to Figure 6.10.

$\Delta_f H\|\ [NH_3(g)]^a$	-45.94
$\Delta_f H\|\ [H_2O(l)]^a$	-285.83
$\Delta_{soln} H\|\ [NH_3(g)]^a$	-30.50
$\Delta_{hyd} H\|\ [NH_4^+(g)] + \Delta_{hyd} H\|\ [OH^-(g)]^b$	-852.07

[a] CRC Handbook of Chemistry and Physics (2001).

[b] Jenkins (1993).

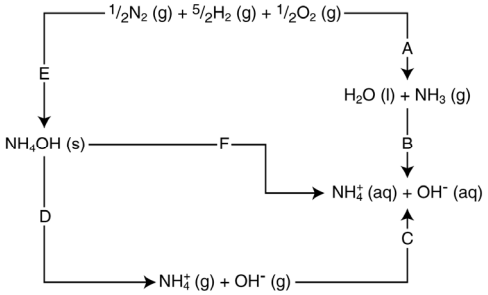

Figure 6.10.
Born-Fajans-Haber cycle for NH^4OH.
Path A = $\Delta_f H\|\ (H_2O,l) + \Delta_f H\|\ (NH_3,g)$
Path B = $\Delta_{soln} H\|\ (NH_3,g)$
Path C = $\Delta_{hyd} H\|\ (NH_4^+,g) + \Delta_{hyd} H\|\ (OH^-,g)$
Path D = $\Delta_L H\|\ (NH_4OH,s) = U_{pot} + {}^3/_2RT$
Path E = $\Delta_f H\|\ (NH_4OH,s)$
Path F = $\Delta_{soln} H\|\ (NH_4OH,s)$

Using the values in Table 6.V, along with the calculated enthalpy of formation, gives a true lattice potential energy (U_{POT}^{true}) of 842 kJ mol^{-1}, and $\Delta_{soln} H\|$ = 6.3 kJ mol^{-1}. A generalized empirical formula, such as Bartlett-Jenkins' relation, is typically used when the formation enthalpy is unknown. It is instructive to use it here because we may estimate the hydrogen bond enthalpy in NH_4OH. This relation is derived from molecular volumes for non-hydrogen-bonded salts, and we would expect the lattice potential to be larger in hydrogen-bonded systems due to the additional bond energy. Indeed, large differences between U_{POT}^{true} and U_{POT} as calculated from equation 6.2 for NH_4F and NH_4SH are attributable to hydrogen bonding. The lattice potential of MX (1:1) salts is given as;

$$U_{POT} = 2I\left(\frac{\alpha}{\sqrt[3]{V}} + \beta\right) \text{ kJ mol}^{-1} \qquad (6.2)$$

where α = 117.3 kJ mol^{-1} nm and β = 51.9 kJ mol^{-1} and I is the ionic strength ($I = \sum n_k z_k^2$, where n_k is the number of ions of charge z_k in the formula unit) (Jenkins *et al*., 1993). V (nm^3) is the volume per formula unit of the salt. Using the molecular volume for ammonium

hydroxide calculated here (0.0529 nm^3) yields U_{POT} = 728.75 kJ mol^{-1}. This differs from U_{POT}^{true} by 113 kJ mol^{-1}. The structure of ammonium hydroxide is that of an NH_4^+ ion tetrahedrally coordinated, donating four hydrogen bonds to it's nearest neighbour OH^- ions (Figure 6.7). The OH^- ions donate and receive one hydrogen bond to / from their neighbouring anions as well as accepting four weaker hydrogen bonds from surrounding cations. Hence there are five hydrogen bonds per molecule, suggesting that the average hydrogen bond enthalpy in ammonium hydroxide is ~113/5 ≈ 22.6 kJ mol^{-1}. The energy of the average hydrogen bond in AMH is (1/5) [$\Delta_f H|\ NH_3{\cdot}H_2O,s - \{\Delta_f H|\ H_2O,g + \Delta_f H|\ NH_3,g\}$] ≈ 13.5 kJ mol^{-1}. The increased electrostatic interactions in the ionic solid help to explain why the hydrogen bond in ammonium hydroxide is stronger.

6.1.6 Summary

I have performed the first *ab initio* pseudopotential plane-wave calculations on the ambient pressure monohydrate of ammonia and found excellent agreement with the experimental structure and equation of state. Significant differences in the pressure dependence of covalent O-H and N-H bond lengths from ice VIII and solid ammonia are seen. The simulated structure spontaneously transforms to an ionic solid (NH_4OH) at ~5 GPa, which, in spite of similarities in the EOS, appears not to be related to the high-pressure molecular phase IV of AMH. Nevertheless, NH_4OH could be stable at temperatures below 100 K.

The enthalpy difference between AMH I and ammonium hydroxide at zero Kelvin is ~15 kJ mol^{-1}, and this figure is used to derive an estimate of the heat of formation of ammonium hydroxide at 298 K of -356 kJ mol^{-1}. This value is consistent with current models describing the energy barrier to cation rotation, and the expected contribution of hydrogen bond enthalpy to the conventional electrostatic lattice enthalpy.

6.2 Ammonia Hemihydrate ($2NH_3{\cdot}H_2O$)

In contrast with AMH, AHH is the least straightforward of the ammonia hydrates to simulate. It has the largest unit cell (44 atoms) which, when combined with the large cut-off energy required to achieve convergence, makes it computationally expensive to do calculations upon. Moreover, the structure exhibits a rotational disorder of one of the symmetry inequivalent NH_3 molecules, a disorder which freezes out at ~ 60 K, resulting in a doubling of

the *a*- and *b*- cell edges. Proper simulation of the low-temperature ordered cell therefore requires the use of a 2x2x1 supercell (176 atoms), and there is no justification for doing fully converged calculations on such a large cell in the context of this work. Given its limited relevance to planetary science, AHH was not investigated as thoroughly as the other hydrates, and is discussed only briefly.

The hemihydrate melts congruently at 194.32 K, and the calorimetric data of Hildenbrand and Giauque (1953) indicates a phase transition at 50-55 K which has since been shown to be an order-disorder transition (Loveday *et al*., 1999b). The structure of the hemihydrate was determined by X-ray diffraction (Siemons and Templeton 1954) to be orthorhombic (space group P*bnm*) with $a = b = 8.41 \pm 0.03$ Å and $c = 5.33 \pm 0.02$ Å at 178 ± 10 K. More recent neutron diffraction work (Loveday and Nelmes 2000) has refined the lattice parameters: $a = 8.3220$ Å, $b = 8.3526$ Å, $c = 5.2799$ Å at 110 K. Detailed neutron diffraction patterns through the order-disorder transition indicate a doubling of the *a*- and *b*- axes and a slight monoclinic distortion (Loveday *et al*., 1999b). Structural changes under pressure are hinted at in preliminary neutron diffraction patterns (Loveday and Nelmes 1999b)

6.2.1 Computational Details

The neutron diffraction derived structure of AHH, from which the simulations were begun, is orthorhombic (space group P*bnm*), at ambient pressure, and contains four molecules per unit cell (Loveday and Nelmes 2000). The structure (Figure. 6.11) consists of moderately strong hydrogen-bonded crankshafts of alternating water and ammonia molecules extending along the *b*-axis, cross-linked by weak hydrogen-bonds. The packing of the crankshafts forms channels along the *c*-axis, within which the N2 ammonia molecules are sited. Above ~60 K the N2 ammonia molecules are disordered over two orientations, but appear to become ordered below this temperature. The transition to the low temperature phase is manifested by a heat capacity anomaly (Hildenbrand and Giauque, 1953), and by the appearance of peak splittings and superlattice reflections in the diffraction pattern (Loveday *et al*., 1999b). The onset of the changes in the neutron diffraction pattern commence at ~110 K, well above the temperature of the heat capacity anomaly. The low temperature pattern (30 K) has been indexed with a monoclinic unit cell whose *a*- and *b*- axes are double those of the disordered cell and $\gamma = 90.22°$ (Loveday *et al*., 1999b).

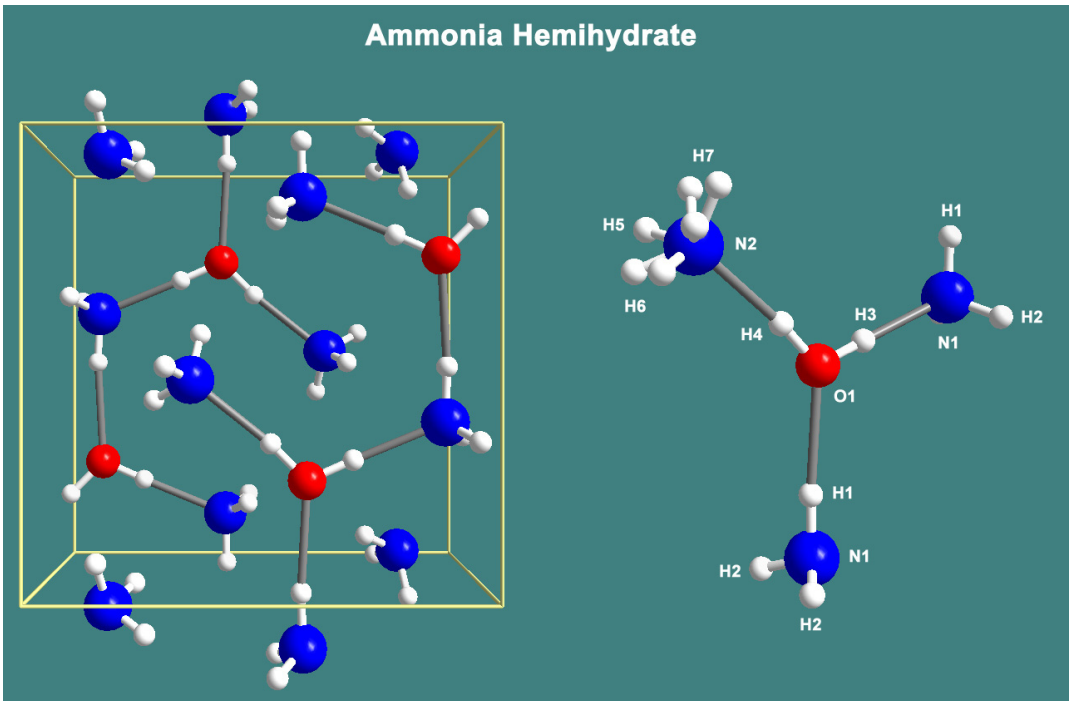

Figure 6.11. Left; the unit cell viewed along the *c*-axis, with the *b*-axis vertical. Right; the designation of the atoms in the asymmetric unit, as given in Table 6.VIII.

Lattice parameters and internal coordinates of the disordered structure are given in Table 6.VIII. The fractional coordinates in Table 6.VIII were the starting point for the structural relaxations. The disorder of the N2 ammonia molecule was essentially ignored, this being fixed into one of the two orientations such that the H5 atoms of one molecule pointed midway between the H6 and H7 atoms of its nearest neighbour (e.g., the two NH_3 molecules in the centre of the structural representation on the left of Figure 6.11).

For a single unit cell, with the disordered ammonia molecules frozen into predefined orientations, fully converged static calculations were possible. Total energy convergence tests were carried out to optimise the sampling of the Brillouin zone and the cut-off of the plane-wave basis set. It was found that a grid with 8 symmetrically unique $\vec{k}$-points in the IBZ, combined with E_{cut} = 1000 eV, yielded total energy convergence to better than 10^{-4} eV per unit cell.

6.2.2 Equation of State

Structural relaxations were carried out at fixed cell volumes from 230 Å^3 (34.63 cm^3 mol^{-1}) to 400 Å^3 (60.22 cm^3 mol^{-1}). These revealed a discontinuity at ~ 270 Å^3 (40.65 cm^3 mol^{-1}) in the slope of the total energy curve (Figure. 6.12), and the pressure (Figure. 6.13), indicative of a

first order phase transition. Examination of the fractional atomic coordinates showed that the molecular AHH structure had become a partially ionic solid, transforming via a solid-state protolytic reaction to ammonium hydroxide ammoniate ($NH_4OH{\cdot}NH_3$). This is the first time that this structure has been observed. Subsequently, I was able to relax the ionic structure at volumes within the field of stability of AHH. An integrated form of the third order Birch-Murnaghan equation of state (BMEOS3), and of the fourth order logarithmic equation of state (LNEOS4) were fitted to the E(V) data for the molecular and ionic phases (Figure. 6.13), and the EoS parameters appear in Table 6.VI.

Figure 6.12. Calculated E(V) curves for AHH and ammonium hydroxide ammoniate.

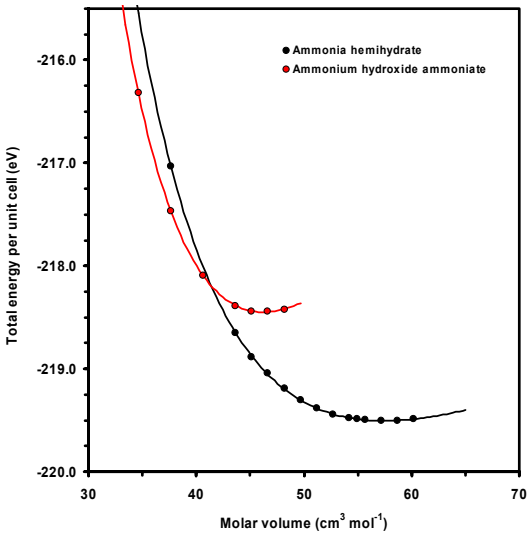

Figure 6.13. Calculated EoS for AHH (black line) and $NH_4OH{\cdot}NH_3$ (red line) from the E(V) results.

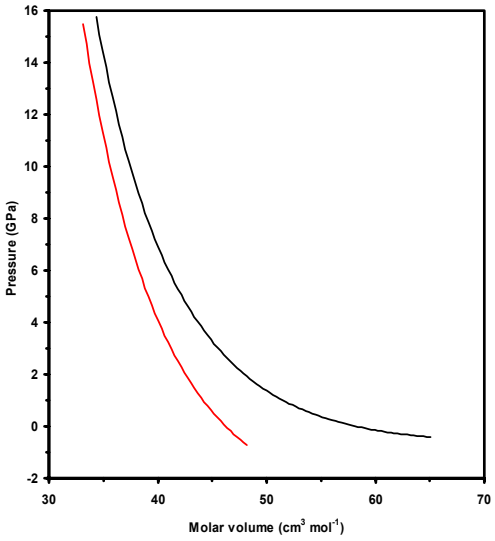

Table 6.VI. Calculated EoS parameters of AHH.

	V_0 ($cm^3\ mol^{-1}$)	K_0 (GPa)	K'_0	K''_0 (GPa^{-1})	E_0 ($eV\ molecule^{-1}$)
BMEOS3: E(V) fit	57.6 ± 0.3	6.5 ± 0.6	5.9 ± 0.4	···	-54.877 ± 0.001
LNEOS4: E(V) fit	57.6 ± 0.3	6.5 ± 0.4	5.8 ± 0.1	-0.40 ± 0.56	-54.877 ± 0.001

The measured molar volume of AHH at 130K (at ambient pressure) is 55.882 ± 0.003 $cm^3\ mol^{-1}$ (Loveday and Nelmes 2000). The calculated molar volume is thus too large by + 3.0%. This is comparable to the over-inflation of the unit cell observed in calculations on ammonia I (see

5.2.1.1). Croft *et al*. (1988) estimated the molar volume of AHH at zero Kelvin to be 55.613 ± 0.588 cm^3 mol^{-1}, indicating that my athermal unit cell is too large by approximately + 3.5%. These results are still very good, however, since the material is sufficiently soft that a pressure of ~ 2.5 kbar will bring the calculated and experimental volumes into agreement.

The incompressibility of AHH is almost indistinguishable from that of ammonia I, which is surprising; the inclusion of stronger O-H…N hydrogen bonds in AHH, as opposed to all N-H…N bonds in ammonia, should make a detectable contribution to the bulk modulus of the crystal. Although it is not at all clear why, this discrepancy may be the result of the need to use a larger supercell for simulating the disordered phase of AHH correctly.

Table 6.VII shows that the novel partially ionic phase, $NH_4OH{\cdot}NH_3$, is much stiffer than AHH. The plot of the enthalpy of AHH and $NH_4OH{\cdot}NH_3$ (Figure 6.14) places the phase transition at 12.5 ± 0.5 GPa.

Table 6.VII. Calculated EoS parameters of $NH_4OH{\cdot}NH_3$.

	V_0 (cm^3 mol^{-1})	K_0 (GPa)	K'_0	K''_0 (GPa^{-1})	E_0 (eV $molecule^{-1}$)
BMEOS3: E(V) fit	46.2 ± 0.1	19.4 ± 0.5	5.2 ± 0.2	···	-54.6124 ± 0.0004
LNEOS4: E(V) fit	46.2 ± 0.1	19.1 ± 0.4	5.8 ± 0.0	-0.70 ± 0.10	-54.6123 ± 0.0004

Figure 6.14. Enthalpy of AHH and $NH_4OH{\cdot}NH_3$ as a function of pressure close to the phase transition.

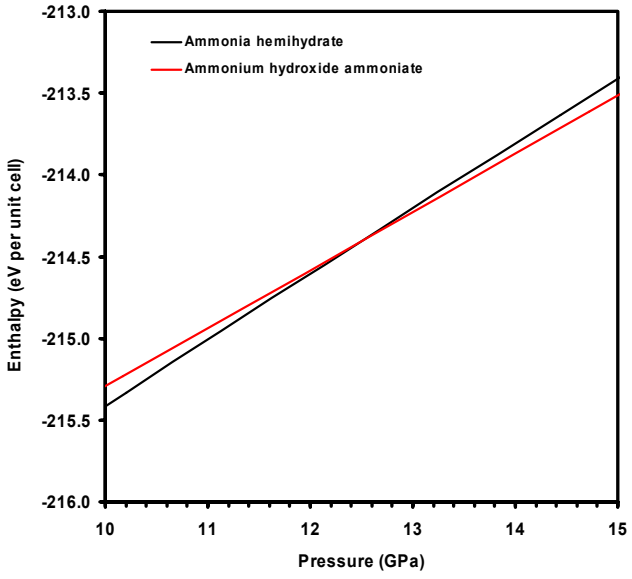

Table 6.VIII. Cell parameters, atomic coordinates, and bond lengths in AHH at ~ 0 GPa.

	Experimental values[a]	Calculated values[b]
a (Å)	8.3220(3)	8.3111
b (Å)	8.3526(3)	8.2884
c (Å)	5.2799(2)	5.5164
b/a	1.00368(7)	0.9973
c/a	0.63445(4)	0.6637
V (Å^3)	367.008(40)	380.000

Fractional atomic coordinates

	x	*y*	*z*	*x*	*y*	*z*
N1	0.4089(4)	0.1280(4)	0.2500	0.3999	0.1239	0.2501
H1	0.4124(5)	0.0057(4)	0.2500	0.4061	-0.0004	0.2461
H2	0.4661(3)	0.1656(4)	0.4065(6)	0.4569	0.1645	0.3967
O1	0.1015(7)	0.2572(6)	0.2500	0.0952	0.2550	0.1944
H3	0.2037(6)	0.2119(5)	0.2500	0.2041	0.2041	0.2268
H4	0.0198(5)	0.1757(5)	0.2500	0.0099	0.1720	0.2327
N2	0.8415(4)	0.0345(5)	0.2500	0.8463	0.0371	0.2769
H5	0.7941(11)	0.0043(7)	0.4196(17)	0.8060	-0.0042	0.4132
H6	0.7543(9)	0.0825(9)	0.1484(13)	0.7526	0.0965	0.1579
H7	0.8608(8)	-0.0695(10)	0.1558(11)	0.8708	-0.0616	0.1829

Bond lengths (Å)

O1-H3	0.931(5)	1.014
O1-H4	0.962(6)	1.011
H3…N1	1.846(5)	1.763
H4…N2	1.895(5)	1.777
N1-H1	1.022(3)	1.031
N1-H2	1.004(3)	1.029
H1…O1	2.079(6)	2.047
H2…O1	2.230(4)	2.077
N2-H5	1.011(9)	1.022
N2-H6	0.988(7)	1.024
N2-H7	1.014(7)	1.025
O1…N1	2.777(6)	2.773
O1…N2	2.852(7)	2.784

[a]Loveday and Nelmes (2000), 0 GPa, 130 K.
[b]This work, 0 GPa, 0 K.

6.2.3 Structure of AHH

The calculated structure of AHH at ~ 0 GPa is compared quantitatively with the experimental structure in Table 6.VIII, on the preceding page. The cell shape, atomic fractional coordinates, and bond lengths agree reasonably well. Noteworthy differences include the *z*-coordinate of those atoms originally placed on $z = ¼$. In particular, the water molecule (O1, H3, and H4) has drifted significantly from $z = ¼$. This is probably the result of the lowered symmetry of the unit cell due to fixing the N2 ammonia molecules into specific orientations.

In all cases, the covalent X-H bonds are longer, and the H…X hydrogen bonds shorter than in the experimental structure. The pattern of bond lengths is closely similar to that in AMH I (Table 6.III) and ADH I (Table 7.II). Once more, I find that the N-H bond lengths of the ammonia molecule cited in the *c*-axis channels (N2-H5, N2-H6, and N2-H7) cluster around similar values (~ 1.024Å), at odds with the spread of values resulting from the refinement of neutron diffraction data.

The protolysis reaction at ~ 12.5 GPa involves the transfer of the H4 atom from the O1 water molecule to the N2 ammonia molecule. This yields a structure consisting of an ammonium ion (N2, H4, H5, H6, and H7), a hydroxide ion (O1, and H3), and an ammonia molecule (N1, H1, and H2), that is $NH_4OH{\cdot}NH_3$ (ammonium hydroxide ammoniate).

6.2.4 Summary

I have performed the first *ab initio* pseudopotential plane-wave calculations on the ambient pressure hemihydrate of ammonia. As expected, based on the simulation of ammonia I, the unit cell is overinflated by ~ 3.5% at zero pressure. The bulk modulus appears to be anomalously soft, essentially the same as pure ammonia I. It is likely that a larger supercell is needed to correctly reproduce the elasticity of AHH. However, experimental equation of state studies are necessary to establish the incompressibility of AHH.

As in AMH I, a protolysis reaction occurs (at ~ 12.5 GPa), yielding a monoammoniate of ammonium hydroxide.

CHAPTER SEVEN

COMPUTER SIMULATION OF AMMONIA DIHYDRATE

7 Introduction

Of the 'rock-forming' minerals that are expected to comprise the mantles of icy moons in the outer solar system, ammonia dihydrate (ADH), $NH_3 \cdot 2H_2O$, is perhaps one of the least well understood.

I present here the results of my initial investigation of the low-pressure phase of ADH (ADH I) using first principles simulation. In the subsequent chapter, I will present results of two experimental studies carried out using time-of-flight neutron diffraction.

In Sec. 7.1.1. I commence with a description of the time and space-averaged structure of ADH I as obtained from literature X-ray and neutron diffraction experiments. I will then describe the rules governing the orientation of water molecules within this structure, and hence derive a set of ordered and disordered cells which reflect the instantaneous local structure of ADH I. This is followed in Sec. 7.1.2. by a brief description of the computational method employed in the simulation of these cells, and Sec. 7.2. describes my results. The results include a comparison of the total energies of the ordered structures and the fitting of an equation of state (EoS) to the calculated energy of the ordered cells as a function of molar volume. In Sec. 7.3. I will discuss the possible implications of these results for the structure and ordering of ADH I throughout its pressure-temperature stability field (0-176.16 K, 0-0.5 GPa), and compare these predictions with the available experimental evidence.

7.1 Dealing with disorder

7.1.1 Structure and ordering

The structure of ADH I observed in X-ray diffraction (Bertie and Shehata 1984) and neutron diffraction (Loveday and Nelmes 2000) experiments is cubic, space group $P2_13$ (with Z = 4). The three-fold site symmetry of the water molecule rules out an ordered structure under this space group, and so the water molecules in ADH I must be orientationally disordered. This disorder is represented crystallographically by partially occupied hydrogen sites. The lattice parameters and internal coordinates of the disordered cubic structure are presented in Table 7.I. ADH I transforms to a denser polymorph, ADH II, of unknown structure at 0.3 – 0.5 GPa (Hogenboom *et al*., 1997: Loveday and Nelmes 1999b).

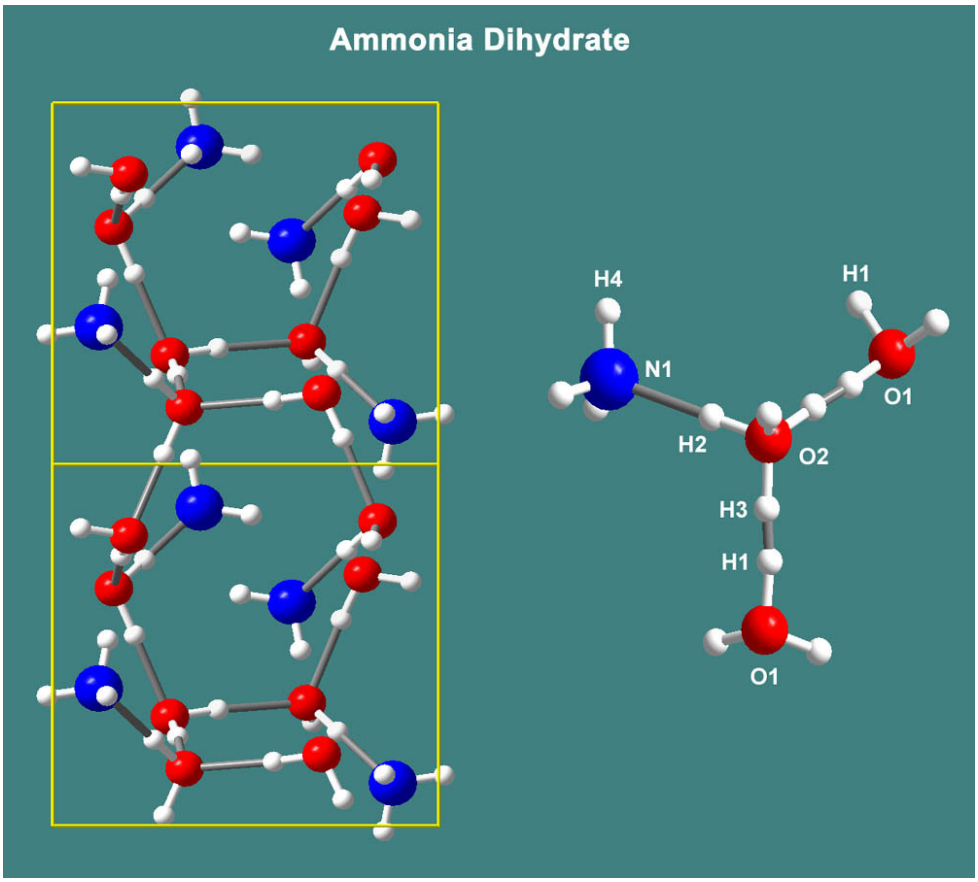

Figure 7.1. The atomic framework in ADH I. Blue ammonia molecules occupy the channels formed by the strongly bound water molecules (red). The structure bears a superficial similarity to the APC zeolite topology.

Figure 7.2. The arrangement of partially occupied hydrogen sites along a section of hydrogen-bonded crankshaft in ADH I. The designation of the atoms in the asymmetric unit refers to the atomic labels in Table 7.I.

The zeolite-like heavy atom structure of ADH I (Fig. 7.1) is dominated by a strongly hydrogen bonded framework of water molecules which has broad channels along the *a*-, *b*-, and *c*-axes. Ammonia molecules are sited in these channels. The ice framework consists of two types of oxygen site (Fig. 7.2). The first, O1, is hydrogen bonded to three neighbouring O2 sites. There are three hydrogen sites (H1) around each O1, over which the two hydrogen atoms covalently bound to O1 are disordered. Thus, these hydrogen sites are 2/3 occupied. The oxygen atoms on the O2 sites are hydrogen bonded to three O1 atoms and to one ammonia molecule. Four hydrogen sites surround O2. The site along the O-N vector (H2) is always occupied. The remaining hydrogen atom is then disordered over the other three possible sites. Hence, these sites (H3) are 1/3 occupied.

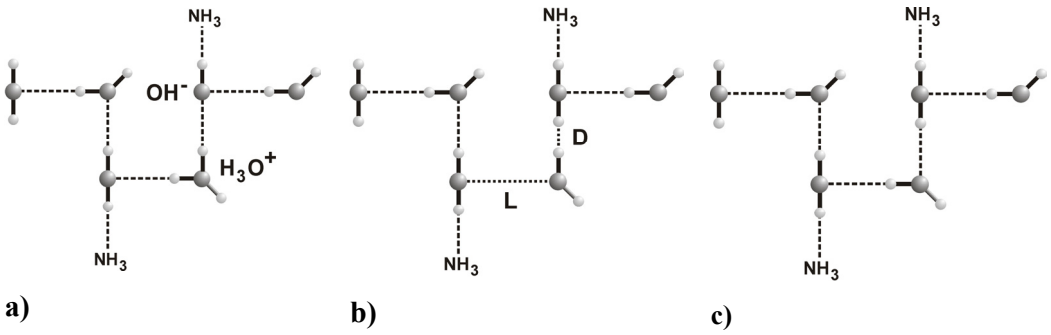

Figure 7.3. a) Cartoon representation of the crankshaft depicted in Figure 7.2 after the introduction of an ionic defect (H_3O^+ and OH^-), thus breaking the ice rules: b) as before but with a Bjerrum defect pair (L and D, described in the text) introduced: c) and with a neatly ordered arrangement of water molecules, obeying the ice rules.

However, this picture only describes the time and space-averaged structure of ADH I. On a local scale, one would expect that the molecular orientations will obey the ice rules proposed by Bernal and Fowler (1933). These rules stipulate the following:

1. Each oxygen atom is bound to two hydrogen atoms by covalent O-H bonds approximately 0.97Å long. In other words, water molecules are preserved in the solid state as distinct structural units.

2. These hydrogen atoms lie more or less along the vectors between neighbouring oxygen atoms, but there can only be one such hydrogen atom between a given pair of oxygen atoms.

Thermally activated reorientation of the water molecule (and hence ordering) can only occur if the ice rules are broken, which in turn requires point defects in the structure (e.g., Gränicher 1958). The first rule is broken at ionic defects. These are the result of proton transfer along a hydrogen bond, yielding neighbouring H_3O^+ and OH^- ions (Fig. 7.3.a). The second rule is broken at rotational defects, known as Bjerrum defects; these are of two varieties (Fig. 7.3.b); L-type defects, in which there are no hydrogen atoms between neighbouring oxygen atoms, and D-type defects where there are two hydrogen atoms between neighbouring oxygen atoms (Bjerrum 1951, 1952). Although molecular dynamics simulations (Podeszwa and Buch 1999) reveal the nature of orientational defects to be rather more complex, I will hold to the simple picture presented by Bjerrum (1951, 1952).

Table 7.I. Structural parameters for the cubic disordered unit cell of ADH I (Loveday and Nelmes 2000) at zero pressure, 150 K.

Space group $P2_13$					
a (Å)	7.1272(8)				
V (Å^3)	362.04(12)				
Fractional atomic coordinates					
	Wyckoff position	Occupancy	*x*	*y*	*z*
O1	4*a*	1	0.69702(30)	0.69702(30)	0.69702(30)
H1	12*b*	2/3	0.75253(51)	0.67696(54)	0.57222(58)
O2	4*a*	1	0.15812(35)	0.15812(35)	0.15812(35)
H2	12*b*	1	0.23785(33)	0.23785(33)	0.23785(33)
H3	12*b*	1/3	0.0282(14)	0.21182(99)	0.17317(107)
N1	4*a*	1	0.38105(30)	0.38105(30)	0.38105(30)
H4	12*b*	1	0.35783(34)	0.35963(35)	0.51403(55)
Bond lengths (Å)					
O1-H1	0.984(5)		H1…O2	1.766(5)	
O2-H2	0.984(3)		H2…N1	1.768(3)	
O2-H3	1.008(10)		H3…O1	1.74(1)	
N1-H4	0.974(5)		H4…O1	2.395(5)	
O1…O2	2.747(3)		O2…N1	2.752(3)	

It is to be expected that the instantaneous local structure in the dynamically disordered ADH I cell will be as depicted in Figure 7.3.c, which obeys the ice rules and which lowers the local symmetry from cubic. This explains the observation of a splitting in the $\nu_3(NH_3)$ branch in the infrared spectrum that is forbidden under cubic symmetry (Bertie and Shehata 1984). Infrared spectroscopy samples length scales of the order of a few unit cells, and will therefore 'sense' the lower local symmetry of an ADH structure that is constrained by the ice rules. There will be some temperature dependent density of ionic defects and Bjerrum defects in the structure. These allow for reorientation and thus for the exhibition of disorder over greater temporal and spatial scales. Neutron diffraction, for example, samples length scales of order 10^3Å (based on the width of the observed Bragg peaks).

Since no experimental evidence for superlattices in ADH has been reported, I confine my discussion here to unit cells that are dimensionally equivalent to the disordered cubic cell. Working with this cell and applying the constraints of the ice rules one finds that there are only nine possible unit cells (variants A to I: Fig 4), which differ in the orientation of their water molecules. Six of these nine cells (variants A to F) retain only a single 2_1-rotation axis (i.e., they belong to the monoclinic symmetry class 2), whilst the remaining three cells (variants G, H, and I) possess three orthogonal 2_1 axes (orthorhombic class 222), losing only the triad axes of the cubic cell (class 23).

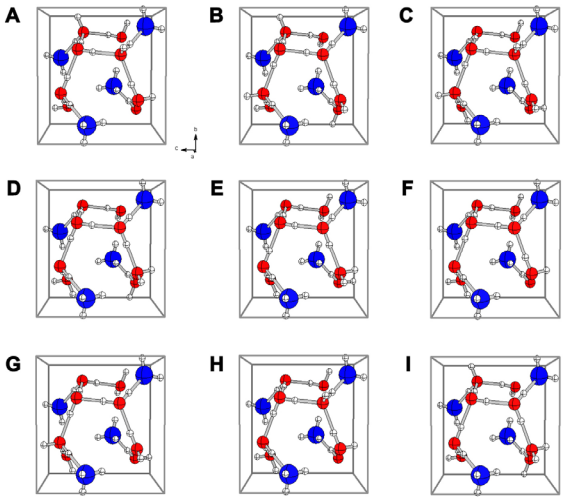

Figure 7.4.

Variants A to I are the nine possible permutations of the water molecules in the ADH unit cell which are allowed by the ice rules. Variants A to F have only a single 2_1 rotation axis. Variants G, H and I have three orthogonal 2_1 axes.

Breaking the ice rules (i.e., by introducing point defects) typically reduces the symmetry of the cell to triclinic, though there are some very unlikely configurations (e.g., with all of the O1 atoms as H_3O^+ and all of the O2 atoms as OH^-) which preserve the symmetry elements of cubic class 23.

The six monoclinic cells all turn out to be identical to one another, as do the three orthorhombic cells; for example, the first cell in Fig. 7.4 (variant A), may be transformed into

variant B by a 120° rotation around one of the missing 3-fold axes. A further 120° rotation about the other missing 3-fold axis yields variant C, and performing the operation of the absent 2_1 axes then yields variants D to F. The same is true of the three orthorhombic cells, which are related to one another by the missing 3-fold axis of the parent cubic cell. There are then, not nine, but only two unique arrangements of the hydrogen atoms in ADH I which satisfy the ice rules. In the monoclinic cell the ordering is rather untidy (the distance between the hydrogen atoms of neighbouring water molecules is not maximised) and the dipole moments of the water molecules do not cancel out, leaving a moment of ~ 6.7×10^{-30} Cm per formula unit along the 2_1-axis, i.e., the crystal is ferroelectric. In the orthorhombic cell the ordering is much neater, maximising the distance between the hydrogen atoms of neighbouring water molecules, and the water molecules are arranged such that their dipole moments cancel each other out, giving an antiferroelectric crystal.

It is important to note that the ordered variants can twin, *whilst preserving the ice rules*, on a number of planes (e.g., on the (100), or (020) planes), although the number of permutations is larger for the orthorhombic variants by virtue of the higher symmetry. The twinning operations correspond to the lost 3-fold axes of the cubic space group; the effect of such twinning will be to produce a composite crystal which might contain, for example, all three of the orthorhombic orientational variants shown in Figure 4 G - I.

In section IV I will report the results of *ab initio* simulations on the two cells that obey the ice rules, but begin first by outlining the computational details.

7.1.2 Computational method

Static DFT calculations (as described in Chapter 2) of the total energy of the ADH I structure were carried out to determine the equation of state (EoS). Table 7.I provides the starting conditions, cell parameter and fractional atomic coordinates, from which the structural relaxations were begun.

Total-energy convergence tests were done to optimise the sampling of the Brillouin zone, and the cut-off of the plane-wave basis set. It was found that a 4x4x4 grid of $\vec{k}$-points, combined with a kinetic energy cut-off of 1100 eV, yielded total energy convergence to better than 10^{-4} eV per unit cell. A series of fixed volume calculations were then performed in which the ions were allowed to move according to the calculated Hellman-Feynman forces. For each volume specified the structure was relaxed in order to optimise the lattice parameters and internal coordinates.

7.2 Results

7.2.1 Equation of State

Structural relaxations were carried out on both the monoclinic and orthorhombic cells at a series of fixed volumes from 42-56 cm^3 mol^{-1} (approximately -1 to 5 GPa). The relaxed cell dimensions and fractional atomic coordinates of the proposed ordered orthorhombic and monoclinic cells (with the volume constrained to be the same as for the neutron-derived cubic cell) are given in Tables 7.IV and 7.V respectively.

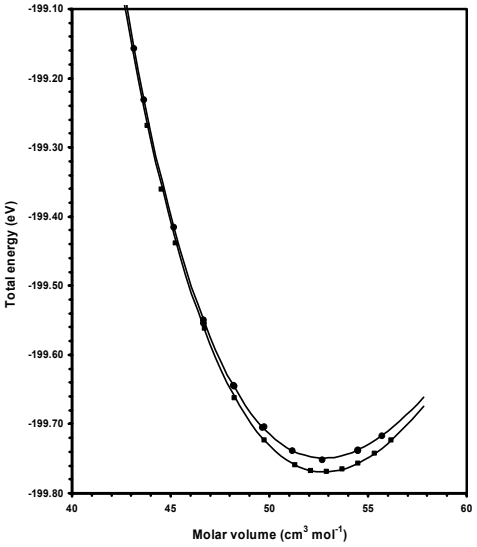

Figure 7.5.

Total energy per unit cell as a function of molar volume, E(V), for the monoclinic ferroelectric cell (filled circles) and the orthorhombic antiferroelectric cell (filled squares). The solid lines are fourth order logarithmic equations of state.

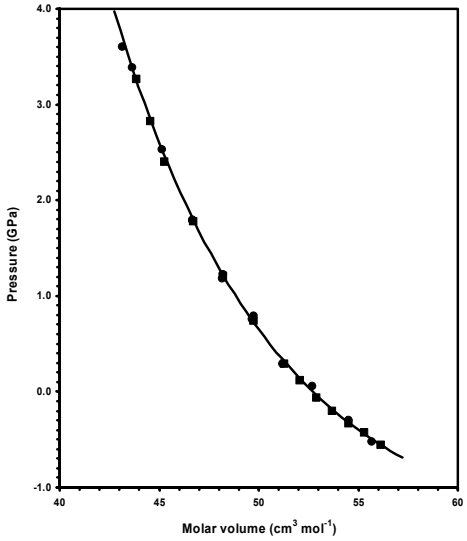

Figure 7.6.

The calculated external pressure as a function of molar volume, P(V), for the monoclinic cell (filled circles) and the orthorhombic cell (filled squares). The solid line is fourth order logarithmic equations of state fitted to the calculated total energy.

The first point of note is that the energies of the monoclinic and orthorhombic cells are not quite the same (see Fig. 7.5 and Tables 5.IV and 5.V). At zero pressure, there is an extremely small energy difference of 5 meV per formula unit (~0.5 kJ mol^{-1}), with the antiferroelectrically ordered orthorhombic cell just being the more energetically favourable. Therefore, all else

being equal, the water molecules in ADH I will prefer any one of the three energetically degenerate variants G, H, or I (Fig. 7.4). I wished to discover if the monoclinic cell was stabilised relative to the orthorhombic cell under pressure, but the energy-volume, E(V), data (Fig. 7.5) show that that the monoclinic cell is energetically disfavoured under all compressions simulated.

Integrated forms of the Birch-Murnaghan equation of state, BMEOS3, and the fourth order logarithmic equation of state, LNEOS4, were fitted to the calculation results as described in Chapter 2, and the parameters are presented in Tables 7.II and 7.III. Within the errors due to fitting the EoS, both the monoclinic and orthorhombic cells have the same EoS. The arithmetic mean values of the EoS parameters in tables 7.II and 7.III, are; V_0 = 52.7 ± 0.1 cm^3 mol^{-1} (350.4 ± 0.7 $Å^3$), K_0 = 10.7 ± 0.5 GPa, and K'_0 = 5 ± 3.

No experimental data on the volume of ADH I as a function of pressure, P(V), existed prior to these calculations being performed. A comparison with my own experimental determination of these parameters is given in the following chapter.

Table 7.II. Calculated EoS parameters of monoclinic ADH.

	V_0 (cm^3 mol^{-1})	K_0 (GPa)	K'_0	K''_0 (GPa^{-1})	E_0 (eV $molecule^{-1}$)
BMEOS3 E(V)	52.72 ± 0.04	10.6 ± 0.3	5.6 ± 0.4	-	-49.937 ± 0.001
LNEOS4 E(V)	52.75 ± 0.06	10.8 ± 0.5	4.5 ± 2.0	1.4 ± 3.3	-49.937 ±0.001

Table 7.III. Calculated EoS parameters of orthorhombic ADH.

	V_0 (cm^3 mol^{-1})	K_0 (GPa)	K'_0	K''_0 (GPa^{-1})	E_0 (eV $molecule^{-1}$)
BMEOS3 E(V)	52.84 ± 0.03	10.8 ± 0.1	5.1 ± 0.2	-	-49.9420 ± 0.0002
LNEOS4 E(V)	52.76 ± 0.04	11.0 ± 0.2	6.2 ± 1.7	-3.7 ± 0.5	-49.9420 ± 0.0002

Table 7.IV. Structural parameters for the ordered orthorhombic unit cell of ADH I (variant G), which is derived from the disordered cubic cell.

Space group $P2_12_12_1$

a = 7.1604 Å b = 7.0639 Å c = 7.1577 Å V = 362.04 Å^3

Fractional atomic coordinates

	Wyckoff position	Occupancy	*x*	*y*	*z*
O1	4*a*	1	0.6562	0.3397	0.8469
H1	4*a*	1	0.2587	0.7562	0.7359
H2	4*a*	1	0.7919	0.6680	0.4764
O2	4*a*	1	0.6936	0.6939	0.7016
H3	4*a*	1	0.9351	0.2542	0.1786
H4	4*a*	1	0.6749	0.5637	0.7551
N1	4*a*	1	0.6258	0.8727	0.1258
H5	4*a*	1	0.1541	0.4860	0.8600
H6	4*a*	1	0.5121	0.3518	0.3427
H7	4*a*	1	0.8540	0.1642	0.4887

Bond lengths (Å)

O1-H1	1.035	H1…N1	1.647
O1-H2	1.000	H2…O2	1.786
O2-H3	1.005	H3…O1	1.726
O2-H4	1.005	H4…O1	1.719
N1-H5	1.024	H5…O2	2.375
N1-H6	1.023	H6…O2	2.359
N1-H7	1.026	H7…O2	2.312
O1…N1	2.682	O2-H3…O1	2.730
O2…H2-O1	2.767	O2-H4…O1	2.723

Table 7.V. Structural parameters for the ordered monoclinic unit cell of ADH I (variant A), which is derived from the disordered cubic cell. The pattern of bond lengths is essentially the same as that given in Table 7.IV for the orthorhombic variant of ADH.

Space group $P2_1$

a = 7.0905 Å b = 7.1870 Å c = 7.1047 Å β = 90.41° V = 362.04 Å^3

Fractional atomic coordinates

	Wyckoff position	Occupancy	*x*	*y*	*z*
O1	2*a*	1	0.6567	0.6587	0.9117
H1	2*a*	1	0.2576	0.2408	0.0041
H2	2*a*	1	0.6652	0.5296	0.9643
O2	2*a*	1	0.1520	0.8449	0.5900
H3	2*a*	1	0.2343	0.7593	0.5076
H4	2*a*	1	0.0216	0.7914	0.5835
O3	2*a*	1	0.2017	0.1896	0.4426
H5	2*a*	1	0.7480	0.6704	0.6879
H6	2*a*	1	0.1782	0.0619	0.4946
O4	2*a*	1	0.6946	0.3054	0.0579
H7	2*a*	1	0.2503	0.8221	0.8127
H8	2*a*	1	0.4344	0.7503	0.9246
N1	2*a*	1	0.8761	0.8775	0.1264
H9	2*a*	1	0.9841	0.3614	0.9045
H10	2*a*	1	0.8589	0.8476	0.2662
H11	2*a*	1	0.1587	0.5145	0.8937
N2	2*a*	1	0.6279	0.1247	0.6216
H12	2*a*	1	0.5111	0.6445	0.4142
H13	2*a*	1	0.3556	0.6542	0.2384
H14	2*a*	1	0.6592	0.9871	0.6017

7.2.2 Elastic anisotropy

Fig. 7.7 shows that the incompressibilities (defined in the case of the *a*-axis, for example, as $a^3 dP/da^3$) of the three cell edges are not the same. In this case (orthorhombic variant G), the *b*- and *c*-axes have linear incompressibilities of 9.6(10) and 9.4(19) GPa, respectively. The linear incompressibility of the *a*-axis is 18(2.4) GPa. The monoclinic cell exhibits a similar pattern of axial incompressibilities. The reason for this anisotropic incompressibility becomes apparent when the arrangement of the water molecules along the crankshafts in each of the three directions (in variant G) is explicitly considered. Thus the pattern along the crankshaft that is seen when looking down the *c*-axis is O-H…O-H…O-H…O-H, etc., and the pattern seen when viewing down the *b*-axis is the same, only reversed: O…H-O…H-O…H, etc. However, when looking down the *a*-axis the pattern is subtly different: O-H…O…H-O-H…O…H-O-H, etc., and this is the cause of the differing axial incompressibilities.

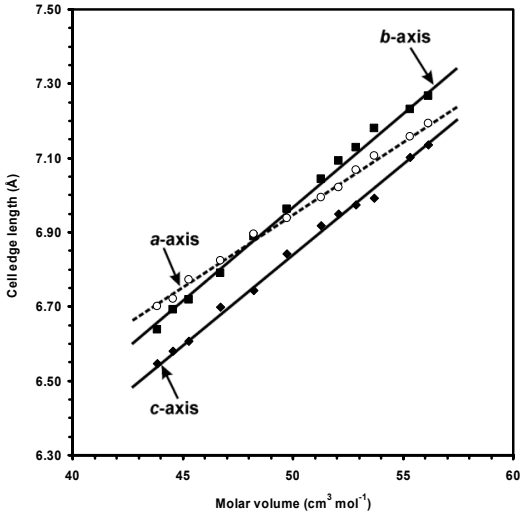

Figure 7.7.
Variation of the lattice parameters with volume in the orthorhombic cell (specifically, variant G: Fig 7.5). Circles: *a*-axis. Squares: *b*-axis. Diamonds: *c*-axis. The *b*- and *c*-axes are significantly more compressible than the *a*-axis. The monoclinic cell exhibits the same behaviour.

7.3 IMPLICATIONS: ORDER-DISORDER

Chan and Giauque (1964) found that the entropy of ADH vanished in the low temperature limit, and concluded that the structure achieved full ordering of its hydrogen bonds at 0 K. My computational results indicate that the lowest energy structure is antiferroelectrically ordered in orthorhombic space group $P2_12_12_1$, admittedly by a very small margin. It is not possible, at absolute zero, for the disordered cubic cell to have a Gibbs Free Energy equal to, or lower, than the proposed orthorhombic cell because the disordered structure cannot be stabilised by entropy. It is physically impossible to disorder the orthorhombic cell without introducing defects into the structure, and since these defects require energy to form, the disordered unit cell must have a higher total energy.

There are then two possible ways in which the structure can behave over the temperature interval between absolute zero and its melting point at 176.16 K.

7.3.1 MODEL A

The heat capacity measurements of Chan and Giauque (1964) reveal no sign of a discontinuity which might be attributed to a sudden order-disorder transition, as in ammonia hemihydrate for example (Hildenbrand and Giauque 1953). Perhaps, then, ADH I is fully ordered throughout its stability field. The diffraction patterns in the literature are readily explained by positing a domain model. It will be recalled from Sec. 7.1.1. that there are three orientational variants with 222 symmetry (which are related by 3-fold rotation axes). If ADH I were constructed from equal numbers of domains of each of these orthorhombic cells, and provided the domains were sufficiently small to diffract coherently and that the lattice strains are sufficiently small to allow a dimensionally cubic average lattice to be maintained throughout, the spatially averaged diffraction pattern would be cubic $P2_13$. It is straightforward to apply a three-fold rotation matrix to the atomic coordinates of the orthorhombic cell so as to generate all of the virtual 1/3 and 2/3 occupied sites in the cubic cell.

Twinning (e.g., on the (020) plane) probably relates neighbouring domains, and it is possible that rapid crystal growth will result in a microtwinned structure whereas slow growth might yield a single domain crystal.

Although domain models *per se* have not enjoyed great success in explaining the structure of disordered minerals, the model described here can satisfy the experimental diffraction patterns, IR spectra, and heat capacity measurements.

7.3.2 MODEL B

The second possibility is that ADH I is not locally ordered throughout its stability field, but undergoes an order-disorder transition at some temperature at which the diffusion of orientational defects is still kinetically favoured (i.e., above ~100 K). Model B may be summarised as follows: ADH I is paraelectrically disordered in space group $P2_13$ above the proposed transition temperature. Upon cooling, the water molecules fix themselves into preferred orientations, forming antiferroelectrically ordered domains. These ordered domains could nucleate in any one of three orthorhombic ($P2_12_12_1$) orientations, related by twin planes, resulting in either a macroscopically multiply twinned orthorhombic crystal or, in the limiting case of very fine-scale twinning, a structure equivalent to that of Model A. Model B is consistent with the IR spectra recorded at 100 K (Bertie and Shehata 1984), and may be consistent with the heat capacity measurements if the transition occurs gradually; the change in entropy upon ordering will be very small, probably similar to that in water ice (~3 J mol^{-1}). The

time-of-flight neutron diffraction experiments (Loveday and Nelmes, 2000) were at temperatures above the proposed transition temperature and so we would not expect to see evidence for peak splittings due to the formation of an orthorhombic microstructure. However, both of the X-ray diffraction experiments were at temperatures *below* the proposed transition temperature (105 K, Bertie and Shehata 1984: 77K, Durham *et al*., 1993). I therefore estimate the extent of the likely peak splitting to determine whether or not it would have been resolvable. The largest orthorhombic strain at 0 K (along the *b*-axis) is -0.89%. Along the *a*- and *c*-axes it is +0.46% and +0.43% respectively. Hence, the maximum splitting at 0 K will be approximately 0.3º in 2θ at 2θ = 40º. At temperatures of 77 - 105 K this strain will be even smaller and the concomitant splitting is certainly irresolvable in the patterns of Bertie and Shehata (1984) and Durham *et al*. (1993).

A gradual ordering transition also bears comparison with the behaviour of a number of pure ice polymorphs: Upon cooling, ice III experiences a gradual proton ordering to become the isostructural (but antiferroelectrically ordered) phase ice IX (Whalley *et al*., 1968: Lobban *et al*., 2000). Similarly, ice V (space group A2/a) may undergo a gradual transformation to an antiferroelectrically ordered structure (space group $P2_1/a$), although the latter is unstable with respect to ice II (Kamb and La Placa 1974: Lobban *et al.,* 2000: Johari and Whalley 2001).

However, we would expect significant changes in other experimentally observable quantities if ADH I undergoes an order-disorder transition, and so we now review literature evidence in support of Model B.

7.3.3 Experimental evidence for an order-disorder transition

There appears to be a very dramatic change in the dielectric behaviour (Lorenz 1998: Lorenz and Shandera 2001), the thermal conductivity as a function of temperature, λ(T) (Lorenz and Shandera 2001), and in the creep behaviour (Durham *et al*., 1993) of ammonia bearing ices in the temperature interval 130 – 150 K (Figs. 7.8 – 7.10). The changes in the creep and dielectric behaviour are consistent with ADH being wholly or partially disordered above 150 K and fully ordered from 130 K down to absolute zero. The meaning of the change in the thermal conductivity is not clear.

7.3.3.1 Dielectric measurements

The dielectric properties are the most leading piece of evidence because of the way that water molecules in ice respond to an applied a.c. electric field. In the dynamically disordered ice phases, reorientation of the water molecules (due to Bjerrum defect diffusion) results in a large contribution to the dielectric permittivity from orientational polarization at lower

frequencies. In the fully ordered phases (e.g., ice II), this orientational polarization is absent, since the water molecules are fixed in place, and the high frequency dielectric permittivity (ε_∞) is the same as the low frequency dielectric permittivity (ε_0). Analysis of this dielectric dispersion is a powerful means of probing the degree of orientational order in ice crystals. The dielectric study of the ice III ↔ ice IX transition is an excellent example (Whalley *et al*., 1968), as is the recent study of partial ordering in ice V (Johari and Whalley 2001).

The temperature dependent complex permittivity measurements of Lorenz and Shandera (2001) show a very dramatic change in the dielectric properties of ice doped with ammonia between 130 –150 K (Fig. 7.8). The sample in question consisted of ice doped with 16 wt % NH_3 (i.e., ~50% water ice, 50% ADH). It is probable that there was a finite quantity of metastable AMH in the sample but since AMH I is fully ordered the conclusion is unaffected. The observed change is characterised by a drop in the loss tangent, tan(δ) (the ratio of the real, ε', to the imaginary part, ε'', of the complex dielectric constant, $\varepsilon_0 = \varepsilon' + i\varepsilon''$) upon cooling. This can only be attributed to a reduction of the orientational polarization contribution from the water molecules in the sample. However, the reorientation of the water molecules in ice becomes frozen in at temperatures of ~100 K, and so the observed dielectric signature must be due to ordering of the water molecules in ADH I. Ice doped with 5 wt % NH_3 exhibits the same behaviour.

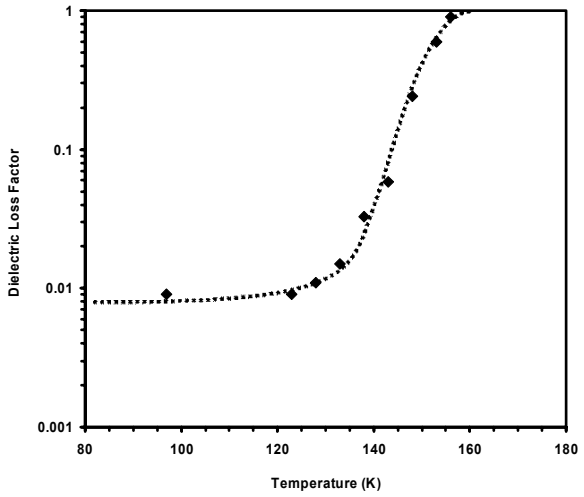

Figure 7.8. The dielectric loss factor (proportional to the loss tangent, tanδ = ε'/ε") for ice doped with 16 wt % NH_3 (i.e., 50:50 ice to ADH) measured at 2kHz. Redrawn after Lorenz and Shandera (2001). The dotted line is a guide to the eye.

7.3.3.2 Thermal conductivity

The measured thermal conductivity as a function of temperature, λ(T), is shown in Figure 7.9 (after Lorenz and Shandera 2001). Above 140 K, the data is well fitted by a function that varies in the same fashion as in ice Ih. The solid black line depicts a temperature dependence based on that of ice (e.g., Andersson and Suga 1994); λ(T) = (500/T)-1.45. Below 140 K, λ appears to be anomalously low. The dotted curve shows the same temperature dependence as the black line but is systematically offset to lower values by ~40%. At the order-disorder transition in hexagonal ice (ice Ih ↔ ice XI) proton ordering is believed to decrease the lattice anharmonicity producing an increase in λ of ~20% at the transition (Andersson and Suga 1994). Invoking a similar mechanism for the ordering transition in ADH, we would therefore expect λ to rise at 140 K rather than dropping. Hence, the thermal conductivity data can be interpreted as showing a change in transport properties near 140 K, but this change is in the opposite sense to that seen through the orientational ordering transition from ice Ih to ice XI.

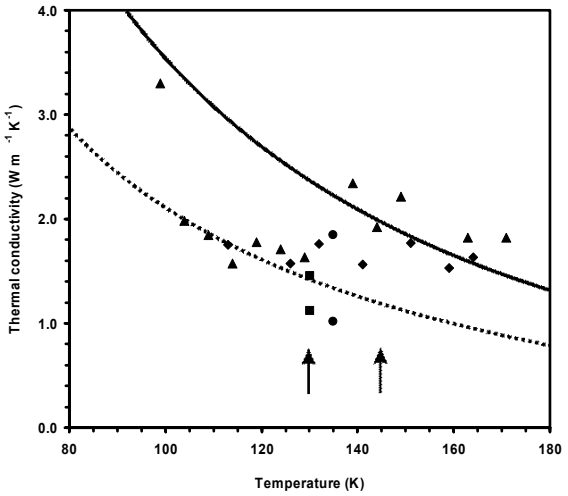

Figure 7.9. The thermal conductivity of ammonia-bearing ice (16 wt % NH_3, as above), redrawn after Lorenz and Shandera (2001). Triangles are hotwire results and diamonds are ammonia-rich samples after warming and refreezing. Circles are differentiated line source (Shandera and Lorenz 2000) and squares are 30 wt % NH_3 from Kargel (1992). The solid black line is intended merely to indicate the expected behaviour of λ(T) and is based on the observed values for pure water ice. The dashed line shows the same temperature dependence but is lower by ~40%. Arrows bracket the proposed transition.

7.3.3.3 Creep behaviour

The creep of ices in the ammonia-water system was studied by Durham *et al*. (1993). Their work revealed that ADH is four orders of magnitude less viscous than pure water ice at temperatures just below its melting point, but exhibits a steeper temperature dependence. This results in ADH becoming as viscous as water ice at ~140 K. Similar mechanical behaviour was observed by Lorenz and Shandera (2001). However, the temperature dependence appears to change below 140 K. Figure 7.10 shows the data for 29 wt % NH_3 (ideally 90% ADH, 10% ice) samples at four strain rates. Solid black lines depict the flow law for this composition as derived from the data points (Durham *et al*., 1993). The dotted lines depict the flow law for pure water ice at the same strain rates (after Durham *et al*., 1992). Note that, below 140 K (1000 / T ≈ 7.15), the strength of the ADH samples lies below the extension of the flow law fitted to the higher temperature measurements. Durham *et al*. (1993) believe that the dominant flow mechanism in ADH changes below 145 K. In ice, creep is dominated by basal slip, which is assisted by the migration of orientational defects. I would therefore argue that the observed softening of ADH above 140 K is due to the appearance of rotational defects as the water molecules become disordered.

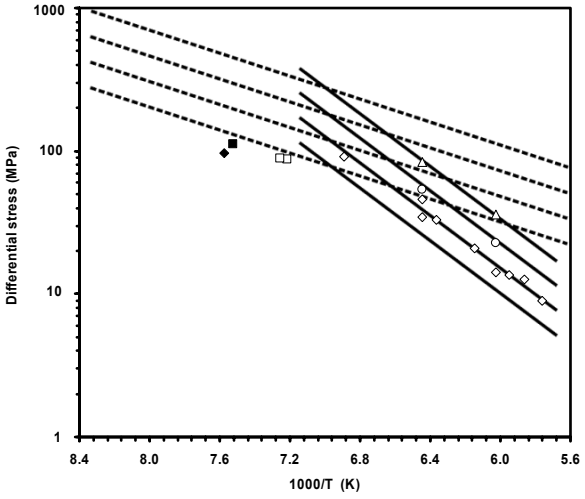

Figure 7.10. Arrhenius plot of the ductile strength of 29 wt % NH_3 ice (almost pure ADH, ideally) redrawn from Durham *et al*. (1993). The strain rates ($\dot{\varepsilon}$) are shown as: Triangles, 3.5×10^{-4} s^{-1}: Circles, 3.5×10^{-5} s^{-1}: Diamonds, 3.5×10^{-6} s^{-1}: Boxes, 3.5×10^{-7} s^{-1}. Filled symbols show samples which failed and therefore represent a lower bound on the true strength. The derived flow laws at the specified strain rates for ADH are shown by solid black lines, and for water ice (after Durham *et al*., 1992) by dashed lines.

The experimental evidence outlined above therefore appears to indicate that there is a change in transport behaviour which may signifiy a phase transition. The evidence is not clear, but an order-disorder transition is not ruled out. The model requires rigorous testing; most useful would be dielectric spectroscopy at a range of temperatures, careful measurements of the heat capacity of both rapidly cooled (and unannealed) samples and annealed samples (see Johari 2000), and high-resolution X-ray or neutron diffraction studies as a function of temperature.

My own neutron diffraction experiments, described in the following chapter, outline an attempt to observe the order-disorder transition upon cooling through 140 K at ambient pressure. As will be described, the experiment failed to observe any change in the structure at low temperatures, the disorder manifested at high homologous temperatures being frozen-in all the way down to 4 K.

7.4 SUMMARY

I have determined that there are only two possible ordering schemes for the water molecules in phase I of ammonia dihydrate that satisfy the ice rules. One is ferroelectrically ordered in space group $P2_1$. The other is antiferroelectrically ordered in space group $P2_12_12_1$. A*b initio* calculations show that the latter is marginally more energetically stable by 5 meV per formula unit (~0.5 kJ mol^{-1}). The calculated energy-volume curves of the ordered cells have been fitted to several equations of state, yielding mean values for the EoS parameters of V_0 = 52.7 ± 0.1 cm^3 mol^{-1}, K_0 = 10.7 ± 0.5 GPa, and K_0' = 5 ± 3. The incompressibility of the *a*-axis is found to be significantly greater than that along the *b*- or *c*-axes.

I believe that the experimental observations show evidence for a gradual order-disorder transition between 130–150 K. Above this temperature, ADH I is paraelectrically disordered. Upon cooling to 150K, antiferroelectrically ordered domains nucleate and grow until the entire structure is ordered below 130 K. Further investigations, in particular of the dielectric properties as a function of temperature, are warranted to establish the degree of ordering in ADH.

CHAPTER EIGHT

NEUTRON DIFFRACTION EXPERIMENTS

8 Introduction

Very little experimental data exists relating to ADH. Where experiments have been done, there typically remain more questions than answers. To remedy this situation, I have carried out two experiments on ADH using time-of-flight neutron diffraction (see 1.2.2).

Experiments were done using two different instruments at the ISIS facility, a pulsed neutron source located at the Rutherford Appleton Laboratory in Chilton, near Didcot, Oxfordshire. The reasoning behind each experiment and the choice of instrument are presented in sections 8.1 and 8.2.

8.1 The HRPD Experiment

The pressure and temperature dependencies of the molar volume of ADH I have never been measured previously, but are of paramount importance to planetary scientists. In order to model the internal structure and thermal history of the icy moons, accurate values for the thermal expansivity and incompressibility of ADH I are required (Consalmagno 1985: Croft *et al*., 1988). In the preceding chapter I presented the results of *ab initio* calculations on ADH, reporting the equation of state in the athermal limit, and consequently have an interest in comparing these results with experimental data.

There were therefore a number of questions regarding ADH I that were to be addressed. What is the thermal expansivity of ADH I throughout its temperature stability field? What is the incompressibility of ADH I? Does ADH I undergo an order-disorder transition near 140 K?

In order to answer these questions I have carried out a neutron powder diffraction study upon perdeuterated ADH I. These experiments were done using the time-of-flight method on the High Resolution Powder Diffractometer (HRPD) beamline at ISIS (Ibberson *et al*., 1992). The unparallelled resolution of this instrument ($\Delta d/d \sim 4 \times 10^{-4}$ in the backscattering detectors[1]) makes it ideal for the rapid and accurate determination of lattice parameters (for measuring thermal expansivity and incompressibility), and for the detection of very fine Bragg peak splittings concomittant with the proposed order-disorder transition.

In addition to measuring the properties of ADH I, I also wished to observe the phase transition to a denser polymorph of ammonia dihydrate (ADH II). This transition has been seen previously in piston compression experiments (Hogenboom *et al*., 1997) and by neutron powder diffraction (Loveday and Nelmes1999b).

In the following section (8.1.1) I describe the sample preparation method and data acquisition strategy: ADH is notoriously difficult to crystallise (Chan and Giauque 1964: Bertie and Shehata 1984: Yarger *et al*., 1993) since it tends to form a glass when supercooled below its melting point and then disproportionates into ammonia monohydrate + ice. I therefore pay particular attention to describing the recipe that was followed to produce crystalline ADH I. In Sec. 8.1.2. I present my results, reporting the pressure and temperature dependence of the unit cell volume and observations regarding the structure at low temperatures.

8.1.1. Experimental method

8.1.1.1. Sample preparation and loading

A liquid of the correct stoichiometry ($33^1/_3$ mol% ND_3) was prepared by Dr Sean McGrady (formerly of Kings College London, but presently at the University of New Brunswick, Canada) by mixing an appropriate volume of condensed heavy ammonia (Aldrich Chemicals Co., 99 atom % D) with heavy water (Aldrich Chemicals Co., 99 atom % D). This liquid was stored in a refrigerator for approximately three months prior to use in the HRPD experiments, and nine months prior to the PEARL experiment (Sec. 8.2).

An aluminium slab-can with vanadium windows was employed for the ambient pressure experimental runs. The sample cavity (~5 cm^3) was loosely padded with silica wool to ensure nucleation of a good powder from the liquid, and $ND_3 \cdot 2D_2O$ solution was dripped onto the wool (at room pressure and temperature) until the space was filled. The can was sealed, attached to a cryostat centre stick, and quenched to 77 K in a nitrogen dewar. This assembly was then placed in a vanadium-tailed helium cryostat pre-cooled to 50 K and allowed to thermally equilibrate before being warmed to 174 K. In order to produce crystalline ADH the

[1] Δd is the full width half maximum of a peak with a lattice spacing of d. However, by using profile refinement (e.g., Rietveld) methods, the instrument can detect shifts in peak positions to two orders of magnitude better than this quoted resolution.

temperature was cycled across the melting point a number of times according to the recipe of Bertie and Shehata (1984); the temperature was ramped up from 174 K to 179 K over fifteen minutes, and then reduced to 174 K over three minutes. The cycle was repeated four times (72 minutes in total), and the sample was then kept at 174 K for ~20 hours before being placed in the neutron beamline.

For the high-pressure experimental runs a cylindrical aluminium gas pressure vessel, with an internal volume of ~ 2 cm^3, was used. Once again, silica wool was utilised as a multinucleator and liquid $ND_3 \cdot 2D_2O$ was poured into the sample space. The can was sealed with a nominal pressure of ~500 bar of He gas. As pressure was released following an offline pressure test the sample was observed to boil, apparently outgassing ammonia vapour from solution. This altered the stoichiometry from ~33 mol% ND_3 to ~29 mol% ND_3, resulting in the crystallisation of a significant amount of ice (~12.5 wt%) along with ADH I.

The same temperature cycling process was used to crystallise ADH I in the pressure cell using a second, larger bore, vanadium-tailed helium cryostat with the sample held at ~400 bar. However, the time required was changed to account for the increased thermal inertia of the pressure can: the temperature was ramped up from 174 K to 179 K over one hour, and then reduced to 174 K over fifteen minutes. The cycle was repeated four times (5 hours total), and the sample was then held at 174 K for ~12 hours before being placed in the neutron beamline.

In both sample environments this process resulted in the formation of a good crystalline powder of ADH phase I (see e.g., Fig 8.1 and 8.2).

8.1.1.2. Data acquisition

For the ambient pressure experiments, it was found that diffraction patterns suitable for the accurate determination of lattice parameters (i.e., with standard errors of order few $x10^{-5}$ Å) could be collected in approximately ten minutes from the backscattering and 90° detector banks (e.g., Figure 8.1). Data were collected at temperature intervals of 2 K whilst cooling the sample from 174 K to 4.2 K; a cooling rate of 8 K hr^{-1}, allowing for five minutes of thermal equilibration before data collection at each temperature point. Data were collected for ~ 1 hour at 4.2 K in order to allow for more detailed structural refinement (see Table 8.I). Since no obvious signs of the expected ordering were observed during this period (i.e., the structure remained cubic), the sample was taken offline and held at 120 K for ~36 hours in an effort to promote the ordering transformation. This sample was then returned to the beamline and cooled to 40 K. Finally, diffraction patterns suitable for high quality structure refinement (~100 minutes per spectrum) were collected at 20 K intervals upon warming from 40 K to 160 K. This latter data set is hereafter referred to as the *post-annealing* data, and the run of spectra at 2 K intervals as the *pre-annealing* data set.

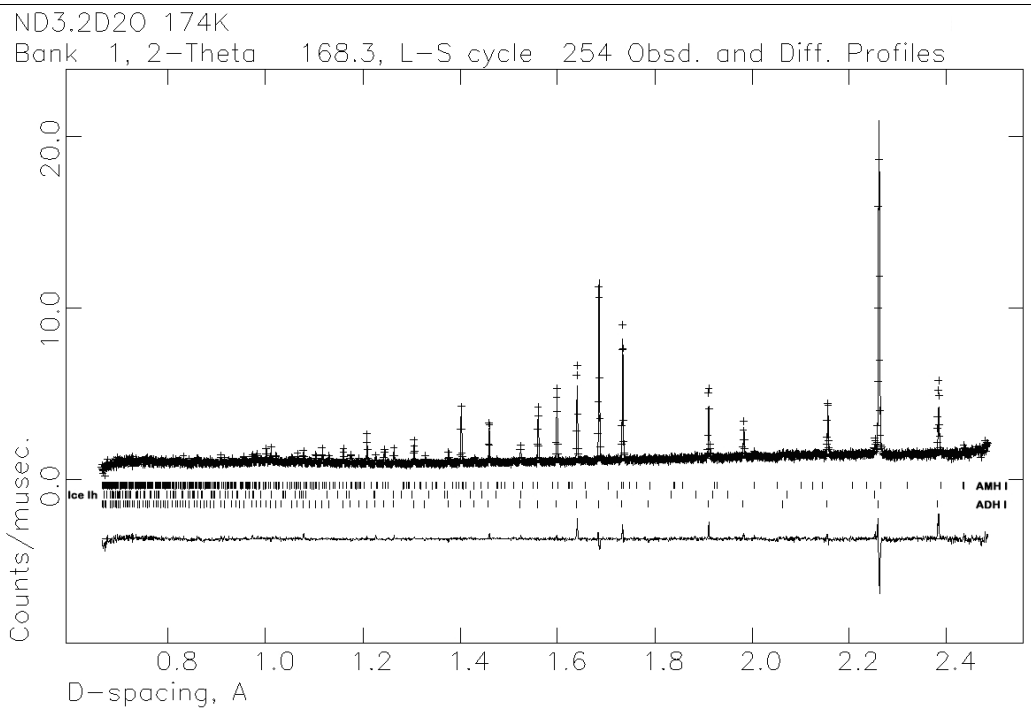

Figure 8.1. Observed and calculated profiles for a diffraction pattern acquired at ambient pressure, 174 K (backscattering detectors, 2θ = 168.3°), including difference profile (bottom). Tick marks, from the top down, show the positions of reflections due to AMH I, ice Ih, and ADH I.

The sample for the high-pressure experiment was introduced to the neutron beamline under a nominal pressure of 410 bar. It was found that 15 minutes was an adequate period of time to accurately determine lattice parameters from the 90° detectors (Figure 8.2). The use of this detector bank enables most of the scattering from the aluminium pressure vessel to be collimated out. The pressure was stepped up (using helium as the pressure transmitting medium) in intervals of ~0.05 GPa to the maximum rated pressure of the aluminium cell (~0.46 GPa). Diffraction patterns confirmed the earlier observation of Loveday and Nelmes (1999b) that helium does not penetrate the ADH I structure. At 0.35 GPa there was a drop in pressure, and the Bragg peaks of ice Ih were replaced by reflections due to ice IX. This solid persisted as an accessory phase up to the maximum pressure investigated. Although not the equilibrium phase under the applied P-T conditions, the transition from ice Ih to ice IX has been seen in the 0.35 – 0.40 GPa pressure range below ~170 K previously (Mishima 1996: Gromnitskaya *et al*., 2001); however, it is known that the use of helium gas as a pressure medium inhibits the formation of ices III, V, and IX in favour of a helium hydrate with the ice II structure (Londono *et al*., 1992). I conclude that the presence of ammonia dihydrate may have a preferential influence on the nucleation of ice IX with respect to helium-stuffed ice II, in spite of the

observation by Londono *et al*., (1992), that they were unable to crystallise phases other than helium hydrate even when using specialised nucleating agents.

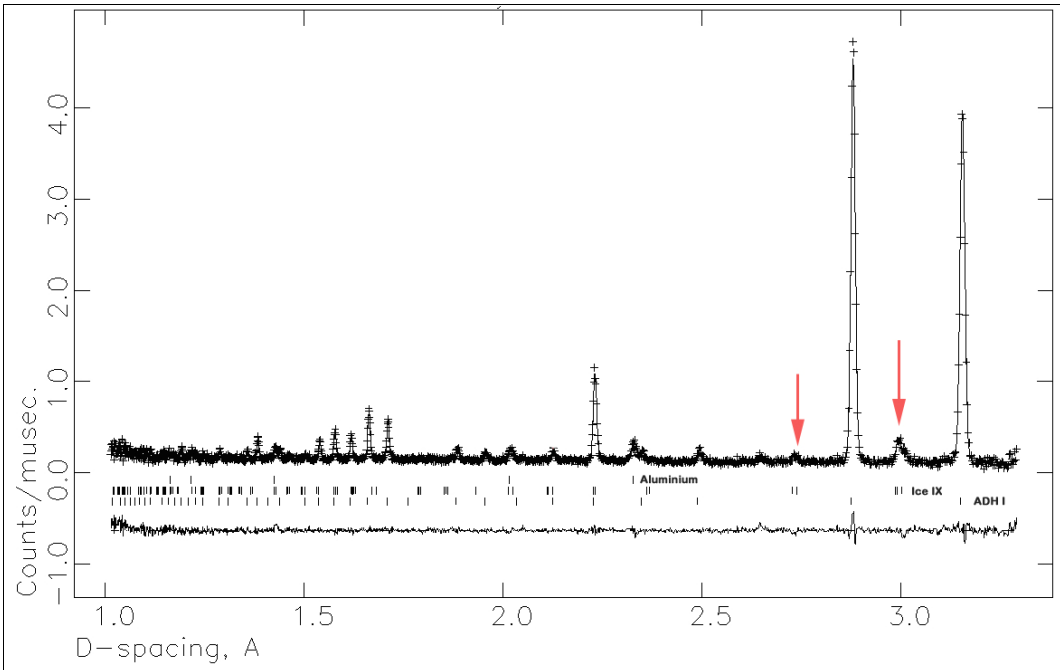

Figure 8.2. Observed and calculated profiles for a diffraction pattern acquired at 3.44 kbar, 174 K (90° detectors), including difference profile (bottom). Tick marks, from the top down, show the positions of reflections due to aluminium, ice IX, and ADH I. The strongest of the ice IX peaks are indicated by arrows.

The anticipated phase transition to ADH II had not occurred at 0.46 GPa, so the sample was warmed by 5 K. The sample promptly melted, probably to a slurry containing ice IX crystals in ammonia-water slush. When cooled back to 174 K, new Bragg peaks appeared along with those of ice IX over a period of ~4 hours (Fig. 8.3). Diffraction data were collected from this new polyphase mixture for ~ 11 hours at 174 K. The sample was then cooled in 5 K steps to 140 K, quenched to ~110 K and subsequently decompressed to ~500 bar, but peaks from the high-pressure phase persisted, albeit with a considerable degree of strain broadening when the pressure was completely released. In my opinion, ADH I was initially compressed *metastably* into the stability field of ADH II, but a great enough overpressure was not applied to make the phase transition occur. After melting, *stable* ADH II crystallised which was able to persist metastably in the stability field of ADH I when cooled and decompressed. Analysis of the data from the high-pressure experiment indicates that the new pattern represents a complex mixture of both ADH II, phase II of ammonia monohydrate (AMH II), ice IX and possibly ice II (Fig.

8.4). Since the structures of ADH II and AMH II are not known at present, it has not been possible to make any progress with this multiphase pattern yet.

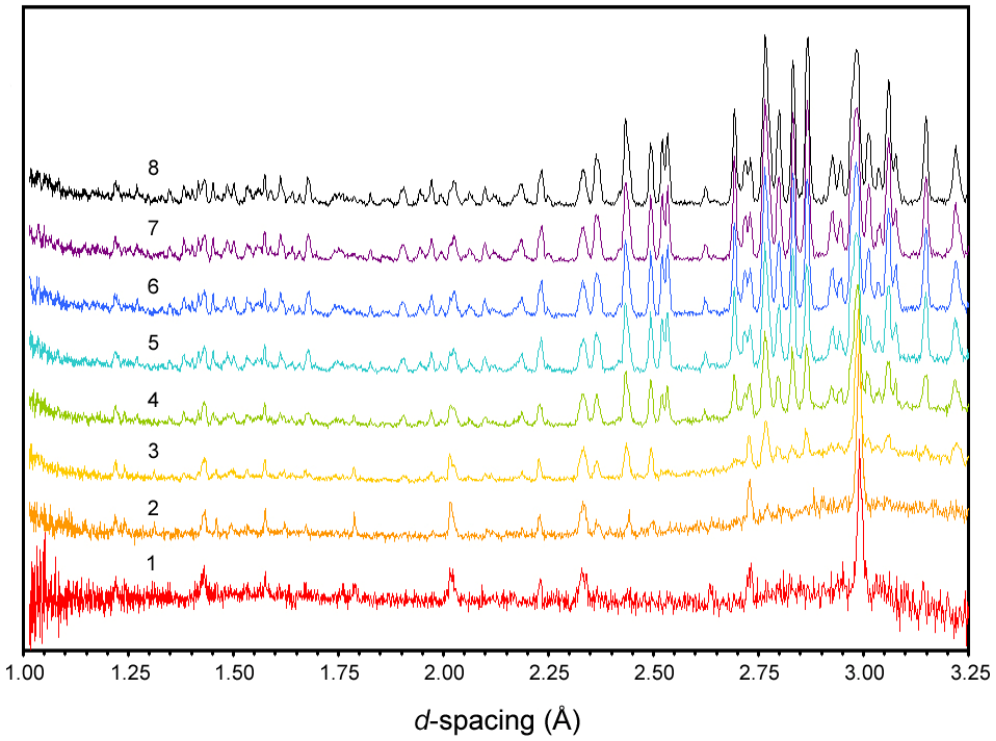

Fig. 8.3. Diffraction patterns acquired at 0.46 GPa as the molten slurry of ice IX + NH_3-solution recrystallised. Pattern 1, at 179 K, represents T = 0. Patterns 2 – 8 are at 174 K and correspond to the following times; (2) T = 9 minutes, (3) T = 45 minutes, (4) T = 1 hour 46 minutes, (5) T = 2 hr 48 m, (6) T = 3 hr 49 m, (7) T = 4 hr 50 m, (8) T = 5 hr 51 m.

Overleaf: Fig. 8.4. Upper panel: the diffraction pattern of ammonia monohydrate II (Loveday and Nelmes 1998), against which I have placed tick marks corresponding to the most intense peaks. Lower panel: the diffraction pattern of ammonia dihydrate II (Loveday and Nelmes 1999b), with tick marks corresponding to the most intense peaks. Middle panel: my polyphase diffraction pattern. The tick marks for AMH II and ADH II explain the majority of the observed peaks. Those that are exclusively from an accessory ice polymorph are marked with blue stars.

Fig. 8.4. (*Caption on preceding page*)

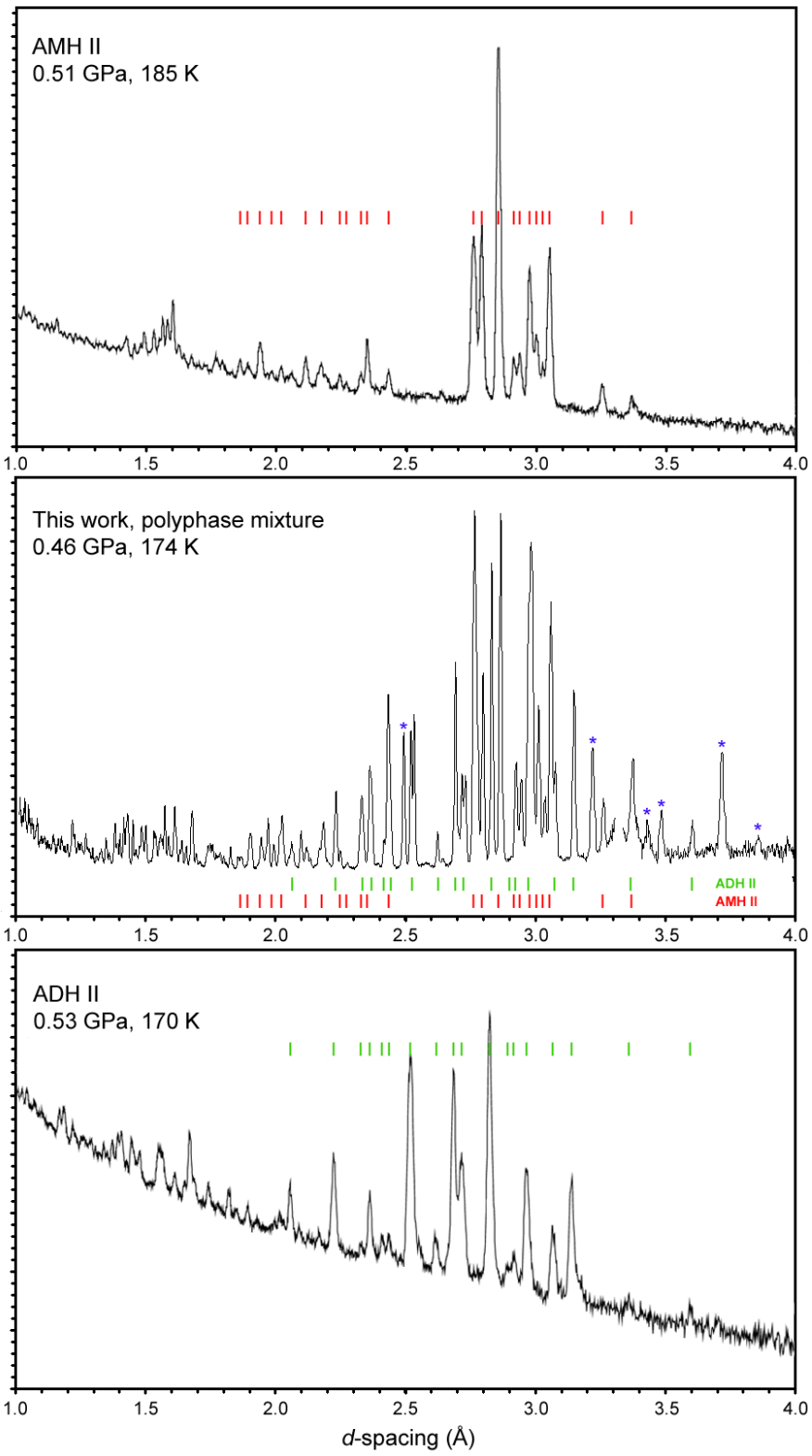

8.1.1.3. Refinement

The cell parameter of ADH I as a function of temperature was extracted from the pre-annealing data set using the "cell and intensity least squares" (CAILS) utility (Pawley 1981) in CCSL (the Cambridge Crystallography Subroutine Library) (RAL 1993). Rietveld multiphase structure refinements of the post-annealing and high-pressure time-of-flight spectra were made using the GSAS package (Larson and Von Dreele 1994). The ADH I structure was refined from the cubic cell of Loveday and Nelmes (2000). At ambient pressure, the minor phases coexisting with ADH I were successfully fitted with the structures of ice Ih (Peterson and Levy 1957) and ammonia monohydrate (AMH phase I) (Loveday and Nelmes 2000). At each temperature, only the unit cell dimensions of ice Ih and AMH I were refined; atomic coordinates were fixed at their literature values and the temperature factors for each atomic species were set to the values refined from the ADH structure. The refinements of the ADH I structure were done with isotropic temperature factors (U_{iso} in Table 8.I). It was found that an anisotropic refinement yielded minimal improvements in the fitting statistics, and also generated unphysical values for the atomic displacement parameters of the partially occupied deuteron sites.

In the high-pressure experiment, ice Ih transformed to ice IX between 0.30 – 0.35 GPa: Cell parameters for this phase were refined on the basis of the fully ordered ice IX structure (Londono *et al*., 1993). This is not strictly correct, since the observed structure of ice IX does exhibit a very small degree of partial disorder at 170 K; the probability of the weakly occupied deuteron sites being occupied is ~ 4% (Londono *et al*., 1992). Additional minor reflections were observed from the aluminium sample cans. Since the high-pressure runs were relatively short (10 – 20 minutes) the structure of ADH I was not refined, only the unit cell.

8.1.2. Results

8.1.2.1. Thermal expansivity

The pre-annealing data set consists of 85 data points at 2K intervals, from which the lattice parameter was refined with a standard deviation on all points of 0.00002 Å (Figure 8.5). A second order Grüneisen approximation to the zero pressure equation of state (Wallace 1998), Equation 8.1, was fitted to the unit cell volumes found from the pre-annealing data set. In this approximation, the thermal expansion is considered equivalent to elastic strain such that,

$$V(T) = V_{0,0}\left[1 + \frac{E(T)}{Q - bE(T)}\right] \qquad (8.1)$$

where $V_{0,0}$ is the unit cell volume at zero pressure and temperature, b = ½ ($K'_{0,0}$-1) and Q = ($V_{0,0} K_{0,0} / \gamma$). $K_{0,0}$ is the zero pressure and temperature isothermal bulk modulus, $K'_{0,0}$ is its first derivative with respect to pressure, and γ is the thermal Grüneisen parameter. The internal

energy due to lattice vibrations, E(T), is determined via a Debye model (e.g., Ashcroft and Mermin 1976):

$$\mathrm{E}(\mathrm{T}) = \frac{9nk_{\mathrm{B}}\mathrm{T}}{(\theta_{\mathrm{D}}/\mathrm{T})^3}\int_0^{\theta_{\mathrm{D}}/T}\frac{x^3}{\mathrm{e}^x - 1}dx \tag{8.2}$$

where θ_D is the Debye temperature, n is the number of atoms per unit cell, and k_B is the Boltzmann constant; the integral term is evaluated numerically.

Table 8.I. Results of the isotropic structure refinement at 4.2 K. Bond lengths quoted are uncorrected for thermal motion.

Rietveld Powder statistics:	wRp = 5.66 %	Rp = 5.00 %
Space group	$P2_13$	
Lattice constant:	7.091771(16) Å	
Unit cell volume:	356.6680(14) Å	

Atom	*x*	*y*	*z*	Occupancy	U_{iso} (x100) Å^2
O1	0.70423(24)	0.70423(24)	0.70423(24)	1	0.73(7)
D1	0.75928(47)	0.67835(50)	0.57701(56)	2/3	1.83(7)
O2	0.15607(26)	0.15607(26)	0.15607(26)	1	1.31(9)
D2	0.23880(26)	0.23880(26)	0.23880(26)	1	1.51(5)
D3	0.01424(133)	0.20723(89)	0.17783(103)	1/3	2.42(17)
N1	0.37944(20)	0.37944(20)	0.37944(20)	1	0.86(5)
D4	0.35734(30)	0.35783(23)	0.51507(31)	1	2.57(6)

Selected bond lengths (Å)

N1-D4	0.9865(21)	D3…O1	1.682(9)
O1-D1	1.0000(35)	D2…N1	1.728(4)
O2-D2	1.0163(32)	D1…O2	1.766(4)
O2-D3	1.080(9)	D4…O1	2.311(3)
O2…N1	2.744(2)	N1…O1	3.258(2)
O1…O2	2.762(3)		

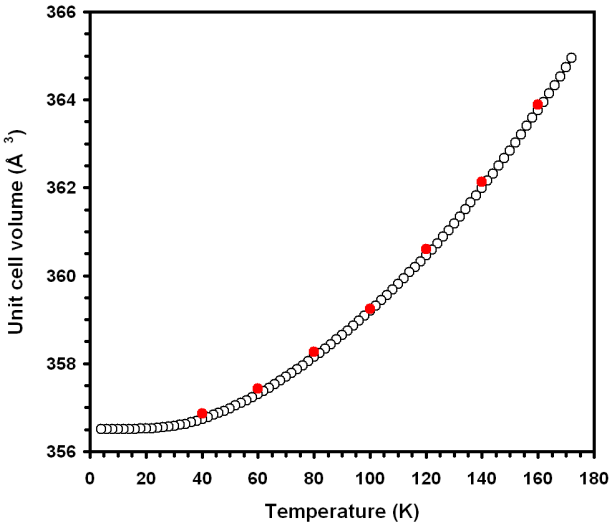

Figure 8.5. Plot of refined unit cell volume against temperature at ambient pressure. The pre-annealing data set is shown as open circles, and the post-annealing data set as filled circles. The slight offset between the two can be explained in terms of small differences in the position of the sample (order 10^{-3} m) in the incident neutron beam.

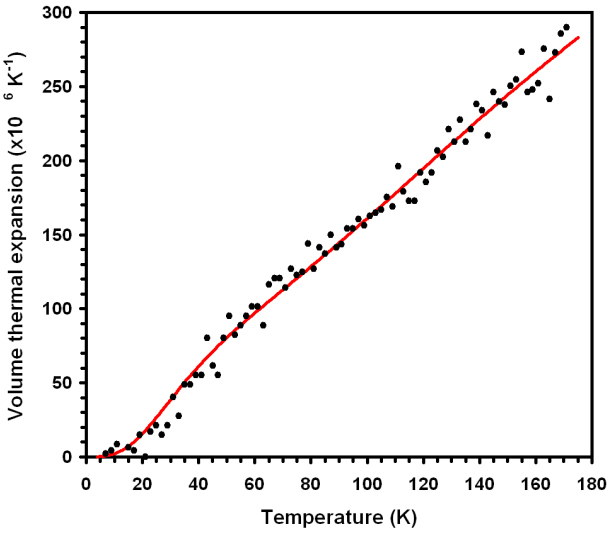

Figure 8.6. The volume thermal expansivity, α_V, as a function of temperature. The filled circles are numerical derivatives of the unit cell volumes with respect to temperature. The red line is from the fitting of Eq.8.1 using the double-Debye model fitted to C_P data.

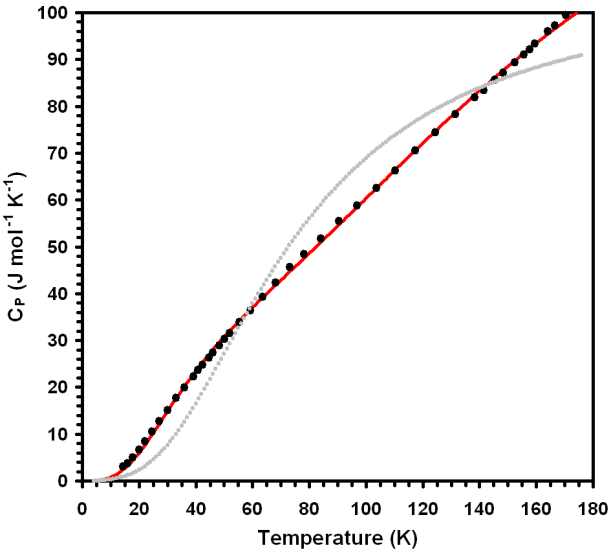

Figure 8.7. Isobaric heat capacity, C_P, of ADH as a function of temperature. Filled circles are the measurements of Chan and Giauque (1964). The grey dotted line represents the best fit of a Debye model with a single Debye temperature. The solid red line is the fit of a model with two characteristic Debye temperatures (Eq. 8.3).

When Eq. 8.1 is fitted to the V(T) data the fit is excellent, both in terms of unit cell volume (Fig. 8.5) and the thermal expansivity (Fig. 8.6). Nevertheless, the elastic parameters resulting from the fit are not sensible ($K'_{0,0}$ = 37.14, for example) and the internal energy of the crystal yields values for the heat capacity which are very seriously at odds with experimental data (Chan and Giauque 1964). Indeed it is impossible to achieve a good fit to the heat capacity data with a single Debye model (Fig. 8.7), and I therefore have little confidence in the parameters resulting from the fitting of Eq. 8.1 to V(T) data as it stands. However, the appearance of the misfit to C_P suggests that ADH I differs radically from Debye (or Debye-like) solids in that there are two Debye moments with very different characteristic temperatures contributing to the internal energy of the crystal. It is a straightforward matter to fit a 'double-Debye' function to the heat capacity data of Chan and Giauque (1964), which has the form,

$$C = 9nk_B\left[Xf\left(\frac{\theta_D^A}{T}\right) + Yf\left(\frac{\theta_D^B}{T}\right)\right] \tag{8.3}$$

where $f(\theta_D / T)$ is the Debye function and X and Y are mixing parameters. It should be noted that this is not intended to be an exact representation of the internal energy of the crystal since I am fitting to C_P data when I should be fitting to C_V values, which have not been measured. Furthermore, with respect to the analysis of our thermal expansion data, I am fitting to C_P data for *hydrogenous* ADH, rather than *deuterated* ADH, wherein the isotopic shift of vibrational frequencies will lead to different Debye temperatures. Nevertheless, this approximation is far superior to the single Debye model fit (Eq. 8.2). The parameters resulting from the fitting of Eq. 8.3 (yielding the solid line in Fig. 8.7) to C_P values are; θ_D^A = 165 ± 3 K, θ_D^B = 729 ± 4 K, X = 0.18122 ± 0.00418, and Y = 0.47746 ± 0.01066. This result is of interest because it shows that the heat capacity of ADH I does not approach the classical high temperature limit of Dulong and Petit ($3nk_B$), but instead trends towards ~ $2nk_B$. The two Debye temperatures correspond to vibrational wavenumbers of, respectively, 115 cm^{-1} and 507 cm^{-1}; these probably represent translational and rotational excitations of the water molecules in ADH (Bertie and Shehata 1984).

Equation 8.1 is now refitted to the V(T) data using the double-Debye model, with E(T) fixed from fitting Eq. 8.3 rather than having θ_D as a free variable. The elastic parameters resulting from this fit are considerably more sensible: $V_{0,0}$ = 356.464 ± 0.005 $Å^3$, ($K_{0,0}$ / γ) = 7.163 ± 0.024 GPa, and $K'_{0,0}$ = 5.41 ± 0.33. It would be useful to extract independent values for $K_{0,0}$ and γ from this fit, and a model-dependent approach by which these may be determined is presented in Sec. 8.1.2.3.

Previous studies (e.g., Croft *et al*., 1988) have estimated the unit cell volume as a function of temperature using an equation of the form

$$\frac{1}{V(T)} = \frac{1}{V_0}\exp\left[-\left(\frac{A}{B+1}\right)T^{B+1}\right] \tag{8.4}$$

where V_0 is the unit cell volume at zero Kelvin and A and B are parameters. The volume coefficient of thermal expansion, α_V, is therefore given by Eq. 8.5.

$$\alpha_V = AT^B \tag{8.5}$$

For comparison with earlier work, and to provide a very simple means of calculating the density of ADH I as a function of temperature, I have fitted Eq. 8.4 to the V(T) data. The resulting fit yields V_0 = 356.391 ± 0.011 Å^3, A = 1.1825 ± 0.0053 x10^{-6}, and B = 1.0662 ± 0.0097. The fit is excellent above ~50 K, but becomes increasingly poor below this temperature as the thermal expansivity changes from a roughly linear dependence on T to a T^3 dependence. Nevertheless, the maximum difference from our measured volumes does not exceed 0.3 % at 4.2 K. Hence, Eq. 8.4 is more than adequate for determining densities in planetary interiors for example.

The final observation I make with regard to the thermal expansivity is in relation to other compounds in the ammonia-water system. The thermal expansivity of ADH I is ~ 300 x10^{-6} K^{-1} at the melting point (176 K); this is approximately double the volume thermal expansivity of ice Ih close to its melting point (Röttger *et al*., 1994), and roughly 60% of the thermal expansivity of solid ammonia near its melting point (Manzhelii and Tolkachev 1966). Since I was also able to extract cell parameters for the low-pressure phase of ammonia monohydrate (AMH I), which occurred as an accessory phase, I can confirm that its thermal expansivity is very similar to ADH I. To be more precise, the density of AMH I as a function of temperature is well fitted by Eq. 8.5 with the parameters A and B identical to those for ADH I; V_0 for deuterated AMH I takes the value 242.260 ± 0.020 Å^3.

The experimental low-temperature molar volumes of both ADH I and AMH I can be compared with my earlier computational results (Chapters 6 and 7). The calculated unit cell volumes of ADH I and AMH I in the athermal limit are 350.4 ± 0.7 Å^3 and 242.0 ± 0.5 Å^3 respectively. Hence the calculated volume of ADH I is in error ($\Delta V/V$) by -1.7 ± 0.2 %, and that of AMH I by -0.1 ± 0.3 %; results which I consider to be excellent.

8.1.2.2. Incompressibility

Diffraction patterns for ADH I were collected at nine pressure points from 0.041 - 0.45 GPa along the 174 K isotherm and refined to obtain the unit cell volume (Fig. 8.8). These data were fitted with a third-order Birch-Murnaghan equation of state (BMEOS) to yield the following parameters: zero pressure unit cell volume, $V_{0,174}$ = 365.69 ± 0.16 Å^3, zero pressure isothermal bulk modulus, $K_{0,174}$ = 7.02 ± 0.25 GPa, and the first pressure derivative of the bulk modulus, $K'_{0,174}$ = 9.56 ± 1.28. Note that these parameters are referenced to a temperature of 174 K. The fitted EoS is shown by the solid line in Figure 8.8.

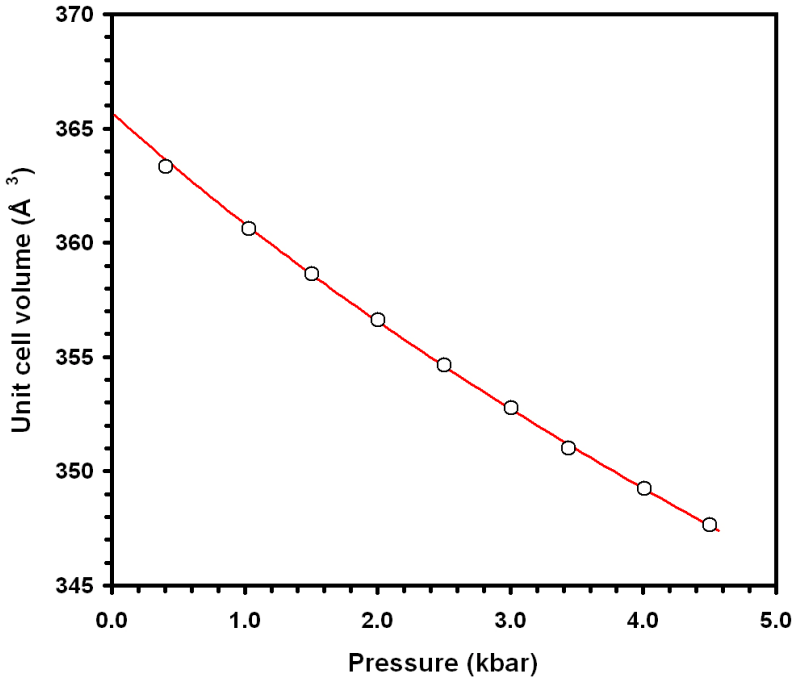

Figure 8.8. Plot of refined unit cell volume against pressure at 174 K. The solid line is a third order Birch-Murnaghan equation of state.

The Bragg peaks due to ice Ih were also refined to yield unit cell parameters as a function of pressure and fitted with a third-order BMEOS having $V_{0,174}$ = 129.02 ± 0.06 Å^3, $K_{0,174}$ = 9.69 ± 0.64 GPa, and $K'_{0,174}$ = 6.71 ± 3.96. These parameters are in excellent agreement with literature values for D_2O ice Ih at this temperature: $V_{0,175}$ = 128.99 ± 0.01 Å^3 and $K_{0,175}$ = 9.45 ± 0.52 GPa (Röttger *et al*., 1994: Mitzdorf and Helmreich 1971).

The incompressibility of ADH I will become larger at lower temperatures; using ice Ih as an analogue (Proctor 1966: Dantl 1968), one might expect K_0 to become stiffer by ~1.2 GPa from 174 K down to absolute zero: i.e., the estimated incompressibility of deuterated ADH at 0 K is ~8.2 GPa (see also Sec. 8.1.2.3). The calculated bulk modulus for hydrogenous ADH I in the athermal limit is 10.7 ± 0.5 GPa (Chapter 7); after correcting this for the 1.7 % error in V_0

(see Sec. 8.1.2.1), my modified K_0 is ~9.7 GPa. Hence the estimated 0 K value for deuterated ADH I from experiment is 1.5 GPa (or ~15 %) smaller than the calculated value, a perfectly reasonable difference to attribute purely to the differing strengths of hydrogen versus deuteron bonds. In both glacial ammonia and water ice the bulk moduli of the deuterated solids are significantly smaller than those of the hydrogenous solids (Mitzdorf and Helmreich 1971: Voitovich *et al*., 1971). At 90 K, the isothermal bulk modulus of ND_3 is 15 % smaller than for NH_3, and the difference increases with falling temperature (Voitovich *et al*., 1971). Similarly, the isothermal bulk modulus of D_2O is 2.6 % smaller than for H_2O at 145 K (Mitzdorf and Helmreich 1971). Again, the difference becomes larger at lower temperature, and may be as much as 10 % at absolute zero. Based on these experimentally observed differences I conclude that my corrected first principles calculations actually reproduce the incompressibility of hydrogenous ADH I very well indeed. Brillouin scattering studies of $NH_3.2H_2O$ and $ND_3.2D_2O$ crystals would resolve this question.

The first pressure derivative of the bulk modulus, $K'_{0,174}$, is quite large (9.56 ± 1.28), which is typical for a very soft material near to its melting point, and will become smaller as the crystal is cooled and it stiffens. My calculated value of $K'_{0,0}$ = 5.44 ± 0.19 from *ab initio* calculations (Chapter 7), agrees very well with the experimental value of $K'_{0,0}$ = 5.41 ± 0.33 reported in Sec. 8.1.2.2 derived from the fitting of Eq. 8.1 with two Debye temperatures.

8.1.2.3. The Grüneisen ratio, and adiabatic bulk modulus

Thermodynamic quantities, such as C_V and C_P, are related to elastic properties, such as the isothermal bulk modulus, K_T, or the adiabatic bulk modulus, K_S, by the Grüneisen ratio, γ, according to equations 8.6 and 8.7.

$$\gamma = \frac{\alpha_V K_T V_m}{C_V} = \frac{\alpha_V K_S V_m}{C_P} \tag{8.6}$$

$$\frac{C_P}{C_V} = \frac{K_S}{K_T} = \left(1 + \alpha_V \gamma T\right) \tag{8.7}$$

The neutron diffraction measurements provide values for the molar volume, V_m, as well as α_V and K_T at 174 K. I can employ the previously measured values of C_P (Chan and Giauque 1964) to solve for the unknowns, C_V, K_S, and γ. The calculated values of these parameters at 174 K are thus C_V = 94.603 J mol^{-1} K^{-1}, K_S = 7.415 GPa, and γ = 1.148. This value for the Grüneisen ratio is interesting because substituting it into the result for ($K_{0,0}$ / γ) = 7.163 GPa, as

found in Sec. 8.1.2.1, yields $K_{0,0}$ = 8.224 GPa. This is very close to the incompressibility at zero Kelvin I estimated in Sec. 8.1.2.2 by assuming that ADH stiffens at the same rate as ice Ih. Hence, it is reasonable to postulate a model in which γ is temperature invariant and thus estimate $K^{T}_{0,T}$ and $K^{S}_{0,T}$. Figure 8.9 shows the temperature dependencies of K_T and K_S found by assuming γ = 1.148 from 0 –176 K.

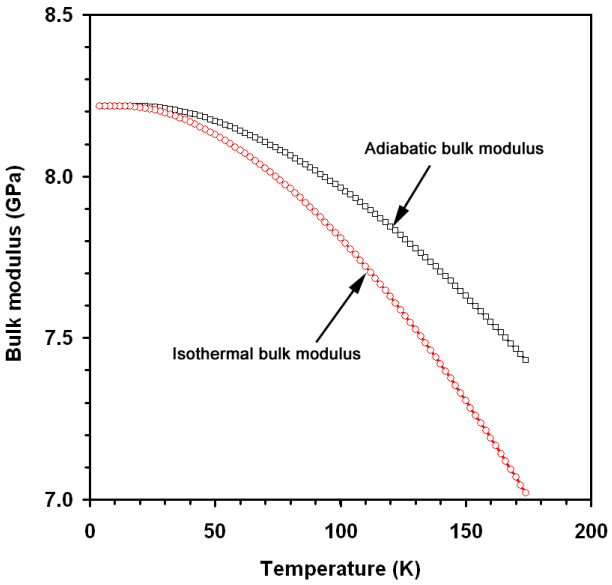

Figure 8.9. The model temperature dependencies of the adiabatic bulk modulus, K_S, and the isothermal bulk modulus, K_T, determined by assuming a temperature invariant Grüneisen ratio of 1.148.

8.1.2.4. The crystal structure

The structure of ADH I (See Chapter 7) consists of two crystallographically distinct water molecules hydrogen bonded into a three dimensional zeolite-like network. This network has large open channels within which ammonia molecules are sited. At high homologous temperatures, the water molecules are known to be orientationally disordered (Loveday and Nelmes 2000), and this is described using partially occupied deuteron sites. Hence ADH I may be termed an "isotropic glassy crystal."

In Chapter 7, I proposed that ADH I should undergo and ordering transition to an antiferroelectric structure at ~140 K, resulting in a lowering of symmetry from $P2_13$ to $P2_12_12_1$. This appeared to be supported by some experimental evidence.

However, during the pre-annealing data collection, no evidence of such a transition was observed. At all temperatures from 174 K down to 4.2 K the observed diffraction pattern was well fitted by the disordered structure. The refined structure at 4.2 K is given in Table 8.I. The sample was subsequently held at 120 K for 36 hours and examined further during warming from 40 K to 160 K. Again, the observed structure was that of the cubic disordered phase at all

temperatures (see Appendix 1 for the tabulated structure refinements). No sign of ordering below the predicted transition temperature was seen. Indeed, as Fig. 8.10 shows, there is no significant difference between the pre-annealing diffraction pattern and the post-annealing diffraction pattern at 40 K.

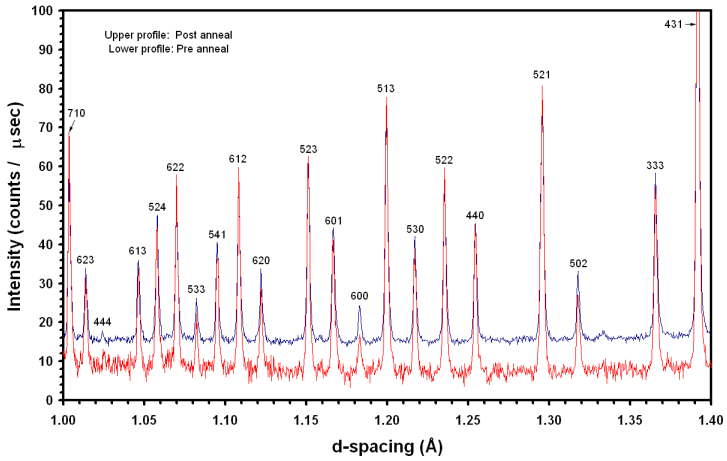

Figure 8.10. Diffraction patterns acquired at 40 K from the pre-annealed ADH I sample, and from the sample annealed at 120 K for 36 hours. There is no discernible difference in the peak widths between the two patterns which would be indicative of strain broadening following a partial ordering transformation. Note, that the pre-annealing pattern is noiser; data collection was just 10 minutes compared with ~100 minutes for the post-annealing pattern. The post-annealing pattern has been displaced upwards for ease of viewing.

Clearly the transition to the ordered phase (which, thermodynamically, *must* be more stable than the disordered phase at zero pressure and temperature) is frustrated by kinetics. The transition apparently takes place at a temperature where the configurational freedom (the mobility of the deuterons) is negligible; i.e., much below 140 K, and probably below 100 K. This is the same phenomenon which frustrates the ordering transition in pure ice Ih (Suga 1997). The question remains, however, "What is responsible for some of the experimentally observed changes near 140 K in, for example, the dielectric properties?" I have observed no microscopic explanation for these changes.

8.1.3. Summary

I have completed the first detailed neutron powder diffraction study of deuterated ammonia dihydrate across the full range of pressure and temperature conditions under which the low-pressure phase is stable (0 - 176 K at ambient pressure, and 0 - 0.45 GPa at 174 K). This has allowed a determination of the equation of state of ADH I, providing values for the thermal

expansivity, incompressibility, and the functional dependence of the internal energy on temperature. My earlier first-principles calculations are found to be in agreement with these experimental results. These properties can be used to place constraints on interior models of large icy moons in the outer Solar System, as I will demonstrate in the following chapter.

The transition to an ordered crystal was kinetically hindered on the timescale of the experimental study, but might run to partial completion with further annealing (perhaps several hundred hours at ~50 K) and perhaps with a suitable dopant. Certainly, on the surface of icy planets, one might expect timescales of order 10^9 years to be adequate for the formation of ordered ADH.

8.2 The PEARL/HiPr Experiment

The phase diagram of ADH at high-pressure (up to ~ 7 GPa) was investigated using a diamond anvil cell (DAC) by Boone (1989). Solid-solid and solid-liquid phase transformations were detected by observing changes in the birefringence of the sample. Boone (1989) concluded that there were no polymorphic phase changes in ADH, but that at pressures > 2.5 GPa (depending upon temperature) ADH decomposed to ammonia monohydrate + ice. This has since been belied at lower pressure (0.5 GPa) by the experimental observation of a higher-density polymorph dubbed ADH II (Hogenboom *et al*., 1997: Loveday *et al*., 1999b). A similar DAC study of AMH purporting to observe no phase changes (Koumvakalis 1988) has also been superseded by neutron diffraction experiments revealing a wealth of new structures (Loveday *et al*., 1999a).

The questions posed in this second experiment are therefore rather straightforward; are there any new high-pressure polymorphs of ADH above 0.5 GPa, and what are their structures? Does ADH really decompose into AMH + ice at pressures exceeding 2.5 GPa?

The strategy for answering these questions can be summarised as 'squash it and see.' This poses several problems. Doing neutron diffraction experiments far below room temperature, and at pressures up to ~10 GPa, is not straightforward. Generating these pressures *in situ*, for the large sample volume needed, requires a rather large hydraulic press. Cooling such a device, or making rapid temperature changes, is not simple. The sample volume is necessarily much smaller than in a gas-pressure vessel (~100 mm^3 vs. ~2 cm^3) leading to greatly increased counting times. Furthermore, pressure determination requires the use of a calibrant (see below) which itself introduces additional Bragg peaks to the diffraction pattern.

This experiment was done using the Paris-Edinburgh high-volume press (Figure 8.11). The P-E cell incorporates its own integral 250-ton hydraulic ram, pressurised (at very low

temperatures) by a mixture of n-pentane and isopentane. The P-E cell, and its use in the study of low-Z materials is described further by Besson *et al*., (1992), Besson and Nelmes (1995), Klotz *et al*., (1996), Loveday *et al*., (1997), and Bailey (2003).

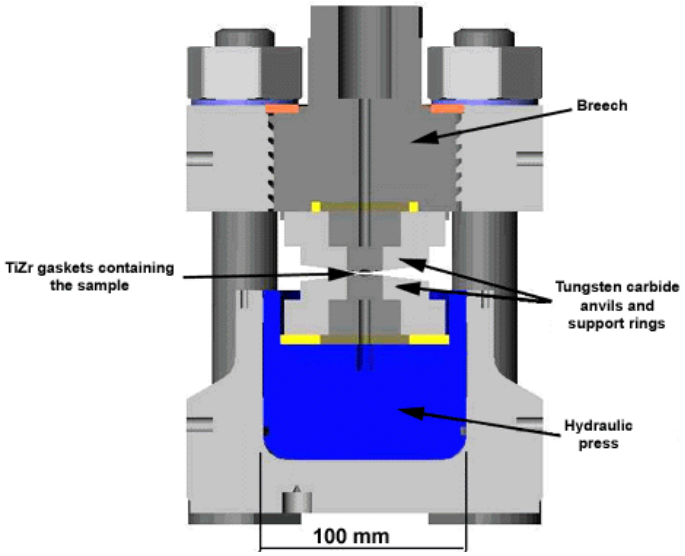

Figure 8.11. Schematic of the Paris-Edinburgh press. The TiZr alloy gaskets, barely 1 cm across, sit between opposed tungsten carbide anvils which are squeezed together by an integral hydraulic press. Neutrons enter from the top and are scattered from the sample and anvils. Detectors collect those neutrons emerging at 90° to the incident beam.

The hydraulic ram pushes opposing anvils together, squeezing the gasketed sample to high pressure. Up to ~10 GPa (on the V3 and V4 P-E cells) tungsten carbide anvils are used; up to ~25 GPa (on the V7 cell) sintered diamond anvils are required. Scattering from the anvils is reduced by coating them with cadmium foil and the use of radial collimators. Nonetheless, small parasitic peaks due to scattering from the anvils do appear in the sample diffraction patterns.

The sample itself is enclosed between TiZr null-scattering alloy gaskets (see 1.2.2). A recent development in gasket shape (so-called encapsulated gaskets) maintains hydrostatic conditions to much higher pressures than previous gasket designs (Marshall and Francis 2002).

The P-E cell is purpose built for use on the S9 test beamline at ISIS, now known as the PEARL/HiPr beamline (see Fig. 1.12). The sample is situated ~12.6 metres from the target station, hence receiving a high neutron flux and achieving a moderate resolution; the 90° detectors have a *d*-spacing independent resolution of $\Delta d/d = 8 \times 10^{-3}$.

My initial aim was to crystallise ADH II directly from the liquid at ~0.6 GPa and then to compress the solid, observing any phase changes, until such time as it decomposed into AMH +

ice (or not). Given that this experiment was intended as an initial survey of the phase diagram, there was insufficient time to collect patterns of very high quality for structure solution (or even indexing). Hence, the results presented here are a general description of my observations and are not intended to be used for detailed crystallographic analysis.

In the following section (8.2.1) I describe the sample loading and data acquisition method. In section 8.2.2 I present the results of this experiment, detailing my observations of phase changes, and avenues of future investigation.

8.2.1 Experimental Method

8.2.1.1 Sample preparation and loading

The preparation of the liquid $ND_3.2D_2O$ solution was described in 8.1.1.1. This sample was stored in a refrigerator for approximately nine months prior to the PEARL experiment.

A small wad of silica wool was rolled into a ball and placed in the sample cavity of the lower gasket, along with a circular chip of polycrystalline lead (see 8.2.1.2). $ND_3.2D_2O$ solution was taken from its storage container and dripped onto the wool ball (at room pressure and temperature) using a syringe. The upper gasket was placed over the sample and then mounted between the anvils of the P-E cell. The gaskets were sealed under an applied load of ~ 7 tons. The P-E cell was then transferred to its loading cradle and craned into position in the PEARL beamline. The cradle sits inside a large cryotank in the beamline (Fig. 8.12), and the cell is cooled by drizzling liquid nitrogen over the sides of the P-E cell and allowing it to pool in the bottom of the tank. Warming is achieved by means of resistance heaters attached to the sides of the P-E cell.

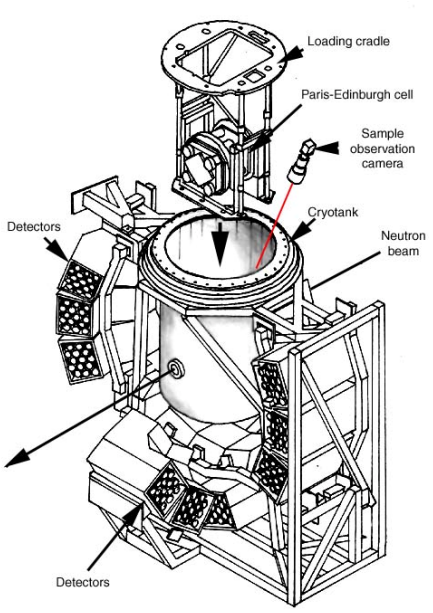

Figure 8.12.

The sample station on the PEARL beamline consists of a large cryotank into which the Paris-Edinburgh cell (mounted in its cradle) is lowered. A camera monitors the position of the sample through a transparent window in the top of the tank, and the sample can be remotely re-centred using this feed. The collection of frost on this window frequently required the closure of the neutron shutter so that frost could be wiped off manually.

A total of four loadings were carried out during the experiment. The first and fourth were successfully compressed up to an applied load of ~80 tons (~8.7 GPa). The second loading ended with a gasket failure at a load of ~60 tons; the third sample leaked under just 7 tons of load and no data was collected for this loading.

The second sample deserves particular comment. After dripping solution into the sample space, residual liquid in the syringe was expelled into a glass jar and observed to be a sky-blue colour. This was believed to be due to the formation of a nickel-ammonia complex, $[Ni(NH_3)_6]^{2+}$ (aq), caused by a reaction between residual ammonia from loading one and nickel in the needle of the syringe. Since this reaction sequestered a significant amount of ammonia, the sample was considerably off-stoichiometry. Indeed, large quantities of ice VI crystallised when this sample was cooled under pressure.

Temperature control was somewhat erratic during the first sample run since topping-up the N_2 in the bottom of the cryotank involved the liquid flowing over the sides of the P-E cell first. During a zealous initial top-up, the temperature of the cell was inadvertently reduced to 110 K, and took ~ 6 hours to stabilise at the required temperature (~170 K). In subsequent loadings, a new tube was introduced which allowed liquid N_2 to be delivered directly to the bottom of the tank.

If a cooling system could be devised which cooled *only* the anvils, many, if not all, of these problems would be overcome.

8.2.1.2 Data acquisition

Temperature monitoring was done with a calibrated Rh-Fe thermocouple. In the first loading, the thermocouple was mounted on the body of the P-E cell, ~5 cm from the sample; in this case, the temperature of the sample may have been as much as 15-20 K higher than the temperature indicated by the thermocouple (see below).

On the fourth loading, a second thermocouple was taped to one of the anvils, much nearer the sample. This thermocouple consistently read temperatures 10-15 K higher than the thermocouple on the P-E cell body, suggesting that the sample was marginally warmer (perhaps by ~2-5 K) than the temperature shown by the second thermocouple.

Pressure monitoring was achieved by use of a marker loaded with the sample; since the anvil geometry of the Paris-Edinburgh cell prevents a simple calculation of the pressure in the sample space from the applied load, a pressure calibrant must be used. Lead is a suitable pressure marker since it is relatively compressible, and unlikely to react with the sample (as opposed to sodium chloride, for example). Lead powder was tried, and quickly dispensed with, since it proved difficult to mix enough powder with the silica wool and ammonia-water solution. Instead, a small chip of polycrystalline lead, punched from a larger sheet, was used. In the first loading, the chip was 4 mm in diameter and 1 mm thick. It transpired that the scattering from this chip was very strong, and 3 mm diameter chips were employed in subsequent loadings.

The Pb equation of state that I used to determine the pressure was based on my own synthesis of literature values for the ambient-pressure thermal expansivity, and ultrasonic determinations of the temperature dependence of K_0 and K'_0 (e.g., Waldorf and Alers 1962: Miller and Schuele 1969: Touloukian *et al*., 1975: Kuznetsov *et al*., 2002, and references therein).

The pressure was determined using a Birch-Murnaghan equation of state,

$$P_{V,T} = \frac{3}{2} K_{0,T} \left(x^{7/3} - x^{5/3} \right) \cdot \left[1 + \frac{3}{4} \left(K'_{0,T} - 4 \right) \left(x^{2/3} - 1 \right) \right] \qquad (8.5)$$

where $x = V_{0,T} / V_{P,T}$; $V_{0,T}$, $K_{0,T}$, and $K'_{0,T}$ are found from temperature dependent polynomials;

$$V_{0,T} = 29.6496 \text{ Å}^3$$

$$a = 1.9301 \times 10^{-3} \text{ Å}^3 \text{K}^{-1}$$

$$b = 9.9177 \times 10^{-7} \text{ Å}^3 \text{K}^{-2}$$

$$K_{0,T} = 48.80 \text{ GPa}$$

c = 2.134 x 10^{-2} GPa K^{-1}

d = 6.762 x 10^{-6} GPa K^{-2}

$K'_{0,T}$ = 5.3944

e = 0.0011 K^{-1}

The estimated precision of these pressure determinations is ± 0.1 GPa.

In samples 1, 2, and 4, the liquid was compressed under a ram load of 12-13 tons (~1 GPa). It was then cooled to a target temperature of 170 K. During cooling and crystallisation the load would drop (due to thermal contraction of the sample) and require pumping up again. Diffraction patterns were acquired in 30-35 minute periods. In this way it was possible to observe crystallisation as it occurred, usually over a period of several hours.

This data acquisition strategy of collecting 30-minute 'snapshots' was continued as the pressure was increased. When a phase change was observed, the pressure was held steady and a series of 30-minute patterns collected for later summation. Pressures were determined 'on the fly' from the [111] reflection of the lead chip, using the EoS given earlier.

In the next section I will describe the evolution of the diffraction patterns with changing pressure and temperature for each of the successful loadings.

8.2.2 Results

8.2.2.1. Loading one

For each successful loading the sample was initially placed under a load of 12-13 tons (~1 GPa) at room temperature. Figure 8.13 is an example of the diffraction pattern seen under these conditions. It exhibits peaks from the Pb pressure marker, the WC anvils, and a broad diffuse hump from the liquid sample. Cooling to ~170 K caused the pressure to drop by ~0.5 GPa as a result of thermal contraction and subsequent crystallisation.

During the first loading, crystallisation took ~3 hours to begin after reaching 170 K, and proceeded fairly rapidly thereafter. The Bragg peaks which appeared at this point seem to belong to a single phase of ADH (Fig. 8.14) and do not match those of ADH II (Fig. 8.4): this phase was later named ADH III.

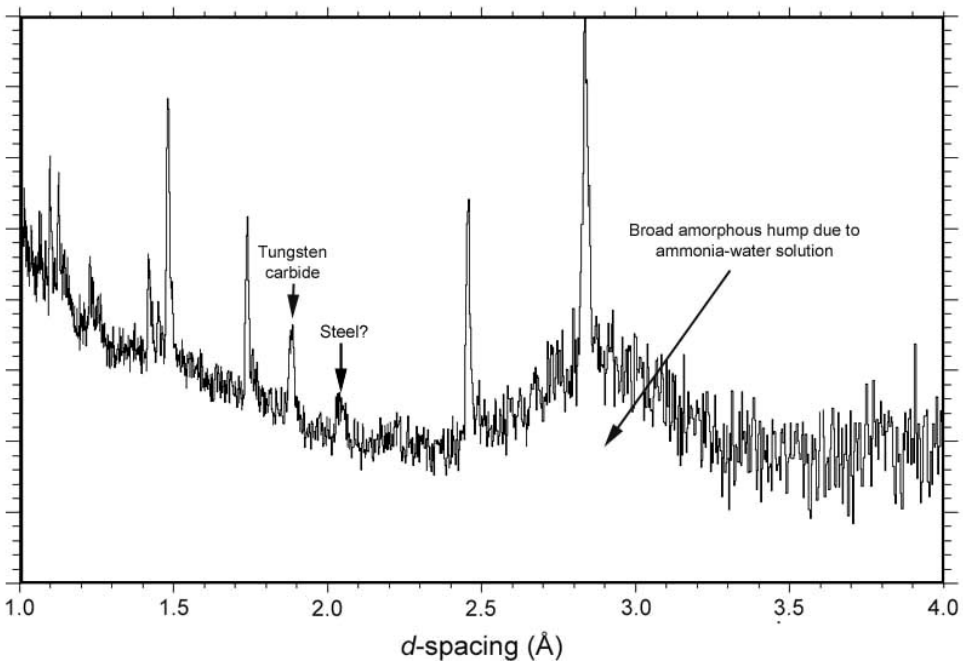

Fig. 8.13. Loading 1: Diffraction pattern from the liquid solution (+Pb) under an applied load of ~13 tons at room temperature (0.96 GPa). All of the sharp peaks are due to scattering from the lead chip, except for the peak marked 'Tungsten carbide' which is due to scattering from the anvils, and the peak at ~2.05 Å that is probably from the steel binding seats around the anvils. The broad hump centred at 2.8 – 2.9 Å represents diffuse scattering from the ammonia-water liquid. I can be certain that it is not due to the silica wool, since the hump vanishes when the liquid crystallises. [~2 hour integration]

Upon compression, ADH III transformed to an amorphous solid at ~2.1 GPa (at 130 K), indicated by the disappearance of the ADH III peaks and the return of the large diffuse hump. Some structure gradually emerged, but the resulting diffractogram displayed only broad humps rather than sharp peaks (Fig. 8.15). This is suggestive of a nano-crystalline solid rather than a good coherently scattering powder. This phase was observed at 3.4 GPa (170 K), and 4.8 GPa (170K) before showing signs of a further transformation at 5.4 GPa (170 K). In the diffraction pattern collected at 6.3 GPa (170 K), the phase transition was seen to be complete.

Overleaf: Fig. 8.14. Loading 1: Diffraction pattern from the newly crystallised phase (ADH III) under a load of 13.8 tons at ~175 K (0.56 GPa). The peaks marked with a red star are from the lead chip, and the tungsten carbide peak is marked with a green dagger. This new phase of ADH does not match the ADH II pattern seen in previous experiments (see Fig. 8.4). [~2.5 hour integration]

Fig. 8.14. (*Caption on preceding page)*

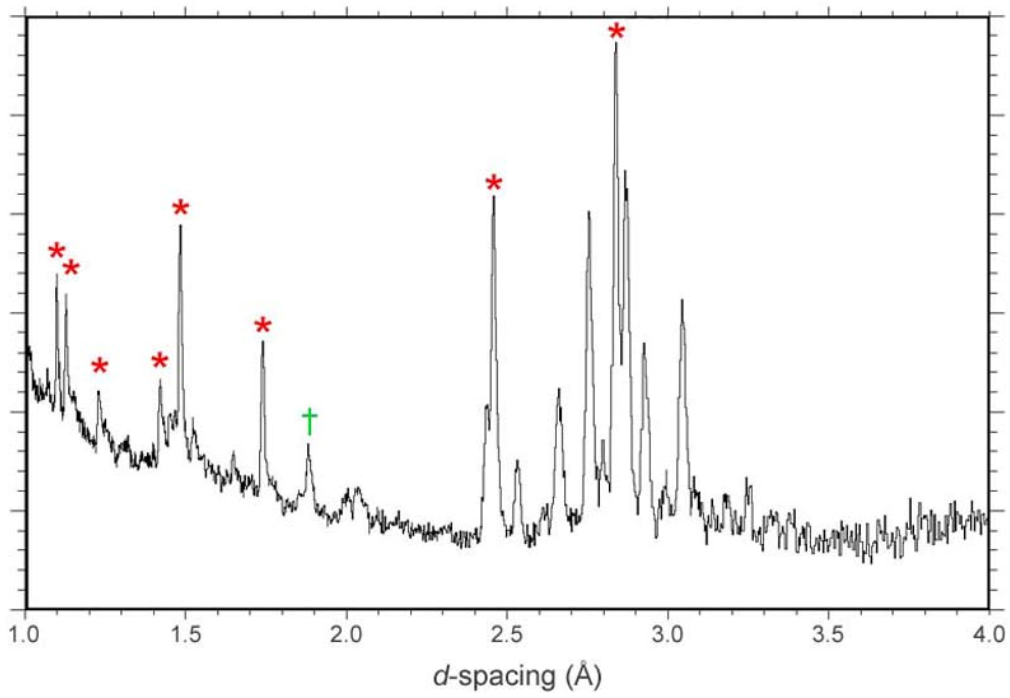

Below: Fig. 8.15. Loading 1: Diffraction pattern of Intermediate Phase A under a load of 50.7 tons at ~180 K (4.8 GPa). The broad humps marked with red stars are those peaks which are not attributable either to the lead pressure marker or interference from the anvils. [~3 hour integration]

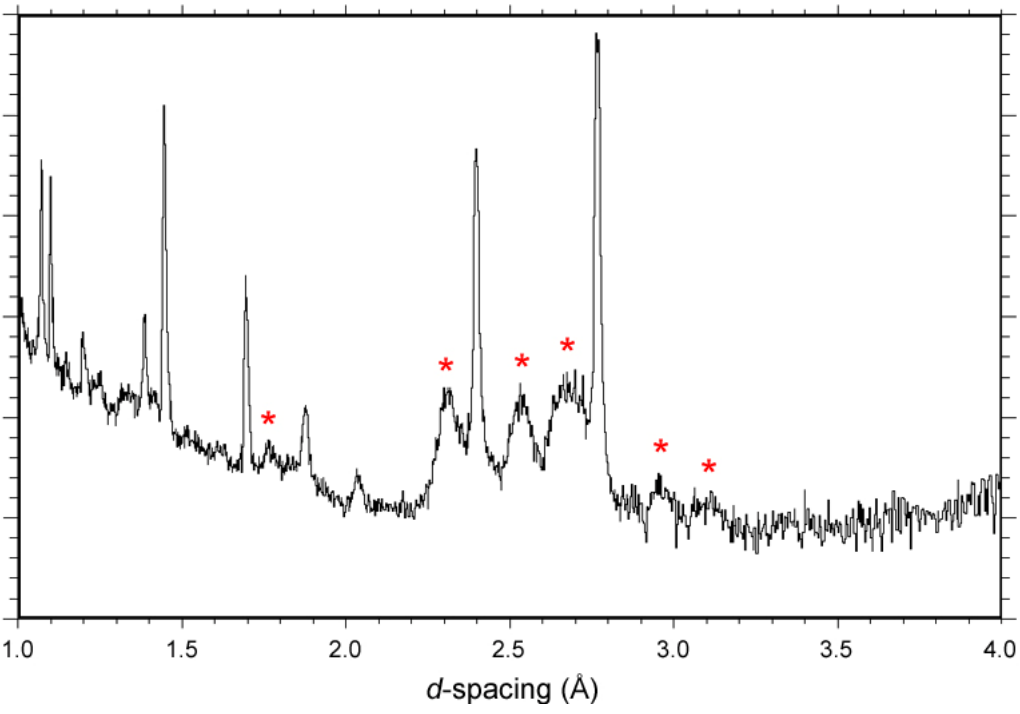

The new pattern (Fig. 8.16) contains only one obvious peak from the sample (the rest are from Pb + WC). This must be a stoichiometric phase of ADH since there is no evidence of any other ice phase present. The pattern is remarkable for its similarity to that of the high-pressure ammonia monohydrate phase, AMH VI (Loveday and Nelmes 1999a). AMH VI is a body-centred-cubic crystal which exhibits substitutional disorder, prompting the discoverers to suggest that a solid-solution series could exist between ice VII and AMH VI. This second new crystalline phase of ADH (later named ADH VI) may well support that hypothesis. If the single large peak at d = 2.310 Å is indeed the [110] peak of a cubic crystal then the cell parameter is 3.267 Å. Compare this with 3.2727 Å for AMH VI at 6.5 GPa, 285 K. There is also evidence of the [211] peak at 1.33 Å; the [220] peak at 1.155 Å is hidden by the lead [004] peak.

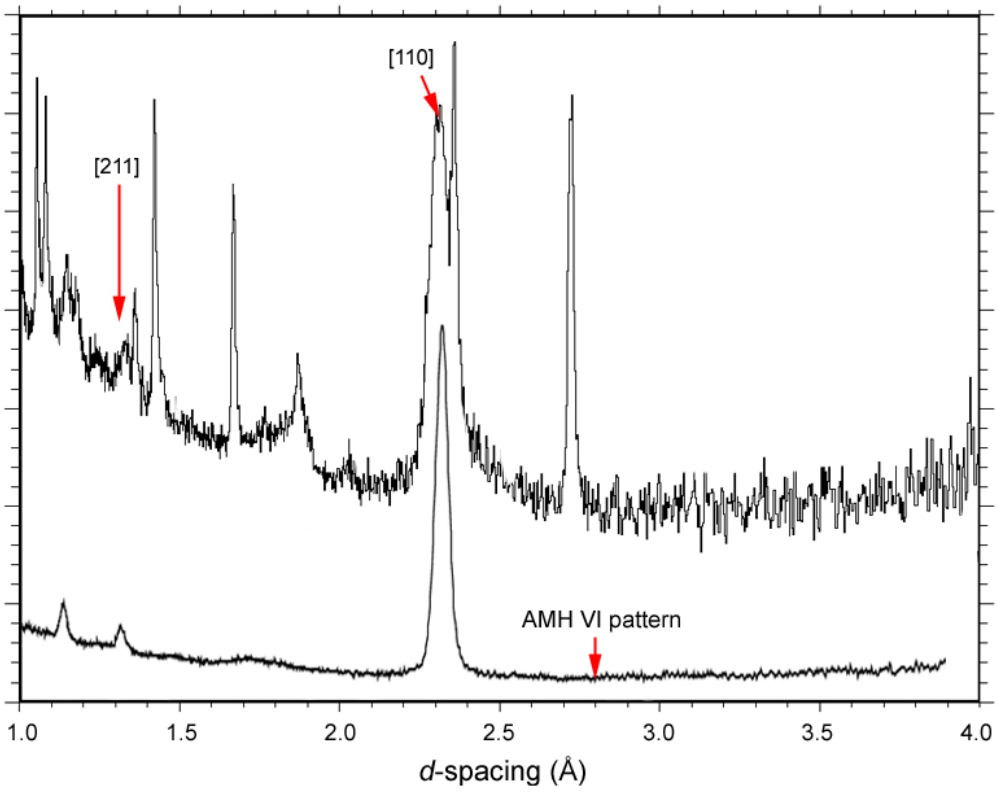

Fig. 8.16. Loading 1: Diffraction pattern acquired under a load of 80 tons at ~170 K (8.6 GPa). Apart from the peaks due to Pb and WC, there is now only a single large peak at 2.310 Å from crystalline ammonia hydrate. This peak is interpreted as the [110] reflection from a body-centred cubic structure with a unit cell of 3.267 Å. A lumpy peak at around 1.33 Å may be the [211] reflection from this phase. Underneath is the diffraction pattern of AMH VI collected by Loveday and Nelmes (1999a) at 6.5 GPa, 285 K. This has been shifted to the left by 0.1 Å in order to bring it into coincidence with my ADH VI pattern.

ADH VI was observed at 6.3, 7.3, and 8.6 GPa (at 170 K), warmed to ~190 K and decompressed to 4.5 and 2.7 GPa. At, ~0.6 GPa it back transformed to a third new crystalline phase of ADH (later named ADH IV), although this was not recognised until it was seen in later experimental runs (see 8.2.2.2 and 8.2.2.3 and Fig.8.19).

It is straightforward to see how reasonable is the hypothesis that ADH VI has the same structure as AMH VI but a different stoichiometry. I have adapted the AMH VI structure determined by Loveday and Nelmes (1999a) to produce a substitutionally and orientationally disordered bcc ADH structure. In space group $Im\bar{3}m$, the 2*a* sites (at 0,0,0) are ⅔ occupied by oxygen atoms and ⅓ occupied by nitrogen atoms. Deuterium atoms are distributed over two sites; 16*f* (0.1722, 0.1722, 0.1722) with an occupancy of 0.372, and 24*h* (0.2109, 0.2109, 0) with an occupancy of 0.044. This yields the correct number of deuterium atoms per unit cell (seven), and mimics the directional distribution seen in AMH VI. This model was used in a Rietveld refinement of the ADH VI powder pattern (Fig. 8.17) and yielded an acceptable fit.

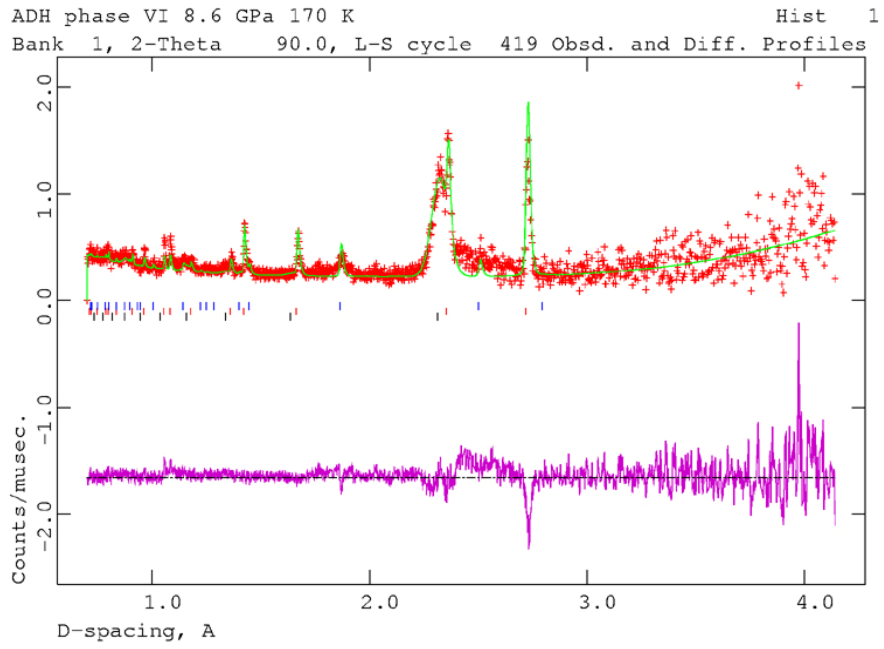

Fig. 8.17. GSAS Rietveld refinement of the ADH VI powder pattern using a model based on the structure of AMH VI (Loveday and Nelmes 1999a) – see text. The observed pattern is marked by red crosses, the fitted pattern by the green line, and the difference curve by the purple line underneath. The most serious mismatches are in the line shape of the ADH phase and in the intensities of the lead peaks (probably due to preferred orientation). Tick marks, from the top down, are the peak positions of tungsten carbide, lead, and ADH VI.

8.2.2.2. Loading two

As described in 8.2.1.1, loading two was contaminated by nickel from the needle of the loading syringe. This was later found to have changed the stoichiometry of the sample and it is therefore no surprise that the first phase to crystallise from the liquid was Ice VI. As Figure 8.18 shows, there is a considerable amount of diffuse intensity from the residual liquid in the broad hump centred near 2.8 Å.

The sample was warmed in the hope of melting the ice VI crystals. Instead, approaching 195 K, further peaks from a new hydrate emerged (Fig. 8.19). I initially feared (unaware of the shift in stoichiometry) that the sample had disproportionated to ice + AMH. However, the new hydrate phase was seen again in stoichiometric loadings (8.2.2.3) and was subsequently identified in the decompressed pattern from loading one (8.2.2.1). Hence, this must be a stoichiometric phase of ADH, and I identify it as ADH IV.

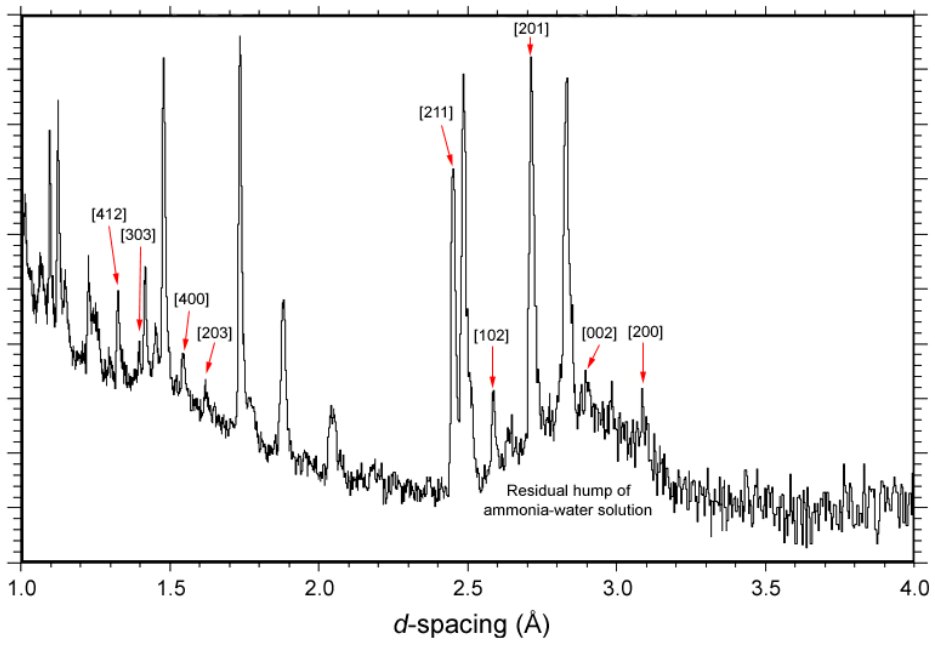

Fig. 8.18. Loading 2: Diffraction pattern acquired at an applied load of 15.3 tons at ~180 K (0.52 GPa). Aside from the obvious peaks due to Pb and WC, a new set of peaks has appeared from ice VI. The Miller indices of the ice VI peaks are indicated. The intensities of several of these peaks are anomalous, in particular the [102] peak is rather weaker than expected; this may be because of preferred orientation in the ice VI crystals. The ice VI peaks in this pattern yield a tetragonal unit cell with a = 6.1806Å, and c = 5.7008Å. Note that there is still a large diffuse hump from the remaining ammonia-water solution. [~6 hour integration]

The mixture of Ice VI + ADH IV was compressed and patterns collected at 1.2 and 2.1 GPa. At 2.6 GPa there was a change which appeared to involve the transition from ice VI to ice VIII

(Fig. 8.20). There is a considerable amount of strain broadening in all of the peaks, making a detailed analysis impossible at present. The mixture of ice VIII + ADH was compressed, patterns being collected at 3.3, 4.7, and 6.4 GPa (~190 K). At a load of ~ 66 tons the gasket burst, ending the run. The sample was decompressed to 55.2 tons, but the Pb [111] peak yielded a sample pressure of 0 GPa.

Fig. 8.19. (*Caption on following page)*

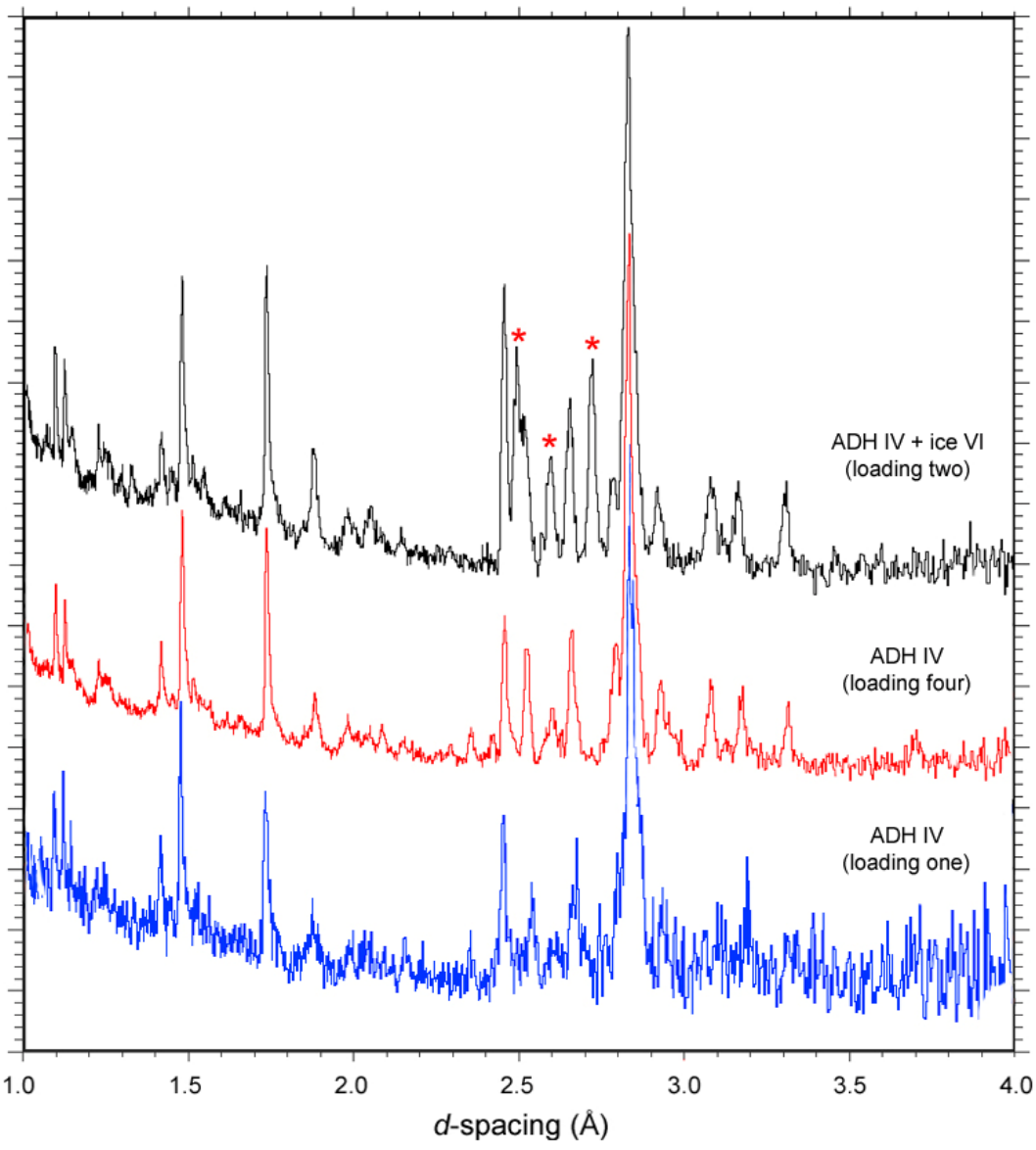

Preceding page: Fig. 8.19. The upper plot (in black) is the diffraction pattern from sample two at a load of 15.6 tons at ~190 K (0.65 GPa). This pattern now contains peaks from Pb, WC, ice

VI, and a new ammonia hydrate phase. The strongest Bragg peaks due to ice VI are marked with red stars. [~3 hour integration]

The middle plot (in red) is the diffraction pattern from sample four at a load of 16.3 tons at ~200 K (0.65 GPa). This pattern contains peaks from Pb, WC, and the same hydrate phase seen in the upper plot. Clearly, the ice VI peaks (the three largest peaks are marked with red stars) are no longer present. [~2.5 hour integration]

The lower plot (in blue) is the diffraction pattern from sample one at a load of 1.8 tons at 190 K (~0.55 GPa) following decompression of ADH VI. This pattern, although noisy, is clearly that of ADH IV seen in later loadings. [~30 minute pattern]

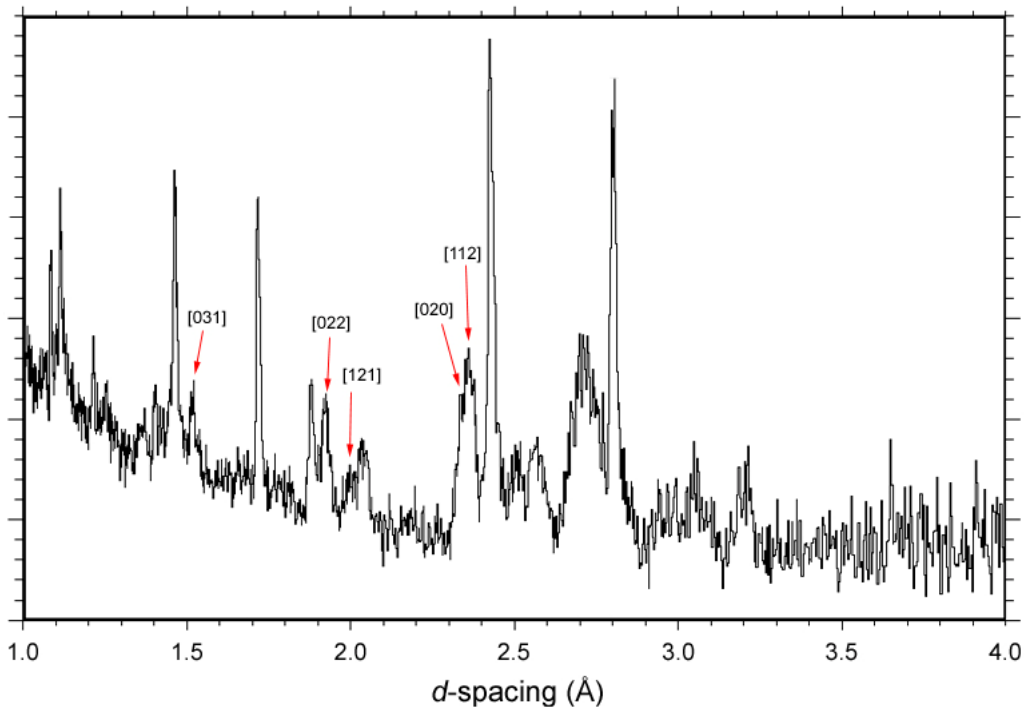

Fig. 8.20. Loading 2: Diffraction pattern acquired under a load of 30.5 tons at 190 K (2.6 GPa). Ice VI which had previously been present has apparently transformed to ice VIII. The Miller indices of the strongest ice VIII peaks are indicated, and these are consistent with a tetragonal unit cell, a = 4.670 Å, c = 6.767 Å. Using the EoS of ice VIII (Appendix 2), this cell volume corresponds to a pressure of 2.59 GPa at 190 K, in reassuring agreement with the lead calibrant (which actually yields 2.58 GPa). All of the broadened peaks at d-spacings of 2.5 Å and above are from the strained ADH sample.

8.2.2.3. Loading four

During cooling, this sample showed signs of crystallising ice VI again. It was decided to try a different approach to that used in loading two. The sample was warmed to ~200 K, where it

was completely liquid. It was then compressed to ~0.65 GPa in the hope of pressure-freezing the liquid. This had the anticipated result, producing an ice-free pattern from ADH IV (Fig. 8.21).

ADH IV was compressed, patterns being collected at 1.3 and 1.9 GPa. At 3.5 GPa, there was a change in the diffraction pattern marked by the appearance of a strong peak at ~2.32 Å (Fig. 8.22). Since the peaks are rather broad, it isn't possible to derive any useful conclusions from this pattern and I have called this structure 'Intermediate Phase B'.

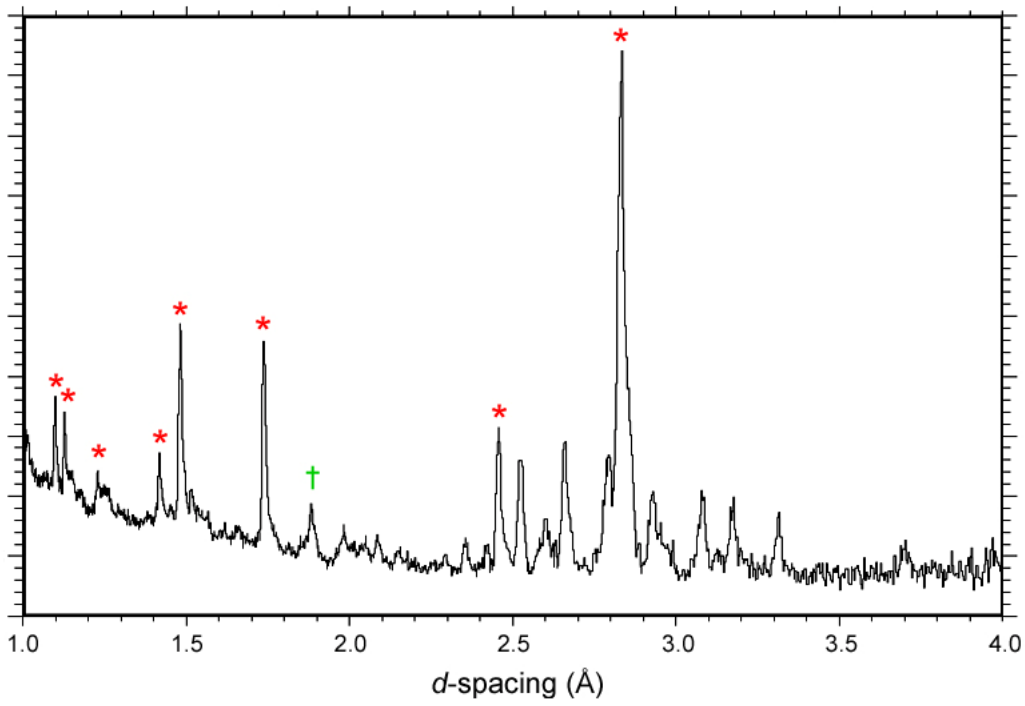

Fig. 8.21. Loading 4: The diffraction pattern of ADH IV (without ice VI) under a load of 16.3 tons at ~200 K (0.65 GPa). The tallest peak, near d = 2.8 Å, is a superposition of the lead [111] with a peak in the dihydrate sample. This and the other lead peaks are marked with a red star, and the strongest tungsten carbide peak with a green dagger. [~2.5 hour integration]

Compression to 6.7 GPa (at 200 K) manifested a further change to a much simpler and clearer diffraction pattern (Fig. 8.23). This pattern is characterised by peaks at 1.84 Å, 2.25 Å and 2.38 Å. Its simplicity is indicative of a single phase, and must therefore be a crystalline phase of ADH (later named ADH V). This experimental run was ended at high-pressure and no patterns were collected on decompression.

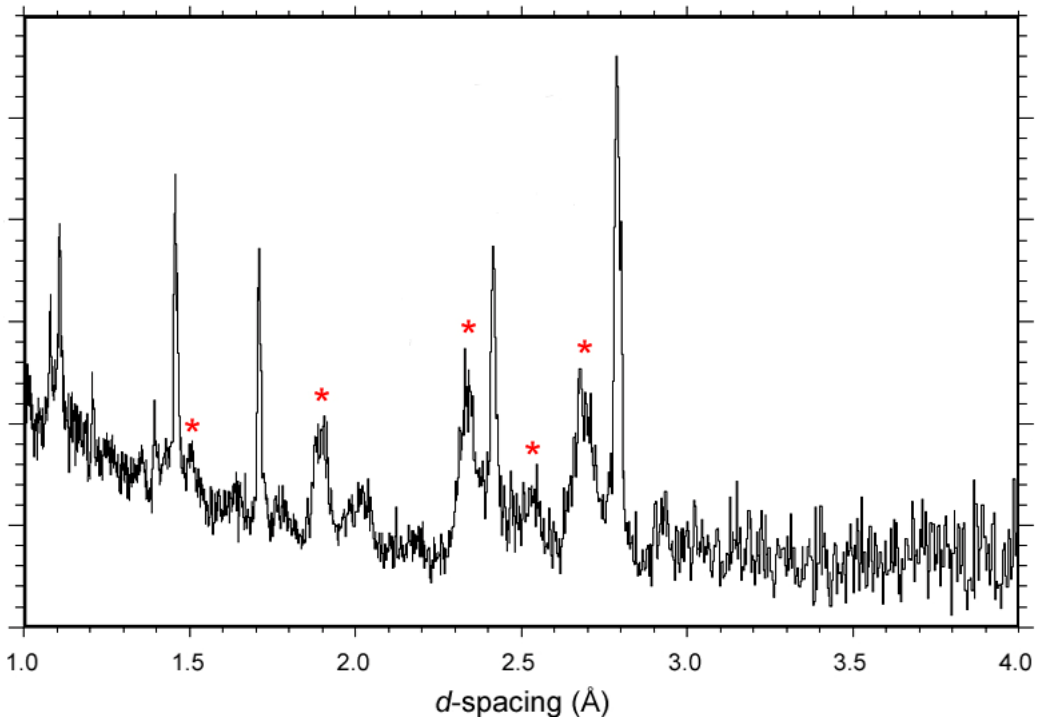

Fig. 8.22. Loading 4: Diffraction pattern of Intermediate Phase B collected under a load of 39.2 tons at 200 K (3.5 GPa). Broad peaks which appear to be due to scattering from the sample are marked with red stars. [~30 minute integration]

ADH V is intriguing; it is observed under very similar P-T conditions to phase VI, and its powder pattern (Fig. 8.23), in common with phase VI, is fairly simple. There are two possibilities: the structure of ADH V may be derived from that of ADH VI, perhaps by some kind of ordering process, or the structure may be wholly unrelated to phase VI.

If derived from phase VI, then there are a number of things which might have occurred. In the first instance, the unit cell may have been stretched, or squashed, along one axis to generate a tetragonal crystal. This is a tempting possibility since the two peaks at 2.38 Å and 2.25 Å could easily represent the splitting of the cubic [110] peak of ADH VI. A [111] peak arises near 1.84 Å from the loss of body centering in such a model. For a tetragonal distortion involving a compression of the *c*-axis, one would expect the peak at 2.25 Å to be roughly twice the intensity of the peak at 2.38 Å, and vice versa for a distortion involving an extension of the *c*-axis. Allowing for the intensity of the superposed lead [002] peak, I find that the ADH V peaks at 2.25 Å and 2.38 Å actually have the same intensity. This is inconsistent with the hypothesis that a tetragonal distortion has taken place.

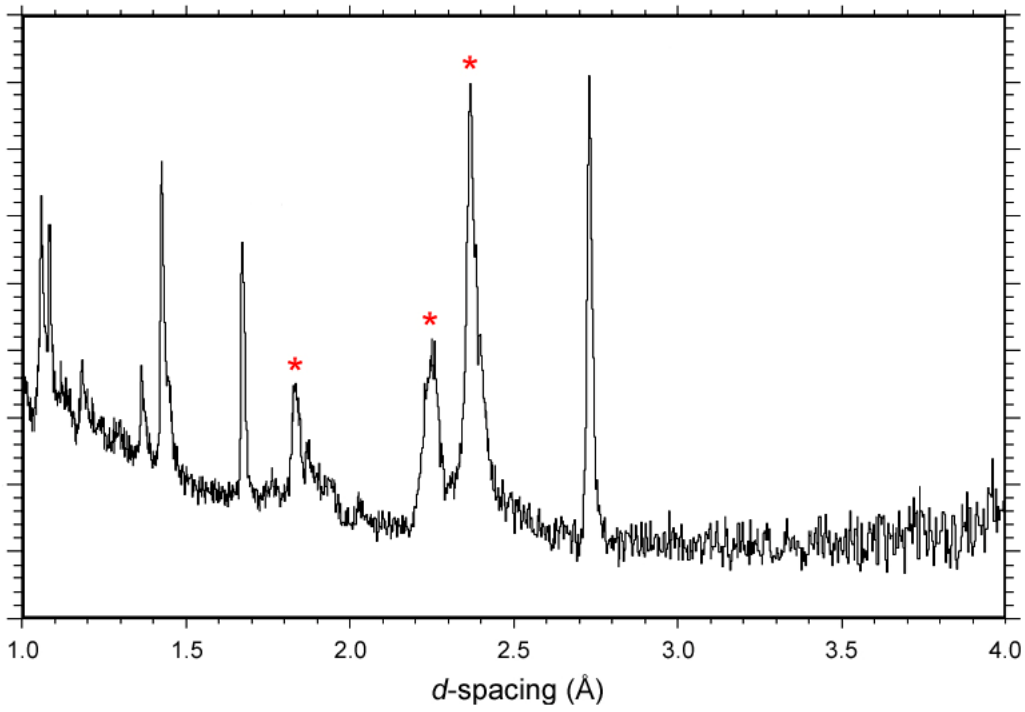

Fig. 8.23. Loading 4: Diffraction pattern of ADH phase V under a load of 77.9 tons at 200 K (8.1 GPa). There are just three peaks which are clearly from the sample, although the peak near 2.38 Å appears very strong because it is superimposed upon the lead [002] peak.

In the second instance, the ADH VI model unit cell may be stretched along a body diagonal to form a trigonal crystal. In this case, one finds that the calculated intensities of the peaks at 2.25 Å and 2.38 Å are very similar. However, the peak at 1.84 Å is of negligible strength, and the next strongest peak is observed at 1.64 Å with a calculated relative intensity of ~50%. This also differs from the observed pattern of ADH V where the peak at 1.84 Å is seen to have an intensity ~75% of the other two peaks.

An orthorhombic distortion, with two of the three axes very similar in length, can also reproduce the near equal intensities of the 2.25 Å and 2.38 Å peaks, but fails to produce a strong peak at 1.84 Å.

On balance, it does not seem likely that the ADH V structure is derived from the ADH VI structure.

8.2.3 The high-pressure phase diagram

Considerable interest in the behaviour of the dihydrate at high pressure has resulted in numerous attempts to reconcile apparent disagreements between high and low pressure

calorimetric data (Johnson and Schwake 1983: Johnson and Nicol 1985, 1987: Croft *et al*., 1988: Cynn *et al*., 1989: Hogenboom *et al*., 1989: Boone and Nicol 1991: Hogenboom and Kargel 1990). The problem has been resolved by Hogenboom *et al*. (1997) who claimed discovery of a new high-pressure phase - ammonia dihydrate II (ADH II) - which is stable above ~ 0.4 GPa at 170 K (Fig. 8.24). Little is known about ADH II at present, although Loveday *et al*. (1999a) reported a diffraction pattern acquired at 0.53 GPa and 170 K (on the POLARIS beamline at ISIS), and I also observed a phase I believe to be ADH II at 0.46 GPa and 175 K (on HRPD). These patterns are shown in Fig. 8.4.

Boone (1989) reported optical studies of ammonia dihydrate in a diamond anvil cell (DAC) up to ~7 GPa, including Raman spectra and images of crystals grown from the melt. No phase transitions were documented between ambient pressure and ~ 2.5 GPa, whereupon ADH appeared to break down into a mixture of AMH + ice VII (Fig 8.25). Boone also attempted to acquire X-ray diffraction patterns at high-pressure but was not successful (S. C. Boone, personal communication).

It has recently been suggested (Pargamin *et al*., 2002: Mousis *et al*., 2002b) that there is a discontinuity in the peritectic melting curve near 0.6 GPa, which may represent further high-pressure phase transitions to one or more post-ADH II polymorph (Fig. 8.24), as discussed shortly.

Workers in the Shimizu Laboratory, Gifu University, Japan, claim to have grown single crystals of ADH (unknown phase) at 0.9 GPa (unknown temperature), which they intend to use to measure elastic constants by Brillouin spectroscopy (T. Kume personal communication).

It is therefore of interest to see how the current experimental work fits in with the existing P-T phase relations for ADH.

The first observation, on HRPD, was the melting of ADH I at 0.46 GPa upon warming from 174 to 179 K. This agrees well with the extension of the peritectic melting line of ADH I to this pressure (see Fig. 8.24). The subsequent crystallisation of ADH II at this P-T point also agrees with the known phase diagram. I cannot make any inference about the equilibrium phase boundary between ADH I and ADH II; I do not believe there is enough data in the literature at present to constrain its slope.

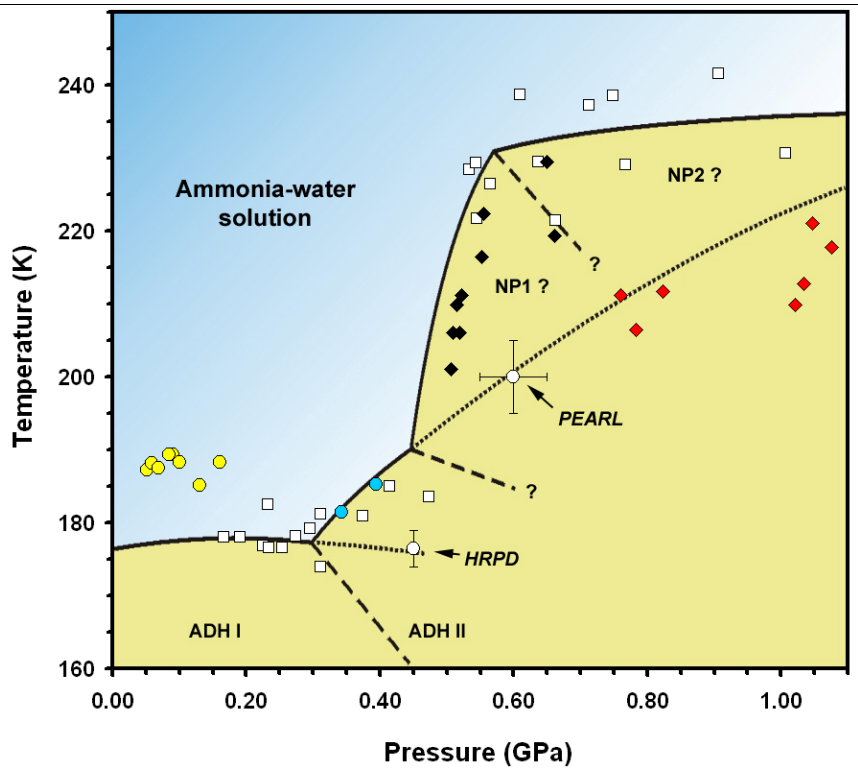

Figure 8.24. The proposed low-pressure phase diagram for ADH combined with my observations from the HRPD and PEARL experiments. The thick line is the suggested peritectic melting line, amended above 0.45 GPa by Mousis *et al*. (2002b), and their peritectic data are shown as white squares. Filled black diamonds show the P-T conditions under which Mousis *et al*. (2002b) observed no melting at all, and the yellow circles denote ice I + liquid (their experiment was at 25 wt % NH_3). The peritectic of ADH I is extended as a dotted line, and intersects nicely with my observed melting point on HRPD. The high-pressure ADH melting curve is also extended as a dotted line, and the pressure-freezing point from loading four of the PEARL experiment agrees well. Red diamonds and blue circles are peritectic melting observations of the UCLA and Lafayette groups, respectively (Hogenboom *et al*., 1997). Mousis *et al*. (2002b) interpret their peritectic as evidence of two new high-pressure polymorphs of ADH; NP1 and NP2.

In the PEARL experiment, crystallisation normally ensued after several hours of undercooling. However, melting took place quite quickly, and pressure freezing was observed to be instantaneous. There was a single instance, in loading four, when the sample was melted and then pressure frozen (the point marked 'PEARL' on Fig. 8.24). In spite of the relatively large uncertainty in P and T, this observation is clearly more consistent with the observations of Hogenboom *et al*. (1997) than with the recent findings of Mousis *et al*. (2002b).

Is the inferred peritectic of Mousis *et al*. (2002b) reasonable? A qualitative mental application of the Clausius-Clapeyron equation suggests that NP2 must be less dense than NP1, which cannot be possible. A qualitative analysis runs as follows.

The Clausius-Clapeyron equation relates the slope of the phase boundary, dP/dT (in this case the melting line), to the volume change, ΔV, and the entropy change, ΔS, as

$$\frac{dT}{dP} = \frac{\Delta V}{\Delta S} \tag{8.6}$$

The peritectic melting temperature (Mousis *et al*., 2002b) of NP1 at 0.5 GPa is 214.7 K, and the gradient, dT/dP = 358.7 $x10^{-9}$ K GPa^{-1}. That of NP2 at 0.6 GPa is 231.5 K, and the gradient is 17.0 $x10^{-9}$ K GPa^{-1}. The EoS of the liquid (Croft *et al*., 1988) yields densities of 1004.5 kg m^{-3} (0.5 GPa, 214.7 K) and 1011.9 kg m^{-3} (0.6 GPa, 231.5 K). If one takes ΔS equal to that measured for ADH I (Chan and Giauque 1964), 39.74 J K^{-1} mol^{-1}, then the value of ΔV at 0.5 GPa is 1.425 $x10^{-5}$ m^3 mol^{-1}, giving a density for NP1 of 1375.8 kg m^{-3}. At 0.6 GPa, ΔV is found to be 6.771 $x10^{-7}$ m^3 mol^{-1}, giving a density for NP2 of 1025.1 kg m^{-3}.

The estimated density of NP1 is not unreasonable, and is similar to the density of ice VI under comparable P-T conditions. However, the density of NP2 is clearly anomalous. In fact, to make the density of NP2 greater than NP1 with such a shallow melting curve requires the melting entropy of NP2 to be 21 times larger than that of ADH I. Since the entropy of the liquid at 230 K (at ambient pressure) is just 179 J K^{-1} mol^{-1}, this is impossible. One must conclude that the interpretation of Mousis *et al*. (2002b) is incorrect.

Three solutions present themselves:

- The observations of Mousis *et al*. (2002b) record no more than the natural metastability in the ammonia-water system at low temperature.
- Mousis *et al*. (2002) observed the melting of an intermediate hydrate with a different stoichiometry (say $NH_3.3H_2O$) that is only stable at higher pressure.
- The observations record the melting of one high-pressure phase not two.

My own observations of the freezing point support either of the first two possibilities. Further work is necessary to clarify this point.

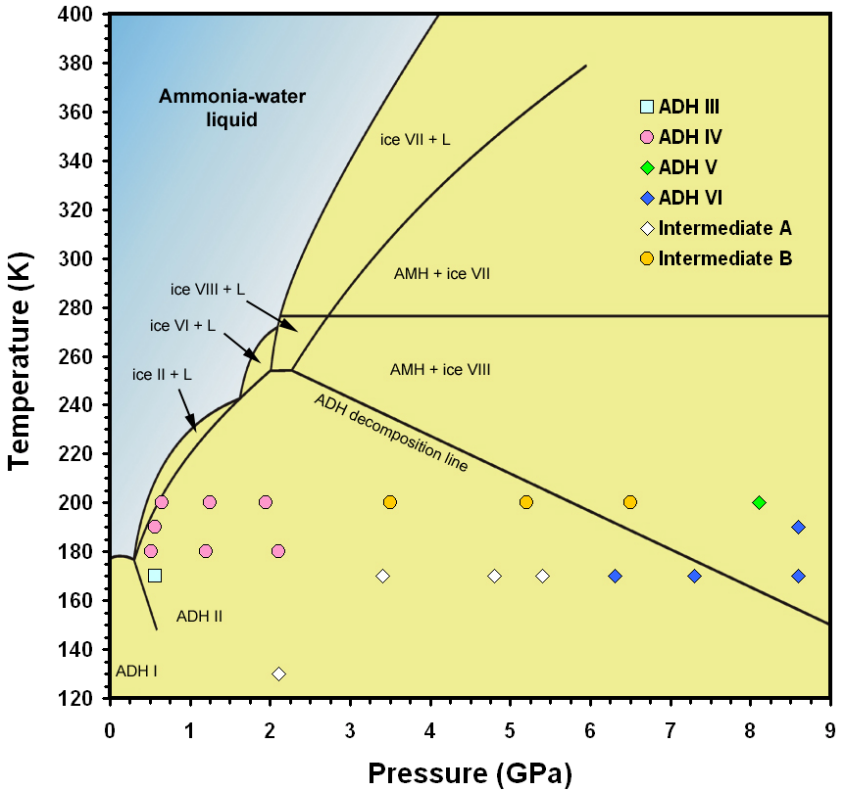

Figure 8.25. The expected high-pressure phase diagram for ADH combined with my observations from the PEARL experiment. Phase boundaries are a synthesis of Boone (1989) and Hogenboom *et al.* (1997). My observations – indicated by the coloured symbols - clearly do not agree with the optical work of Boone (1989).

Determining solid-solid phase boundaries at low-temperature is challenging. Like the monohydrate system, and the pure ice system, there is a great deal of metastability evinced at low-temperature. Phases often require much undercooling or overcompression in order to undergo transformations, and may even end up forming wholly metastable structures or glasses.

In this work, ADH III was observed under similar P-T conditions to ADH II whilst ADH IV appeared to be the liquidus phase at ~0.5 – 0.7 GPa (see Fig. 8.25). In the 2 – 6 GPa region there were phase transitions, but the quality of the crystalline powders were rather poor, and it is not at all clear what was seen (Intermediate Phases A and B). At still higher pressure, and again under very similar P-T conditions, I observed phases V and VI of ADH. I believe I can state categorically that ADH did not decompose to AMH + ice. The high-pressure patterns were consistent with the presence of only one phase, which must be stoichiometric ADH.

8.2.4 Summary

The PEARL experiment resulted in the observation of four new crystalline phases of ADH and two phases of uncertain nature. These observations show that ADH does not break down to AMH + ice under pressure, as had been thought.

The new phases require further study to establish their structures. At the time of writing, I have applications submitted to study phases III, IV, V, and VI on PEARL at ISIS (using the Paris-Edinburgh cell once more), and to study Intermediate phases A and B on D2B at ILL (in clamped McWhan-type pressure cells). I have been granted beam time to study ADH II on HRPD at ISIS (using a TiZr or BeCu gas pressure vessel). Future work will eschew the pressure calibrant, since it is now possible to broadly estimate the pressure from the load, the lead peaks being seen to interfere with the reflections from the sample more often than not.

Figure 8.26. Graphical summary of observed diffraction patterns.

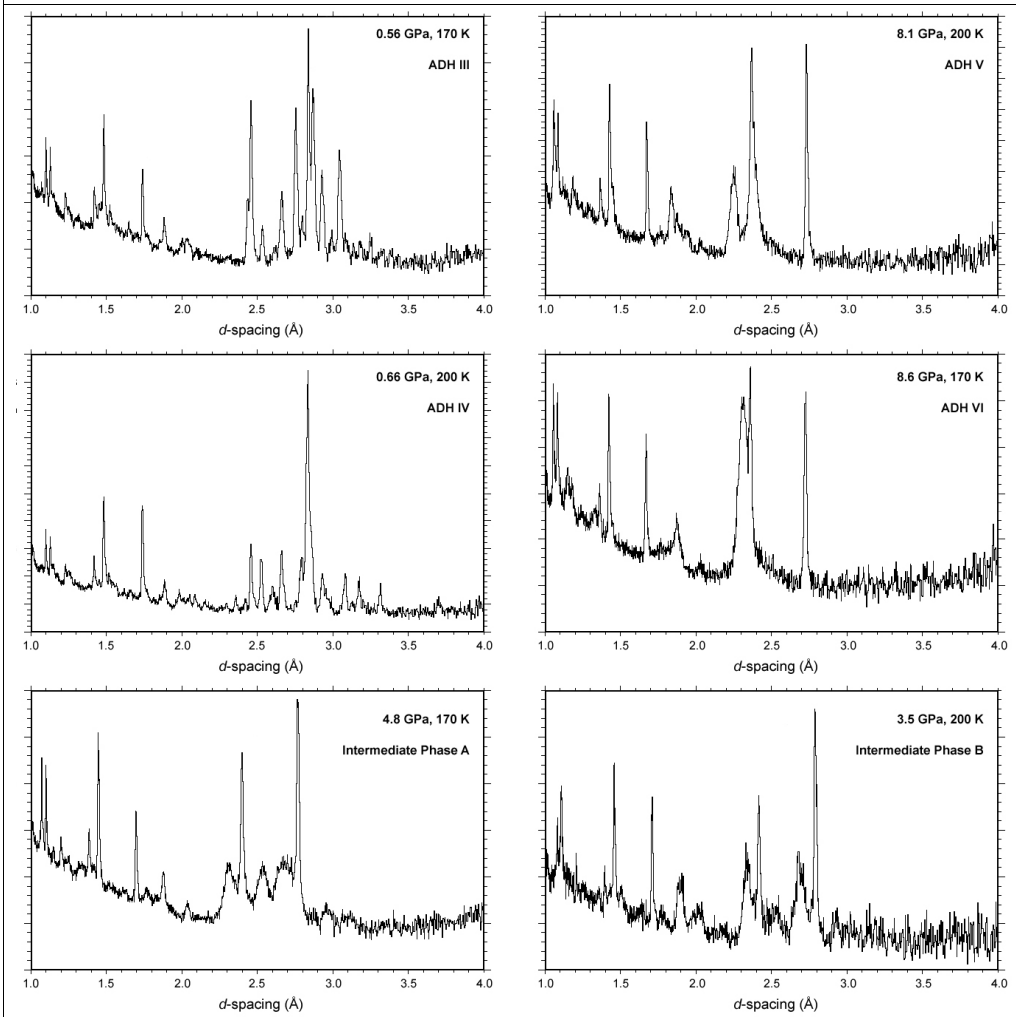

CHAPTER NINE

DISCUSSION AND PLANETARY MODELLING

9 Introduction

As I indicated in Chapter One, there were two primary reasons for doing this work; to determine how well one can calculate the properties of solids in the ammonia-water system using DFT with the PW91 GGA functional, and to improve our understanding of the materials which comprise the volatile fraction of icy moons in the solar system. The first part is addressed in Section 9.1, next, and the second in Section 9.2

9.1 Implications for simulating hydrogen bonded systems

It is apparent that the GGA simulation of solids in the ammonia-water system encountered varying degrees of success. In some cases, the calculated zero-pressure molar volumes (as well as the incompressibility) were either much too large (e.g., ammonia I, AHH), or much too small (e.g., ice XI). In fewer cases, the agreement between my calculations and the experimental data was nearly perfect (ice VIII, AMH). In still other cases, the agreement was neither excellent or poor, merely fair (e.g., ice II, ADH). Was there any systematic trend to the difference between calculations and experiments?

The simple answer is, 'yes.' In ice, the agreement becomes better for the denser structures, suggesting that the long-range non-bonded interactions – unaccounted for by the GGA representation of E_{XC} – are less important in the high-pressure phases.

Of greater interest is the trend as a function of composition at ambient pressure. In figure 9.1 I have plotted the relative difference between the calculated volume at 0 K and the experimental volume (usually at 2 – 4 K), $\Delta V/V$, against the estimated mean hydrogen bond enthalpy. The latter is determined as follows. The lattice energies of ammonia and ice were used to work out, respectively, the strength of the N-H…N and O-H…O hydrogen bonds in each end-member. I have assumed the strengths of N-H…O bonds are equal to those of O-H…O bonds, and the strength of O-H…N bonds equal to those of N-H…N bonds. This appears justified by an inspection of the comparative length of each type of bond in the solid state. By counting the numbers of hydrogen bonds of each type per formula unit, I have been able to arrive at a mean hydrogen-bond energy for each solid. Error bars of ± 1kJ mol^{-1} indicate the uncertainty arising from this approach. Errors on $\Delta V/V$ arise from uncertainties in the true molar volume at 0 K (for AHH) and from errors on V_0 in the fitted EoS of all phases.

When plotted in this way, there is a clear linear relationship between $V_{calc} - V_{expt}$ and the binding energy of the solid.

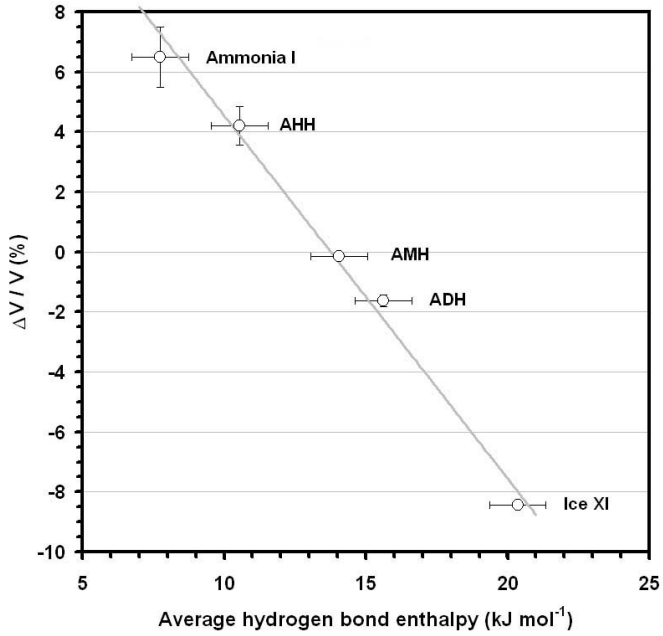

Fig. 9.1. $V_{calc} - V_{expt}$ as a function of binding energy.

As I have discussed in the relevant chapters, correcting the calculated V_0 to the experimental V_0 yields essentially correct values for the incompressibility. What this implies is that if figure 9.1 is transferable to other hydrogen-bonded systems, then one could actually estimate the overbinding, or underbinding, arising from GGA DFT calculations *a priori*, something one cannot do at present. A transferable correction would be extraordinarily valuable.

The question of whether figure 9.1 applies to systems other than H_2O-NH_3 needs testing. It would be particularly interesting to see how well the H_2O-CH_4 or H_2O-CH_3OH systems, for example, fitted into the observed pattern. Not only would this advance our understanding of hydrogen bonded solids, but it would yield useful results on two systems of potential planetary significance.

Having evaluated the value of my calculations in DFT simulations of hydrogen bonding, I will now discuss the implications of my findings for the structure and evolution of icy moons in the outer solar system.

9.2 Planetary modelling

One cannot, at present, collect samples from the surface and interior of icy moons. One cannot yet make *in situ* surface measurements. Typically, the only information available to constrain the internal structure comes from the gravity field (or from the magnetic field); either by the effect it has on a passing (or orbiting) spacecraft, or its manifestation in the equilibrium shape of the moon. The density distribution determined from gravity data is inherently non-unique, it is necessary to generate a suite of likely structural models for comparison with spacecraft observations.

On July 1st 2004 the Cassini spacecraft will carry out an orbital insertion manoeuvre that marks the beginning of a four-year tour of the Saturnian system, observing the planet, its rings, magnetosphere, and icy moons. This tour will include more than 40 flybys of Titan at distances of 900 – 2500 km, and several flybys of the other icy moons at close range (500-1000 km). In addition, the Huygens lander, piggybacked aboard Cassini, will become the first robotic vehicle to sample the surface of an icy moon when it touches down on Titan on January 14th 2005.

It is for this reason that I have chosen to construct models of Saturn's two largest moons, Titan (radius 2575 km) and Rhea (radius 764 km). First I shall outline the construction of the model, and the calculation of those properties observable by the Cassini spacecraft.

9.2.1 Static structural modelling

To begin with I describe the construction of a structural model which can be used to calculate several important quantities that will be measured by the Cassini spacecraft during its orbital tour. These include low-order components of the gravity field, and the static deformation of the solid figure.

I have gone back to the literature to collect P-V-T and EoS data for all of the phases of interest; ices I, II, V, VI, VII / VIII, CH_4-clathrate phase I, San Carlos Olivine, liquid iron

sulfide, and ammonia-water liquid. In the case of ice V, S-C Olivine, liquid FeS, and NH_3-H_2O liquid, I have used the published EoS parameters (see Appendix). For the remaining phases I have used P-V-T data (the majority of which post-dates previous planetary models) to fit new equation of state parameters. For ice II and ice VIII, I have used my athermal calculation results as constraints on the shape of the P-V-T surface at 0 K. For ammonia dihydrate I have used the experimentally determined values given in Chapter 8. Full details are given in the Appendix.

9.2.1.1 Building the model

The model describes a spherically symmetrical body of radius R_P, mass M_P, and moment of inertia I_P. This sphere is divided into concentric shells of finite thickness Δr. For all of the models , $\Delta r = 1$ km.

The outer radius of the i^{th} shell is defined as r_i, such that $r_i = i\Delta r$ and $r_{i-1} = r_i - \Delta r$ is the inner radius of the i^{th} shell (Fig. 9.2).

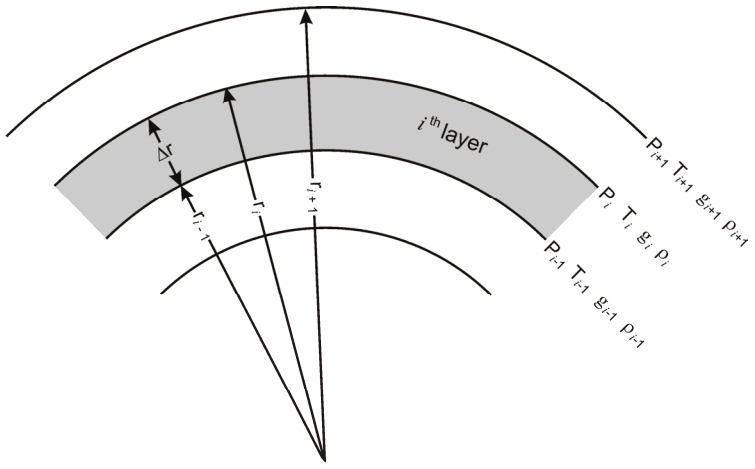

Figure 9.2. A graphical definition of terms in the shell model.

Hence, the volume of the i^{th} shell, $V_i = \frac{4}{3}\pi\left[r_i^3 - r_{i-1}^3\right]$ and the mass of the i^{th} shell, $M_i = \rho_i V_i$

The mass of the planet, M_P, is simply the sum of the masses of all shells = $\sum_{1}^{(R/\Delta r)} M_i$

The summation begins at $i = 1$ since the first shell is a sphere with zero internal radius.

The moment of inertia of the i^{th} shell, $I_i = \frac{8}{15}\pi\rho_i\left[r_i^5 - r_{i-1}^5\right]$

and the moment of inertia of the planet, $I_P = \sum_{1}^{(R/\Delta r)} I_i$ which is normalised as $I_P / (M_P \cdot R_P^2)$

The density, ρ_i, pressure, P_i, temperature, T_i, and gravitational acceleration, g_i, are explicitly calculated at r_i, the outer radius of the i^{th} shell. These values are then assumed constant over the radius interval Δr from r_i to r_{i-1}. The effect of this is to very slightly underestimate the true mass of the shell, but the impact on the overall planetary mass is negligible.

The pressure at r_i is $P_i = P_{i+1} + (\rho_{i+1} g_i \Delta r)$ with the boundary condition of zero pressure at the surface.

The temperature as a function of depth is taken from published thermal models (e.g., Grasset *et al*., 2000 for Titan). The density of each shell can then be calculated, for a given composition, using P_i, T_i, and an appropriate material equation of state.

The model is built from the surface downwards. However, the most difficult quantity to calculate is g_i, since the gravitational acceleration depends on the total mass inside r_i, which is not known *a priori* when constructing the model. It is necessary to make a 'best guess' at the correct density profile and then iterate the calculation of g_i until it is consistent with the model density profile.

The 'best guess' density profile is found by using the observed density of the planetary body being modelled as a starting point. So, the value of g_i will be given in this case as

$$g_i = \frac{G}{r_i^2}\left(M_{obs} - \sum_{i}^{i=(R/\Delta r)} M_i \right) \qquad (9.1)$$

where G is the universal gravitational constant.

In other words, g_i is found by subtracting the mass of the shells above r_i (which have been determined as the model is built) from the observed mass of the planet, M_{obs}.

Provided the mass of the model planet is identical to the observed mass of the planet, then this yields g_i precisely and the value of g_i goes to zero as r_i goes to zero (Fig. 9.3).

It is, of course, rather unlikely that $M_P \equiv M_{obs}$. There are two possible results: If $M_P > M_{obs}$ then g_i will become negative at some finite value of r_i. If $M_P < M_{obs}$ then g_i will become very large indeed in the inner core. This creates very large pressures and unrealistically large values for the masses of the core shells. As long as some effort has been made to predict the internal density distribution beforehand, this effect can be contained to the innermost few tens of kilometres of the core (Fig. 9.3).

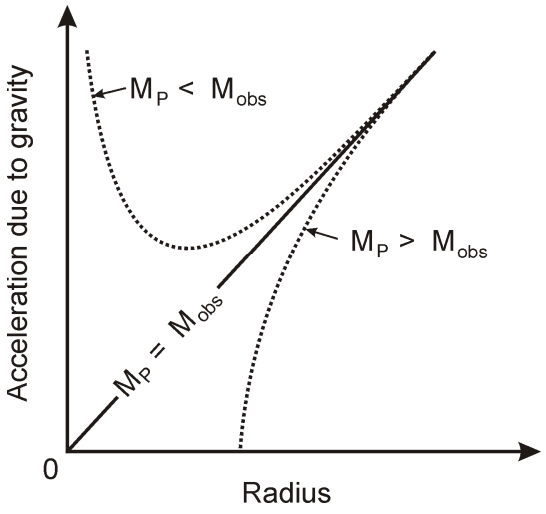

Figure 9.3.

Variation of g_i in the *core shells* (outside the core, g_i varies in a different way). Note the effect on the calculated value of g_i when the mass of the model differs from M_{obs}.

In producing a first 'best guess' model, the aim is to confine this region of unphysical g_i to the smallest possible volume in the core. Once this is achieved, the equation above is replaced with the following equation, which is exact for any value of $M_P \neq M_{obs}$:

$$g_i = \frac{G}{r_i^2} \sum_{i=1}^{i} M_i \qquad (9.2)$$

Since the values of g_i in the 'best guess' are not consistent with the radial distribution of mass in the shells, $M_i(r)$, the first step is to update g_i to values consistent with the 'best guess' $M_i(r)$. This in turn affects $P_i(r)$, and subsequently $\rho_i(r)$. A new set of M_i can then be determined and used to re-update g_i. The cycle of iterations (Fig. 9.4) continues until some predefined cut-off is reached; in the case of the models described here, the cut-off is achieved when the maximum change in any g_i is smaller than 1mm s^{-2} (100mGal). In most cases the number of iterations required is 15 – 25. The calculations were carried out in a Microsoft Excel spreadsheet.

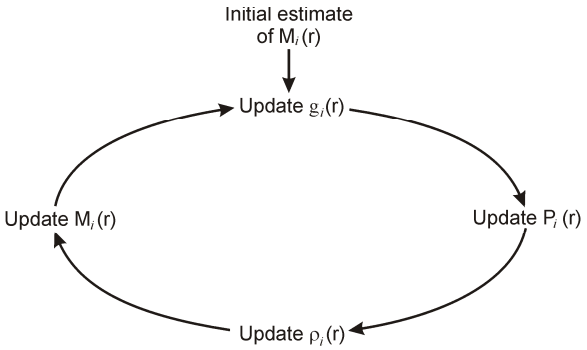

Fig. 9.4. The cycle of iteration used to arrive at a self-consistent density profile.

9.2.1.2 Observables: Gravity and Love numbers

Values for the moment of inertia factor (MoI) are widely quoted for different planetary bodies and are used to constrain the radial distribution of density. However, the MoI is a derived quantity.

During a spacecraft flyby of a planet or moon, the acceleration of the spacecraft along the line of sight between spacecraft transmitter and earth-based receiver is measured using the doppler shift of the telemetry signal. The force acting on the spacecraft is therefore determined and this yields the gravitational potential, U, at the spacecraft (Anderson 1974: Anderson and Giampieri 1999: Rappaport *et al*. 2001). The variation of the potential along the flyby track is used in the fitting of a spherical harmonic approximation to the gravity field. Accurate fitting requires numerous flybys along differing geometries with respect to the planetary body.

To second order, the gravitational potential of a rotationally and tidally distorted synchronously rotating satellite in a spherical orbit is (Kaula 1966)

$$U = \frac{GM}{r}\left[1 - \left(\frac{a}{r}\right)^2 \frac{J_2}{3}\left(3\cos^2\theta - 1\right) + \left(\frac{a}{r}\right)^2 C_{22}\, 3\sin^2\theta\cos 2\lambda \right] \tag{9.3}$$

where G is the Universal gravitational constant, M is the mass of the satellite, r, θ, and λ are spherical coordinates, a is the mean radius, and J_2 and C_{22} are gravitational coefficients.

For a satellite in a circular orbit, the distortion due to its own rotation, and due to the tidal force of the parent body, is constant along the whole orbit. Thus the distortion is static and the satellite responds to this deformation as though it were a fluid, i.e., with zero rigidity. The magnitude of the deformation depends on a fluid response coefficient, which is a function of the internal density distribution. This coefficient is called the fluid Love number, k_f (Schubert *et al*. 1994).

$$J_2 = \frac{5}{6} k_f \left(\frac{\omega^2 a^3}{GM}\right) \tag{9.4}$$

$$C_{22} = \frac{1}{4} k_f \left(\frac{\omega^2 a^3}{GM}\right) \tag{9.5}$$

where ω is the rotation rate in radians per second.

The values of J_2 and C_{22} determined from a fit to U from spacecraft radio tracking should yield identical values of k_f, provided the satellite is in hydrostatic equilibrium.

The fluid Love number can be used to determine the largest MoI (the polar MoI) from the Radau equation (see Hubbard 1984):

$$\frac{C}{MR^2} = \frac{2}{3}\left[1 - \frac{2}{5}\left(\frac{5}{k_f + 1} - 1\right)^{\frac{1}{2}}\right] \tag{9.6}$$

Most planetary bodies are defined as triaxial ellipsoids with three orthogonal principal axes. The longest axis, *a*, for a synchronously rotating body is directed along the satellite-planet line. The next longest axis, *b*, points along the direction of orbital motion. The shortest, *c*, is the rotation axis. Hence the MoI will be different along each axis. The largest value of the MoI factor will be along the polar axis, and this is written C/MR^2. The mean MoI, I/MR^2, is the value found by assuming the body to be spherical.

For a perfectly uniform sphere, k_f will be 3/2 and I/MR^2 will be 2/5. Values smaller than these indicates some degree of central concentration of matter.

It is possible to calculate k_f for an arbitrary model density profile through a planetary body, but this is a non-trivial problem involving the solution of complex integral equations. The model developed here gets around this by making a small assumption and employing the reverse method used to find the MoI from spacecraft flybys.

The model yields I/MR^2 for a given density profile. I then assume that $I/MR^2 = C/MR^2$. For slowly rotating bodies where the difference in radius along the principal axes is very small, this is a reasonable assumption. In fact the difference between A/MR^2 and C/MR^2 is simply J_2, which is approximately three parts in 100,000 for Titan, so the assumption that $I/MR^2 = C/MR^2$ is fair.

This estimate of C/MR^2 is then used to find k_f and thus J_2 and C_{22}.

I also calculate h_f (another Love number = $1+k_f$) to determine the degree of triaxial distortion via (Schubert *et al*. 1994),

$$a - c = 2ah_f\left(\frac{\omega^2 a^3}{GM}\right) \tag{9.7}$$

$$b - c = \frac{1}{4}(a - c) \tag{9.8}$$

Things become more complicated for Titan, which has a large free orbital eccentricity. In this case, the magnitude of the tidal distortion varies as Titan moves along its orbit. Hence the shape of Titan, as well as J_2 and C_{22} will vary with the same period as Titan's orbital period.

The values of the gravitational coefficients measured by the Cassini spacecraft will therefore have a static component (as described above) plus a tidal component (Rappaport *et al*. 1997):

$$J_2 = J_{2,s} + J_{2,t} \quad (9.9)$$

$$C_{22} = C_{22,s} + C_{22,t} \quad (9.10)$$

The tidal components also depend on a response coefficient. In this case it is an elastic response, so the relevant Love number, k_2, is a function of the radial shear modulus profile, i.e., the bulk rigidity of the satellite. k_2 is actually a complex number; the real part is a function of shear modulus, the complex part is a function of viscosity and Titan's true anomaly, f.[1] In other words, the complex part of k_2 yields the magnitude of the phase lag in the elastic response due to the finite viscosity of the material.

$J_{2,t}$ and $C_{22,t}$ also depend on a term in $e \cos f$, where e = orbital eccentricity. Therefore, at two points in Titan's orbit, $\cos f = 0$ and so $J_{2,t}$ and $C_{22,t} = 0$. At these positions, assuming zero phase lag, the observed value of J_2 and C_{22} would be the static values only.

- Predicted values of the amplitude of J_2's variation (J_2 itself is ~25×10^{-6}) around Titan's orbit is ~ 10^{-7} - 10^{-8} (Castillo *et al*. 2002).
- Cassini is expected to be able to determine J_2 and C_{22} to better than "a few" $\times 10^{-9}$ (Rappaport *et al*., 1997). Note that the standard error on J_2 for the *Earth* is ~1×10^{-9}.

Due to the complexity of calculating k_2, I am only calculating the static component of the gravitational coefficients.

9.2.1.3 Rhea

Rhea is Saturn's second largest moon, after Titan. The radius is 764 ± 4 km (Davies and Katayama 1983), and the mass is 2.308 ± 0.060 $\times 10^{21}$ kg (Campbell and Anderson 1989: Jacobson 2003), yielding a bulk density of 1236 ± 38 kg m^{-3}. Rhea orbits Saturn with a period of 4.5175 days.

Rhea's internal structure has previously been modelled by Lupo (1982), Ellsworth and Schubert (1983), Federico and Lanciano (1983), Zharkov *et al*. (1985), and Anderson *et al*. (2003). I have generated a series of models using the methods outlined in the preceding section. These models consist of a 'rock' component (modelled using the equation of state of San Carlos olivine; appendix I) and a 'volatile' component (H_2O, NH_3, CH_4 ices). I have calculated the

[1] The true anomaly is the angle between Titan's position in its orbit and the periapsis position. At periapse, $f = 0°$, and at apoapsis $f = 180°$, for example.

structure and gravitational field of models in which these two components are mixed homogeneously from core to surface, and models which consist of a differentiated rocky core overlain by an icy mantle. In all cases, the 'geotherm' is anchored to a surface temperature of 80 K and a core temperature of 120 K (after Ellsworth and Schubert 1983). Equation of state parameters of all phases modelled are given in Appendix I.

A feature of the H_2O phase diagram (Fig. 3.1) worthy of note in this context is the equilibrium phase boundary between ice I and ice II. At the very low temperatures expected in the interior of Rhea, this boundary may be crossed at pressures as low as 0.07 GPa, if one assumes that the boundary observed at higher temperatures can be extrapolated to circa 100 Kelvin. Given the uncertainty in this matter, I have produced models in which ice I does transform to ice II at some depth, and models in which it does not. For the structural models, this scarcely makes a difference; for the evolutionary models it makes an extraordinary difference (see 9.2.2.3). The equilibrium transition pressure (in GPa) is taken equal to (T – 11) / 1175.3, where T is in Kelvin.

To begin with, I explored the effect of changing the chemistry of the ice layer in the differentiated models. Rhea 'A' has a pure H_2O ice Ih mantle; Rhea 'B' has a pure H_2O ice Ih + ice II mantle; Rhea 'C' contains 15 wt % NH_3, resulting in a layer of ammonia dihydrate being present beneath a crust of ice Ih; and Rhea 'D' is a somewhat extreme case of a pure CH_4-clathrate mantle. Table 9.I shows the range of values for I/MR^2, k_f, J_2, C_{22}, *a-c*, *b-c*, and core size for each model that are consistent with a mean density of 1236 ± 38 kg m^{-3}. Fig. 9.5 illustrates the variation of gravity, density, pressure, and temperature with depth through Rhea 'B'.

Table 9.I. Calculated gravitational coefficients and triaxial distortion of four Rhea models having a mean density of 1236 ± 38 kg m^{-3}.

	RHEA 'A' ice Ih	RHEA 'B' ice Ih + ice II	RHEA 'C' 15 wt % NH_3	RHEA 'D' CH_4 clathrate
I/MR^2	0.327 ± 0.005	0.328 ± 0.005	0.328 ± 0.005	0.333 ± 0.005
k_f	0.909 ± 0.034	0.911 ± 0.037	0.917 ± 0.033	0.948 ± 0.035
J_2 (x10^{-6})	526 ± 20	530 ± 22	534 ± 19	553 ± 22
C_{22} (x10^{-6})	159 ± 6	159 ± 6	160 ± 6	165 ± 6
a-c (metres)	2038 ± 37	2040 ± 40	2046 ± 35	2080 ± 38
b-c (metres)	510 ± 9	510 ± 10	512 ± 9	520 ± 9
Core radius (km)	377 ± 16	369 ± 19	371 ± 16	367 ± 16
Core mass (%)*	33 ± 3	31 ± 4	31 ± 3	30 ± 3

*core mass as a percentage of the total mass of Rhea

One can see that even quite radical changes in the chemistry of the icy mantle have little effect on the gravity field or shape of Rhea. However, in light of later findings (9.2.2.3), I explored the effect of different ammonia concentrations in the mantle. Figure 9.6 shows how the density varies as a function of core size and ammonia abundance. This plot only shows ammonia concentrations higher than 3 wt % since at lower concentrations ice II becomes stable in the lower mantle and there is a step discontinuity in the density. This is important because the evolutionary models described later suggest that ice II cannot be present inside Rhea, and a small amount of ammonia (> 3 wt %) alleviates this problem.

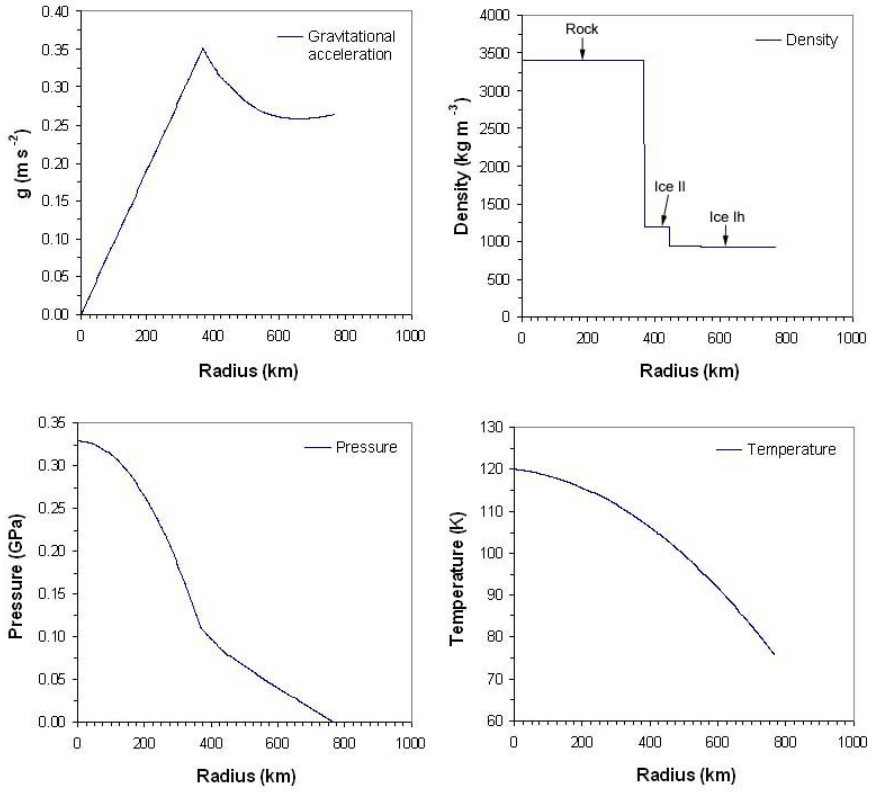

Figure 9.5. The variation of gravity, density, pressure, and temperature with depth in Rhea 'B'

The Cassini spacecraft will make only one close flyby of Rhea (altitude 500 km on Nov 27 2005), and two more distant flybys (5500 km on Aug 30 2007, and 81,000 km on Nov 16 2007). Anderson *et al*. (2003) demonstrated that the close flyby could determine C_{22} to an accuracy of ~ $2x10^{-6}$ which, taken with improved measurements of the mean radius, mass, and figure, will be sufficient to more closely constrain the internal mass distribution.

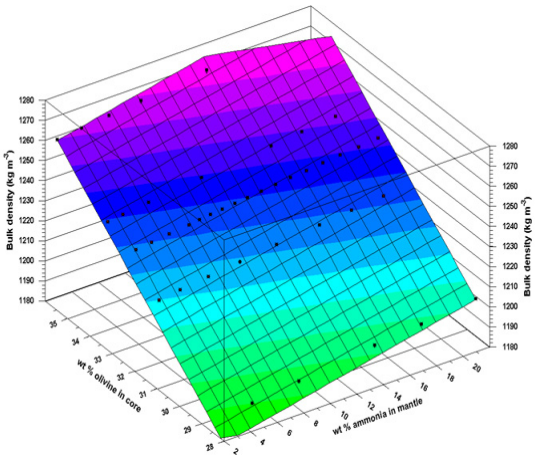

Figure 9.6.

Variation of bulk density in the Rhea model for ice II-free ammonia-bearing mantles. The density is plotted as a function of the rocky-core mass (in wt % of the total mass of the satellite) and the ammonia abundance in the icy mantle.

Table 9.II. Comparison of my differentiated and undifferentiated models with earlier work.

	Differentiated models			*Undifferentiated models*	
	Zharkov A[1]	Zharkov B[1]	This work[2]	Zharkov C[1]	This work[3]
I/MR[2]	-	-	0.328	-	0.391
k_f	0.970	0.863	0.911	-	1.414
J_2 (x10^{-6})	553	493	530	873	823
C_{22} (x10^{-6})	166	148	159	262	247
a-c (metres)	2106	1992	2040	2672	2576
b-c (metres)	526	498	512	668	644

[1]Zharkov *et al*. (1985) A - Two layer. Ice (1000kg m^{-3}) + Rock (3000kg m^{-3}) with $m_{core}/m = 0.370$: B - Two layer. Ice (900kg m^{-3}) + Rock (3000kg m^{-3}) with $m_{core}/m = 0.460$: C – Uniform model.

[2]Rhea B: three layer model, ice Ih + ice II + rock with $m_{core}/m = 0.31$.

[3]Homogeneous rock ice-rock mixture containing 10.42 % rock by volume. Ice I – II interface at depth of 326 km.

9.2.1.4 Titan

Titan is Saturn's largest moon. The radius is 2575 ± 2 km (Lindal *et al*., 1983), and the mass is 1.3455 ± 0.0001 x10^{23} kg (Jacobson 2003), yielding a bulk density of 1881 ± 4 kg m^{-3}. Titan orbits Saturn with a period of 15.94542 days.

I have generated a series of models using the methods outline in the 9.2.1.1. These models consist of a 'rock' component (modelled using the equation of state of San Carlos olivine), a 'metal' component (a liquid alloy of composition $Fe_{0.9}S_{0.1}$), and a 'volatile' component (water ice and NH_3-H_2O liquid). Uncertainty in the likely distribution of CH_4 in the interior of Titan, and limited data regarding the equation of state of high-pressure methane clathrate phases, means that I have not included methane in these structural models. NH_3 is likely to be present

as an aqueous solution, and its incorporation is discussed later. Equation of state parameters of all phases modelled are given in Appendix I.

There are three main models; Titan 'A' is a 'two-layer' model consisting of ice + rock; Titan 'B' is a 'three-layer' model consisting of ice + rock + metal. Although it is largely taken for granted that Titan will be differentiated, the observation that Callisto (a body of similar dimensions) is only partially differentiated (Anderson *et al*., 2001), and in light of recent theoretical conclusion that Titan may have taken so long to form that it could not differentiate (Mosqueira and Estrada 2003), I have prepared an undifferentiated model. Titan 'C' is an undifferentiated ice + rock model. The thermal profiles in 'A' and 'B' are after Grasset *et al*. (2000). In detail therefore,

- Titan 'A' consists of an ice shell 830km deep overlying an olivine core of radius 1744 km. The ice shell is subdivided into layers of ice Ih (155km), ice II (133km), ice V (112km) and ice VI (430km). The ice : rock ratio is 44.47 : 55.53. The total mass is 1.34553×10^{23} kg, and the density is 1881.4 kg m^{-3} (see Fig. 9.7).

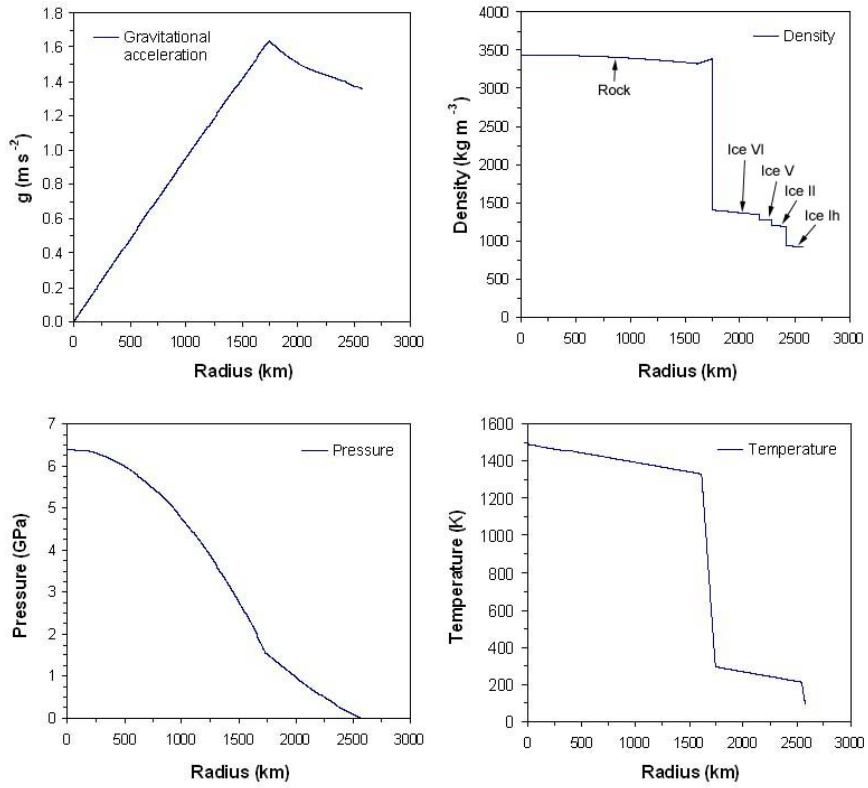

Fig. 9.7. Profiles of gravity, density, pressure and temperature inside Titan 'A'. The phase structure of the ice mantle is indicated. Notice the small density inversion in the top of the core caused by the large thermal gradient in the boundary layer.

- Titan 'B' consists of an ice shell 928 km deep overlying an olivine outer core 826 km deep, and a liquid $Fe_{0.9}S_{0.1}$ inner core of radius 820 km. In this case the ratio of ice to rock to metal is 48.16 : 40.95 : 10.89. The phase structure of the ice shell is identical to Titan 'A'. The total mass is 1.34547×10^{23} kg, and the density is 1881.3 kg m^{-3} (see Fig. 9.8).

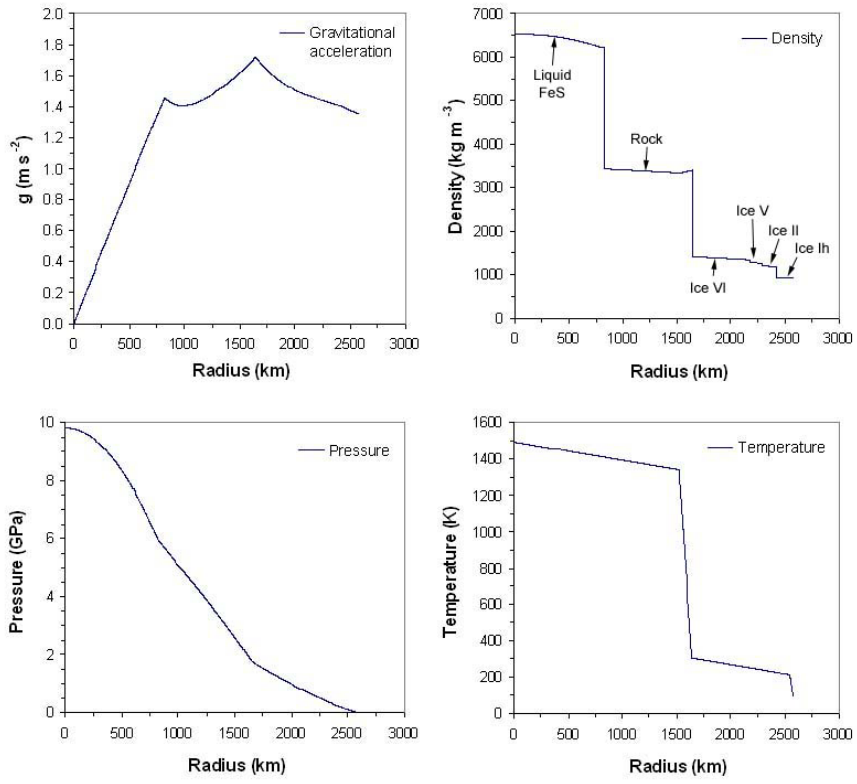

Fig. 9.8. Profiles of gravity, density, pressure and temperature inside Titan 'B'.

- Titan 'C' consists of a homogeneous ice + rock mixture containing 24.2 % rock by volume. The ice I + rock layer is 38 km deep, and overlies shells of ice II + rock (188 km thick) and ice VI + rock (721 km thick). The core of ice VIII + rock has a radius of 1628 km. The core temperature is fixed at 300 K and the surface temperature at 93 K. The total mass is 1.34529×10^{23} kg, and the density is 1881.03 kg m^{-3} (see Fig. 9.9, overleaf).

The gravity field and triaxial figure calculated for each model is compared with earlier literature values (Zharkov *et al.* 1985) in Table 9.III.

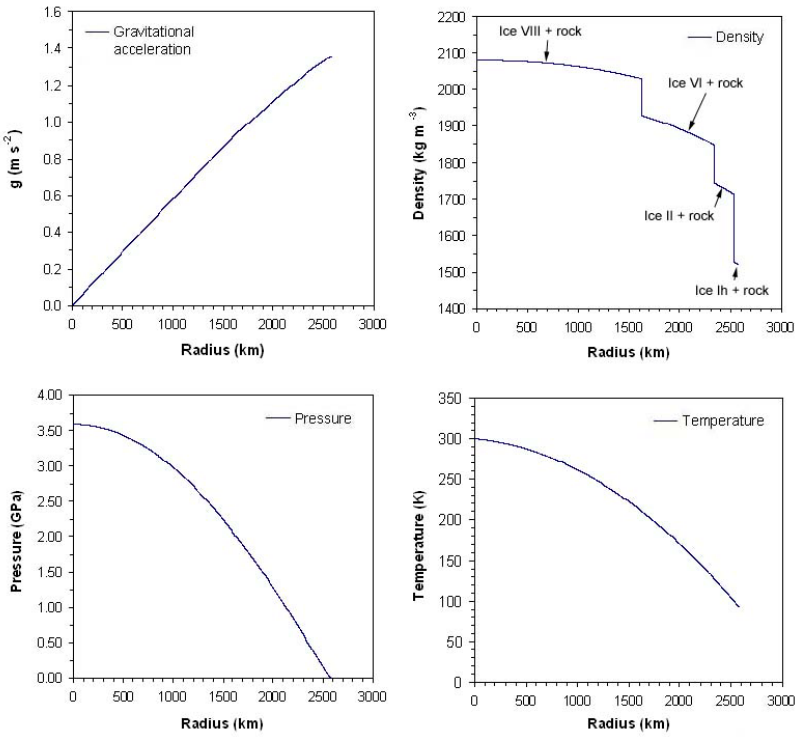

Fig. 9.9. Profiles of gravity, density, pressure and temperature inside Titan 'C,' the undifferentiated model.

Ammonia inside Titan is likely to be in aqueous solution. I have investigated the effect of a deep subsurface ammonia-water ocean on the shape and gravity field of Titan using the equation of state of Croft *et al*. (1988). Neglecting the change in the bulk rigidity of Titan (and consequences for the tidal amplitude of J_2 and C_{22}: Rappaport *et al*., 1997), the principal effect of an ammonia-water ocean is to displace dense ice polymorphs (II, and V) from the upper mantle, increasing the density contrast between surface and interior, and therefore reducing I/MR^2. For a baseline model containing 15 wt % NH_3 (as a percentage of the entire ice layer) the ocean is 350 km deep and directly overlies the ice VI lower mantle (Fig. 9.10). That is, ices II and V, with densities of ~1200 kg m^{-3} have been replaced with a liquid of density ~1000 kg m^{-3}. I/MR^2 is reduced to 0.297, $J_2 = 23.4 \times 10^{-6}$, $C_{22} = 7.0 \times 10^{-6}$. Lower bulk ammonia contents reduce the depth of the ocean, allowing shells of ice V to become stable on the ocean floor. The suggestion of Mousis *et al*. (2002b) that there is a step change in the peritectic melting temperature of ammonia dihydrate – resulting in the crystallization of high-pressure ADH on the ocean floor – does not agree with my own melting observations (see 8.2.3), and cannot be modelled at present because of the unknown properties of high-pressure ADH polymorphs.

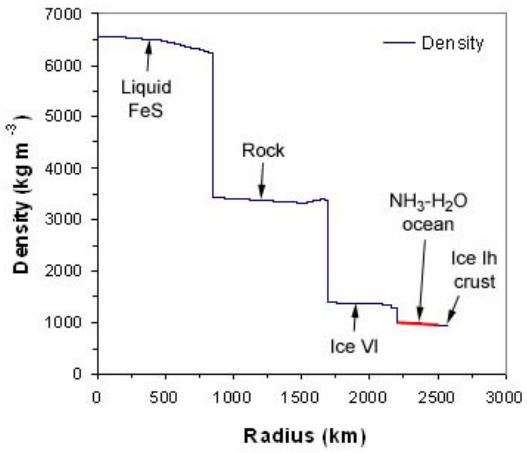

Figure 9.10.

The effect of a 350 km deep eutectic NH_3-H_2O subsurface ocean on the density profile through the three-layer model (Titan B). Note that the ocean is sandwiched between a crust of ice Ih and a lower mantle of ice VI; the shells of ice II and V present in pure H_2O models are absent.

Table 9.III. Comparison of my Titan models with earlier work.

	Two layer models		*Three layer models*		*Undifferentiated models*	
	Zharkov A[1]	This work[2]	Zharkov C[1]	This work[2]	Zharkov E[1]	This work[4]
I/MR[2]	-	0.317	-	0.304	-	0.388
k_f	0.865	0.838	0.693	0.757	-	1.394
J_2 ($x10^{-6}$)	28.6	27.6	22.8	24.9	49.5	46.0
C_{22} ($x10^{-6}$)	8.6	8.3	6.8	7.5	14.8	13.8
a-c (metres)	380	374	344	358	509	488
b-c (metres)	95	94	86	90	127	122

[1]Zharkov *et al*. (1985) A – Two layer. Ice (1000kg m^{-3}) + Rock (3000kg m^{-3}) with $m_{core}/m = 0.703$: C – Three layer. Ice (900kg m^{-3}) + Rock (3280kg m^{-3}) + Metal (5000kg m^{-3}) with $m_{metal}/m = 0.139$ and $m_{core}/m = 0.701$: E – Uniform model.

[2]Titan 'A. [3]Titan 'B'. [4]Titan 'C'.

9.2.2 'Breathing' evolutionary models

Having developed a static model of a planetary body, the next step is to see how the model changes, or adapts itself, to changes in the model geotherm. In other words, one wishes to determine how the radius and internal mass distribution has changed since the object originally accreted, warmed up, and subsequently cooled off.

This is important for some of the small icy moons of Saturn, such as Rhea, where it has been suggested (Consolmagno 1985) that thermal expansion following the freezing of a subsurface ocean could account for extensional features (e.g., small grooves or graben) at the surface (Moore *et al*., 1985).

The means of achieving this, using the static model as a starting point, is described next.

9.2.2.1 Making the model dynamic

Making the model expand or contract in response to changes in temperature requires a redefinition of what constitutes the i^{th} layer (as given in 9.2.1.1). Instead of being a shell of fixed radius and variable mass, the shell must be defined as having a fixed mass and variable radius. Now, the mass of the layer is fixed at whatever value was found in the static model. So, for example, in the static model, the 468th shell of Rhea would have a radius, r_{468} = 468 km (by definition) and a mass (for a particular model) of 2.7224×10^{18} kg. In the dynamic model, the mass of the 468th shell, M_{468}, is fixed at 2.7224×10^{18} kg, and r_{468} is allowed to change in response to a change in T_{468} and consequently ρ_{468}.

The radius of the i^{th} layer is now given as

$$r_i = \left(\frac{3}{4} \frac{M_i}{\pi \rho_i} + r_{i-1}^3 \right)^{1/3} \tag{9.11}$$

One very simply takes the static model, fixes M_i for each layer, and replaces r_i with the above expression.

Now, when the temperature is increased or decreased, the radii of the shells increases or decreases; the planet effectively inflates or deflates, which is why I refer to the dynamic model as a 'breathing' model.

Unlike the static model, which normally iterates to self-consistency in 15-25 cycles, the breathing model can require upwards of 1000 iterations to settle into a new equilibrium.

9.2.2.2 Observables; strain

Of course, if one uniformly increases the temperature of every layer by the same amount, then each layer undergoes thermal expansion and the planetary radius increases, but there is little or no strain imposed at the surface. Such a scenario is not realistic; the surface temperature is determined by radiative equilibrium between solar insolation and surface emission, and consequently remains more or less the same. In this case, raising the internal temperature whilst maintaining the surface temperature results in thermal expansion of the interior but no change in the volume of the surface layers. Hence, the overall planetary radius (and circumference) increases, and since the volume of the surface layers is conserved, this implies that there is a strain acting in the outermost shells.

The magnitude of the surface strain resulting from a given change in radius may be found using the following equation (Huang and Solomon 1982),

$$\sigma = \left[\frac{E}{(1-\nu)} \frac{\Delta r}{3r} \right] \tag{9.12}$$

where σ is the strain, E is Young's modulus, ν is Poisson's ratio, Δr is the change in radius, and r is the radius.

The Young's modulus of ice at 80 K is found from the elastic constants (Proctor 1966) to be 11 GPa and the Poisson ratio is 0.326. One can now use the magnitude of the stress, be it compressional or extensional, to explain observed surface geomorphologies.

At ~ 100 K the fracture strength of unconfined ice in compression is exceeded by a differential stress of 40 – 50 MPa (Durham *et al.,* 1983). In the case of Rhea, therefore, this requires a reduction in radius of 5.6 – 7.0 km. The brittle fracture of ice in extension is exceeded by a differential stress of ~ 3 – 10 MPa (Jaeger and Cook 1969), requiring an increase in radius of 0.4 – 1.4 km. One must not forget that a planetary crust is already likely to be heavily fractured by impact cratering. It seems reasonable to assume that thermal expansion will actually activate existing fracture patterns without needing to generate sufficient stress to overcome the strength of the surface layers.

Nevertheless, I have determined Δr (and hence σ) for an undifferentiated structural model of Rhea containing a pure H_2O ice component plus 'rock'. The thermal profiles used, and the results of this work are described next.

9.2.2.3 The evolution of Rhea

As shown by Consolmagno (1985) Rhea, as the largest icy moon of Saturn – after Titan – is the most likely to have undergone internal melting and experienced significant episodes of expansion and contraction. It is for this reason that I have chosen to extend my static structural models of Rhea back in time, using new values for the thermal expansivity of ice.

I have <u>not</u> developed my own thermal history model. Instead, I rely on the work of Ellsworth and Schubert (1983) to provide thermal profiles at different periods in Rhea's history. In particular, I employ the cold evolutionary model of Ellsworth and Schubert (1983), shown in Figure 9.11. So as to provide enough temporal resolution I have interpolated between the lines on Fig. 9.11, and the resulting thermal profiles (as used in the dynamic models) are shown in Figs. 9.12 and 9.13. It is important to stress that the results of this work are *entirely dependent* on the validity of the thermal model employed. Whilst the model is suitable for application to an undifferentiated ice + rock model, it is not suitable for use with an ammonia-bearing model,

since this involves partial melting and fractional crystallisation effects that will seriously alter the imposed thermal profile. Indeed, latent heat of crystallisation may keep an ammonia-water ocean from completely freezing (as in the model of Consolmagno 1985). Whilst this is presently beyond the scope of the model I have described, the development of a fully responsive thermal model represents a direction for future endeavour.

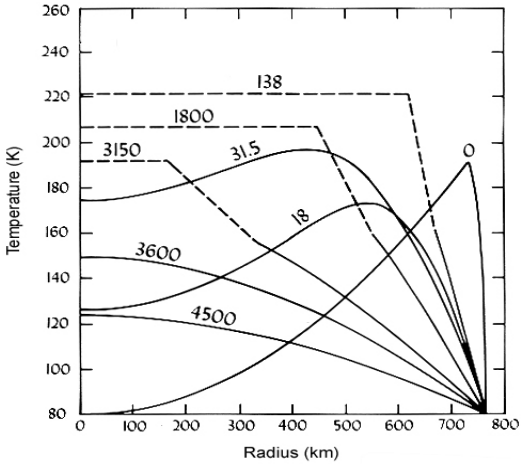

Left: Fig. 9.11. The published thermal history of Rhea from Ellsworth and Schubert (1983). Numbers next to the lines are the time in Ma from Rhea's accretion.

Below left: Fig. 9 12. Interpolated thermal profiles for the warm-up period of Rhea's history.

Below right: Fig. 9.13. Interpolated thermal profiles for the cool-down of Rhea. Ages in Ma are marked.

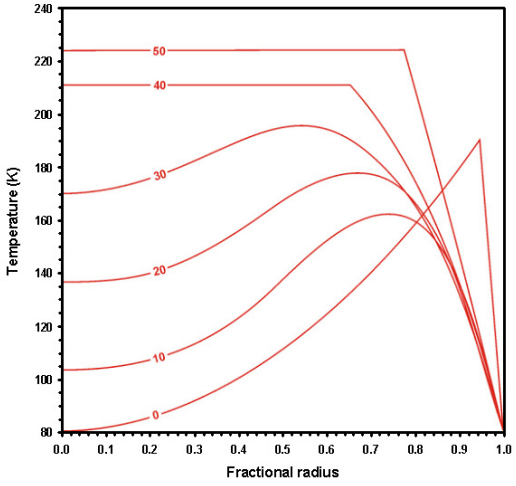

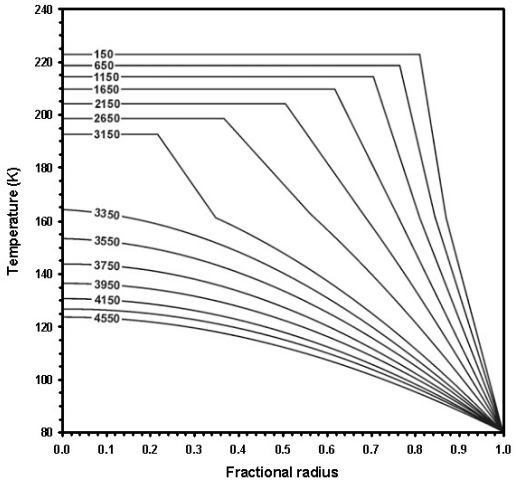

The dynamic model is run backwards in time, starting from the present-day structural model. The thermal history models of Ellsworth and Schubert (1983) show that Rhea's interior did not become sufficiently warm to melt pure water ice at any time since its accretion. The pure H_2O model is therefore an undifferentiated mixture of rock and ice at all times.

A present-day structural model with a uniform distribution of rock through all layers, and using the 4550 Ma geotherm of Ellsworth and Schubert (1983), contains 10.42 wt % rock, has a

radius of 764 km and a bulk density of 1236.01 kg m^{-3}. In this model, the extrapolated ice I-II boundary is found at a depth of 326 km. Running the model backwards in time reveals the following story.

At t = 0 (i.e., immediately after accretion) the radius is 766.42 km and the ice I-II boundary is at a depth of 357.49 km. As the moon warms, the pressure at which ice II becomes stable increases rapidly. The result of this is that ice II is eliminated from the core in just 30 million years, after which the entire moon is a homogeneous mixture of ice I + rock.

Converting all of the ice II to ice I has a remarkable effect; Rhea expands dramatically, increasing in radius by 7.35 km (Fig. 9.14). The resultant extensional stress in the surface layers is thus ~53 MPa, greater than the fracture strength of ice in extension by roughly an order of magnitude. The evidence of such remarkable extension (in the form of global rifting) is likely to have been destroyed by heavy post-accretional meteorite bombardment of the surface, which probably lasted ~800 Ma.

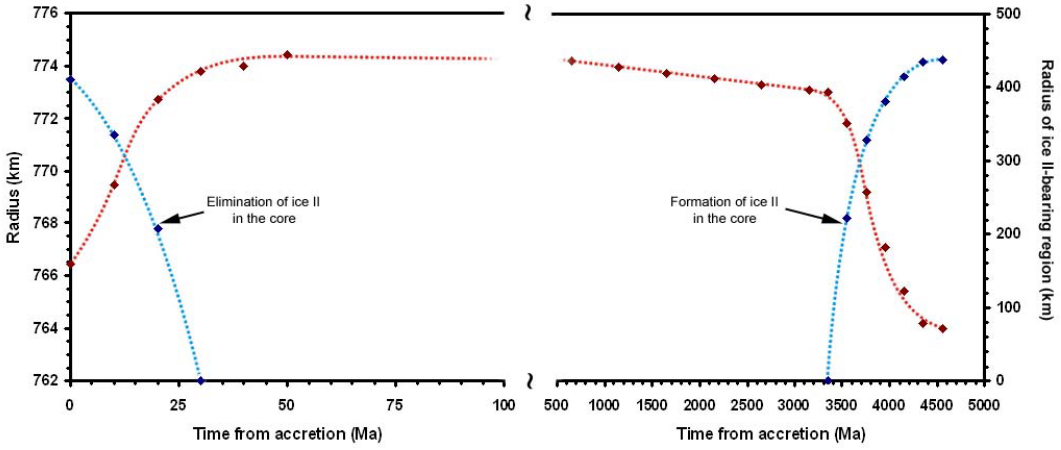

Fig. 9.14. Evolution of the radius and ice II content for an undifferentiated NH_3-free model of Rhea. The red dotted line is the radius, and values should be read from the left-hand axis. The radius of the ice II bearing region is shown by the blue dotted line, and values should be read from the right-hand axis. The lines are a guide to the eye.

The radius reaches a maximum value of 774.40 km around t = 150 Ma and Rhea then contracts by ~1.4 km over the following 3200 Ma. At this point (t = 3350 Ma), the temperature in the deep interior has once again become low enough to allow ice I to transform to ice II. Ice II builds up in the core rapidly and causes the moon to contract. This phase of contraction sees the radius drop by 9 km, to its current value of 764 km, between 3350 Ma and the present day.

If one assumes that evidence of the earlier expansion phase was obliterated during the heavy bombardment era, then Rhea's surface ought to exhibit evidence of massive compressional

stress (roughly 64 MPa) from the late contraction phase. Since it in fact exhibits fairly inconclusive evidence of surface compression, in the form of scarps which *may* be low-angle thrust faults (Moore *et al.* 1985), I conclude that the growth of ice II in (or near) the core has not occurred. This implies one, or more, of the following:

- The extrapolated ice I-II equilibrium phase boundary is wrong.
- The transformation of ice I to ice II is chemically inhibited (possible) or kinetically inhibited (unlikely on planetary timescales).
- Other materials are present as discrete layers which prevent ice I from experiencing high enough pressures to transform to ice II.
- The thermal evolution model I have used is incorrect.

Since the earlier static modelling showed that having > 3 wt % NH_3 in the mantle prevented ice I from reaching high enough pressures to transform to ice II, the third possibility seems like a promising solution.

Ellsworth and Schubert (1983) arrived at a similar conclusion, finding that ice II appeared in the core region of Rhea at ca. 3600 Ma and grew to encompass a region of radius 400 km, resulting in a decrease in overall radius of 15.5 km.

As a matter of interest I modelled the cooling of a *differentiated* NH_3-free model. At 4550 Ma this model has a radius of 764 km, a rocky core with a radius of 370 km, and an ice I-II interface at a depth of 324 km. The bulk density is 1235.48 kg m^{-3}. Running the model backwards showed the following (Fig. 9.15): at t = 150 Ma the model has a radius of 770.74 km and is too warm to contain any ice II. The radius shrinks by 1.47 km between 150 – 3750 Ma. At the latter juncture the temperature at the base of the mantle becomes low enough for ice II to form.

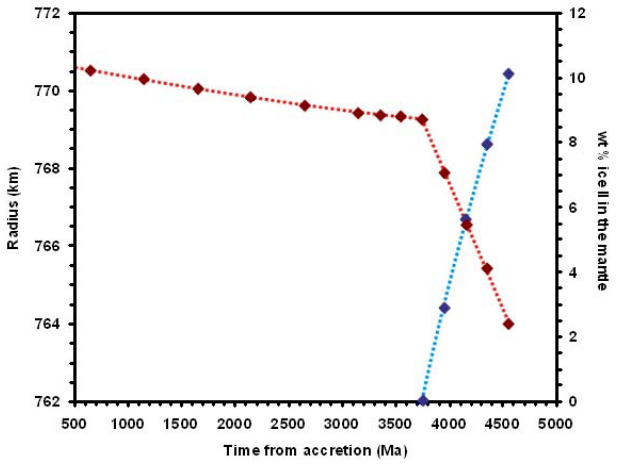

Fig. 9.15. Evolution of the radius and ice II content for a differentiated NH_3-free model of Rhea. The red dotted line is the radius, and values should be read from the left-hand axis. The proportion of ice II in the mantle is shown by the blue dotted line, and values should be read from the right-hand axis. The lines are a guide to the eye.

As in the undifferentiated model, there is an 'ice II catastrophe' where a relatively rapid increase in ice II abundance takes place with an associated drop in radius. In the space of 800 Ma the radius decreases by 5.27 km (producing a compressional strain at the surface of ~38 MPa).

9.2.2.4 Summary

This modelling reveals that the low-order gravity and static distortion is scarcely influenced by the chemical composition, or phase composition, of the ice mantles of Rhea or Titan. Indeed, to first order, these properties are determined by the size and density of the core.

However, for Rhea, it seems likely that the lack of evidence for a 5 – 10 km decrease in radius, which occurs in both differentiated and undifferentiated pure ice + rock models, is evidence for the incorporation of > 3 wt % NH_3, in line with cosmochemical arguments (see 1.2).

For Titan, incorporation of ammonia results in a subsurface ocean. Not only will this be observable in the tidal variation of J_2 (Rappaport *et al.,* 1997), but my results indicate that a deep ocean yields the lowest values of I/MR^2.

I reiterate that gravity is inherently non-unique, and cannot directly determine the internal density distribution. This requires more direct techniques, such as seismography, which are unlikely to be deployed on the surfaces of icy moons for some decades.

9.3 Future work

It would be worthwhile to pursue DFT calculations on high-pressure ammonia hydrates (at such time as their crystal structures are known). *Ab initio* molecular dynamics simulations of the disordered AMH VI and ADH VI (and indeed non-stoichiometric compounds with this structure) would be of interest, not least in terms of materials science, but planetary science as well: ammonia-water mixtures inside Uranus and Neptune are likely to experience pressure of order 10^2 GPa.

Further experimental studies are desperately needed. As a result of my own work, and that of the Edinburgh Group (J. S. Loveday and R. J. Nelmes), at least five polymorphs of ADH (phases II – VI), and possibly more, have been discovered but have not had their structures determined. At the time of submitting this work, I have beam-time to study ADH II on HRPD at ISIS (RB14885), and have submitted applications to study the other phases on PEARL at ISIS, and on the D2B instrument at the Institut Laue-Langevin (ILL) in France.

In addition to studying the *structures* of the high-pressure dihydrate phases, it is important to make further measurements of the melting point in the 0.4 – 1.0 GPa region, since there is a clear difference in interpretation between different groups (Hogenboom *et al*., 1997: Mousis *et al.,* 2002b: and myself). Moreover, better constraints need to be placed on the slope of the ADH I – II phase transition, as well as (any) constraints on higher pressure phase boundaries.

It seems likely that a full study of the dihydrate system could occupy a great many years.

ADH is not the only hydrate requiring further study. AMH is the subject of continuing work by the Edinburgh Group, but the hemihydrate warrants further attention too. Although not of any great planetary interest, an understanding of its thermoelastic properties, and the behaviour of the orientationally disordered NH_3 molecule, would contribute to a fuller picture of the ammonia-water system as a whole.

Equation of state studies of ammonia polymorphs, and even certain ice polymorphs, are not abundant. It became clear whilst compiling P-V-T data for the planetary modelling that the EoS of ices II and VI were not very well known. Since these phases may form significant fractions of icy moon interiors it seems necessary to accurately determine their equations of state. To this end I have very recently carried out a detailed study of ice II on HRPD, and have beam time to study ice VI on the D20 station at ILL.

As indicated in the earlier discussion of Rhea's internal structure, the equilibrium ice I – II phase boundary at low-temperature is not well known, and this offers scope for further research.

And yet this work, and this discussion of future work, is barely the beginning. I have made no mention of methane hydrates or salt hydrates (e.g., epsomite, $MgSO_4.7H_2O$), which are likely to be important constituents of icy moon interiors. As spacecraft like Galileo (Jupiter orbiter 1995 – 2003) and Cassini (Saturn orbiter , commencing 2004) reveal the complexities of the solar system's icy moons, it is up to the mineral physicist to ensure we understand the properties of the materials from which they are made through a combination of experimental work and *ab intio* simulation.

REFERENCES

Alavi, A., R. M. Lynden-Bell, and R. J. C. Brown (1999) J. Chem. Phys. **110**(12), 5861.

Amano, T. (1984) J. Mol. Spectros. **103**(2), 436.

Anders. E., and N. Grevesse (1989) Geochim Cosmochim Acta **53**(1), 197.

Anderson. J. D. (1974) In, *Experimental Gravitation* (B. Bertotti, Ed), Academic Press, New York, pp163-199.

Anderson. J. D., and G. Giampieri (1999) Icarus **138**(2), 309.

Anderson. J. D., R. A. Jacobson, T. P. McElrath, W. B. Moore, G. Schubert, and P. C. Thomas (2001) Icarus **153**(1), 157.

Anderson. J. D., N. J. Rappaport, G. Giampieri, G. Schubert, and W. B. Moore (2003) Phys. Earth Planet. Int. **136**(3-4), 201.

Andersson, O., and H. Suga (1994) Phys. Rev. B **50**(10), 6583.

Andrews. S. B., N. A. Burton, and I. H. Hillier (1997) Chem. Phys. Lett. **280**(1-2), 73.

Andrews. S. B., N. A. Burton, I. H. Hillier, J. M. Holender, and M. J. Gillan (1996) Chem. Phys. Lett. **261**(4-5), 521.

Aoki. K., H. Yamawaki, M. Sakashita, and H. Fujihisa (1996) Phys. Rev. B. **54**(22), 15,673.

Arakawa. M., and N. Maeno (1994) Geophys. Res. Lett. **21**(14), 1515.

Argaman. N., and G. Makov (2000) Am. J. Phys. **68**(1), 69.

Arnold, G. P., R. G. Wenzel, S. W. Rabideau, N. G. Nereson, and A. L. Bowman (1971) J. Chem. Phys. **55**, 589.

Ashcroft, N. W., and N. D. Mermin (1976) In, *Solid state physics*. Harcourt Brace College Publishers, Orlando, Florida.

Atreya. S. K., T. M. Donohue, and W. R. Kuhn (1978) Science **201**, 611.

Bader. R. F. W. (1990) In, *Atoms in Molecules—A Quantum Theor*y, International Series of monographs on Chemistry 22. Oxford University Press, Oxford.

Báez, L. A., and P. Clancy (1995) J. Chem. Phys. **103**(22), 9744.

Bailey. I. F. (2003) Z. Krist. **218**(2), 84.

Becke. A. D. (1988) Phys. Rev. A **38**(6), 3098.

Behnke, G., H. Bilz, and H. Buttner (1986) Phys. Rev. Lett. **56**(12), 1276.

Benoit. M., D. Marx, and M. Parinello (1998a) Nature **392**(6673), 258.

Benoit. M., D. Marx, and M. Parrinello (1998b) Comput. Mat. Sci. **10**(1-4), 88.

Benoit. M., M. Bernasconi, P. Focher, and M. Parinello (1996) Phys. Rev. Lett. **76**(16), 2934.

Bernal, J. D., and R. H. Fowler (1933) J. Chem. Phys. **1**, 515.

Bertie, J. E., and M. R. Shehata (1984) J. Chem. Phys. **81**(1), 27.

Bertie, J. E., and M. R. Shehata (1985) J. Chem. Phys. **83**(4), 1449.

Besson. J. M., Ph. Pruzan, S. Klotz, G. Hamel, B. Silvi, R. J. Nelmes, J. S. Loveday, R. M. Wilson, and S. Hull (1994) Phys. Rev. B. **49**(18), 12540.

Besson. J. M., R. J. Nelmes, G. Hamel, J. S. Loveday, G. Weill, and S. Hull (1992) Physica B **180/181**, 907.

Besson. J. M., and R. J. Nelmes (1995) Physica B **213-214**, 31.

Besson. J. M., S. Klotz, G. Hamel, W. G. Marshall, R. J. Nelmes, and J. S. Loveday (1997) Phys. Rev. Lett. **78**(16), 3141.

Bhattacharyya. D., and R. Majumdar (2001) Indian J. Biochem. Biophys. **38**(1-2), 16.

Birch, F. (1952) J. Geophys. Res. **57**(2), 227.

Bizhigitov, T. B. (1987) Ph.D Thesis, Moscow.

Bjerrum, N. (1951) Kgl. Danske. Videnskab. Selskab. Math. Fys. Medd. **27**(1), 3.

Bjerrum, N. (1952) Science **115**, 385.

Boese. R., N. Niederprijm, D. Blaser, A. Maulitz, M. Y. Antipin, and P. R. Mallinson (1997) J. Phys. Chem. B **101**(30), 5794.

Boldyreva. E. V. (2003) J. Mol. Struct. **647**(1-3), 159.

Boone. S. C. (1989) Ph.D Thesis, University of California, Los Angeles. 326pp.

Brink, G., and L. Glasser (1987) J. Mol. Struct.**160**(3-4), 357.

Brown, R. J. C. (1995) J. Mol. Struct. **345**, 77.

Brown. M. E., and W. M. Calvin. (2000) Science **287**, 107.

Brown. R. H., and D. P. Cruickshank. (1997) Ann. Rev. Earth. Planet. Sci. **25**, 243.

Burke. K., J. P. Perdew, and M. Ernzehof (1997) Int. J. Quantum Chem. **61**(2), 287.

Calvin. W. M., R. N. Clark, R. H. Brown, and J. R. Spencer (1995) J. Geophys. Res. **100**(E9), 19041.

Campbell. D. B., G. J. Black, L. M. Carter, and S. J. Ostro (2002) Bull. Am. Astr. Soc. **34**, abstract 22.04.

Campbell. J. K., and J. D. Anderson (1989) Astron. J. **97**(5), 1485.

Carloni. P (2002) Quant. Struct. Act. Rel. **21**(2), 166.

Carr. M. H., and 21 others (1998) Nature **391**, 363.

Castillo. J., N. Rappaport, A. Mocquet, and C. Sotin (2002) Lunar Planet. Sci. Conf. **32**, abstract 1989.

Cavazzoni, C. (1998) Ph.D Thesis. International School for Advanced Studies (Scuola Internzionale Superiore di study Avanzati), Trieste, Italy.

Cavazzoni, C., G. L. Chiarotti, S. Scandolo, E. Tosatti, M. Bernasconi, and M. Parinello (1999) Science **283**, 44.

Ceperley. D. M., and B. J. Alder (1980) Phys. Rev. Lett. **45**(7), 566.

Chan. J. P., and W. F. Giauque (1964) J. Phys. Chem. **68**(10), 3053.

Chick. K. M., and P. Cassen (1997) Astrophys. J. **477**(1), 398.

Cizek. J. (1966) J. Chem. Phys. **45**, 4256.

Clark. R. N., A. Steele, R. H. Brown, and P. D. Owensby (1984) Icarus **58**(2), 265.

Clifford. I. L., and E. Hunter (1933) J. Phys. Chem. **37**(1), 101.

Cohen. M. L., and V. Heine (1970) Solid State Phys. **24**, 37.

Consolmagno. G. J. (1985) Icarus **64**(3), 401.

Courtin. R., D. Gautier, and C. P. McKay (1995) Icarus **114**(1), 144.

Coustenis. A., A. Salama, B. Schulz, S. Ott, E. Lellouch, Th. Encrenaz, D. Gautier, and H. Feuchtgruber (2003) Icarus **161**(2), 383.

Coustenis. A., and nine others (2001) Icarus **154**(2), 501.

CRC Handbook of Chemistry and Physics, 81st edition. David R. Lide (Editor in Chief). CRC Press, Boca Raton, Ann Arbor, London, Tokyo (2001).

Croft. S. K., J. I. Lunine, and J. S. Kargel (1988) Icarus **73**(2), 279.

Croft. S. K., and L. A. Soderblom (1991) In, *Uranus* (J. T. Bergstralh, E. D. Miner, and M. S. Matthews., Eds), University of Arizona Press, Tucson, pp 561-628.

Cruz León, G., S. Rodríguez Romo, and V. Tchijov (2002) J. Phys. Chem. Solids **63**(5), 843.

Dalton. J. B., J. M. Curchin, and R. N. Clark (2001) Proc. Lunar Planet. Sci. Conf. **32**, abstract 1496.

Dantl, G. (1968) Phys. Condens. Matt. **7**, 390.

Davies. M. E., and F. R. Katayama (1983) Icarus **56**(3), 603.

DeKock, R. L., and H. B. Gray (1989) In, *Chemical Structure and Bonding,* University Science Books, Mill Valley, CA.

Demaison, J., L. Margulès, and J. E. Boggs (2000) Chem. Phys. **260**(1-2), 65.

Demontis, P., M. L. Klein, and R. LeSar (1989) Phys. Rev. B **40**(4), 2716.

Demontis, P., R. LeSar, and M. L. Klein (1988) Phys. Rev. Lett. **60**(22), 2284.

Demuth, Th., Y. Jeanvoine, J. Hafner, and J. G. Angyan (1999) J. Phys. Condens. Matt. **11**(19), 3833.

Dobson. J. F., K. McLennan, A. Rubio, J. Wang, T. Gould, H. M. Le, and B. P. Dinte (2001) Austral. J. Chem. **54**(8), 513.

Dong, S. L., Y. Wang, A. I. Kolesnikov, and J. C. Li (1998) J. Chem. Phys. **109**(1), 235.

Dumas. C., R. J. Terrile, R. H. Brown, G. Schneider, and B. A. Smith (2001) Astrophys. J. **121**(2), 1163.

Durham. W. B., H. C. Heard, and S. H. Kirby (1983) Proc. Lunar Planet. Sci. Conf. **14**, B377.

Durham, W. B., S. H. Kirby, and L. A. Stern (1992) J. Geophys. Res. **97**(E12), 20883.

Durham, W. B., S. H. Kirby, and L. A. Stern (1993) J. Geophys. Res. **98**(B10), 17667.

Eckert. J., R. L. Mills, and S. K. Satija (1983) J. Chem. Phys. **81**(12), 6034.

Elliott. L. D. (1924) J. Phys. Chem. **28**(8), 887.

Ellsworth. K., and G. Schubert (1983) Icarus **54**(3), 490.

England. C. (2002) Bull. Am. Astr. Soc. **34**, abstract 41.08.

Faraday. M. (1845) Phil. Trans. Royal Soc. London **135**, 155.

Federico. C., and P. Lanciano (1983) Ann. Geophys. **1**, 469.

Fermi. E. (1928) Z. Phys. **48**, 73.

Feynman. R. P. (1939) Phys. Rev. **56**(4), 340.

Finch, E. D., S. W. Rabindeau, R. G. Wenzel, and N. G. Nereson (1971) J. Chem. Phys. **49**, 4361.

Fock. V. (1930) Z. Phys. **61**, 126.

Fuchs, M., M. Bockstedte, E. Pehlke, and M. Scheffler (1998) Phys. Rev. B **57**(4), 2134.

Fukazawa, H., S. Ikeda, M. Oguro, T. Fukumura, and S. Mae (2002) J. Phys. Chem. B **106**(23), 6021.

Gagnon, R. E., H. Kiefte, M. J. Clouter, and E. Whalley (1990) J. Chem. Phys. **92**(3), 1909.

Gale. J. D. (1997) Phil. Mag. B **73**(1), 3.

Gale. J. D. (1998) J. Phys. Chem. B **102**(28), 5423.

Gauthier. M., Ph. Pruzan, J. C. Chervin, and J. M. Besson (1988) Phys. Rev. B **37**(4), 2102.

Giguere, P. A. (1983) Rev. Chim. Min. **20**, 588.

Gillan. M. J. (1989) J. Phys: Condens. Matt. **1**(4), 689.

Gillan. M. J. (1997) Contemp. Phys. **38**(2), 115.

Gilli. G., and P. Gilli (2000) J. Mol. Struct. **552**(1-3), 1.

Goldsby. D. L., and D. L. Kohlstedt (1994) Lunar Planet. Sci. Conf. **25**, 439.

Goncharov. A. F., V. V. Struzhkin, M. S. Somayazulu, R. J. Hemley, H. K. Mao (1996) Science **273**, 218.

Goncharov, A. F., V. V. Struzhkin, H. K. Mao, and R. J. Hemley (1999) Phys. Rev. Lett. **83**(10), 1998.

Gränicher, H. (1958) Proc. Roy. Soc. London A **247**(1251), 453.

Grasset. O., and C. Sotin (1996) Icarus **123**(1), 101.

Grasset. O., C. Sotin, and F. Dechamps (2000) Planet. Space. Sci. **48**(7-8), 617.

Greeley. R., J. E. Klemaszewski, R. Wagner, and the Galileo Imaging Team (2000) Planet. Space. Sci. **48**(9), 829.

Gromnitskaya. E. L., O. V. Stal'gorova, V. V. Brazhkin, and A. G. Lyapin (2001) Phys. Rev. B **64**, 094205.

Hafner, J. (2000) Acta Materialia **48**(1), 71.

Haines, J., and J. M. Leger (1993) Phys. Rev. B **48**(18), 13344.

Hama, J., Y. Shiomi, and K. Suito (1990) J. Phys. Condens. Matt. **2**(40), 8107.

Hamann. D. R. (1997) Phys. Rev. B **55**(16), 10157.

Hammer. B., L. B. Hansen, and J. K. Nørskov (1999) Phys. Rev. B **59**(11), 7413.

Hartree. D. R. (1928) Proc. Cambridge. Phil. Soc. 24, **89**.

Hellens. R. L. (1951) Ph.D. thesis. Yale University.

Hellmann. H. (1937) *Einfuhrung in die Quantumchemie*. Deuticke, Leipzig.

Hemley, R. J., and H-K. Mao (1998) J. Phys. Condens. Matt **10**(49), 11157.

Hemley. R. J., A. P. Jephcoat, H. K. Mao, C. S. Zha, L. W. Finger, and D. E. Cox (1987) Nature **330**, 737.

Hewat. A. W., and C. Riekel (1979) Acta Cryst. A **35**(4), 569.

Hidayat. T., A. Marten, B. Bezard, D. Gautier, T. Owen, H. E. Matthews, and G. Paubert (1998) Icarus **133**(1), 109.

Hildenbrand, D. L., and W. F. Giauque (1953) J. Am. Chem. Soc. **75**(12), 2811.

Hirsch. K. R., and W. B. Holzapfel (1984) Phys. Lett. **101A**(3), 142.

Hogenboom, D. L., J. S. Kargel, T. C. Holden, and M. Buyyounouski (1995) Proc. Lunar Planet. Sci. Conf. **26**, 613.

Hogenboom, D. L., J. S. Kargel, G. J. Consolmagno,T. C. Holden, L. Lee, and M. Buyyounouski (1997) Icarus **128**(1), 171.

Hohenberg. P., and W. Kohn (1964) Phys. Rev. **136**(3B), B864.

Holzapfel. W. B. (1972) J. Chem. Phys. **56**, 712.

Howe. R. (1987) J. Phys. (Paris) **48**(C-1), 599.

Howe. R., and R. W. Whitworth (1989) J. Chem. Phys. **90**(8), 4450.

Huang. P. Y., and S. C. Solomon (1982) Proc. Lunar Planet. Sci. Conf. **13**, 344.

Hubbard. W. B. (1984) *Planetary Interiors*. Van Norstrand-Reinhold, New York.

Hubbard. W. B., and J. J. McFarlane (1980) J. Geophys. Res. B **85**, 225.

Hull. S. (1998) Mater. Sci. Forum **278**-2, 342.

Hunten. D. M., M. G. Tomasko, F. M. Flasar, R. E. Samuelson, D. F. Strobel, and D. J. Stevenson (1984) In, *Saturn* (T. Gehrels and M. S. Matthews, Eds), University of Arizona Press, Tucson, pp 671-759.

Ibberson. R. M., W. I. F. David, and K. S. Knight (1992) RAL-92-031, Rutherford Appleton Laboratory, Oxfordshire, U.K: http://www.isis.rl.ac.uk/crystallography/hrpd

Irwin. P. G. J. (1999) Surv. Geophys. **20**(6), 505.

Jackson. S. M., and R. W. Whitworth (1995) J. Chem. Phys. **103**(17), 7647.

Jacobson. R. A. (2003) Am. Astr. Soc. DDA Meeting **34**, abstract 6.05.

Jaeger. J. C., and N. G. W. Cook (1969) *Fundamentals of Rock Mechanics*. Chapman & Hall, London.

Jenkins, H. D. B. (1993) J. Sol. Chem. **22**(11), 1029.

Jenkins, H. D. B., H. K. Roobottom, J. Passmore and L. Glasser (1999) Inorg. Chem. **38**(16), 3609.

Johari, G. P. (2000) Chem. Phys. **258**(2-3), 277.

Johari, G. P., and E. Whalley (2001) J. Chem. Phys. **115**(7), 3274.

Johnson, D. A. (1988) J. Chem. Soc. Dalt. Trans. **1988**, 445.

Johnson, D. A. (2000) Phys. Chem. Chem. Phys. **2**(13), 2903.

Johnson, T. V. (1998) In, *Solar System Ices* (B. Schmitt, C. de Bergh, and M. Festou., Eds), Kluwer Academic Publishers, Dordrecht.

Johnson. R. E. (1990) In, *Energetic charged-particle interactions with atmospheres and surfaces*. Springer, Berlin.

Johnson. R. E. (1996) Rev. Mod. Phys. **68**(1), 305.

Johnson. T. V., and T. B. McCord (1971) Astrophys. J. **169**, 589.

Jones. R. O., and O. Gunnarsson (1989) Rev. Mod. Phys. **61**(3), 689.

Jorgensen. J. D., R. A. Beyerlein, N. Watanabe, and T. G. Worlton (1984) J. Chem. Phys. **81**(7), 3211.

Kamb, B., and S. J. La Placa. (1974) EOS: Trans. Am. Geophys. Union. **55**, 1202.

Kamb, W. B. (1964) Acta Cryst. **17**(11), 1437.

Kamb, W. B., W. C. Hamilton, S. J. La Placa, and A. Prakash (1971) J. Chem. Phys. **55**, 1934.

Karapet'yanets, M. Kh., and M. L. Karapet'yanets (1970) In, *Thermodynamic constants of inorganic and organic compounds*. Translated by J. Schmorak. Ann Arbor. Humphrey Scientific Publishers.

Kargel. J. S. (1987) Lun. Planet. Sci. **XVIII**, 475.

Kargel. J. S. (1990) Ph.D thesis. University of Arizona, Tucson.

Kargel. J. S. (1991) Icarus **94**(2), 368.

Kargel. J. S. (1992) Icarus **100**(2), 556.

Kargel. J. S. (1995) In, *Comparative Planetology with an Earth Perspective* (M. T. Chahine, M. F. A'Hearn, and J. Rahe, Eds.), pp. 101-113. Kluwer Academic, Boston.

Kargel. J. S., and D. L. Hogenboom (1995) Proc. Lunar. Planet. Sci. Conf. **26**, 725.

Kargel. J. S., and S. Pozio (1996) Icarus **119**(2), 383.

Kargel. J. S., S. K. Croft, J. I. Lunine, and J. S. Lewis (1991) Icarus **89**(1), 93.

Katoh. E., M. Song, H. Yamawaki, H. Fujihisa, M. Sakashita, and K. Aoki (2000) Phys. Rev. B. **62**(5), 2976.

Kaula. W. M. (1966) *Theory of Satellite Geodesy*. Blaisdell, Waltham, MA.

Kiefte. H., S. W. Breckon, R. Penney, and M. J. Clouter (1985) J. Chem. Phys. **83**(9), 4738.

Kiefte. H., R. Penney, S. W. Breckon, and M. J. Clouter (1987) J. Chem. Phys. **86**(2), 662.

Kivelson. M. G., K. K. Khurana, and M. Volwerk (2002) Icarus **157**(2), 507.

Klotz. S., and J. S. Loveday (1999) ISIS experimental report RB 10412 (POLARIS).

Klotz. S., J. M. Besson, G. Hamel, R. J. Nelmes, J. S. Loveday, and W. G. Marshall (1996) High Press. Res. **14** (4-6), 249.

Klug. D. D., and E. Whalley (1984) J. Chem. Phys. **81**(3), 1220.

Koch. W., and M. C. Holthausen (2001) In, *A Chemist's Guide to Density Functional Theor*y, 2nd ed. (Wiley-VCH), Verlag GmbH, Weinheim, Germany.

Kock. U., and P. L. A. Popelier (1995) J. Phys. Chem. **99**(24), 9747.

Kohn. W., and L. J. Sham (1965) Phys. Rev. **140**(4A), A1133.

Koumvakalis. A. (1988) Ph.D Thesis, University of California, Los Angeles. 137pp.

Kresse. G., and J. Furthmüller (1996) Phys. Rev. B **54**(16) 11,169: Kresse. G., and J. Furthmüller. *Vienna Ab-initio Simulation Package, VASP the Guide*. Technical University Vienna, Austria, http://cms.mpi.univie.ac.at/vasp/vasp/vasp.html.

Kuhs. W. L., J. L. Finney, C. Vettier, and D. V. Bliss (1984) J. Chem. Phys. **81**(8), 3612.

Kuiper. G. P. (1957) Astron. J. **62**, 295.

Kume. T., S. Sasaki, and H. Shimizu (2001) J. Raman Spectrosc. **32**(5), 383.

Kurth. S., J. P. Perdew, and P. Blaha (1999) Int. J. Quant. Chem. **75**(4-5), 889.

Kuznetsov. A. Z., V. Dmitriev, L. Dubrovinsky, V. Prakapenka, and H.-P. Weber (2002) Solid State Comm. **122**(3-4), 125.

Lammer. H., W. Strumptner, G. J. Molina-Cuberos, S. J. Bauer, and T. Owen (2000) Planet. Space Sci. **48**(6), 529.

Langreth. D. C., and M. J. Mehl (1981) Phys. Rev. Lett. **47**(6), 446.

Langreth. D. C., and M. J. Mehl (1983) Phys. Rev. B **28**(4), 1809.

Lanzerotti. L. J., W. L. Brown, K. J. Marcantonio, and R. E. Johnson (1984) Nature **312**, 139.

Larson, A. C., and R. B. Von Dreele (1994) LAUR 86-748, Los Alamos Laboratory.

Latimer. W. M., and W. H. Rodebush (1920) J. Am. Chem. Soc. **42**(7), 1419.

Lawson, A. C., R. B. Roof, J. D. Jorgensen, B. Morosin, and J. E. Schirber (1989) Acta Cryst. B **45**(3), 212.

Leadbetter. A. J., R. C. Ward, J. W. Clark, P. A. Tucker, T. Matsuo, and H. Suga (1985) J. Chem. Phys. **82**(1), 424.

Leclercq, F., P. Damay, and M. Foukani (1995) J. Chem. Phys. **102**(11), 4400.

Lee. C., D. Vanderbilt, K. Laasonen, R. Car, and M. Parrinello (1992) Phys. Rev. Lett. **69**(3), 462.

Lee. C., D. Vanderbilt, K. Laasonen, R. Car, and M. Parrinello (1993) Phys. Rev. B. **47**(9), 4863.

Lee. C., W. Yang, and R. G. Parr (1988) Phys. Rev. B **37**(2), 785.

Lewis. J. S. (1971) Icarus **15**(1), 174.

Lewis. J. S. (1972) Icarus **16**(2), 241.

Lewis. J. S. and R. G. Prinn (1980) Astrophys. J. **238**, 357.

Lindal. G. F., G. E. Wood, H. B. Holz, D. N. Sweetnam, V. R. Eshleman, and G. L. Tyler (1983) Icarus **53**(2), 348.

Line. C. M. B., and R. W. Whitworth (1996) J. Chem. Phys. **104**(24), 10,008.

Liu. L-G. (1982) Earth. Planet. Sci. Lett. **61**, 359.

Lobban, C. (1998) Ph.D Thesis, University of London.

Lobban, C., J. L. Finney, and W. F. Kuhs (1998) Nature (London) **391**, 268.

Lobban, C., J. L. Finney, and W. F. Kuhs (2000) J. Chem. Phys. **112**(16), 7169.

Lobban, C., J. L. Finney, and W. F. Kuhs (2002) J. Chem. Phys. **117**(8), 3928.

Londono, J. D., J. L. Finney, and W. F. Kuhs (1992) J. Chem. Phys. **97**(1), 547.

Londono. J. D., W. F. Kuhs, and J. L. Finney (1993) J. Chem. Phys. **98**(6), 4878.

Lopes-Gautier. R., and 14 others (1999) Icarus **140**(2), 243.

Lorenz, R. D., and S. E. Shandera (2001) Geophys. Res. Lett. **28**(2), 215.

Lorenz, R.D. (1998) Icarus **136**(2), 344.

Lorenz. R. D. (1999) Proc. Lunar. Planet. Sci. Conf. **30**, 1197.

Lorenz. R. D., and J. I. Lunine (1997) Planet. Space. Sci. **45**(8), 981.

Loubeyre, P., R. LeToullec, E. Wolanin, M. Hanfland, and D. Hausermann (1999) Nature **397**(6719), 503.

Loveday, J. S., and R. J. Nelmes (1998) ISIS experimental report RB 9411a (POLARIS).

Loveday, J. S., R. J. Nelmes, D. J. Francis, and S. Klotz (1998) ISIS experimental report RB 9412 (PEARL).

Loveday, J. S., and R. J. Nelmes (1999a) Phys. Rev. Lett. **83**(21), 4329.

Loveday, J. S., and R. J. Nelmes (1999b) ISIS experimental report RB 9859 (POLARIS).

Loveday. J. S., R. J. Nelmes, M. Guthrie, S. Klotz, G. Hamel, and J. M. Besson (1999a) ISIS experimental report 9858a (POLARIS).

Loveday, J. S., M. Guthrie, and R. J. Nelmes (1999b) ISIS experimental report RB 9860 (HRPD).

Loveday, J. S., M. Guthrie, S. Klotz, and R. J. Nelmes (1999c) ISIS experimental report RB 10181a (PEARL).

Loveday, J. S., M. Guthrie, R. J. Nelmes, and D. J. Francis (2000a) ISIS experimental report, RB 11246 (PEARL).

Loveday. J. S., G. Hamel, R. J. Nelmes, S. Klotz, M. Guthrie, and J. M. Besson (2000b) High Press. Res. **17**, 149.

Loveday. J. S., R. J. Nelmes, W. G. Marshall, J. M. Besson, S. Klotz, and G. Hamel (1997) Physica B **241**, 240.

Loveday. J. S., R. J. Nelmes, W. G. Marshall, J. M. Besson, S. Klotz, and G. Hamel (1996) Phys. Rev. Lett. **76**(1), 74.

Loveday. J., and R. J. Nelmes (2000) In *Science and Technology of High Pressure: Proceedings of AIRAPT-17* (M. H. Manghnani, W. J. Nellis, and M. T. Nicol, Eds), pp133-136. Universities Press, Hyderabad, India.

Löwdin. P. –O. (1959) Phys. Rev. **97**(6), 1474.

Lunine. J. I., and D. J. Stevenson (1987) Icarus **70**(1), 61.

Lunine. J. I., Y. L. Yung, and R. D. Lorenz (1999) Planet. Space. Sci. **47**(10-11), 1291.

Lutz. H. D. (2003) J. Mol. Struct. **646**(1-3), 227.

Manzhelii. V. G., and A. M. Tolkachev (1966) Fiz. Tverd. Tela **8**, 1035.

Marshall. W. G., and D. J. Francis (2002) J. Appl. Cryst. **35**(1), 122.

Matsuo, T., Y. Tajima, and H. Suga (1986) J. Phys. Chem. Solids **47**, 165.

McEwan. A. S., and 14 others (1998) Science **281**, 87.

McKay. C. P., T. W. Scattergood, J. B. Pollack, W. J. Borucki, and H. T. van Ghyseghem (1988) Nature **332**, 520.

Meier. R. J. (1999) J. Mol. Struct: Theochem. **467**(1), 79.

Mercury, L., P. Vieillard, and Y. Tardy (2001) Appl. Geochem. **16**(2), 161.

Mezoar. M., T. Le Bihan, Y. Libotte, Y. Le Godec, and D. Häusermann (1999) J. Synchr. Rad. **6**, 1115.

Miller. R. A., and D. E. Schuele (1969) J. Phys. Chem. Solids **30**, 589.

Mironov. K. E. (1955) Zh. Obschch. Khim. **25**, 1081.

Mishima, O., L. D. Calvert, and E. Whalley (1984) Nature **310**, 393.

Mishima. O. (1996) Nature **384**, 546.

Mitzdorf. U., and D. Helmreich (1971) J. Acoust. Soc. Am. **49**, 723.

Møller. C., and M. S. Plesset (1934) Phys. Rev. **46**(7), 618.

Monkhorst. H. J., and J. D. Pack (1976) Phys. Rev. B **13**(12), 5188.

Moore. J. M., V. M. Horner, and R. Greeley (1985) J. Geophys. Res. Suppl. **90**, C785.

Mosqueira. I., and P. R. Estrada (2003) Icarus **163**(1), 198.

Mousis. O., D. Gautier, and D. Bocklée-Morvan (2002a) Icarus **156**(1), 162.

Mousis,. O., J. Pargamin, O. Grasset, and C. Sotin (2002b) Geophys. Res. Lett. **29**(24), 2192.

Munro. R. G., S. Block, F. A. Mauer, and G. Piermarini (1982) J. Appl. Phys. **53**(9), 6174.

Nelmes. R. J., J. S. Loveday, R. M. Wilson, J. M. Besson, P. Pruzan, S. Klotz, G. Hamel, and S. Hull (1993) Phys. Rev. Lett. **71**(8), 1192.

Oganov. A. R., J. P. Brodholt, and G. D. Price (2000) Phys. Earth Planet. Int. **122**(3-4), 277.

Ojamäe. L., K. Hermansson, R. Dovesi, C. Roetti, and V. R. Saunders (1994) J. Chem. Phys. **100**(3), 2128.

Olinger. B., and P. M. Halleck (1975) J. Chem. Phys. **62**(1), 94.

Olinger. B., and R. L. Mills (unpublished). Kindly supplied by Dr Stefan Klotz, Paris Jussieu.

Olovsson. I., and D. H. Templeton (1959a) Acta Cryst. **12**(11), 827.

Olovsson. I., and D. H. Templeton (1959b) Acta Cryst. **12**(11), 832.

Otto. J. W., R. F. Porter, and A. L. Ruoff (1989) J. Phys. Chem. Solids **50**(2), 171.

Owen. T. C. (2000) Planet. Space. Sci. **48**(7-8), 747.

Pappalardo. R. T., and 31 others (1999) J. Geophys. Res. **104**(E10), 24,015.

Pargamin. J., O. Mousis, and O. Grasset (2002) Lunar Planet. Sci. Conf. **33**, 1461.

Pauling. L. (1939) In, *The nature of the chemical bond*. Cornell University Press, Ithaca, NY.

Pawley. G. S. (1981) J. Appl. Cryst. **14**(6), 357.

Payne. M. C., M. P. Teter, D. C. Allan, T. A. Arias, and J. D. Joannopoulos (1992) Rev. Mod. Phys. **64**(4), 1045.

Perdew. J. P. (1986) Phys. Rev. B **33**(12), 8822.

Perdew. J. P. (1991) In, *Electronic Structure of Solids '91* (P. Ziesche and H. Eschrig, Eds.), Akademie Verlag, Berlin.

Perdew. J. P., and Y. Wang (1986) Phys. Rev. B **33**(12), 8800.

Perdew. J. P., and Y. Wang (1992) Phys. Rev. B **45**(23), 13244.

Perdew. J. P., K. Burke, and M. Ernzehof (1996) Phys. Rev. Lett. **77**(18), 3865.

Peterson, S. W., and H. W. Levy (1957) Acta Cryst. **10**(1), 70.

Petrenko, V. F., and R. W. Whitworth (1999) In, *Physics of Ice*. Oxford University Press, Oxford.

Phillips. J. C. (1958) Phys. Rev. **112**(3), 685.

Pickering. S. U. (1893) J. Chem. Soc. London **63**, 141.

Podeszwa, R., and V. Buch (1999) Phys. Rev. Lett. **83**(22), 4570.

Poirier, J. –P., and A. Tarantola (1998) Phys. Earth. Planet. Int. **109**(1-2), 1.

Polian. A., and M. Grimsditch (1984) Phys. Rev. Lett. **52**(15), 1312.

Pople. J. A. (1999) Rev. Mod. Phys. **71**(5), 1267.

Postma. S. (1920) Recl. Trav. Chim. Pays-Bas. **39**, 515.

Prieto. O., and J. S. Kargel (1997) Lunar Planet. Sci. Conf. **28**, 1139.

Prinn. R. G., and B. Fegley (1981) Astrophys. J. **249**(1), 308.

Proctor. T. M. (1966) J. Acoust. Soc. America **39**, 972.

Pruzan. Ph., J. C. Chervin, and B. Canny (1993) J. Chem. Phys. **99**(12), 9842.

Pulay. P. (1969) Mol. Phys. **17**, 197.

RAL (1993) *Profile analysis of neutron powder diffraction data*. RAL-92-032 Rutherford Appleton Laboratory, Oxfordshire, U.K.

Rappaport. N., B. Bertotti, G. Giampieri, and J. D. Anderson (1997) Icarus **126**(2), 313.

Rappaport. N. J., G. Giampieri, and J. D. Anderson (2001) Icarus **150**(1), 168.

Rappé. A. K., and E. R. Bernstein (2000) J. Phys. Chem. A **104**(26), 6117.

Redfern. S. A. T. (2002) Eur. J. Min. **14**(2), 251.

Reed, J. W., and P. M. Harris (1961) J. Chem. Phys. **35**, 1730.

Rollet. A. P., and G. Vuillard (1956) C. R. Acad. Sci. Paris. **243**, 383.

Roothann. C. C. J. (1951) Rev. Mod. Phys. **23**(2), 69.

Röttger. K., A. Endriss, J. Ihringer, S. Doyle, and W. F. Kuhs (1994) Acta Cryst. B **50**, 644.

Rozas. I., I. Alkorta, and J. Elguero (1998) J. Phys. Chem. A **102**(48), 9925.

Ruffle. D. P., and E. Herbst (2000) Mon. Not. Roy. Astr. Soc. **319**(3), 837.

Ruiz. J., and A. Torices (2000) Lunar Planet. Sci. Conf. **31**, abstract 1298.

Ruoff, A. L., X. Hui, and X. Qing (1992) Rev. Sci. Instr. **63**(10), 4342.

Rupert. F. F. (1909) J. Am. Chem. Soc. **31**(8), 866.

Rupert. F. F. (1910) J. Am. Chem. Soc. **32**(6), 748.

Sagan. C., and W. R. Thompson (1984) Icarus **59**(2), 133.

Sakashita. M., H. Yamawaki, H. Fujihisa, and K. Aoki (1998) Rev. High Pressure Sci. Technol. **7**, 796.

Scheiner. S. (1997) In, *Hydrogen bonding: A theoretical perspective*. Oxford University Press.

Schenk. P. M. (1991) J. Geophys. Res. **96**(B2), 1887.

Schubert. G., T. Spohn, and R. Reynolds (1986) In, *Satellites* (J. A. Burns, Ed.), pp. 224-292. University of Arizona Press, Tucson.

Schubert. G., D. Limonadi, J. D. Anderson, J. K. Campbell, and G. Giampieri (1994) Icarus **111**(2), 433.

Shandera. S. E., and R. D. Lorenz (2000) Proc. Lunar. Planet. Sci. Conf. **31**, 1485.

Shimizu, H., T. Nabetani, T. Nishiba, and S. Sasaki (1996) Phys. Rev. B **53**(10), 6107.

Shipman. L. L., A. W. Burgess, and H. A. Scheraga (1975) Proc. Natl. Acad. Sci. U.S.A. **72**, 543.

Shipman. L. L., A. W. Burgess, and H. A. Scheraga (1976) J. Phys. Chem. **80**(1), 52.

Siemons. W. J., and D. H. Templeton (1954) Acta Cryst. **7**(2), 194.

Simakov. M.B. (2001) Proc. Lunar Planet Sci. Conf. **32**, abstract 1514.

Sirota, N. N., and K. T. Zhapparov (1994) Dokl. Akad. Nauk. **334**(5), 577.

Sirota, N. N., and T. B. Bizhigitov (1987) Dokl. Akad. Nauk. **297**(5) 1112.

Sirota, N. N., and T. B. Bizhigitov (1988) Cryst. Res. Tech. **23**(5), 595.

Slater. J. C. (1930) Phys. Rev. **35**(2), 210.

Slater. J. C. (1951) Phys. Rev. **81**(3), 385.

Smith. P. H., M. T. Lemmon, R. D. Lorenz, L. A. Sromovsky, J. J. Caldwell, M. D. Allison (1996) Icarus **119**(2), 336.

Smits. A., and S. Postma (1910) Versl. Akad. Wet. Amsterdam. **12**, 110.

Snir. J., R. A. Nemenoff, and H. A. Scheraga, (1978) J. Phys. Chem. **82**(23), 2527.

Sohl. F., H. Hussmann, B. Schwentker, T. Spohn, and R. D. Lorenz (2001) Bull. Am. Astr. Soc. **33**, abstract 38.05.

Sohl. F., T. Spohn, D. Breuer, and K. Nagel (2002) Icarus **157**(1), 104.

Sohl. F., W. D. Sears, and R. D. Lorenz (1995) Icarus **115**(2), 278.

Spohn. T., and G. Schubert (2003) Icarus **161**(2), 456.

Stern. S. A., and W. B. McKinnon (1999) Lunar Planet. Sci. Conf. **30**, abstract 1766.

Strazulla. G., and M. E. Palumbo (1998) Planet. Space. Sci. **46**(9-10), 1339.

Struzhkin. V. V., A. F. Goncharov, R. J. Hemley, and H. K. Mao (1997) Phys. Rev. Lett. **78**(23), 4446.

Suga. H. (1985) Solid State Phys. **20**, 125.

Suga. H. (1997) Thermochim. Acta **300**(1-2), 117.

Tajima, Y., T Matsuo, and H. Suga (1982) Nature **299**, 810.

Tchijov, V. E. (1993) Prikl. Mekh. Tekh. Fiz. **2**, 113.

Teter. M. P., M. C. Payne, and D. C Allan (1989) Phys. Rev. B **40**(18), 12255.

Thomas. L. H. (1926) Proc. Camb. Phil. Soc. **23**, 542.

Touloukian. Y. S., R. K. Kirby, R. E. Taylor, and P. D. Desai (1975) In, *Thermal Expansion, Metallic Elements and Alloys, Vol. 12 of TPRC series on thermophysical properties of matter* (Eds. . S. Touloukian and C. Y. Ho), Plenum, New York.

Tse, J. S., and D. D. Klug (1998) Phys. Rev. Lett. **81**(12), 2466.

Tsuzuki, S., and H. P. Lüthi (2001) J. Chem. Phys. **114**(9), 3949.

Van Kasteren. P. H. G. (1973) Bull. Inst. Intl. Froid-Annexe **1973-1974**, 81.

Van Reeuwijk, S. J., K. G. van Beek, and D. Feil (2000) J. Phys. Chem. A **104**(46) 10,901.

Vanderbilt. D. (1990) Phys. Rev. B **41**(11), 7892.

Voitovich. E. I., A. M. Tolkachev, and V. G, Manzhelii (1971) J. Low Temp. Phys. **5**, 435.

Von Dreele. R. B. (1984) Acta Cryst. C **40**(10), 1635.

Waldorf. D. L., and G. A. Alers (1962) J. Appl. Phys. **33**(11), 3266.

Wallace. D. C. (1998) In, *Thermodynamics of crystals*. Dover, New York.

Walrafen. G. E., M. Abebe, F. A. Mauer, S. Block, G. J. Piermarini, and R. Munro (1982) J. Chem. Phys. **77**(4), 2166.

Wang. J., B. G. Johnson, R. J. Boyd, and L. A. Eriksson (1996) J. Phys. Chem. **100**(15), 6317.

Whalley, E., J. B. R. Heath, and D. W. Davidson (1968) J. Chem. Phys. **48**, 2362.

Wilson, G. J., R. K. Chan, D. W. Davidson, and E. Whalley (1965) J. Chem. Phys. **43**, 2384.

Wolanin, E., Ph. Pruzan, J. C. Chervin, B. Canny, M. Gauthier, D. Hausermann, and M. Hanfland (1997) Phys. Rev. B **56**(10), 5781.

Wood. J. A. (2000) Space. Sci. Rev. **92**(1-2), 87.

Yarger. J., J. I. Lunine, and M. Burke (1993) J. Geophys. Res. **98**(E7), 13109.

Yoder. C. F. (1979) Nature **279**, 767.

Yung. Y. L., M. A. Allen, and J. P. Pinto (1984) Astrophys. J. Suppl. Ser. **55**, 465.

Zahnle. R., J. P. Pollack, D. Grinspoon, and L. Done (1992) Icarus **95**(1), 1.

Zharkov. V. N., V. V. Leontjev, and A. V. Kozenko (1985) Icarus **61**(1), 92.

Zheligovskaya, E. A., G. G. Malenkov, and A. A. Averkiev (2001) Zh. Strukt. Khim. **42**, 10.

Zimmer. C., K. K. Khurana, and M. G. Kivelson (2000) Icarus **147**(2), 329.

PUBLICATIONS, ABSTRACTS, AND REPORTS

Fortes, A. D. (2000) Exobiological implications of a possible ammonia-water ocean inside Titan. Icarus **146**(2), 444-452.

Fortes, A. D., J. P. Brodholt, I. G. Wood, and L. Vočadlo (2001) *Ab initio* simulation of ammonia monohydrate ($NH_3.H_2O$) and ammonium hydroxide (NH_4OH). J. Chem. Phys. **115**(15), 7006-7014.

Fortes. A. D., I. G. Wood, J. P. Brodholt, and L. Vočadlo (2002) *Ab initio* simulation of ammonia hydrates. 18th General Meeting of the International Mineralogical Association, p81.

Fortes, A. D., I. G. Wood, J. P. Brodholt, and L. Vočadlo (2003a) The structure, ordering, and equation of state of ammonia dihydrate ($NH_3.2H_2O$). Icarus **162**(1), 59-73.

Fortes. A. D., J. P. Brodholt, I. G. Wood, and L. Vočadlo (2003b) Hydrogen bonding in solid ammonia from density-functional-theory calculations. J. Chem. Phys. **118**(13), 5987-5994.

Fortes. A. D., I. G. Wood, J. P. Brodholt, and L. Vočadlo (2003c) *Ab initio* simulation of the ice II structure. J. Chem. Phys. **119**(8), 4567-4572.

Fortes. A. D., I. G. Wood, K. S. Knight, J. P. Brodholt, M. Alfredsson, G. S. McGrady and L. Vočadlo (2003d) A high resolution neutron powder diffraction study of ammonia dihydrate ($ND_3.2D_2O$) phase I. J. Chem. Phys. **119**(20), 10,806-10,813.

Fortes. A. D., I. G. Wood, J. P. Brodholt, M. Alfredsson, and L. Vočadlo (2003e) ISIS experimental report RB 13233 (PEARL).

Fortes. A. D., I. G. Wood, J. P. Brodholt, M. Alfredsson, and L. Vočadlo (2003f) ISIS experimental report RB 13234 (HRPD).

Experimental and Theoretical Studies of Ammonia Hydrates to High Pressure

A. D. Fortes

Principal Supervisor: Dr Lidunka Vočadlo

1. Introduction: The nature of ammonia hydrates and their relevance to Planetary Science

The system H_2O-NH_3 contains five stoichiometric solids: water ice, solid ammonia, ammonia dihydrate ($NH_3.2H_2O$), ammonia monohydrate ($NH_3.H_2O$), and ammonia hemihydrate ($2NH_3.H_2O$). The ambient pressure solid-liquid equilibria in this system have been extensively studied over the last century (Pickering 1893; Rupert 1909, 1910; Smits and Postma 1910; Postma 1920; Elliott 1924; Clifford and Hunter 1933; Mironov 1955; Rollet and Vuillard 1956; Van Kasteren 1973; Kargel 1990), and the equilibrium phase diagram is depicted in figure 1 below.

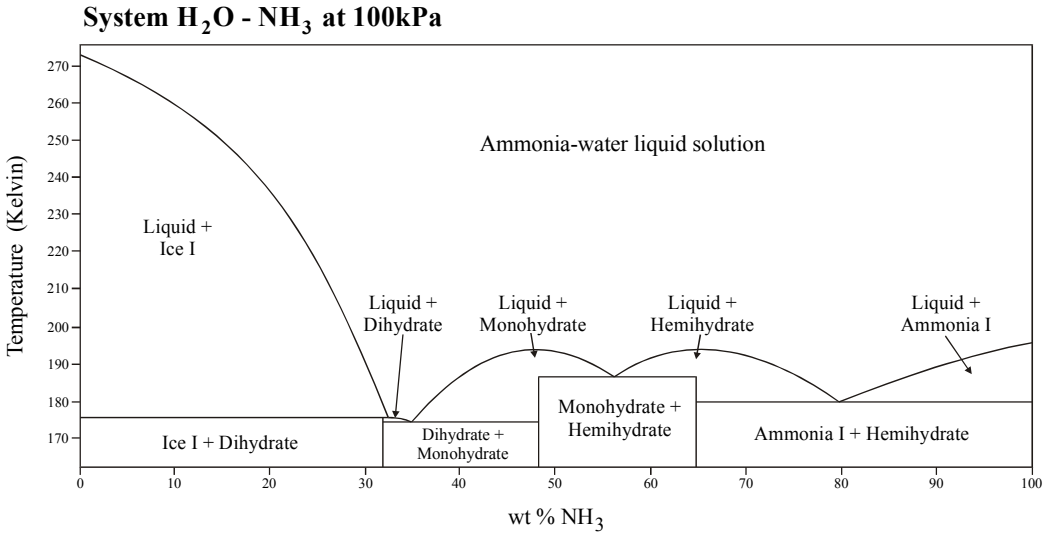

Fig 1. After Kargel (1992).

Interest in the low and high pressure melting behaviour in the system H_2O-NH_3 has increased significantly over the last two decades as it has become clear that ammonia hydrates must play a potentially important role in the dynamics of many icy planetary bodies - most notably the satellites of Saturn, Uranus and Neptune.

The surfaces of these objects are known, from spectroscopic data (Kuiper 1957), to be dominated by water ice, and there are strong cosmochemical arguments favouring bulk compositions in the region of 50% water ice. This is supported by the densities inferred from space-craft flybys. The interiors of icy satellites are likely to be differentiated into rocky cores overlain by icy mantles (Lewis 1971).

There are also cosmochemical grounds for expecting nitrogen to be a significant component of icy planet mantles (Lewis 1972). In the outer PSN, N_2 should have persisted metastably (being kinetically inhibited from reacting to form NH_3: Prinn and Fegley 1981) and would be incorporated into condensing ices as a clathrate, this being a non-stoichiometric solid consisting of a water ice 'cage' structure containing a van der waals bonded 'guest' molecule (in this case N_2). However, giant protoplanetary nebulae in the outer solar system are believed to have been warm enough and dense enough to permit a minimal yield of ammonia via the reaction $N_2 + 3H_2 \leftrightarrow 2NH_3$ (*cf*. The Haber Process), which should have been incorporated into condensing ices as stoichiometric hydrates of ammonia. An ammonia abundance of ~15wt% implies that ammonia dihydrate is likely to be the predominant component, after water ice, of many planetary mantles.

Although ammonia hydrates have not been directly observed, there is some circumstantial evidence for their presence. The majority of icy satellites show signs of endogenic activity inconsistent with the expected thermal history and a pure water-ice mantle (Schubert *et al*. 1986). The lowering of the solidus by incorporation of ammonia reduces the heat flow required, and increases the time

available, for endogenic activity to occur. Potentially continuous cryovolcanic activity on Enceladus (radius 249km) appears to demand the presence of a cosmically abundant antifreeze such as ammonia (Kargel and Pozio 1996).

Moreover, those features which appear to be cryovolcanic lava flows (e.g., Kargel 1995) have a morphology consistent with the known rheological properties of ammonia-water slurries (Arakawa and Maeno 1994), as opposed to highly fluid brine solutions expected from an ammonia-deficient mantle (Kargel 1991). Other candidate materials for producing highly viscous flows (e.g., methanol or formaldehyde) are unlikely, by themselves, to be sufficiently abundant, though they almost certainly occur as accessory phases in cryomagmas.

Finally, the dense nitrogen atmosphere of Titan can be explained in terms of impact dissociation of a primitive ammonia-water ocean (Lunine and Stevenson 1987; Zahnle *et al*. 1992), analogous to the supposed lunar magma ocean, which may or may not persist at depth in the present epoch (Grasset *et al*. 1995; Grasset and Sotin 1996a, 1996b).

2. Current understanding of solids and liquids in the system H_2O-NH_3

2.1 Water ice

Pure water ice has as many as fifteen experimentally identified crystalline polymorphs, several of which are wholly metastable but which may be important at planetary surfaces as shock induced phases. The equilibrium phase diagram (figure 2, below) can be divided into two groups of solids either side of the Ice V - Ice VI phase boundary (which corresponds to a first order liquid-liquid transition in the supercooled metastable fluid). Those phases on the right of the boundary achieve denser structures by organising into interlocking lattices that have been referred to as 'self-clathrates.' Ice VIII, for example, can be described in terms of two interpenetrating ice Ic sublattices.

Ices may also be categorised according to whether or not the orientation of the water molecule is ordered. All of the 'high' temperature phases, except Ice II and Ice VIII, show some degree of proton disorder, whereas all of the low temperature phases are ordered.

At very high pressures, the hydrogen bonds become symmetrical (Ice X), and at yet higher pressures, simulations indicate that the protons wander freely, yielding a superionic form of ice (i.e., hydrogen delocalisation into a heavy fermion state: Holzapfel 1999). In the latter form, an fcc oxygen lattic forms, and hydrogen becomes diffusive (Hashimoto *et al*. 1997)

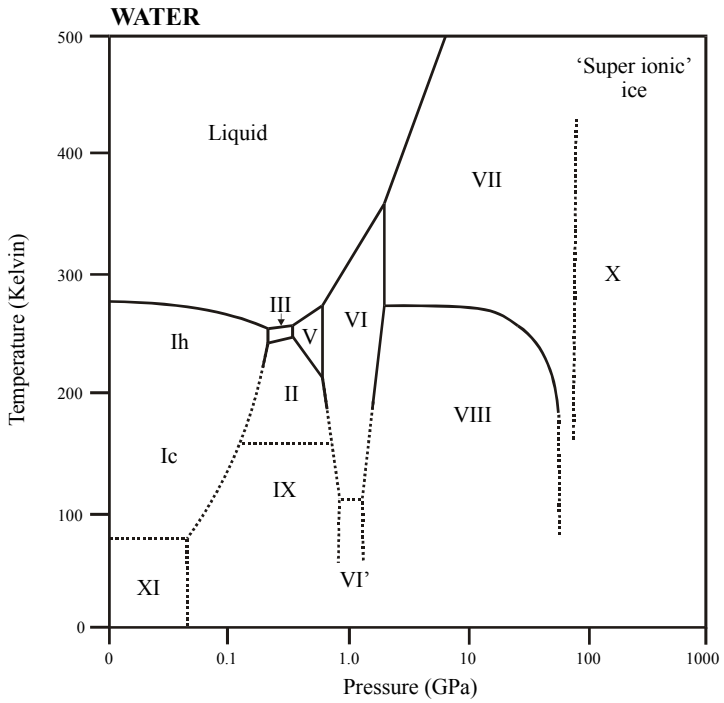

Fig. 2. After Lobban *et al*. (1998)

Water ice, as one of the archetypal hydrogen bonded solids, has been studied extensively, and is reasonably well understood. All of the ordered phases have been simulated by lattice dynamics (e.g., Dong *et al*. 1997) and molecular dynamics (e.g., Borzsák and Cummings 1999) methods, and *ab initio* simulations are beginning to impact on studies of disordered phases such as Ice Ih (e.g., Morrison *et al*. 1997).

2.2 Solid Ammonia

Studies of pure ammoniacal solids are not so well advanced as those of water ice, though some data is available on recently identified phases up to 75GPa (see phase diagram - figure 3 - below). This is partly due to the particular difficulties of working with the material. Ammonia is of interest, however, because it is only weakly hydrogen bonded (if at all in phase I), and it is of relevance to this discussion in as much as the ammonia hydrates contain a mixture of weak and strong hydrogen bonds.

The crystal structure of ammonia I was established by Olovsson and Templeton (1959), using the single crystal and powder XRD methods, to be cubic (space group $P\,2_13$ (T^4)) with a=5.084Å at 77 K. This phase is known to orientationally ordered and melts at 195.4 K.

Ammonia II and III are rotationally disordered, assigned respectively to space groups $P6_3/mmc$ (D^4_{6h}) and $Fm3m$ (O^5_h). Ammonia IV is ordered and recent neutron diffraction analysis (Loveday *et al.* 1998) has revealed it to be orthorhombic (space group $P\,2_12_12_1$) rather than hexagonal, as previously believed. Gauthier *et al*. (1988) were able to identify a cubic ($I43m$?) phase V and an apparently bond symmetrized cubic phase VI (analogous to ice X) at ~60GPa. At higher pressures still, ammonia should transform into a superionic or metallic phase (Cavazzoni *et al*. 1999).

The elastic properties of ammonia III were determined by Kume *et al*. (1998).

Presently, the only simulations of solid ammonia attempted have used lattice dynamics methods (Zeng and Anderson 1990), although the ammonia dimmer has been studied by *ab intio* methods (Lee and Park 2000; Park 2000), as has liquid ammonia (Jursic 1998; Diraison *et al*. 1999).

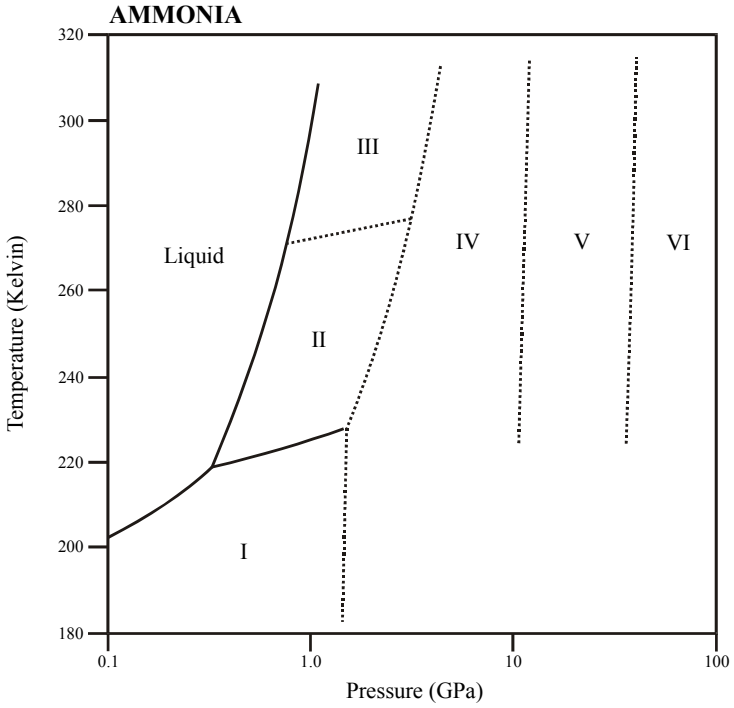

Fig. 3. After Gauthier *et al*. (1988)

2.3 Ammonia Dihydrate

Metastability in the region of 33wt% NH_3 prevented the identification of the dihydrate until 1956 Rollet and Vuillard 1956). The eutectic liquid becomes so viscous that a glass forms, or else monohydrate is preferentially nucleated and a protracted period of temperature cycling is necessary to

crystallise the dihydrate. Very little information exists on the dihydrate phase, in spite of its marked interest to planetary scientists. In part, this may be the result of difficulties in making and handling the material (e.g., Yarger *et al*. 1993), particularly at elevated pressures.

The heat capacity and entropy of the dihydrate have been measured at ambient pressure (Chan and Giauque 1964), and a single analysis of the crystal structure has been made: Combined powder XRD and infrared spectroscopy (Bertie and Shehata 1984) revealed a suspected orthorhombic (pseudocubic; a=7.118Å) structure of space group $P\,2_12_12_1$ with O-H--O distances of 2.76Å, O-H--N distances of 2.74±0.02Å, and N-H--O distances of 3.1Å. Symmetry considerations indicated that the orientation of the water molecules is *disordered*. The structure of ammonia dihydrate has been determined by neutron diffraction (Loveday and Nelmes, 1999a) to be cubic, with space group $P\,2_13$ (a=7.1272Å at 150K).

Interest in the possible solid state extrusion of ammonia hydrates on icy satellite surfaces prompted a study of hydrate rheology (Durham *et al*. 1993; Goldsby and Kohlstedt 1994) showing that the viscosity is a very sensitive function of temperature: Dihydrate is four orders of magnitude less viscous that water ice just below the peritectic, but exceeds the viscosity of ice below 140K.

Considerable interest in the behaviour of the dihydrate at high pressure has resulted in numerous attempts to reconcile high and low pressure calorimetric data (Johnson and Schwake 1983; Johnson and Nicol 1985, 1987; Cynn *et al*. 1989; Hogenboom *et al*. 1989; Boone and Nicol 1991; Hogenboom and Kargel 1990). The problem appears to have been resolved by Hogenboom *et al*. (1997) who claim discovery of a new high-pressure phase - ammonia dihydrate II. The inferred phase diagram is illustrated in figure 4. Nothing is known about ammonia dihydrate II at present, although structural work is ongoing at Rutherford Appleton (J. S. Loveday, pers com). Ammonia dihydrate is known to decompose into ammonia monohydrate + Ice VII in the region of 3.45GPa, but it is anticipated that at least one more post-dihydrate II phase remains to be identified.

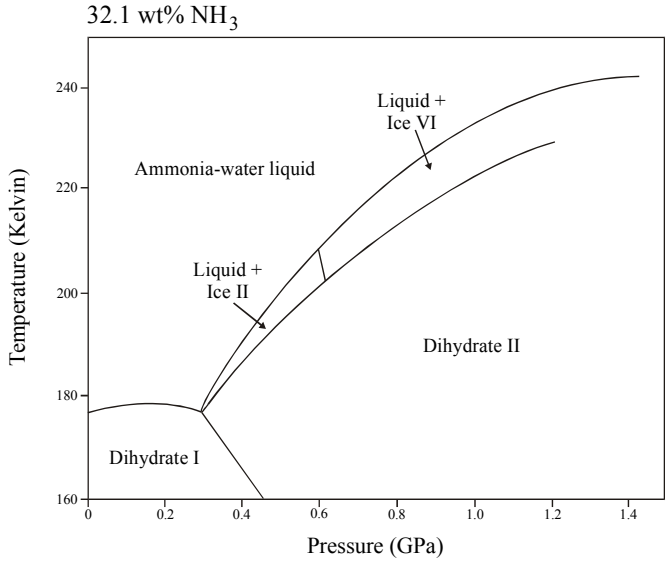

Fig. 4. After Hogenboom *et al*.(1997)

2.4 Ammonia Monohydrate

Early structural work on the more ammonia rich monohydrate phase, which melts congruently at 194.15K, (Olovsson and Templeton 1959) showed that the ambient pressure monohydrate is orthorhombic (space group $P\,2_12_12_1$) with a=4.51±0.01Å, b=5.587±0.003Å, and c=9.700±0.005Å at 113K. An earlier study (Siemons and Templeton 1954) erroneously purported to show that the monohydrate was hexagonal (a=11.21±0.05Å, c=4.53±0.02Å). Neutron diffraction studies of the deuterated monohydrate were performed by Loveday *et al*. (1998) at Rutherford Appleton Laboratory

and confirmed the space group assignment ($P\ 2_12_12_1$, a=4.51108 Å, b=5.58691 Å, c=9.71452 Å at 110K: Loveday and Nelmes, 1999a).

In addition to confirming the suspected detection of a higher pressure monohydrate II by Hogenboom *et al*. (1995, 1997), the Rutherford group identified five new monohydrate phases (Loveday and Nelmes 1999a). Work is continuing at present to index the diffraction data, although the simplicity of the monohydrate VI diffraction pattern has allowed a rapid structural determination, showing it to be cubic (space group I*m*3*m*, a=3.2727Å: Loveday and Nelmes 1999b)

The thermal and microwave conductivity of ammonia monohydrate was recently determined by Lorenz (1999) and Shandera and Lorenz (2000).

Work on monohydrate VI has shown it to be an H-bonded substitutionally disordered molecular alloy. This type of structure may accommodate a degree of non-stoichiometry and be stable to very high pressures (i.e. several hundred GPa). This has implications for the interiors of Uranus and Neptune where a solid solution of monohydrate VI and ice VII may be stable over a wide P-T range (Loveday and Nelmes 1999b)

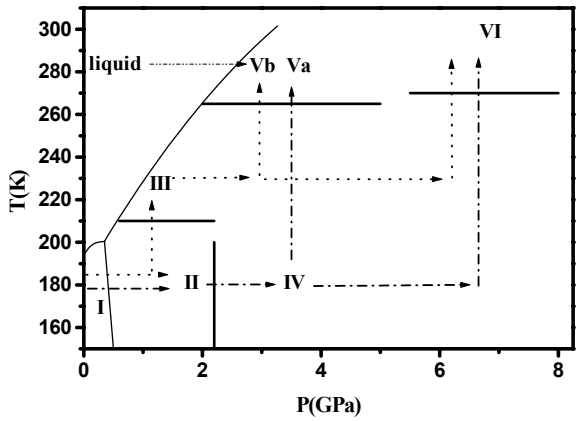

Fig. 5. Reproduced from Loveday and Nelmes (1999a).

2.5 Ammonia Hemihydrate

The hemihydrate melts congruently at 194.32 K, and the calorimetric data of Hildenbrand and Giauque (1953) indicates a phase transition at 50-55 K which has since been shown to be an order-disorder transition (Loveday and Nelmes, 1999a). The structure of the hemihydrate was determined by x-ray diffraction (Siemons and Templeton 1954) to be orthorhombic (space group *Pbnm*) with a=b=8.41±0.03Å and c=5.33±0.02Å at 178±10 K. More recent neutron diffraction work (Loveday and Nelmes, 1999a) has refined the lattice parameters: a=8.3220Å, b=8.3526Å, c=5.2799Å at 110K.

No other information exists on the hemihydrate and studies at high pressure are in progress (J. S. Loveday, pers com).

2.6 Ammonia-water liquid

The ammonia-water solution has been studied in considerable detail, initially from the point of view of refrigeration science, later by physical chemists investigating hydrogen bonding, and most recently by planetary scientists investigating the possible properties of cryomagmas.

Vapour pressure equilibria (Clifford and Hunter 1933), density (Dalrymple *et al*. 1988; Hogenboom and Kargel 1990), viscosity (McKinnon and Meadows 1984; Kargel 1987) and equation of state (Croft *et al.* 1988) of ammonia-water fluids as functions of composition and pressure are well understood. The rheologies of partial-melts, of interest in cryovolcanism, have been determined by Kargel *et al*. (1991), Durham *et al*. (1993) and Goldsby and Kohlstedt (1994).

No attempts to simulate ammonia-water solutions have been made.

3. THE SCOPE OF THIS PROJECT

3.1 Prioritising problems

In terms of planetary science, the material of greatest interest is the dihydrate phase. The potential for fractionation of ammonia-water magmas suggests that monohydrate may be planetologically important as well. The hemihydrate is unlikely to occur. Hence, the scope of this work will initially encompass only the dihydrate and monohydrate phases, and consider the hemihydrate and liquid solution as secondary problems to be broached if time and resources allow.

There are then a number of questions relating to each material:

Structures: In light of work being undertaken at Rutherford Appleton to determine the structures of ammonia hydrates throughout accessible P-T space (approx 25GPa using the modified Paris-Edinburgh cell), it is no longer necessary to contemplate undertaking such experiments either at UCL or elsewhere. The publications of Loveday and Nelmes provide all of the data with which to begin simulations (see below) of the many ammonia hydrate phases now known to exist.

Equation of state: This, and bulk properties (incompressibility, thermal expansion, etc.,) derived from it, are useful input parameters in developing future seismic models of icy planet mantles.

Transport properties: Transport properties (sound speed, thermal and electrical conductivity, and self-diffusion rates) are of interest in the development of more advanced thermal history models than currently exist. This has a particular bearing on larger satellites where there is a potential for residual sub-surface fluid to persist over geological time as an ammonia-water ocean (as in the case of Titan, cited earlier). It is noteworthy that thermal models using even recent values of thermal conductivity for high-pressure water-ice phases do not yet exist.

This work certainly aims to evaluate the structures and equations of state of the dihydrate and monohydrate phases as a priority.

3.2 Methods: Experimental and Theoretical

The project has much scope for experimental work, which could be undertaken either at UCL or at other facilities.

Experimental work on the monohydrate can be expected to be reasonably straightforward, using reagent grade ammonium hydroxide. However, the dihydrate is notoriously difficult to crystallise and even to obtain data from when in the crystalline state. It is to be anticipated that much trial and error will be involved in making this material.

I anticipate working initially on the ambient pressure phase (at temperatures <175K) to provide measurements that will confirm the validity of computer simulations. From this perspective, it will be useful to measure the vibrational frequencies of the solid hydrates and the elastic constants. This can be achieved through combination of transmission infra-red, Raman, and Brillouin spectroscopy.

Theoretical work on ammonia hydrates, and possibly ammonia-water liquid, will be achieved by computer simulation; modelling the ground state of these materials from quantum mechanical first principles by solving Schrödinger's equation (or rather a modified form thereof). This is the *ab initio* pseudopotential method employing the generalised gradient approximation (GGA) to density functional theory (DFT) as implemented in the Vienna Ab Initio Simulation (VASP) computer code. Single particle states and charge densities are obtained as plane-wave expansions.

This powerful and accurate method has a proven record of accomplishment with a range of materials, and has been demonstrated to provide a good quantitative description of hydrogen bonding in water ice (Hamann 1997). More specifically, the Perdew-Wang form of the GGA (Perdew and Wang 1992) has been shown to provide the best agreement with experimental data on ice I and ice VIII (Tse and Klug 1998).

Simulations will determine the relative energies of various potential structures to identify the stable phase under varying conditions of pressure and temperature. It is hoped that complementary experimental and theoretical data sets on the phase stability and equations of state of ammonia hydrates will agree closely.

3.3 Summary Roadmap

Project goals: Determine the vibrational frequencies and elastic constants of low pressure monohydrate and dihydrate phases.

Perform *ab initio* simulation of the monohydrate and dihydrate, leading to EOS.

Perform *ab initio* simulation of the ammonia-water liquid solution.

---

4. References

Arakawa. M., and N. Maeno. (1994) Effective viscosity of partially melted ice in the ammonia-water system. *Geophys. Res. Lett*. **21**, 1515-1518.

Bertie. J. E., and M. R. Shehata. (1984) Ammonia dihydrate: Preparation, x-ray powder diffraction pattern and infrared spectrum of $NH_3 \cdot 2H_2O$ at 100K. *J. Chem. Phys*. **81**, 27-30.

Boone. S., and M. F. Nicol. (1991) Ammonia-water mixtures at high pressures: Melting curves of ammonia dihydrate and ammonia monohydrate and a revised high-pressure phase diagram for the water-rich region. *Proc. Lunar. Planet. Sci. Conf*. **21**, 603-612.

Borzsák. I., and P. T. Cummings. (1999) Molecular dynamics simulations of ice XII. *Chem. Phys. Lett*. **300**, 359-369.

Cavazzoni. C., G. L. Chiarotti, and S. Scandolo. (1999) Superionic and metallic states of water and ammonia at giant planet conditions. *Science* **283**, 44-46.

Chan. J. P., and W. F. Giaque. (1964) The entropy of $NH_3 \cdot 2H_2O$ and heat capacity from 15 to 300K. *Phys. Chem*. **68**, 3053-3057 (erratum 3912).

Clifford. I. L., and E. Hunter. (1933) The system ammonia-water at temperatures up to 150°C and at pressures up to 20 atmospheres. *J. Phys. Chem*. **37**, 101-118.

Croft. S. K., J. I. Lunine, and J. S. Kargel. (1988) Equation of state of ammonia-water liquid: Derivation and planetological implications. *Icarus* **73**, 279-293.

Cynn. H. C-., S. Boone, A. Koumvakalis, M. Nicol, and D. J. Stevenson. (1989) Phase diagram for ammonia-water mixtures at high pressure: Implications for icy satellites. *Proc. Lunar. Planet. Sci. Conf*. **19**, 433-441.

Dalrymple. W., III, D. L. Hogenboom, and G. J. Consolmagno. (1988) The density of ammonia-water solution to 400MPa (4 kilobars). *Proc. Lunar. Planet. Sci. Conf*. **19**, 241-242.

Diraison. M., G. J. Martyna, and M. E. Tuckerman. (1999) Simulation studies of liquid ammonia by classical ab initio, classical, and path integral molecular dynamics. *J. Chem. Phys*. **111**(3), 1096-1103.

Dong. S., A. I. Kolesnikov, and J. -C. Li. (1997) Lattice dynamical calculations of ice VIII. *J. Phys. Chem. B*. **101**, 6087-6089.

Durham. W. B., S. H. Kirby, and L. A. Stern. (1993) Flow of ices in the ammonia-water system. *J. Geophys. Res*. **98**, 17667-17682.

Elliott. L. D. (1924) The freezing point curve of the system water-ammonia. *J. Phys. Chem*. **28**, 887-888.

Gauthier. M., Ph. Pruzan, J. C. Chervin, and J. M. Besson. (1988) Raman scattering study of ammonia up to 75 GPa: Evidence for bond symmetrization at 60GPa. *Phys. Rev. B*. **37**(4), 2103-2115.

Goldsby. D. L., and D. L. Kohlstedt. (1994) Structure and rheology of partially molten ammonia-water ices. *Lunar. Planet. Sci. Conf*. **25**, 439-440.

Grasset. O., S. Beauchesne, and C. Sotin. (1995) Investigation of the NH_3 (15%)-H_2O (85%) phase diagram close to the liquidus in the range 100-1500MPa using in-situ Raman spectroscopy:

Application to Titan's dynamics. In *Solar System Ices: An International Symposium, 27-30 March 1995, Toulouse, France*, p49.

Grasset. O., and C. Sotin. (1996a) The liquidus of H_2O-NH_3 up to 1.5GPa: Implications for the presence of a liquid shell in Titan's interior. *Lun. Planet. Sci*. **27**, p453.

Grasset. O., and C. Sotin (1996b) The cooling rate of a liquid shell in Titan's interior. *Icarus* **123**, 101-123.

Hamann. D. R. (1997) H_2O bonding in density functional theory. *Phys. Rev. B*. **55**(16) 10157-10160.

Hashimoto. T., S. Sugawara, and Y. Hiwatari. (1997) Structural transformation of ice at normal and high pressure via molecular dynamics simulations. *J. Phys. Chem. B*. **101**, 6293-6300.

Hildenbrand. D. L., and W. F. Giaque. (1953) Ammonium oxide and ammonium hydroxide: Heat capacity and thermodynamic properties from 15 to 300° K. *J. Am. Chem. Soc*. **75**, 2811-2828.

Hogenboom. D. L., and J. S. Kargel. (1990) Ammonia-water densities and phase relations to four kilobars. *Proc. Lunar. Planet. Sci. Conf*. **21**, 522-523.

Hogenboom. D. L., J. S. Kargel, G. J. Consalmagno, T. C. Holden, L. Lee, and M. Buyyounouski. (1997) The Ammonia-Water system and the chemical differentiation of icy satellites. *Icarus* **128**, 171-180.

Hogenboom. D. L., J. S. Kargel, T. C. Holden, and M. Buyyounouski. (1995) The phase diagram of ammonia monohydrate: A new high pressure polymorph. *Proc. Lunar. Planet. Sci. Conf*. **26**, 613-614.

Hogenboom. D. L., J. Winebrake, G. J. Consolmagno, and W. Dalrymple III. (1989) Preliminary densities and phase diagram of the water/NH_3 system at P-T conditions relevant to the icy moons of the outer planets. *Proc. Lunar. Planet. Sci. Conf*. **20**, 420-421.

Holzapfel. W. B. (1999) Evasive ice X and heavy fermion ice XII: facts and fiction about high pressure ices. *Physica B*. **265**, 113-120.

Johnson. M. L., and A. Schwake. (1983) Preliminary phase diagram for the water-rich region of the system NH_3-H_2O to 4.0GPa. *EOS, Trans. Am. Geophys. Union*. **64**, p875.

Johnson. M. L., and M. Nicol. (1985) The ammonia-water phase diagram II: Extent and significance of ammonia dihydrate, $NH_3.2H_2O$. *EOS. Trans. Am. Geophys. Union*. **66**, p944.

Johnson. M. L., and M. Nicol. (1987) The ammonia-water phase diagram and its implications for icy satellites. *J. Geophys. Res*. **92**, 6339-6349.

Jursic. B. S. (1998) Computational study of water and ammonia dimmers with density functional theory methods. *Theochem-J. Mol. Struc*. **434**, 29-36.

Kargel. J. S. (1987) Density and viscosity measurement of NH_3-H_2O liquids. *Lun. Planet. Sci*. **XVIII**, 475-476.

Kargel. J. S. (1990) Cryomagmatism in the outer solar system. Ph. D thesis. University of Arizona, Tucson.

Kargel. J. S. (1991) Brine volcanism and the interior structure of asteroids and icy satellites. *Icarus* **94**, 368-390.

Kargel. J. S. (1992) Ammonia-water volcanism on icy satellites: Phase relations at 1 atmosphere. *Icarus* **100**, 556-574.

Kargel. J. S. (1995) Cryovolcanism on the icy satellites. In *Comparative Planetology with an Earth Perspective* (M. T. Chahine, M. F. A'Hearn, and J. Rahe, Eds.), pp. 101-113. Kluwer Academic, Boston.

Kargel. J. S., and Hogenboom. D. L. (1995) The ammonia-water system: An attempt to reconcile the Lafayette and UCLA investigations. *Proc. Lunar. Planet. Sci. Conf*. **26**, 725-726.

Kargel. J. S., and S. Pozio. (1996) The volcanic and tectonic history of Enceladus. *Icarus* **119**, 383-404.

Kargel. J. S., S. K. Croft, J. I. Lunine, and J. S. Lewis. (1991) Rheological properties of ammonia-water liquids and crystal-liquid slurries: Planetological applications. *Icarus* **89**, 93-112.

Kuiper. G. P. (1957) Infrared observations of planets and satellites. *Astron. J*. **62**, 295-295.

Kume. T., M. Daimon, S. Sasaki, and H. Shimizu. (1998) High pressure elastic properties of liquid and solid ammonia. *Phys. Rev. B*. **57**(21), 13347-13350.

Lee. J. S., and S. Y. Park. (2000) Ab initio study of $(NH_3)_2$: Accurate structure and energetics. *J. Chem. Phys*. **112**(1), 230-237.

Lewis. J. S. (1971) Satellites of the outer planets: Their physical and chemical nature. *Icarus* **15**, 174-185.

Lewis. J. S. (1972) Low temperature condensation from the solar nebula. *Icarus* **16**, 241-252.

Lobban. C., J. L. Finney, and W. F. Kuhs. (1998) The structure of a new phase of ice. *Nature* **391**, 268-270.

Lorenz. R. D. (1999) Radar absorptivity of planetary materials measured using a microwave oven. *Lunar. Planet. Sci. Conf*. **30**, 1197-1198.
Loveday. J. S., and R. J. Nelmes. (submitted paper) Structural studies of ammonia hydrates.
Loveday. J. S., and R. J. Nelmes. (1999a) Proc. XVIIth AIRAPT conference, Hawaii, 1999.
Loveday. J. S., and R. J. Nelmes. (1999b) Ammonia monohydrate VI: A hydrogen-bonded molecular alloy. *Phys. Rev. Lett*. **83**(21), 4329-4332.
Loveday. J. S., R. J. Nelmes, W. G. Marshall, J. M. Betz, S. Klotz, and G. Hamel. (1998) Structural studies of ices at high pressure. *Physica B* **241-243**, 240-246.
Lunine. J. I., and D. J. Stevenson. (1987) Clathrate and ammonia hydrates at high pressure: Application to the origin of methane on Titan. *Icarus* **70**, 61-77.
McKinnon. W. B., and M. Meadows. (1984) Rheological measurement of ammonia-water melt. *Bull. Am. Astr. Soc*. **16**, p686.
Mironov. K. E. (1955) The phase diagram of the system H_2O-NH_3. *Zh. Obschch. Khim*. **25**, 1081-1086.
Morrison. I., J. -C. Li, S. Jenkins, S. S. Xantheas, and M. C. Payne. (1997) Ab initio total energy studies of the static and dynamic properties of ice Ih. *J. Phys. Chem. B*. **101**, 6146-6150.
Olovsson. I., and D. H. Templeton. (1959) The crystal structure of ammonia monohydrate. *Acta. Cryst*. **12**, 827-832
Olovsson. I., and D. H. Templeton. (1959) X-ray study of solid ammonia. *Acta. Cryst*. **12**, 832-837.
Park. J. K. (2000) Ab initio studies for geometrical structures of ammonia cluster cations. *J. Phys. Chem. A*. **104**(21), 5093-5100.
Perdew. J. P., and Y. Wang. (1992) Accurate and simple analytical representation of the electron-gas correlation energy. *Phys. Rev. B*. **45**(23), 13244-13249.
Pickering. S. U. (1893) X. - The hydrate theory of solutions. Some compounds of alkyl-amines and ammonia with water. *J. Am. Chem. Soc*. **63**, p141.
Postma. S. (1920) The system ammonia-water. *Recl. Trav. Chim. Pays-Bas*. **39**, 515-536.
Prinn. R., and B. Fegley. (1981) Kinetic inhibition of CO and N_2 reduction in circumplanetary nebulae: Implications for satellite composition. *Astrophys. J*. **249**, 308-317.
Rollet. A. P., and G. Vuillard. (1956) Sur un novel hydrate de l'ammoniac. *C. R. Acad. Sci. Paris*. **243**, 383-386.
Rupert. F. F. (1909) The solid hydrates of ammonia. *J. Am. Chem. Soc*. **31**, 866-868.
Rupert. F. F. (1910) The solid hydrates of ammonia. II. *J. Am. Chem. Soc*. **32**, 748-749.
Schubert. G., T. Spohn, and R. Reynolds. (1986) Thermal histories, compositions and internal structures of the moons of the outer solar system. In *Satellites* (J. A. Burns, Ed.), pp. 224-292. Univ. of Arizona Press, Tucson.
Shandera. S. E., and R. D. Lorenz. (2000) Thermal conductivity and microwave absorptivity of ammonia hydrate ice. *Proc. Lunar. Planet. Sci. Conf*. **31**, 1485-1486.
Siemons. W. J., and D. H. Templeton. (1954) The crystal structure of ammonium oxide. *Acta. Cryst*. **7**, 194-
Smits. A., and S. Postma. (1910) Het stelsel ammoniak-water. *Versl. Akad. Wet. Amsterdam*. **12**, 110-118.
Tse. J. S., and D. D. Klug. (1998) Anomalous isostructural transformation in ice VIII. *Phys. Rev. Lett*. **81**(12), 2466-2469.
Van Kasteren. P. H. G. (1973) The crystallization behaviour and caloric properties of water/ammonia mixtures between 70 and 300K. *Bull. Inst. Intl. Froid-Annexe* 1973-1974, 81-87.
Yarger. J., J. I. Lunine, and M. Burke. (1993) Calorimetric studies of the ammonia-water system with application to the outer solar system. *J. Geophys. Res*. **98**, 13109-13117.
Zahnle. R., J. P. Pollack, D. Grinspoon, and L. Done. (1992) Impact generated atmospheres over Titan, Ganymede and Callisto. *Icarus* **95**, 1-23.
Zeng. W. Y., and A. Anderson. (1990) Lattice dynamics of ammonia. *Physica. Status. Solidi. B*. **162**(1), 111-117.

First Year Report

A. D. Fortes

Project title: *Ab initio* simulation of ammonia hydrates

Principal supervisor: Dr Lidunka Vočadlo

Supervisory Panel: Dr John Brodholt, Dr Ian Wood.

1. First year objectives

The goals for the first year of this project were to gain an initial understanding of density functional theory (DFT) and related simulation methods, and to become comfortable with the application of this theory in the Vienna *ab initio* simulation package (VASP) code. This was to be achieved by reproducing existing work done using the same DFT method on the high-pressure H_2O polymorph ice VIII. The work was then to proceed on to the ammonia hydrates ($NH_3{\cdot}xH_2O$, where x = ½, 1, or 2), starting with the orientationally ordered low-pressure polymorph of the monohydrate (x = 1: AMH I).

These goals have been met and significantly extended, as will now be described.

2. First year results

2.1. Ice

The first application of DFT using VASP was to ice VIII, aiming to reproduce the specific results of Tse and Klug (Phys. Rev. Lett. v81 p2166, 1998), in particular the equation of state (EOS), pressure dependence of the cell parameters, internal coordinates, and bond lengths, and the minor isomorphic phase transition seen in pressure-quenched ice VIII samples. The work that I undertook reproduced the results of Tse and Klug extremely closely in all respects. Moreover, the calculated equation of state was an excellent match to experimental data collected over the past seven decades.

It was straightforward to continue the simulations at greater compressions than Tse and Klug had examined, and this yielded a singularly exciting result; the spontaneous symmetrisation of the hydrogen bond. It has been speculated for over fifty years, and only recently experimentally confirmed, that ice does indeed acquire symmetrical hydrogen bonds: i.e., the proton ceases to be covalently bonded to a single oxygen atom but instead migrates to a point midway between neighbouring oxygen atoms. This 'ionic' form of ice has the Cu_2O structure (body centred cubic). My work revealed that the lattice of ice VIII achieved hydrogen bond symmetrisation as predicted by earlier quantum simulations, and at the pressure seen experimentally (60-70GPa). My equation of state for this polymorph (dubbed ice X) is an excellent match to recent experimental x-ray data, which extends up to 200GPa.

Molecular dynamics (MD) simulations carried out over the last ten years have proposed two further high-pressure modifications to the ice structure above 200GPa, one having the antifluorite structure, and the other being a pseudo-hcp (space group P*bcm*) modification of the ice X structure. As a further test of my own capabilities, and those of DFT, I undertook simulations of both of these lattices. Once again, the results of earlier studies were confirmed by my work. The P*bcm* structure yielded an EOS, structural parameters, and phase transition pressures in accordance with MD simulations, and the antifluorite structure was found to be energetically disfavoured at all pressures (up to 2000GPa). The P*bcm* structure underwent a displacive transition to ice X at lower pressures, as expected.

In addition I explored a number of other potential structures observed in SiO_2, and other metal dioxides, specifically the Pa3, $CaCl_2$, and α-PbO_2 structures, to determine if any had a field of stability at ultrahigh pressure. It seems, however, that the P*bcm* phase is the more stable structure up to 2TPa.

2.2. Ammonia

Although not initially a target for investigation, I felt that it was important to simulate the behaviour of pure ammonia. There were two reasons for this: Firstly, the hydrogen bonding in ammonia is much weaker than in water ice (1kcal mol^{-1} vs. 5kcal mol^{-1}), and dispersive van der Waals forces (which are dealt with poorly within DFT) are more important. Secondly, ammonia in the solid state has not been the subject of quantum mechanical simulation to anything like the extent that water ice has been. However, there is sufficient experimental data for comparison, and this makes it the ideal stepping-stone between water ice and the ammonia hydrates (for which there is scarcely any experimental or theoretical data).

Two orientationally ordered phases were studied; the ambient pressure phase I, and the higher pressure phase IV. The EOS, cell parameters, and internal coordinates are a good match to experimental data. I was able to further extend my abilities by using VASP to calculate elastic constants and electron distributions. The elastic constants of ammonia I are an excellent match to experimental values, as are the electron densities at the bond critical points. Moreover, this latter method has enabled me to show that ammonia IV does not contain a bifurcated hydrogen bond as has proposed on the basis of neutron diffraction results.

As with water ice, I continued to compress the ammonia I and IV lattices to ultrahigh pressures (~500GPa) so as to observe the point at which the hydrogen bonds became symmetrical. Experimental data rules out bond symmetrisation to 120GPa, and an earlier DFT study (the Doctoral thesis of Carlo Cavazzoni) ruled it out up to 300GPa. My results confirm this finding, showing that the hydrogen bond remains asymmetrical to 500GPa.

A paper entitled ‘Hydrogen bonding in ammonia IV’ is in preparation for submission to the Journal of Chemical Physics shortly.

2.3. Ammonia Monohydrate

The monohydrate of ammonia ($NH_3 \cdot H2O$) is the simplest of the hydrates to study, since it is orientationally ordered, has a reasonably small unit cell, and relatively high symmetry. Moreover, it has been the subject of neutron diffraction studies over the last four years, providing some scope for comparison with my results.

The most significant result of this work has been the observation of a protolytic reaction at a pressure of ~5GPa; in other words, a hydrogen atoms attached to one of the water molecules breaks its covalent bond and forms another with the neighbouring ammonia molecule, yielding ammonium hydroxide (NH_4OH). Solid ammonium hydroxide does not exist in nature, and only a few speculative papers regarding its stability have ever been published. Using thermochemical data on the monohydrate, and incorporating the relative energy difference of the monohydrate and the hydroxide, it proved possible to calculate the thermodynamic stability of NH_4OH. This, in itself, led to a whole new avenue of research when it transpired that conventional empirical equations for calculating the lattice energies of salts make no allowance for hydrogen bonding. I have explored this problem in collaboration with Professor Don Jenkins (University of Warwick Department of Chemistry).

My EOS for AMH is a very good match to the rather limited experimental data, and I have predicted the pressure dependence of cell parameters, internal coordinates and bond lengths.

These results will be published in the October 2001 issue of the Journal of Chemical Physics (volume 115, number 13) as '*Ab initio* simulation of ammonia monohydrate ($NH_3{\cdot}H_2O$) and ammonium hydroxide (NH_4OH).'

2.4. Ammonia hemihydrate and ammonia dihydrate.

Both of these phases exhibit some degree of orientational disorder of the ammonia and water molecules, which is a problem since not all orientational permutations will be energetically equal. To date I have completed an initial run of energy vs. volume calculations for one orientational permutation of each phase. These preliminary results are somewhat troublesome, in that they yield zero pressure molar volumes which are significantly in error (i.e., by > 10%) and, for the dihydrate, unexpected distortions of the unit cell.

2.5. Collaborations

The most significant collaboration has been with Professor Don Jenkins of Warwick University, a noted thermochemist. We have worked closely on my results for ammonium hydroxide and Professor Jenkins is a co-author on the JCP paper. In addition I have forged ties with Dr Jeffrey Kargels' group in the United States which has worked on ammonia-water liquid and ammonia dihydrate in the past. I have also had fruitful discussions regarding my work with Dr Stefan Klotz (Paris), Dr Carlo Cavazzoni (Trieste), Dr Willem Vos (Amsterdam), and Dr Michelle Warren (Manchester).

3. The Future

After a highly productive and successful first year, my aim for the next year is to focus on a few key objectives. The most important is to develop a computational method, with Dr John Brodholt, for reducing the number of orientational permutations of ammonia dihydrate that need to be examined. The results of this will be used to perform DFT calculations on the dihydrate. Secondly, I intend to make applications to the Rutherford Appleton Laboratory to study the dihydrate phase at high pressures using the Paris-Edinburgh cell. I also wish to follow up on promising discussions with Professor Mikhail Strzhemechny (Kharkov Institute of Low Temperature

Physics, Ukraine) with regard to the possibility of doing ambient pressure experiments on the dihydrate to determine elastic constants and thermal conductivity. Kharkov has an established record of excellence in the field of cryogenic studies which I am certain would greatly benefit my work.

Along with these specific problems, I intend to work on the more open ended issue of developing a planetary model for large icy moons. This model will be based on an existing model devised to study the cooling history of Titan's ice shell, but extended to incorporate the most up to date physical properties of relevant ices.

Summary.

The original goals for the first year have been met and exceeded to the satisfaction of myself and my supervisors. I have developed a sufficient understanding of DFT and its application within VASP to reproduce existing work and to produce my own high quality results. As a result, I have a paper in press, and two in preparation.

I have a clear idea of my goals for the second year of this project, and the means to achieve them. By the end of the second year I expect to have completed a DFT study of ammonia dihydrate, to have some new experimental data on this phase in hand, and have the basis of a planetary model to develop in my third year.

September 1st 2001

APPENDIX 1

Refinements of the ADH I structure

Temperature: **174 K**
Rietveld Powder statistics: wRp = 5.07 % Rp = 4.77 % χ^2 = 2.195 %
Lattice constant: 7.148745(19) Å
Unit cell volume: 365.3334(17) Å

Atom	*x*	*y*	*z*	Occupancy	U_{iso} (x100)
O1	0.6940(5)	0.6940(5)	0.6940(5)	1	3.86(16)
D1	0.7660(11)	0.6729(10)	0.5723(17)	2/3	6.05(20)
O2	0.1605(5)	0.1605(5)	0.1605(5)	1	3.50(16)
D2	0.2438(5)	0.2438(5)	0.2438(5)	1	4.01(10)
D3	0.0154(31)	0.2194(23)	0.1851(15)	1/3	5.50(52)
N1	0.3867(4)	0.3867(4)	0.3867(4)	1	5.02(13)
D4	0.3719(9)	0.3529(5)	0.5116(6)	1	6.99(14)

Temperature: **160 K**
Rietveld Powder statistics: wRp = 5.10 % Rp = 4.45 % χ^2 = 4.623 %
Lattice constant: 7.139332(17) Å
Unit cell volume: 363.8922(15) Å

Atom	*x*	*y*	*z*	Occupancy	U_{iso} (x100)
O1	0.6960(4)	0.6960(4)	0.6960(4)	1	3.83(14)
D1	0.7554(10)	0.6739(8)	0.5713(11)	2/3	5.53(16)
O2	0.1605(4)	0.1605(4)	0.1605(4)	1	4.20(15)
D2	0.2440(4)	0.2440(4)	0.2440(4)	1	4.69(9)
D3	0.0083(23)	0.2062(18)	0.1832(13)	1/3	5.13(40)
N1	0.38214(35)	0.38214(35)	0.38214(35)	1	4.86(10)
D4	0.3697(7)	0.3574(4)	0.5104(5)	1	7.28(13)

Temperature: **140 K**
Rietveld Powder statistics: wRp = 5.03 % Rp = 4.47 % χ^2 = 4.485 %
Lattice constant: 7.127840(16) Å
Unit cell volume: 362.1378(14) Å

Atom	*x*	*y*	*z*	Occupancy	U_{iso} (x100)
O1	0.6982(4)	0.6982(4)	0.6982(4)	1	3.39(12)
D1	0.7558(8)	0.6745(7)	0.5734(10)	2/3	4.79(13)
O2	0.1596(4)	0.1596(4)	0.1596(4)	1	4.05(14)
D2	0.2427(4)	0.2427(4)	0.2427(4)	1	4.11(8)
D3	0.0117(21)	0.2082(15)	0.1812(12)	1/3	4.89(33)
N1	0.38188(30)	0.38188(30)	0.38188(30)	1	4.11(8)
D4	0.3662(5)	0.3570(3)	0.5114(5)	1	6.27(10)

Temperature: **120 K**
Rietveld Powder statistics: wRp = 5.30 % Rp = 4.62 % χ^2 = 4.976 %
Lattice constant: 7.117721(16) Å
Unit cell volume: 360.5977(14) Å

Atom	*x*	*y*	*z*	Occupancy	U_{iso} (x100)
O1	0.6999(4)	0.6999(4)	0.6999(4)	1	2.84(11)
D1	0.7543(7)	0.6749(7)	0.5745(9)	2/3	4.25(11)
O2	0.1588(4)	0.1588(4)	0.1588(4)	1	3.99(14)
D2	0.2421(4)	0.2421(4)	0.2421(4)	1	3.88(8)
D3	0.0099(19)	0.2067(13)	0.1819(12)	1/3	4.34(30)
N1	0.38036(28)	0.38036(28)	0.38036(28)	1	3.37(7)
D4	0.3642(5)	0.3580(3)	0.5112(4)	1	5.67(9)

Temperature: **100 K**
Rietveld Powder statistics: wRp = 5.50 % Rp = 4.87 % χ^2 = 5.317 %
Lattice constant: 7.108759(16) Å
Unit cell volume: 359.2372(14) Å

Atom	*x*	*y*	*z*	Occupancy	U_{iso} (x100)
O1	0.70145(33)	0.70145(33)	0.70145(33)	1	2.52(10)
D1	0.7549(7)	0.6764(6)	0.5751(8)	2/3	3.73(10)
O2	0.15732(37)	0.15732(37)	0.15732(37)	1	3.66(13)
D2	0.2409(4)	0.2409(4)	0.2409(4)	1	3.45(13)
D3	0.0120(18)	0.2066(12)	0.1811(12)	1/3	4.12(27)
N1	0.37933(27)	0.37933(27)	0.37933(27)	1	2.97(7)
D4	0.3619(4)	0.3583(3)	0.5113(4)	1	4.95(8)

Temperature: **80 K**
Rietveld Powder statistics: wRp = 5.95 % Rp = 5.26 % χ^2 = 6.207 %
Lattice constant: 7.102338(17) Å
Unit cell volume: 358.2647(15) Å

Atom	*x*	*y*	*z*	Occupancy	U_{iso} (x100)
O1	0.7023(3)	0.7023(3)	0.7023(3)	1	2.10(10)
D1	0.7559(7)	0.6763(7)	0.5752(8)	2/3	3.45(10)
O2	0.15675(37)	0.15675(37)	0.15675(37)	1	3.21(13)
D2	0.2402(4)	0.2402(4)	0.2402(4)	1	3.19(7)
D3	0.0117(19)	0.2064(12)	0.1806(12)	1/3	3.96(27)
N1	0.37954(27)	0.37954(27)	0.37954(27)	1	2.55(7)
D4	0.3608(4)	0.3578(3)	0.5122(4)	1	4.42(8)

Temperature: **60 K**
Rietveld Powder statistics: wRp = 6.35 % Rp = 5.66 % χ^2 = 7.108 %
Lattice constant: 7.096791(17) Å
Unit cell volume: 357.4259(15) Å

Atom	*x*	*y*	*z*	Occupancy	U_{iso} (x100)
O1	0.7032(3)	0.7032(3)	0.7032(3)	1	1.80(10)
D1	0.7564(6)	0.6771(6)	0.5744(8)	2/3	3.03(9)
O2	0.15630(37)	0.15630(37)	0.15630(37)	1	2.87(12)
D2	0.2394(4)	0.2394(4)	0.2394(4)	1	2.87(7)
D3	0.0132(19)	0.2045(12)	0.1796(12)	1/3	3.95(26)
N1	0.37899(26)	0.37899(26)	0.37899(26)	1	2.16(7)
D4	0.3596(4)	0.3579(29)	0.5129(4)	1	4.06(8)

Temperature: **40 K**
Rietveld Powder statistics: wRp = 6.27 % Rp = 5.34 % χ^2 = 6.724 %
Lattice constant: 7.093056(18) Å
Unit cell volume: 356.8619(16) Å

Atom	*x*	*y*	*z*	Occupancy	U_{iso} (x100)
O1	0.7040(3)	0.7040(3)	0.7040(3)	1	1.38(9)
D1	0.7555(6)	0.6762(6)	0.5752(7)	2/3	2.49(8)
O2	0.15585(33)	0.15585(33)	0.15585(33)	1	2.54(11)
D2	0.2394(3)	0.2394(3)	0.2394(3)	1	2.59(7)
D3	0.0114(16)	0.2036(11)	0.1811(12)	1/3	3.26(22)
N1	0.37859(24)	0.37859(24)	0.37859(24)	1	1.59(6)
D4	0.3588(4)	0.3584(3)	0.5124(4)	1	3.54(7)

Temperature: **4.2 K**
Rietveld Powder statistics: wRp = 5.66 % Rp = 5.00 % χ^2 = 5.763 %
Lattice constant: 7.091771(16) Å
Unit cell volume: 356.6680(14) Å

Atom	*x*	*y*	*z*	Occupancy	U_{iso} (x100)
O1	0.70423(24)	0.70423(24)	0.70423(24)	1	0.73(7)
D1	0.75928(47)	0.67835(50)	0.57701(56)	2/3	1.83(7)
O2	0.15607(26)	0.15607(26)	0.15607(26)	1	1.31(9)
D2	0.23880(26)	0.23880(26)	0.23880(26)	1	1.51(5)
D3	0.01424(133)	0.20723(89)	0.17783(103)	1/3	2.42(17)
N1	0.37944(20)	0.37944(20)	0.37944(20)	1	0.86(5)
D4	0.35734(30)	0.35783(23)	0.51507(31)	1	2.57(6)

APPENDIX 2

Equation of State parameters

For use with 3rd order Birch-Murnaghan equation of state,

$$P_{V,T} = \frac{3}{2} K_{0,T} \left(x^{7/3} - x^{5/3} \right) \left[1 + \frac{3}{4} \left(K'_{0,T} - 4 \right) \left(x^{2/3} - 1 \right) \right]$$

where $x = \rho / \rho_0$. Density as a function of temperature at ambient pressure is found from either a temperature independent thermal expansivity, α, given in the tables at some reference temperature, or from the expression below.

$$\rho_T = \rho_0 \exp\left[-\left(\frac{A}{B+1} \right) T^{B+1} \right]$$

The bulk modulus is described by a polynomial of the form,

$$K_T = K_0 + CT + DT^2$$

The first pressure derivative of the bulk modulus, K', is taken to be independent of temperature.

Equation of state (EoS) parameters given on the following pages are taken either from single literature sources at reference P-T conditions, or have been derived by fitting to many experimental data sets; pressure-volume-temperature data, melting volumes, and ultrasonic measurements. The parameters have been chosen to yield the best agreement with experimentally observed density values at pressure and temperature, and the greatest error is approximately 2 %.

EoS parameters

	Ice I	Ice II	Ice V[a]
ρ_0 (kg m^{-3})	934.6	1182.0	1267.0
α (K^{-1})	-	-	4.50×10^{-5}
A	2.522×10^{-8}	4.551×10^{-7}	-
B	1.582	0.9662	-
K_0 (GPa)	10.995	14.259	9.67
C	-0.00407	-0.0399	-
D	-2.051×10^{-5}	1.554×10^{-4}	-
K'	4.669	5.50	5.70

[a]All parameters at reference P = 0.48 GPa, reference T = 237.65 K

	Ice VI	Ice VIII	ADH I
ρ_0 (kg m^{-3})	1326.8	1502.2	988.93
α (K^{-1})	-	-	-
A	3.408×10^{-7}	1.7255×10^{-5}	1.1825×10^{-6}
B	1.2796	0.3610	1.0662
K_0 (GPa)	17.82	26.25	8.238
C	-0.0385	-0.0186	-0.000414
D	3.625×10^{-5}	1.619×10^{-5}	-3.845×10^{-5}
K'	5.40	4.00	5.50

	CH_4-clathrate	San Carlos Olivine[a]	Liquid $Fe_{0.9}S_{0.1}$ [b]
ρ_0 (kg m^{-3})	964.7	3343	5220
α (K^{-1})	-	2.66×10^{-5}	1.10×10^{-4}
A	7.77×10^{-8}	-	-
B	1.5578	-	-
K_0 (GPa)	10.025	131.1	45.6
C	-0.00407	-0.0223	-0.0104
D	-2.0513×10^{-5}	0	0
K'	5.2	3.8	5.0

[a]All parameters at reference P = ambient, reference T = 300 K

[b]All parameters at reference P = ambient, reference T = 1770 K

Equation of state references

Ice Ih

Dantl, G. (1968) Phys. Condens. Matt. **7**, 390.

Gagnon. R. E., H. Kiefte, M. J. Clouter, and E. Whalley (1988) J. Chem. Phys. **89**, 4522.

Gagnon, R. E., H. Kiefte, M. J. Clouter, and E. Whalley (1990) J. Chem. Phys. **92**, 1909.

Proctor. T. M. (1966) J. Acoust. Soc. America **39**, 972.

Röttger. K., A. Endriss, J. Ihringer, S. Doyle, and W. F. Kuhs (1994) Acta Cryst. B **50**, 644.

Shaw. G. H. (1986) J. Chem. Phys. **84**(10), 5862.

Ice II

Bizhigitov, T. B. (1987) PhD Thesis, Moscow.

Cruz León, G., S. Rodríguez Romo, and V. Tchijov (2002) J. Phys. Chem. Solids **63**, 843.

Kamb, W. B. (1964) Acta Cryst. **17**, 1437. [4.9, 4.10, 4.12, 4.14]

Kamb, W. B., W. C. Hamilton, S. J. La Placa, and A. Prakash (1971) J. Chem. Phys. **55**, 1934.

Lobban C. (1998) Ph.D Thesis, University of London.

Lobban, C., J. L. Finney, and W. F. Kuhs (2002) J. Chem. Phys. **117**, 3928.

This work, chapter 4

Ice V

Lobban C. (1998) Ph.D Thesis, University of London.

Lobban, C., J. L. Finney, and W. F. Kuhs (2000) J. Chem. Phys. **112**, 7169.

Shaw. G. H. (1986) J. Chem. Phys. **84**(10), 5862.

Tulk. C. A., H. Kiefte, M. J. Clouter, and R. E. Gagnon (1997) J. Phys. Chem. B **101**, 6154.

Ice VI

Bridgman. P. W. (1912) Proc. Am. Acad. Arts Sci. **48**, 307.

Bridgman. P. W. (1935) J. Chem. Phys. **3**, 597.

Bridgman. P. W. (1937) J. Chem. Phys. **5**, 964.

Gaffney. E. S. (1986) EOS: Trans. AGU **67**(16), 374.

Gagnon, R. E., H. Kiefte, M. J. Clouter, and E. Whalley (1990) J. Chem. Phys. **92**, 1909.

Kamb. B. (1965) Science **150**, 205.

Kuhs. W. L., J. L. Finney, C. Vettier, and D. V. Bliss (1984) J. Chem. Phys. **81**(8), 3612.

Shimizu. H. (1996) Physica B 219&220, 559.

Shimizu. H., T. Nabetani, T. Nishiba, and S. Sasaki (1996) Phys. Rev. B **53**(10), 6107.

Tulk. C. A., H. Kiefte, M. J. Clouter, and R. E. Gagnon (1997) J. Phys. Chem. B **101**, 6154.

Tulk. C. A., R. E. Gagnon, H. Kiefte, M. J. Clouter (1997) J. Chem. Phys. **107**(24), 10684.

Ice VIII

Baer. B. J., J. M. Brown, J. M. Zaug, D. Schiferl, and E. L. Chronister (1998) J. Chem. Phys. **108**(11), 4540.

Besson. J. M., Ph. Pruzan, S. Klotz, G. Hamel, B. Silvi, R. J. Nelmes, J. S. Loveday, R. M. Wilson, and S. Hull (1994) Phys. Rev. B. **49**(18), 12540.

Fei. Y., H. K. Mao, and R. J. Hemley (1993) J. Chem. Phys. **99**(7), 5369.

Hemley. R. J., A. P. Jephcoat, H. K. Mao, C. S. Zha, L. W. Finger, and D. E. Cox (1987) Nature **330**, 737.

Jorgensen. J. D., R. A. Beyerlein, N. Watanabe, and T. G. Worlton (1984) J. Chem. Phys. **81**(7), 3211.

Klotz. S., and J. S. Loveday (1999) ISIS experimental report RB 10412 (POLARIS).

Klotz. S., J. M. Besson, R. J. Nelmes, J. S. Loveday, and W. G. Marshall (1999) Nature **398**, 681.

Kuhs. W. L., J. L. Finney, C. Vettier, and D. V. Bliss (1984) J. Chem. Phys. **81**(8), 3612.

Liu. L-G. (1982) Earth. Planet. Sci. Lett. **61**, 359.

Loubeyre, P., R. LeToullec, E. Wolanin, M. Hanfland, and D. Hausermann (1999) Nature **397**(6719), 503.

Munro. R. G., S. Block, F. A. Mauer, and G. Piermarini (1982) J. Appl. Phys. **53**(9), 6174.

Olinger. B., and P. M. Halleck (1975) J. Chem. Phys. **62**(1), 94.

Shimizu. H. (1996) Physica B **219&220**, 559.

Shimizu. H., M. Ohnishi, S. Sasaki, and Y. Ishibashi (1995) Phys. Rev. Lett. **74**(14), 2820.

Shimizu. H., T. Nabetani, T. Nishiba, and S. Sasaki (1996) Phys. Rev. B **53**(10), 6107.

Walrafen. G. E., M. Abebe, F. A. Mauer, S. Block., G. J. Piermarini, and R. Munro (1982) J. Chem. Phys. **77**(4), 2166.

Wolanin, E., Ph. Pruzan, J. C. Chervin, B. Canny, M. Gauthier, D. Hausermann, and M. Hanfland (1997) Phys. Rev. B **56**(10), 5781.

This work, chapter 3

Ammonia dihydrate I

This work, chapter 8

Methane clathrate

Davidson. D. (1983) In, Gas hydrates – properties, occurrence and recovery (J. Cox, Ed), Butterworth, Woburn MA. pp1-6.

Gutt. C., B. Asmussen, W. Press, M. R. Johnson, Y. P. Handa, and J. S. Tse (2000) J. Chem. Phys. **113**(11), 4713.

Hirai. H., Y. Uchihara, H. Fujihisa, M. Sakashita, E. Katoh, K. Aoki, K. Nagashima, Y. Yamamoto, and T. Yagi (2001) J. Chem. Phys. **115**(15), 7066.

Shpakov. V. P., J. S. Tse, C. A. Tulk, B. Kvamme, and V. R. Belosludov (1998) Chem. Phys. Lett. **282**, 107.

Waite. W. F., M. B. Helgerud, A. Nur, J. C. Pinkston, L. A. Stern, S. H. Lirby, and W. B. Durham (2000) Ann. New York Acad. Sci. **912**, 1003.

San Carlos Olivine

Abramson, E. H., M. Brown, L. J. Slutsky, and J. Zaug (1997) J. Geophys. Res. **102**, 12252.

Duffy, T. S. and T. J. Ahrens (1993) Geophys. Res. Lett. **20**, 1103.

Zha. C.-S., T. S. Duffy, R. T. Downs, H. K. Mao, and R. J. Hemley (1998) Earth Planet. Sci. Lett. **159**(1-2), 25.

Liquid iron sulfide

Hixson. R. S., M. A. Winkler, and M. L. Hodgdon (1990) Phys. Rev. B **42**(10), 6485.

Sanloup. C., F. Guyot, P. Gillet, G. Fiquet, M. Mezouar, and I. Martinez (2000) Geophys. Res. Lett. **27**(6), 811.